On the Catalytically Active State and Structure-Activity Correlations of 3d Transition Metal Oxide Catalysts for Electrochemical Water Splitting

vorgelegt von
Diplom-Physiker
Arno Bergmann
geb. in Aachen

von der Fakultät II – Mathematik und Naturwissenschaften
der Technischen Universität Berlin
zur Erlangung des akademischen Grades

Doktor der Naturwissenschaften
– Dr. rer. nat. –

genehmigte Dissertation

Promotionsausschuss:

Vorsitzender:	Prof. Dr. Arne Thomas
Gutachter:	Prof. Dr. Peter Strasser
Gutachterin:	Prof. Dr. Christina Roth

Tag der wissenschaftlichen Aussprache: 13. Januar 2016

Berlin 2016

„ I try to hang on to myself
I don't believe in no one else
And I'm shaking like a leaf
As I fall into the street
But the girl with X-ray eyes
She's gonna see through my disguise”

Noel Gallagher

Danksagung

Eine Dissertation kann niemals ohne die Hilfe von anderen Menschen erfolgreich zum Abschluss gebracht werden. Hiermit möchte ich mich bei all diesen bedanken:

Zu allererst gilt mein Dank Prof. Peter Strasser, welcher mir es ermöglicht hat meine Dissertation in seiner Arbeitsgruppe unter großer wissenschaftlicher Freiheit anzufertigen. Dieser Umstand ermöglichte mir es viel zu lernen und doch war er mir, wenn nötig, immer eine große Hilfe und ermöglichte mir die Teilnahme an inspirierenden Konferenzen.

Des Weiteren möchte ich mich bei Prof. Christina Roth bedanken, dass sie sich bereiterklärt hat meine Arbeit als Gutachterin zu bewerten. Ich bedanke mich außerdem bei der BIG-NSE für das Stipendium und Dr. Jean-Philippe Lonjaret sowie meinen „Kesselkameraden“ für die spannende „initial phase“ und die interessanten Begegnungen danach.

Außerdem danke ich den freundlichen und kompetenten Menschen aus der Arbeitsgruppe von Prof. Holger Dau der FU Berlin und dabei vor allem Dr. Ivelina Zaharieva, Dr. Petko Chernev und Dr. Elias Martinez-Moreno für die produktive und lehrreiche Zusammenarbeit und die vielen Stunden, welche Sie u.a. mit meinen Proben am Bessy verbracht haben. Ein großer Dank geht auch an Dr. Detre Teschner vom Fritz-Haber-Institut für die äußerst kompetente, zuverlässige und sorgfältige Zusammenarbeit und seine Hilfe.

In der Arbeitsgruppe Strasser möchte ich mich vor allem bei Tobias Reier für produktive und inspirierende Unterredungen über Ergebnisse, Konzepte oder anderes sowie für seine Zeit am Mikroskop bedanken. Ich bedanke mich bei allen Studenten, die ihre Praktika sowie Bachelor- und Masterarbeiten unter meiner Anleitung angefertigt haben. Dabei möchte ich vor allem Manuel Gliech hervorheben, der stets hilfsbereit und zuverlässig ist und immer ein offenes Ohr hat. Eine Arbeit, welche zu großen Teilen auf Synchrotronmesszeiten beruht, benötigt die Hilfe vieler Menschen. Vielen Dank an alle, die mir geholfen haben. Ein besonderer Dank gilt hierbei an Frau Hong Nhan Nong, Camillo Spöri und Dr. Stefan Rudi, welche zusammen mit Tobias Reier auch die älteste und beste Kickerrunde der TC bilden. Ich möchte mich auch bei Dr. Nastaran Ranjbar für die schöne Zeit und die netten Gespräche innerhalb und außerhalb der TC bedanken.

Außerdem möchte ich mich bei der Nachwuchsgruppe von Dr. Ralph Krähnert bedanken. Bei Ralph bedanke ich mich für die kritischen Nachfragen, die guten Ratschläge und Hinweise. Ich weiß es zu schätzen, dass ich bis zuletzt mit seinen äußerst angenehmen und hilfsbereiten Mitarbeitern in einem Büro sitzen durfte. Dabei möchte ich vor allem Dr. Erik Ortel, Benjamin Paul, Denis Bernsmeier, Dr. Björn Eckhardt, Katrin Schulz und Roman Schmack danken! Vielen Dank für die vielen lustigen und musikalischen Stunden in Raum TC203!

Außerdem danke ich den Kollegen der Feinmechanischen Werkstatt, dem Glasbläser Carsten, Annette, Annegret, Sabrina und Astrid und ich danke allen, die ich vergessen habe!

Zusammenfassung

Die Entwicklung von aktiven, stabilen und kostengünstigen Elektrokatalysatoren für die Sauerstoffevolutionsreaktion (OER) ist der Schlüssel, um elektrische Energie mittels Wasserelektrolyse effizient in die chemische Energie von molekularem Wasser- und Sauerstoff umzuwandeln. Dieser Wasserstoff kann in großem Maßstab als Energiespeicher für die unstetig verfügbaren erneuerbaren Energieträger dienen. Die Entwicklung von verbesserten Elektrokatalysatoren aber benötigt ein besseres Verständnis über deren aktivitätsbestimmenden Eigenschaften und deren Struktur im katalytisch-aktiven Zustand. In dieser Arbeit wurden Katalysatoren basierend auf den Übergangsmetallen Mn und Co hergestellt und auf ihre OER Aktivität und Redoxchemie im neutralen und alkalischen Elektrolyten untersucht. Die Katalysatoren wurden vor und nach der OER umfangreich im Hinblick auf ihre Morphologie, Kristall- und lokale atomare Struktur sowie auf ihre elektronische Struktur und Komposition in den oberflächennahen Bereichen untersucht. Des Weiteren wurde die Struktur im katalytisch-aktiven Zustand mittels röntgenbasierten *in situ* Methoden bestimmt. Das Ziel dieser Arbeit ist es Struktur-Aktivitäts-Beziehungen zu identifizieren und die Ergebnisse in den wissenschaftlichen Kontext zu setzen.

Die Untersuchungen von zwei nanostrukturierten, geträgerten Mn Oxiden deckten dabei einen positiven Einfluss einer 3D statt einer 2D Verknüpfung von Mn-O Oktaedern auf die OER-Aktivität auf. Der katalytisch-aktive Zustand von beiden Mn-Oxiden besteht aus Mn^{4+} Ionen. Die Untersuchung von Co-basierten Elektrokatalysatoren enthüllte ein gemeinsames Strukturmotiv von di-μ-oxo verknüpften $Co^{3+/4+}$ O_h Ionen im katalytisch-aktiven Zustand. Dabei verwandeln sich die oberflächennahen Bereiche der Co_3O_4 Kristallite während der OER reversibel in eine röntgenamorphe $CoO_x(OH)_y$ Schale mit 3D verknüpften Co Oktaedern, welche unter nichtkatalytischen Bedingungen wieder kristallisiert. Im Gegensatz dazu verändern Co^{2+} Oxide ihre Struktur durch die OER partiell aber irreversibel in ein $CoO_x(OH)_y$ mit hauptsächlich Co^{3+} O_h Ionen. Es wurde entdeckt, dass die Anwesenheit von reduzierbaren Co^{3+} Ionen sehr vorteilhaft für die OER Aktivität ist und diese Ionen konnten mit einer speziellen oktaedrischen Bindungsumgebung in den oberflächennahen Regionen des $CoO_x(OH)_y$ erklärt werden. Außerdem wurden deren elektrochemischen und spektroskopischen Fingerabdrücke identifiziert.

Diese Arbeit zeigt die Wichtigkeit einer speziellen Koordination der Metallionen mit terminierenden O Atomen sowie einer Verknüpfung über di-μ_2-oxo Brücken für eine hohe OER-Aktivität. Diese Zentren können in ein mechanistisches Konzept integriert werden und entstehen durch strukturelle Unordnung wie eine kleine Domänengröße oder sind wegen einer speziellen Kristallstruktur vorhanden. Die Ergebnisse dieser Arbeit können zu einem vereinheitlichten Verständnis der elektrochemischen Wasserspaltung sowie der Identifizierung von bisher unentdeckten aktivitätsbestimmenden Eigenschaften führen und wird dabei helfen weiter verbesserte Katalysatoren für die Wasserelektrolyse zu entwickeln.

Abstract

The development of active, stable and inexpensive electrocatalysts for oxygen evolution reaction (OER) is a key step to efficiently transform electrical energy into the energy of chemical bonds of molecular hydrogen and oxygen using water electrolysis. This hydrogen can serve as storage medium for renewable energy sources with intermittent availability on large grid-scale. But the design of improved electrocatalysts requires better understanding of their activity-determining properties and their structure in the catalytically active state. In this work 3d transition metal oxides based on Mn and Co were synthesized and tested for their OER activity and redox electrochemistry in neutral and alkaline electrolyte. These electrocatalysts were extensively investigated before and after OER with respect to their morphology, their crystal and local atomic structure as well as their electronic structure and near-surface composition. Furthermore, the structure of their catalytically active state was identified using *in situ* X-ray techniques. This work aims at identifying structure-activity correlations and at relating the findings to state-of-art OER catalyst materials.

The investigation of two nanostructured, supported Mn oxides uncovered a beneficial influence of a 3D compared to a 2D layered cross-linking of Mn-O octahedra on the resulting OER activity. The catalytically active state of both Mn oxides exhibits mainly Mn^{4+} ions. The investigation of structurally-different Co-based electrocatalysts revealed a common structural motif of di-μ-oxo bridged $Co^{3+/4+}$ O_h ions in the catalytically active state. Therein, the near-surface region of the Co_3O_4 crystallites transforms reversibly during OER characterized by an amorphous $CoO_x(OH)_y$ shell with 3D octahedral cross-linking. This shell recrystallizes under non-catalytic rest conditions. In contrast, the structure of initially Co^{2+} oxides transforms partially but irreversibly after OER to a $CoO_x(OH)_y$ with mainly Co^{3+} O_h. The presence of reducible Co^{3+} sites was found to be highly beneficial for OER activity and could be explained by a special octahedral Co bonding environment in the near-surface structure of the $CoO_x(OH)_y$. The electrochemical and spectroscopic fingerprints of this activity-determining property were identified.

This work reveals the importance of special metal coordination with di-μ_2-oxo bridging as well as terminating O sites for high OER activity. These sites can be integrated into a mechanistic framework and originate from structural disorder as in case of low domain size or are prevalent due to the specific crystal structure. The results of this work can lead to a unified understanding of heterogeneous electrochemical water oxidation as well as to the identification of activity-determining properties and will help to develop improved electrocatalysts for water electrolysis.

Table of Contents

Danksagung V

Zusammenfassung VII

Abstract IX

Chapter 1 Introduction and Motivation 13

Chapter 2 Oxygen Evolution Reaction on 3d Transition Metal Oxides 17
2.1 Mechanism and Activity Descriptors 17
2.2 Electrocatalysts for Water Oxidation and OER 32

Chapter 3 Experimental 45
3.1 Physicochemical Characterization 45
3.2 Electrochemical Characterization 46
3.3 Experimental Setup for *in situ* X-ray based Structural Analysis 47

Chapter 4 Correlating Structural Motifs and Catalytic Activity of Layered and 3D Cross-linked MnO_x for OER 51
4.1 Experimental Details 52
4.2 Results 53
4.3 Discussion 65
4.4 Summary 67

Chapter 5 Reversible Amorphization and the Catalytically Active State of Crystalline Co_3O_4 during Oxygen Evolution 69
5.1 Experimental Details 70
5.2 Results 71
5.3 Discussion 80
5.4 Summary 82

Chapter 6 Linking Near-surface Structure, Redox Chemistry and Oxygen Evolution of Co Oxides and Their Catalytically Active State 85
6.1 Experimental Details 86
6.2 Results 89
6.3 Discussion 122
6.4 Summary 128

Chapter 7 Summary and Outlook 131

Bibliography 135

Acronyms 143

List of Tables 145

List of Figures 147

List of Publications 153

Appendix 155
A1 Supplementary Information to Chapter 4[121] 155
A2 Supplementary Information to Chapter 5[68] 160
A3 Supplementary Information to Chapter 6 171

Chapter 1 Introduction and Motivation

Climate change and global warming caused by increasing green house gas emissions as well as air pollution in western countries and especially in growing economies of Asia demand action to avoid tremendous effects on the ecosystem of planet earth and thus, on the basis of human living.[1-2] Therefore, an industrial transformation towards elevated sustainability by a more efficient utilization of resources and a change in primary energy supply (including electrical energy and heat), individual mobility and public transport is necessary. The contribution of renewable energy sources such as solar, wind and water power grew significantly in the past decades and still exhibit enormous economical potential and growing markets. However, application of renewable primary energy sources in the framework of a nuclear-free power supply needs a storage media which allows mitigating the intermittency of solar and winding power.[3-6]

Besides a great variety of technologies to transform and/or store electrical energy using mechanical and electrical methods such as pumped-storage facilities, compressed air, flywheel storage, capacitors and superconducting magnetic energy storage[7], electrochemical methods exhibit an efficient and clean way to transform electrical into chemical energy and vice versa. The most famous electrochemical storage devices are rechargeable batteries, flow batteries and supercapacitors.[7] Furthermore, water electrolysers and fuel cells can be used to utilize molecular hydrogen as chemical storage medium. Using H_2 has several great advantages because it exhibits a large gravimetrical energy density and is easily storable and transportable. In addition to that it can also partially be implemented into town-gas based heating systems by using today’s technology of the town gases infrastructure. But above all these advantages, energy transformation in electrolysers and fuel cells is free of carbon dioxide emission which is known to, *inter alia,* cause the green house effect.[6-9]

Water electrolysis was first discovered in Leyden (Netherlands) in 1789 by two Dutchmen, Adriaan Paets van Troostwijk and Johan Rudolph Deiman.[10] The first observation of the fuel cell effect (a voltage between a Pt/O_2 and a Pt/H_2 electrode dispersed in the same electrolyte) was published by Carl Friedrich Schönbein in January 1839. William Robert Grove unravelled the same effect almost simultaneously. In 1845 he developed the first fuel cell as power source called “gas battery”.[11]

The development of fuel cells was strongly influenced by their application as energy and water source in space missions. Nowadays they are applied as electrical power sources in cars, busses, submarines, and caravanning.[9, 12] Electrolysis is an established technique in industry to produce chlorine and other chemicals as well as electroplating and electrolytic etching.

However, water electrolysis for the production of molecular hydrogen is not yet commercialized. Hydrogen and oxygen molecules are generated from water molecules in the two electrochemical half-cell reactions of water electrolysis. The anodic water oxidation and oxygen evolution reactions (OER) exhibit strong efficiency losses whereas the cathodic hydrogen evolution reaction (HER) is comparably efficient, especially in acidic reaction conditions. A major cornerstone in the commercialization of electrolysers is the reduction of the costs which are strongly influenced by the choice of electrocatalysts for the anodic OER. In industrial applications electrolysers are mostly operated in acidic reaction condition which limits the choice of OER electrocatalysts to noble metals like Ru and Ir. Ru-based electrocatalysts represent the most-active electrocatalysts but lack of sufficient stability due to severe metal dissolution.[13] Ir-based electrocatalysts are also highly active but exhibit a significantly higher stability. Therefore, these materials are often used as bimetallic oxides.[8] For industrial applications the stability is further improved at sufficiently high catalytic activity by dispersing the Ru-Ir oxide in a Ti oxide matrix. Thereby, the noble metal content of these so-called dimensionally-stable anodes (DSA) is significantly reduced and the stability increased.[14-15] But the largest disadvantage of these catalysts is the scarcity of noble metals which leads to a high price. Therefore, it is questionable whether the abundance in the earth crust is high enough to enable water electrolysis to generate hydrogen on large grid-scale.[3] The use of non-noble metals like Mn, Fe, Co and Ni would reduce the costs of the OER electrocatalysts significantly due to a substantially higher abundance.[3] However, these 3d TM oxides are not sufficiently stable in acidic electrolytes and thus, their application is limited to neutral and alkaline electrolyte.

Besides choosing metals which are abundant and inexpensive, the mass-based catalytic activity of the catalysts needs to be optimized. Catalytic activity is strongly related to the availability of active catalyst sites for the corresponding reaction. In a first approximation the number of active sites is directly related to the physical surface area of the catalyst. Thus, dispersion of a nanostructured catalyst on a conductive and stable high surface area support is a well-established strategy to increase the mass-activity and to decrease the catalyst costs. However, optimal catalyst design requires extended knowledge about the nature of the active site and activity-determining structural properties. There is an ongoing controversy about the importance of structural disorder to achieve high catalytic activity. This structural disorder incorporates special coordination or oxidation state of metal ions, defects and vacancies in the bulk of an amorphous material or at its surface, sub-nanometre sized catalyst domains, presence of super-active sites. Thus, the nature of the catalytically active sites for OER is still unknown and their electrochemical and spectroscopic fingerprints are not yet identified.

Furthermore, OER proceeds under highly oxidizing conditions in an aqueous electrolyte which represent harsh conditions for 3d TM oxides and typically redox transitions of the metal ions precede the OER electrocatalysis.[16] Therefore, the structure of the catalytically-relevant near-surface in the resting and oxygen-evolving state likely differ and the structural motif leading the oxygen evolution remain unknown. The application of surface-sensitive techniques under OER conditions can in principle close this knowledge gap. But their application is strongly limited as these techniques are mostly based on the detection of photoelectrons which have an extremely short mean free path in aqueous solutions. Therefore, structural analysis of electrocatalysts under electrochemical reaction conditions based on hard X-ray radiation is very important because it enables the identification of the activity-determining properties of the electrocatalysts and the structure of the catalytically active state.

This work aims at determining the structure and properties of the oxygen-evolving state of 3d transition metal oxide electrocatalysts for OER in neutral electrolyte and at identifying correlations between catalytic activity and the long-range order, local atomic and (near-surface) electronic structure. These findings will lead to a better understanding of OER electrocatalysis and thus, will aid to develop improved electrocatalysts. This work is structured as follows:

In Chapter 2 the theoretical background and state-of-knowledge of the electrochemical water oxidation and oxygen evolution reaction are described. Special emphasis is placed on activity descriptors and possible reaction mechanisms on 3d transition metal based oxides, hydroxides and perovskites in neutral and alkaline electrolyte. This introduction will allow integrating the results of this work into the scientific context.

In Chapter 3 the experimental details of the syntheses and applied physicochemical characterization methods of the electrocatalysts are presented. An experimental setup for *in situ* X-ray based structural characterization of catalytic coatings, which was developed within this work, is explained.

In Chapter 4 the findings on a correlation between the octahedral cross-linking of Mn ions in two, nanostructured, supported Mn oxides and the electrocatalytical properties as well as their redox electrochemistry are presented. Therefore, the crystal and local atomic structure of these Mn oxides were investigated using X-ray based techniques in the as-prepared state and the apparent changes upon electrocatalytic operation were determined. Furthermore, the influence of the buffer capacity on the catalytic activity of these Mn oxides was investigated by pH titration experiments. From these findings first correlations between local atomic structure and the catalytic properties are formulated.

In Chapter 5 findings on the catalytically active state of *crystalline* Co_3O_4 film catalysts in neutral phosphate-containing electrolyte are presented. The crystallinity and local atomic structure of the Co_3O_4 were determined under electrochemical reaction conditions at various electrode potentials as well as in the dry state before and after electrocatalysis using advanced *in situ* X-ray studies. Additionally, the differences in the surface chemistry and electronic structure of the as-prepared state and after OER are described. A reversible structural transformation of the near-surface between resting and catalytically active state was revealed and is discussed with respect to general implications for oxygen evolution on crystalline catalyst materials.

In Chapter 6 the influence of initial crystallinity, Co coordination and oxidation state of four differently coordinated Co oxides on their redox electrochemistry and electrocatalytic properties is identified. For this purpose, the physicochemical properties of the as-prepared and the OER-conditioned state of the Co oxide catalysts were extensively investigated using bulk and surface sensitive techniques and the findings are presented. Additionally, the local atomic structure of the oxygen-evolving state as determined by *in situ* X-ray absorption spectroscopy is described. A correlation between the Co oxide redox chemistry, electronic and atomic structure of the near-surface is identified. These findings offer new insights into the activity-determining properties of Co-based OER electrocatalysts, their electrochemical and spectroscopic identification and the importance of special Co coordination to achieve high OER activity in neutral electrolyte.

In Chapter 7 the results of this work are summarized and general conclusions on structure-activity-correlations of 3d transition metal oxides/oxyhydroxides are drawn. Additionally, perspectives for further investigations on the basis of the findings of this work and their integration into the state-of-knowledge are given.

Chapter 2 Oxygen Evolution Reaction on 3d Transition Metal Oxides

In this chapter the principles of electrochemical water oxidation and oxygen evolution on 3d TM ion based electrocatalysts as they are known today are described. This introduction is necessary to integrate the results of this work into the state-of-knowledge. First, the thermodynamics and kinetics of electrochemical reactions are formulated and then related to an exemplary OER mechanism. After this an overview on descriptors used for the electrocatalytic OER activity is given. The section is followed by detailed examination of the OER mechanism with special emphasis on the participation of lattice oxygen and on Co oxides in neutral conditions as known from experimental and computational studies. Furthermore, the structure and properties of Co oxides and (oxy)hydroxides electrocatalysts as well as their electrochemical characterization in neutral and alkaline electrolyte are explained. Thereafter, Mn oxides and their application as OER electrocatalysts are shortly summarized.

2.1 Mechanism and Activity Descriptors

Water electrolysis can be divided into two half-cell reactions; the oxygen evolution reaction (OER) at the anode and the hydrogen evolution reaction (HER) at the cathode side. Both electrodes are separated by an electrolyte which is ideally ion-conductive, gas-impermeable and electrically insulating.

The overall chemical equation of water electrolysis is shown in Scheme 1 for acidic and neutral electrolyte and in Scheme 2 for alkaline electrolyte. Water electrolysis proceeds via different reaction pathways in acidic/neutral and alkaline reaction conditions. In acidic and neutral electrolyte water is the reagent at the anode side where it gets electrochemically oxidized yielding in molecular oxygen, electrons and protons. The protons travel through the electrolyte and the electrons through the electrical circuit to the cathode side where they form H_2.

Scheme 1: Water electrolysis in acidic and neutral electrolyte

Anode	$2\ H_2O$	$\leftrightarrow$	$O_2 + 4\ H^+ + 4\ e^-$	OER
Cathode	$4\ H^+ + 4\ e^-$	$\leftrightarrow$	$2\ H_2$	HER
Overall	$2\ H_2O$	$\leftrightarrow$	$O_2 + 2\ H_2$	

Scheme 2: Water electrolysis in alkaline electrolyte

Anode	4 OH^-	↔	$O_2 + 2\ H_2O + 4\ e^-$	OER
Cathode	4 $H_2O + 4\ e^-$	↔	$2\ H_2 + 4\ OH^-$	HER
Overall	2 H_2O	↔	$O_2 + 2\ H_2$	

In alkaline electrolyte the hydroxyl ions are the reagent at the anode side yielding in water molecules, molecular oxygen, and electrons. Water molecules get reduced at the cathode side and form molecular hydrogen and hydroxyl ions together with the electrons. The hydroxyl ions travel through the electrolyte to the anode side.

Thus, OER demands the extraction of four electrons and protons from the water molecules which travel to the counter electrode through the electrical circuit and the electrolyte, respectively. The cathodic HER is a fast reaction in neutral and acidic electrolyte which does not lead to large efficiency losses. In contrast OER is more complex because it involves the formation of the O-O bond. The majority of the electrochemical efficiency losses in water electrolysis are caused at the anode side.

To describe the reaction rate of an electrochemical reaction it is necessary to take their thermodynamics and the kinetics into account. These aspects are discussed in the next section.

2.1.1 Thermodynamics and Kinetics of Electrocatalytic Reactions[17]

The open circuit potential of an H_2/O_2 cell is in the ideal case 1.229 V which is equal to the redox potential E^0 of H_2O/O_2 redox couple on the reversible hydrogen electrode (RHE) scale. Therein, the potential of hydrogen electrode is defined as zero. This redox potential defines the thermodynamic Gibbs free energy limit for the anodic water oxidation and cathodic oxygen reduction reaction (ORR). It is thermodynamically possible to reduce O_2 to H_2O below this electrode potential whereas above H_2O can be oxidized to O_2. E^0 can be calculated on the reversible hydrogen electrode scale via $E^0 = -\Delta G^0 \cdot (nF)^{-1}$ in which ΔG^0 is the Gibbs free energy of the reaction ($-474.4\ kJ \cdot mol^{-1}$), n is the number of transferred electrons (four), and F is the Faraday constant ($96485\ C \cdot mol^{-1}$). The RHE is generally used as reference because the redox potential of H_2O/O_2 is independent from pH.[17]

The current i of an electrocatalytic reaction depends on the reaction rate k_i, the number of electrons n transferred per catalytic turnover, and on the concentration of the reagent c_i. Additionally, anodic and cathodic reaction proceed always simultaneously at the electrode and thus, the current i has to be described via

$$i = i_{anodic} + i_{cathodic} = n \cdot F \cdot (k_{ox}c_{red} - k_{red}c_{ox}). \qquad 1$$

The reaction rate k_i follows Arrhenius law and it is

$$\mathrm{k_i} = \mathrm{B_i} \cdot \mathrm{e}^{\frac{-\Delta\ ^{\ddagger}\mathrm{G(E)}}{\mathrm{RT}}}, \qquad 2$$

in which $\Delta\ ^{\ddagger}\mathrm{G(E)}$ is the Gibbs free energy of activation or activation energy of the reaction which depends on the electrode potential E. The reaction rate k_i depends also on catalyst and reaction specific constant B, the gas constant R, and the temperature T. The constant B incorporates catalyst properties such as active site density and the rate constant k_0. The activation energy is the potential-dependent energy difference between transition state and the reagent and is thus, an energy barrier that has to be passed to drive the electrochemical reaction. Taylor extension of the activation energy $\Delta\ ^{\ddagger}\mathrm{G(E)}$ yields in first approximation a linear relationship with

$$\Delta\ ^{\ddagger}\mathrm{G(E)} = \Delta\ ^{\ddagger}\mathrm{G}(E^0) \pm \beta nF(E - E^0), \qquad 3$$

in which β denotes the asymmetry parameter of the reaction. This parameter reflects the asymmetry of the energy barrier and incorporates the possible influence of the counter reaction during the current flow. The asymmetry parameter β can be replaced by the symmetry factor α which is $\alpha = -\beta_{ox}$ and $1-\alpha = \beta_{red}$. The difference between electrode potential E and redox potential of the reaction E^0 is the overpotential η. Combining the Eqns. 1-3 leads to the Butler-Volmer equation which describes the dependence of the catalytic current on the overpotential, symmetry factor and temperature by

$$\mathrm{i} = \mathrm{i_0} \cdot \left(\mathrm{e}^{\frac{\alpha \mathrm{nF}}{\mathrm{RT}}\eta} - \mathrm{e}^{\frac{-(1-\alpha)\mathrm{nF}}{\mathrm{RT}}\eta}\right). \qquad 4$$

Therein, i_0 is the exchange current density which depends on the catalyst and reaction specific constant B and is given by

$$\mathrm{i_0} = \mathrm{n} \cdot \mathrm{F} \cdot \mathrm{B} \cdot \mathrm{c} \cdot \mathrm{e}^{\frac{-\Delta\ ^{\ddagger}\mathrm{G}(E^0)}{\mathrm{RT}}}. \qquad 5$$

At a sufficiently high overpotential of ~100 mV the counter reaction path and thus, the negative term in Eqn. 4 can be neglected. The reaction rate increases exponentially with overpotential and the Butler-Volmer equation can be rewritten as the Tafel equation which is given by

$$\eta = b \cdot \log\left(\frac{\mathrm{i}}{\mathrm{i}_0}\right) \text{with } \mathrm{b} = 2.302 \cdot \frac{\mathrm{RT}}{\alpha\mathrm{nF}}. \qquad 6$$

Therein, b is defined as the Tafel slope which describes the slope of the linear E-$\log_{10}(i/i_0)$ profile. In the ideal case the Tafel slope is related to the reaction mechanism and the rate-determining step but in a real electrochemical system the Tafel slope can be influenced by various kinetic processes. The overpotential of an electrochemical reaction arises due to the kinetics of the electrochemical reaction but additional overpotentials can be present in an electrochemical setup. These processes are mostly related to transport processes of electrons, protons or hydroxyls. Furthermore, mass transport phenomena like limited convection/diffusion of reagents and products can limit or hamper the reaction rate and thus, the current density. Mass transport losses are minimized by conducting rotating disk electrode (RDE) experiments in which a hydrostatic equilibrium is established at the electrode-electrolyte interface. The concentration of the reagents (especially in case of water oxidation in aqueous electrolyte) is thus, independent from reaction conditions and the removal of the gaseous products is fast. Overpotentials due to electron conduction through the electrical circuit and proton transport through the electrolyte are compensated by an Ohmic correction of the electrode potential. The overall Ohmic resistance of the electrochemical setup is usually determined by potentiostatic electrochemical impedance spectroscopy (PEIS). Thus, in RDE experiments the kinetic processes at the electrode-electrolyte under electrochemical conditions can be investigated.

Historically, the Tafel slope was used to identify the rate-determining step of electrode reactions and to get insights into the reaction mechanism.[18] This has been done for electrochemical reactions such as hydrogen or chlorine evolution. However, it was shown that any additional transport processes that cannot be easily corrected influence the Tafel slope.[19] The determination of the reaction mechanism purely based on Tafel slope analysis therefore demands various assumptions and is questionable for complex reactions. As a result, the Tafel slope has to be discussed carefully and has to be combined with other methods e.g. *in situ* spectroscopic investigations and density functional theory (DFT) calculations to draw conclusion on reaction mechanism and the rate-determining step. But the Tafel slope can be used to identify trends in the kinetic processes of OER on similar electrocatalysts investigated under identical reaction conditions. These trends are investigated in this work for Mn- and Co-based electrocatalysts.

2.1.2 Reaction Mechanism of Water Oxidation and Oxygen Evolution

The development of highly-active electrocatalysts for OER needs understanding of the reaction mechanism and the *rate-determining step* (*rds*). All other reaction steps prior to and after the *rds* are in equilibrium during the reaction. In OER the formation of the O-O bond and/or the release of O_2 at the anode side are key steps. Only with knowledge about the *rds* it is possible to tailor electrocatalysts with elevated OER activity.

However, to enable an electrocatalytic reaction it is necessary to transport electrons between the reagents or reaction intermediates and the catalyst surface which is realized by chemical bonds. Thus, chemical bonds to the catalyst surface are needed to oxidize water/hydroxyl ions electrochemically. So far, the reaction mechanism of OER is not definitely known and many different mechanisms have been proposed by researchers.[20] These mechanisms differ e.g. by the number of catalytic sites involved in the reaction and by the nature of O-O bond formation.

The reaction mechanism given in Eqns. 7-10 was used to calculate theoretical overpotential for OER based on the thermodynamics. It received lot of attention and was applied for various metal and oxide surfaces in acidic or neutral electrolyte.[21-25]

$$\mathrm{M\text{-}*} + 2\,\mathrm{H_2O} \leftrightarrow \mathrm{M\text{-}OH} + \mathrm{H_2O} + \mathrm{H^+} + e^- \qquad \Delta G_{OH} \tag{7}$$

$$\mathrm{M\text{-}OH} + \mathrm{H_2O} + \mathrm{H^+} + e^- \leftrightarrow \mathrm{M\text{-}O} + \mathrm{H_2O} + 2\,\mathrm{H^+} + 2\,e^- \qquad \Delta G_{O} \tag{8}$$

$$\mathrm{M\text{-}O} + \mathrm{H_2O} + 2\,\mathrm{H^+} + 2\,e^- \leftrightarrow \mathrm{M\text{-}OOH} + 3\,\mathrm{H^+} + 3\,e^- \qquad \Delta G_{OOH} \tag{9}$$

$$\mathrm{M\text{-}OOH} + 3\,\mathrm{H^+} + 3\,e^- \leftrightarrow \mathrm{M\text{-}*} + \mathrm{O_2} + 4\,\mathrm{H^+} + 4\,e^- \qquad \Delta G_{O2} \tag{10}$$

Therein, only one metal site participates in the reaction. In the first step a water molecule is deprotonated and the adsorbed hydroxyls are subsequently stepwise oxidized. The O-O bond is formed via nucleophilic attack of an adsorbed O by a water molecule. This reaction mechanism can be translated to the alkaline reaction conditions by replacing water by hydroxyl ions and adjusting the charge balance.[20] In this case, the adsorbed hydroxyls are chemically deprotonated by OH^- from the electrolyte. According to DFT calculations, the formation of the OOH intermediate from adsorbed O and H_2O from electrolyte is the most important reaction step and involves the formation of the O-O bond. Desorption of molecular O_2 yields in a free metal site at the surface of the catalyst.

However, this reaction mechanism represents a simplified pathway because it neglects various possible processes during OER. The participation of adjacent metal sites and multiple O atoms from the catalyst surface is not taken into account. Furthermore, the removal of the protons from the intermediates is not specifically considered. Other reaction mechanisms have been proposed which involve the participation of adjacent metal sites although these sites might not play a role in O-O bond formation and thus, the *rate-determining step* of OER. An overview on possible OER reaction mechanisms with special emphasis on the participation of lattice O and Co oxides is described in section 2.1.4-5 in more detail as the experimental results of this work have to be integrated into the state of knowledge.

2.1.3 Activity-determining Properties of OER Electrocatalysts

The understanding of OER catalysis and the design of improved electrocatalysts needs the identification of activity-determining properties. These can be identified by a comparison of the physicochemical properties and the catalytic activity of various electrocatalysts. In this section, a set of possible descriptors are described.

Thermodynamics and Scaling Relationship

In the 1980's Sabatier principle which proposes an optimal degree of interaction between the catalyst and the educts or reaction intermediates was experimentally extended to OER. An optimal enthalpy of the transition from a lower to a higher oxidation state of the metal oxide leads to an optimal catalytic activity in acidic and alkaline electrolyte.[26] Similarly, the electrocatalytic activity of perovskite catalysts and earlier for metal electrodes could be correlated to the enthalpy of hydroxide formation.[27-28] Thus, the catalytic activity is related to the thermodynamics of the electrochemical redox transitions on the catalyst surface. These redox transitions can in turn be related to the binding energy of OH or OOH which are crucial reaction intermediates of OER.

According to rule of BEP (Brønsted-Evans-Polany) the enthalpy change of the reaction step is linearly related to the activation energy of the transition step. In this way, the transition state influences the catalytic activity. The binding energy of OH is furthermore related to the binding energy of OOH on the same catalyst surface by an offset and scales linearly with catalyst surface. Thus, the binding energy of the key intermediates of OER cannot be tuned independently and the so-called scaling relationship limits the optimization of catalysts. The electrocatalytic activity depends on the potential-dependent activation energy of the reaction but the overall activation energy as used in Eqn. 2 and 3 can be replaced by the activation barriers of individual reaction steps.

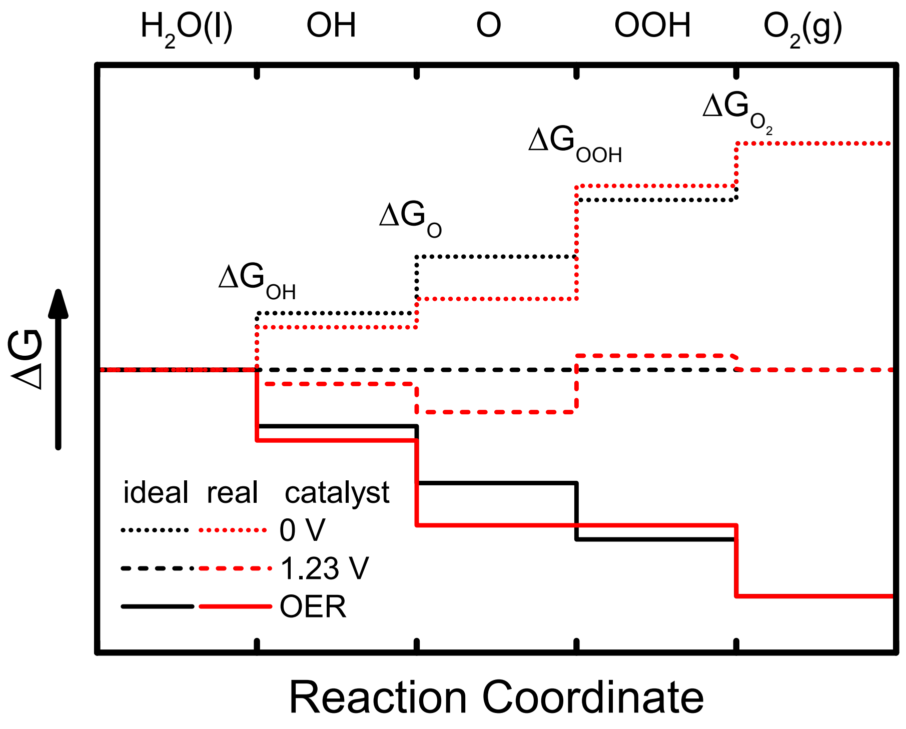

Figure 1: Schematic diagram of Gibbs free energy of reactive species and intermediates as function of reaction coordinate within the four step mechanistic framework considered by Rossmeisl.[21-25] The educt, reaction intermediates and product as well as the activation energies for the reaction intermediates are denoted. In case of an ideal catalyst (black) all activation energies are equally large. On a real catalyst (red) one reaction step defines the lowest overpotential at which all reaction steps are energetically downhill and thus, occur spontaneously. See Eqns. 7-10 and the next section. Figure adapted from Dau et.al.[29] and Hong et.al.[20].

Energy diagrams for OER can be generated by assuming a particular reaction pathway in which the individual activation energies are known. In the schematic diagram shown in Figure 1 it can be seen that the activation energies differ between the individual reaction steps for a real catalyst. Tuning the electrode potential or overpotential changes the energy difference between the reagent and the product. On a real catalyst one reaction step appears to be potential-determining because this reaction step needs the highest overpotential to turn energetically downhill. Above this overpotential all reaction steps occur spontaneously. In the ideal catalyst case, all activation barriers are equally high leading to the case that all reaction steps turn energetically downhill e.g. above the H_2O/O_2 redox potential of 1.23 V. Referring to the scaling relationship described above, an optimal catalyst would exhibit a 1:1 scaling of the activation barriers with an offset of ~2.46 eV between the binding energy of OH and OOH. Unfortunately, the scaling between OH and OOH binding energy on metal and metal oxide surfaces is 1:1 but with an offset of ~3.2-3.4 eV. Thus, the formation of OOH intermediate appears to be potential-determining step in most cases. In contrast, the scaling of the binding energy of O and OH is 2:1. Thus, the difference in binding energy of O and OH changes with catalyst surface. The difference in binding energy between O and OH has often been used as descriptor for the catalytic activity determined from DFT calculations.[21-23, 30-31] These relations lead to optimal binding energies of reaction intermediates on the catalyst sites and the formulation of a volcano-like activity profiles.[20]

Due to this scaling relationship the optimization of the binding energy and catalytic activity is limited. However, concepts appeared recently to mitigate the scaling relation by the design of multiple active sites on the catalyst surface. The catalytic activity was shown to increase in presence of two adjacent metal sites with different binding energies for OH and OOH. In this way, the activation barriers for reaction steps can be tuned individually. It was shown experimentally that the presence of nanoparticular Au and other noble-metal on the catalyst surface enhances the OER activity of Mn- and Co oxides.[32-33] DFT calculations showed that the presence of AuO_x sites on MnO_x and CoO_x surfaces can extract protons from the reaction intermediates more easily and thus, decrease the activation barriers of the potential-determining step which is the formation of M-OOH from M=O.[34] The same effect was seen in calculations for OER on Ru-Ni and Ru-Co oxide surfaces which appeared more active than pure RuO_2. The presence of hydrogen-accepting O sites connected to Co/Ni atoms was identified to decrease the theoretical overpotential.[30] Experimentally, electrocatalysts of Ni- and Co-doped RuO_2 were found to be more active than bare RuO_2 but the presence of Ni/Co on the catalyst surface during acidic reaction conditions was not verified and might be questionable.

Electronic Structure

Another descriptor of OER activity used for perovskites with 3d transition metal on the B sites is the estimated occupancy of 3d e_g electrons. A volcano profile was found for the catalytic current in alkaline electrolyte when the (estimated) occupancy of e_g electrons was used as descriptor. The optimal occupancy of e_g electrons is slightly above 1.0 and a $Ba_{0.5}Sr_{0.5}Co_{0.8}Fe_{0.2}O_{3-\delta}$ exhibit the lowest overpotential.[35] The number of e_g electrons is related to the relative occupancy of the antibonding states which influences strength of the metal-oxygen bond. Thus, it was concluded that perovskites in which the TM ions exhibit an e_g occupancy <1 bind OH too strong whereas an occupancy significantly >1 leads bond strength of the OH which is too weak. This effect can also be seen as the OER activity along the 3d transition metals from Mn to Ni increases with the electronegativity and the number of 3d electrons of the TM ions in perovskites.[27, 36] The bond strength of the OH decreases along this series and this finding is in agreement with the results for pure $MO_x(OH)_y$ for OER in alkaline electrolyte.[37]

The findings about the influence of electronegativity and the occupancy of e_g states on OER activity show that the electronic structure of the electrocatalysts significantly influences the OER activity. In ORR on Pt, the position of the metal d-band centre was found to significantly influence the catalytic activity by tuning the Pt-O bond strength. This has been *inter alia* shown for the enhanced catalytic activity of PtM_x core-shell nanoparticles with $M \in$ (Ni, Co, Cu) compared to bare Pt. The lattice strain in the Pt–rich shell induces a downward shift of the d-band centre which weakens the Pt-O bond.[38] Thus, the electronic configuration can be used as a descriptor for catalytic activity in perovskites and metals for oxygen electrocatalysis but it finally represents the thermodynamics of the binding energy of the key intermediates.

In case of metal oxides and perovskites, it is not sufficient to consider the electronic configuration of the TM ions but the complete TM-O_6 building block has to be taken into account. This is especially important because the potential/rate-determining step might involve an electron transfer most likely via oxygen ions to form the O-O bond. In metal oxides and perovskites ionic bonds are formed between metal ions and oxygen atoms. But the spatial overlap of the 3d orbitals of TM ions with the adjacent O 2p orbitals lead to covalent mixing or hybridization and to the formation of a band structure. The metal-oxygen bonds in TM oxides have mixed ionic-covalent character. The spatial overlap of the O 2p orbitals differs strongly between metal $t_{2(g)}$ states and $e_{(g)}$ states leading to π- and σ-(anti)bonding states, respectively. The electron donation of the O atoms in the crystal leads to a splitting of the 3d states and their energy difference is called crystal field stabilization energy (CFSE). In the octahedral coordination of TM-O_6 the t_{2g} states are energetically lower than the e_g states because the t_{2g} states have a lower spatial overlap with the 2p orbitals than the e_g states. In case of a tetrahedral coordination of TM-O_4 this order is reversed.[39]

Considering the aspects discussed above the influence of the charge transfer properties on the electrocatalytic activity has to be taken into account. Many TM oxides/oxyhydroxides which are considered as electrocatalysts are not electrically conductive in ground state. However, the electrical conductivity was already used to classify electrocatalysts in early works.[40] Recently, this aspect was reconsidered for TM oxyhydroxides in alkaline electrolyte and especially the influence of the Fe incorporation on the catalytic activity. Therein, it was revealed that the electrical conductivity of the films as measured under electrochemical conditions increases significantly anodic of the typical redox transition preceding the catalytic wave (e.g. the Ni^{2+}/Ni^{3+}). This can be explained by low spin d^6 configuration of Ni^{2+} (and also of Co^{3+}) in which the t_{2g} orbitals and thus, the valence band are completely filled. The e_g orbitals are empty and strongly separated by a large band gap of e.g. 1.60 eV for Co_3O_4.[41] Anodic of the redox transition one d electron is electrochemically removed leading to d^5 configuration of the TM ions. Thereby, unoccupied states in the t_{2g} orbitals lead to a conduction band in the oxide which significantly increases electrical conductivity.[42-43] This transition from a semiconductor to a conducting or metallic oxide significantly enhances the electron transport through the catalysts and possibly enables catalytic activity.

Furthermore, the importance of the orbital hybridization during OER was shown for Co-containing perovskite surface during elevated temperature electrochemical oxygen evolution and oxygen incorporation.[44] A strong influence of the redox transitions on the metal-oxygen covalency was identified. During anodic polarization the occupancy of the σ-bonding states decreases which can only partially be explained by the shift in Fermi level due to the electrode potential. In addition, a change in metal-oxygen covalency was found under OER conditions. A narrow state of O 2p character has been proposed to exchange charge with O adsorbates. Thus, the whole TM-O_6 octahedron might be considered as redox-active building block and charge transfer via hybridized TM-O orbitals are of great importance.

In addition to the thermodynamic properties of the metal-oxygen bond and properties related to the charge transport between adsorbates and catalyst surface as well as within the catalysts the catalytic activity strongly depends on the active site density. The importance and possible measures of this activity-determining property are described in the next section.

Active Site Density

The catalytic activity of a material strongly benefits from a larger active site density and is expected to scale with the number of catalytically active sites. This can be seen in the Butler-Volmer equation (Eqn. 4) in which the factor B_i incorporates the number/density of active sites (Eqn. 5). However, to determine the number of active sites of a catalyst their electrochemical and spectroscopic fingerprints have to be known. This is difficult as long as their structure and properties remain unknown. So far, there is no developed strategy to specifically determine the OER active sites in oxides or perovskite electrocatalysts.

Therefore, the physical or electrochemical surface area is usually a first approximation assumed to be correlated in to the number of active sites. The physical surface area can be probed using adsorption/desorption experiment like Brunauer-Emmet-Teller (BET) analysis in which the number of physisorbed N_2 or Kr is determined.[45] This technique is widely applied to powder and high-surface area catalysts. More specifically, the number of sites was determined by pulsed CO chemisorption.[46] Also Zn^{2+} adsorption followed by elemental analysis e.g. via ICP-OES or –MS experiments can be used but convincing agreement with other techniques could not been shown for most oxide electrocatalysts, except for MnO_2.[47-48]

The electrochemical surface area (ECSA) can be determined by the oxidation of adsorbed probe molecules such as CO in voltammetric stripping experiments or via the hydrogen underpotential deposition (Hupd) peak. These techniques are widely used for Pt-based electrocatalysts but its application for oxides is limited due to the absence the Hupd and the weak binding energy of CO on their surface.[49-50] The determination of the ECSA of oxides/oxyhydroxides is performed via the determination of the electrochemical capacitance or via the voltammetric surface charge. The electrochemical capacitance can be determined using electrochemical impedance spectroscopy. An equivalent circuit consisting of a resistor representing the Ohmic character of electrolyte and a resistor-capacitance element representing the electrode/electrolyte interface is then used to fit the experimental data. In addition, the capacitance of an electrocatalyst can be determined from a series of cyclic voltammograms recorded at selected scan rates in a potential range where no redox transitions or catalytic reaction occurs. The charging current of a capacitor depends linearly on the scan rate and thus, the capacitance can be obtained from the slope of a linear fit. By using a specific capacitance (determined from model catalysts which were measured in the same electrolyte) the ECSA could be estimated from the electrochemical capacitance. The specific capacitance varies between 22 and 130 $\mu F \cdot cm^{-2}$.[51]

For Ru- and Ir-oxide thin film electrocatalysts the anodic surface charge is established as a relative measure of the ECSA. This value is determined by integrating the anodic charge transferred during a potential scan in a certain potential range.[52]

Furthermore, the number of redox active metal sites can be estimated from the redox transitions identifiable by cyclic voltammograms.[53] Therefore, the charge transferred during redox transitions has to be determined in analogy to the voltammetric surface charge. This method has also the advantage of being an *in situ* method but exact quantification of metal ions can be quite complicated as the redox peaks can be broad and can interfere each other or can be superimposed by the catalytic current.

In summary, there are many ways to measure properties of electrocatalysts which are related to the (electrochemical) surface area and to the active site density. But so far, no method has been established to measure active site density, especially on 3d TM oxides. Therefore, the identification of the nature and (electrochemical) fingerprint of the active site has to be unravelled. Before this will be achieved these described techniques can be used to estimate specific OER activities of electrocatalysts and compare this (at least) with similar materials measured under identical conditions.

2.1.4 Participation of Lattice Oxygen in OER Mechanism

In section 2.1.2 a generalized OER mechanism which is the basis for many DFT calculations was discussed. But to gain deeper insights into the OER mechanism especially on Co oxides it is necessary to choose a broader approach and to take into account additional processes. This is especially necessary to explain the experimental results of this work. Specifically, the participation of oxygen atoms from the oxide lattice is an important aspect in understanding OER and the catalytically active state of the near-surface of electrocatalysts. It has been shown in studies for various electrocatalysts that oxygen from the oxide lattice participates in the OER mechanism independently from TM ion and electrolyte.[54-56]

One of the first investigations using ^{18}O-labelled electrolyte for electrocatalytical OER was performed on $M_xCo_{3-x}O_4$ electrocatalysts with $M \in$ (Ni, Li). [57-58] The intention of this study was to determine the number of active sites. It was found that an increasing amount of Li significantly increases the active site density. In addition it was concluded that the participation of bridging O in the OER mechanism is possible.

OER on noble metal electrodes was investigated using isotope-labelled acidic electrolyte and differential electrochemical mass spectrometry (DEMS).[54-55] It was shown that on Pt oxygen is solely formed from the electrolyte whereas in case of RuO_2 and electrochemically-oxidized Ru lattice oxygen participates in the reaction mechanism. But the electrocatalyst was found to dissolve under OER conditions in the electrolyte due to the formation of a soluble RuO_4.[59] The participation of lattice oxygen was also shown for IrO_2 in which thermally-prepared electrocatalysts were found to exchange O atoms with the isotope-labelled electrolyte during potential cycling in the OER range.[60] This O exchange led to a depletion of the $^{16}O_2$ signal and a rise of the $^{16}O^{18}O$ signal. From their results the authors concluded that only a small fraction of O sites (~1% of the total amount of oxygen) in the IrO_2 participates in the OER.

The influence of the overpotential and reaction rate on the product composition was investigated for RuO_2 and $Ru_{0.9}Ni_{0.1}O_{2-\delta}$.[61] The authors revealed that at low overpotential the evolved oxygen is predominantly formed from the electrolyte leading to $^{18}O_2$ during chronoamperometric experiments. At high overpotential the formation of a short pulse (~10 s) of $^{16}O^{18}O$ above the background signal could be seen. This effect was stronger for the $Ru_{0.9}Ni_{0.1}O_{2-\delta}$ than for the RuO_2 sample. Thus, the reaction mechanism might change with overpotential and at elevated reaction rates lattice oxygen might participate to a larger fraction in the reaction mechanism.

In contrast to these studies, no indications for the participation of lattice O were found during photocatalytic oxygen evolution on crystalline Co_3O_4 nanoparticles in neutral electrolyte.[62]

This phenomenon might be explained by the reaction conditions which appear to be quite moderate compared to electrocatalytic oxygen evolution at high overpotential. As found for the Ru-based oxide electrocatalysts the O_2 is predominantly formed from the electrolyte at low overpotentials which might also be the case for the photocatalytic OER on Co_3O_4.

For the CoCat (see Section 2.2.1), a thin catalyst coating was electrochemically-deposited from isotope-labelled, neutral phosphate buffer and tested for oxygen evolution in unlabeled electrolyte.[56] Applying OER conditions to this catalyst led to the formation of $^{18}O_2$, $^{16}O^{18}O$ and $^{16}O_2$ as determined by in-line mass spectrometry. These results indicate that O atoms from the CoCat participate in the OER mechanism. However, these experiments had the major disadvantage that the catalysts had to be equilibrated for 1 h in the unlabelled electrolyte prior to product analysis. Therefore, an exchange of ^{18}O and ^{16}O between catalyst and electrolyte might have preceded the OER leading to an underestimation of the $^{16}O^{18}O$ and thus, to an underestimation of the participation of O atoms from the Co oxide.

Assuming lattice O participates in the OER mechanism, a universal correlation between OER activity and instability of the electrocatalyst was formulated by a thermodynamic analysis of the oxygen evolution reaction. The thermodynamic instability of the O^{2-} ions in the lattice under reaction conditions leads to the partial dissolution of M^{2+} ions.[63] Experimental studies pointed out that catalytic activity and instability might be correlated.[13, 64] But the formulation of activity-stability correlations needs to be referred to a unified normalisation. It was shown that in case of Ir-Ni oxides the OER activity and instability with respect to geometric surface area are correlated whereas the dissolution of Ir per electrochemical surface area (surface charge) does not follow the specific activity.[65]

For noble metal electrodes in acidic electrolyte a correlation between stability and electrocatalytic properties was revealed.[13] It was shown that the Tafel slope and the steady-state metal dissolution rate are anticorrelated. The metal dissolution rate decreases exponentially with Tafel slope which was explained by differences in the reaction mechanism. The more stable but less active metals like Pt form O_2 predominantly from the electrolyte whereas preferred Tafel slopes are found for unstable metals like Ru which form O_2 (at least partially) from the oxide lattice. Thus, the OER activity and stability of electrocatalysts might be related to the dominant reaction mechanism.

2.1.5 Oxygen Evolution Mechanism on Co Oxides in Neutral Electrolyte

The first mechanistic investigation of a Co based electrocatalyst in neutral, phosphate-containing electrolyte was performed for the CoCat, a Co-phosphate electrocatalysts (see section 2.2.1). The electrokinetic investigations showed that the rate-determining step is most probably a chemical step preceded by a proton-coupled electron transfer (PCET) step in equilibrium independent from film thickness between 10 and 90 nm.[56] Furthermore, the reaction rate was independent from phosphate concentration above 0.03M. It was concluded that the reaction mechanism involves a fast oxidation of Co^{3+}-OH to Co^{4+}-O in equilibrium and the rate-determining step includes the formation of the O-O bond. The phosphate ions are thought to participate in the proton abstraction of the equilibrium PCET step.

But how does oxygen evolution proceed under participation of lattice oxygen? During the electrocatalytic cycle oxygen vacancies have to be formed in the reaction zone of the catalyst according to a majority of the discussed reaction mechanisms.[20] (see also section 2.1.2) These anionic vacancies lead to a change in local charge density and possibly to the temporary reduction of the adjacent TM sites. These vacancies are expected to be immediately healed by oxygen atoms from water or hydroxyls and the adjacent TM ions are expected to get oxidized. Generally, there are three types of O sites from which the O_2 molecule could be formed – terminating O sites (O^T) as well as $O_{\mu 2}$ and $O_{\mu 3}$ sites which are bridging O between two and three TM ions, respectively. Thus, to take into account the participation of lattice oxygen the formation energies of O vacancies at these different sites have to be taken into account.

The binding energy of a terminating O is generally lower than of bridging O.[66] According to DFT+U calculations on the thermodynamics and structure of Co_3O_4 surfaces under various redox transitions the formation energy of an anionic vacancy at the $Co_3O_4(100)$ surface is significantly lower for a μ_2-bridge (0.91 eV) compared to a μ_3-bridge (1.90 eV).[67] The formation energy of oxygen vacancy in sub-surface atomic layers was found to be lower than at the surface. This enables migration of the anionic vacancies from the surface to the sub-surface atomic layers. In addition, the presence of O vacancies was found to induce a change in coordination of the Co T_d ions to Co O_h at the surface which was explained by the localization of two electrons from the oxygen ions at the adjacent Co O_h ions distorting the local bonding environment. Thus, it can be concluded that participation of lattice oxygen during OER on a Co_3O_4 surface proceeds preferably at μ_2-oxo bridges compared to μ_3-bridges. But oxygen evolution reaction proceeds faster under (at least partial) participation of terminating O because the binding energy of a terminating O on a metal oxide surface is significantly lower compared to $O_{\mu 3}$ species. In addition the participation of bridging O in the OER mechanism might induce structural changes in the near-surface of the Co_3O_4 which are experimentally confirmed in this work (see Chapter 5 and ref. [68])

The participation of lattice oxygen is strongly supported by *ab initio* DFT+U calculations on possible reaction pathways for oxygen evolution on a Co oxide cluster of six Co ions in neutral electrolyte.[69] According to this study the O-O bond is always preferably formed by geminal coupling of two O atoms bonded to the same Co ion. This reaction pathway is independent from the structural motif of the Co oxide cluster. The formation of the O-O bond by nucleophilic attack of the O^T by water molecules is thermodynamically unfavoured even compared to the formation of O_2 from a O^T and a $O_{\mu2}$ atom. However, nucleophilic attack by OH^- might be possible in alkaline electrolyte leading to a different reaction mechanism.

The preferred reaction pathway of OER on this Co oxide clusters as revealed by these calculations is described in the following. Herein, four electrons were extracted from the cluster in the presence of water molecules. First, deprotonation of a terminating OH occurs and then a $Co^{4+}=O^{\bullet}$ is formed. In an earlier study, it was shown that O^T form low-barrier hydrogen bonds and the $O_{\mu2}$ are likely participating in the deprotonation of the reaction intermediates under working conditions.[70] Due to the electron hole located at the terminating O atom it couples with an adjacent terminating OH, O^T or $O_{\mu2}$ and forms the O-O bond in a Co(OO) or Co(OOH) species. This process leads to a rearrangement of the charge in the cluster and to the capture and localization of the two holes in the Co (hydro)peroxo. These additional holes are needed to complete the oxidation of the O^{2-}. After fast deprotonation of the hydroperoxo, the peroxo is transformed to a Co-O_2 superoxo species. This reaction intermediate is highly stable with a lifetime of up to 10 ps in case of O-O bond formation from two O^T atoms. The other reaction intermediates have lifetimes shorter than 2 ps. Thus, according to these calculations the rate-determining step is likely to be the O_2 release. Interestingly, in case of water oxidation on a CoOOH the activation energy for the deprotonation of OOH and the desorption of the O_2 molecule (see Eqn. 10) from a $O_{\mu2}$ site was found to be very low (0.03 eV) compared to the same reaction step if the OOH is formed solely on a terminating O site (0.8 eV).[25]. Combining these results points out the importance of the $O_{\mu2}$ ions at the surface as their crucial role in OER mechanism might not be limited to the deprotonation of the reaction intermediates but might also be valid for the rate-determining step.

Thus, the mechanism of OER in neutral and acidic electrolyte can proceed under different reaction pathways depending on the nature of O sites are available and involved. Experimental results suggested the potential-dependent participation of lattice oxygen. Generally, the number of O atoms from the oxide that participate is comparably small. This indicates a very small fraction of the metal sites on the electrocatalysts to be OER-active sites. If this is the case, the exchange of the O atoms from the catalytically active sites is very fast and the turn over frequency (TOF) at the active site has to be significantly larger than estimated from the total number of surface metal sites. Furthermore, the participation of bridging O in the OER mechanism might significantly enhance O_2 desorption which is possibly the rate-determining step but can induce substantial structural rearrangement in the near-surface of the catalysts. These findings are important as the results of this work on structure-activity correlations and the structure of the catalytically active state of 3d TM-based electrocatalysts are explained within the mechanistic framework described above.

2.2 Electrocatalysts for Water Oxidation and OER

Water electrolysis and OER was firstly discovered by using noble metal electrodes of Au and Pt immersed in the same highly-acidic electrolytes.[10] Today, the established and most active electrocatalysts for the anodic OER are based on Ru- and Ir oxides.[51] According to experimental studies and DFT calculations, these catalysts occupy the top region of the OER volcano curve. IrO_2 and RuO_2 crystallise in a rutile-type lattice (space group: $P4_2/mnm$) consisting of corner-sharing chains of edge-sharing MO_6 octahedra as shown in Figure 4a for β-MnO_2. The structural similarity to TiO_2 allows the preparation of single phase $M_xTi_{1-x}O_2$ with $M \in [Ru, Ir]$.[71] TiO_2 excels with a strong resistance against (electro-)chemical reduction leading to an extraordinary stability under OER conditions. Electrodes based on these ternary (or quaternary) oxides are called dimensionally-stable anodes (DSA®) and were invented by Beer in the 1960's.[14-15] These anodes are often used in industrial applications and exhibit a significantly increased stability of the catalytic activity in acidic electrolyte in comparison to pure Ir and esp. Ru oxides. But the application of noble-metal electrocatalysts at higher pH is largely limited due to metal dissolution and thus, poor stability. Ir oxide shows significant OER activity in acidic and alkaline electrolyte. Common electrocatalysts in alkaline electrolyte are based on 3d TM ions such as Co and Ni applied as oxides, (oxy)hydroxides and perovskites.[20, 51]

Two kinds of OER electrocatalysts in alkaline electrolyte have received a lot of attention in recent years and are shortly described in the following. First, NiFe-based electrocatalysts which are often applied as layered oxyhydroxides or double hydroxides and second (double) perovskites which excel by the variety of TM ions and lanthanides which can be isostructurally incorporated.[20, 35, 72-74] The underlying principles of the high OER activity of NiFe-based catalysts are still under investigation. The variation in catalytic activity with Ni/Fe ratio is correlated to the metal oxygen distance in the catalysts structure.[74] The structural perturbation due to the Fe incorporation in the Ni-rich host lattice leads to a preferred strength of the metal oxygen bond for OER activity as the length of the metal-oxygen bond is inversely related to its strength. This led also to the conclusion that Fe is the active site for OER in these materials. Furthermore, it was found that Fe impurities enhance the electric conductivity of the NiOOH catalyst and limit crystallization of the oxyhydroxide domains. A purification protocol for the alkaline electrolyte was developed decreasing the Fe content which led to a cathodic shift of the Ni^{2+}/Ni^{3+} redox couple and significant decrease in catalytic activity of the Fe-free Ni-based catalysts. Thus, the high activity of Ni-based electrocatalysts as applied alkaline electrolysers was thus, attributed to accidental Fe impurities in the KOH.[73]

Another example for active electrocatalysts for OER in alkaline electrolyte is perovskites-based materials. A volcano-like profile of the OER activity was found with varying composition. Initially, the most active perovskite based on oxide surface area was a double perovskite in which Ba and Sr equally occupy the A sites and Co and Fe occupy the six-coordinated B-sites in a 4:1 ratio.[20, 35] This perovskite was found to irreversibly loose crystallinity during OER due to the dissolution of lanthanides. This leads to a structural rearrangement of the near-surface because the Co octahedral cross-linking changes from corner-sharing to edge-sharing.[75-76] Later, a more active double perovskite was found in which only Co occupies the B sites and the A sites are occupied by one part Ba and one part Pr, Ho, or Sm.[77] The advantage of this material is the enhanced structural stability during OER. Furthermore, a correlation between computed O p-band centre and the overpotential could be revealed by varying the composition of A sites.

In this work, oxygen evolution reaction on pure Mn- and Co-based electrocatalysts will be investigated. These materials excel by the high abundance and their straightforward synthesis of nanostructured materials compared to perovskites. The Ni-based electrocatalysts are generally not stable at neutral pH and are rather applied in borate buffer at pH 9. In the next section an introduction on the structure of Co and Mn oxides and findings on their electrocatalytic properties in alkaline electrolyte is given. This includes the special case of the electrodeposited CoCat which serves as reference material for OER electrocatalysis in neutral electrolyte.

2.2.1 Water Oxidation and OER on Co Oxide Electrocatalysts

Crystal Structure and Electronic Configuration of Selected Cobalt Oxides

Co oxide structures consist of Co ions with oxidation states of +2, +3, and possibly +4. Selected structures of Co oxides and oxyhydroxides are shown in Figure 2. The thermodynamically most stable Co oxide is the Co_3O_4 which exhibits the normal spinel structure (space group: Fd-3m, PDF#00-042-1467) with a mixed valency of Co^{2+} and Co^{3+}.[78-82] [83]

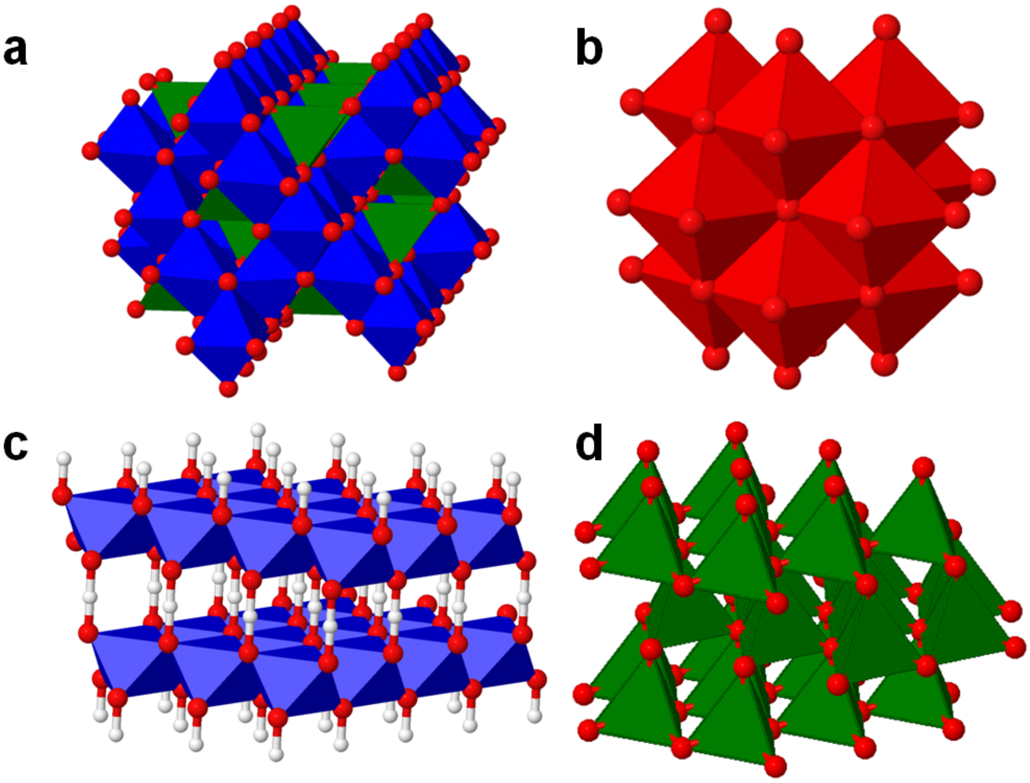

Figure 2: Ideal structures of selected Co oxides and Co oxyhydroxides: Co_3O_4 (a), rocksalt-CoO (b), CoOOH (c) and wurtzite-CoO (d). The CoO_6 coordination octahedra and CoO_4 coordination tetrahedra are shown. Co^{3+}, Co^{2+} octahedra and Co^{2+} tetrahedra are shown in blue, red, and green, respectively. Hydrogen atoms are shown in white.

Therein, the Co^{2+} ions occupy one quarter of tetrahedral sites whereas Co^{3+} ions occupy half of the octahedral sites within a pseudo-cubic close-packed (ccp) O^{2-} lattice. The structure of Co_3O_4 consists of Co-deficient CoO_6 kagomé layers which contain exclusively di-μ-oxo bridged Co^{3+} O_h ions (O_h, octahedral coordination by six oxygen atoms). Between these layers Co^{3+} O_h and Co^{2+} T_d ions (T_d, tetrahedral coordination by four oxygen atoms) are located and act as linkers. The Co^{2+} T_d ions are connected via mono-μ-oxo bridges and the linking Co^{3+} O_h ions via di-μ-oxo bridges to Co^{3+} O_h ions of the kagomé layers. Co_3O_4 is a semiconductor with a band gap of 1.60 eV.[41]

In contrast to the mixed valent Co_3O_4 three structures of Co^{2+} oxides are described in the following. The most prominent structure is the rocksalt-CoO (rs-CoO, space group: Fm-3m, PDF #01-075-0533) which exhibits an ideal ccp O^{2-} lattice and all octahedral sites are occupied by Co^{2+} ions. But rocksalt-CoO is often non-stoichiometric due to cationic vacancies in the oxide lattice. The electronic structure of ideal and defective CoO was calculated using *ab initio* DFT+U and the cationic vacancies in the Co sub-lattice were found to lead to Co^{3+} ions in the lattice and acceptor states within a band gap of ~2.5 eV.[41, 84] The cationic vacancies also induce structural changes because in vicinity of the vacancies Co-O distances are contracted with 2.05 Å compared to 2.15 Å in an ideal lattice. Thus, the presence of defects in the crystal lattice positively influences the electron transport properties of the CoO by decreasing the band gap.

Furthermore, two CoO structures are known wherein the Co^{2+} ions are purely tetrahedrally-coordinated. In wurtzite-CoO (w-CoO, space group: $P6_3/mmc$, PDF#01-089-2803) the Co^{2+} T_d ions arrange in a hexagonal close-packed (hcp) O^{2-} lattice. It was found that it exhibits a band gap of ~1.5 eV.[85-87] Also in zincblende-CoO (spacegroup: F-43m, PDF#01-075-0419) are only tetrahedrally-coordinated Co^{2+} ions present which arrange cubically in a ccp O^{2-} lattice. The zincblende-CoO is structurally very similar to the ZnO which has various applications as semiconductor and as additive due to its distinct white colour. The addition of Co ions in the ZnO yields the pigment called cobalt green which excels with its magnetic properties at room temperature.[88]

Co (oxy)hydroxides and oxides are also present as layered structures in which Co ions are octahedrally-coordinated and exclusively connected via di-μ-oxo bridges. Their oxidation state ranges from +2 to +4 and is determined by the intercalation chemistry which is known to have a significant influence on the physical properties of the material. A layered Co(oxy)hydroxides is presumably the basis of the CoCat, a Co-based OER electrocatalysts applied in neutral electrolyte (see below). The Co ions in layered $Co(OH)_2$ - also called Co LDH (layered double hydroxides) - are in +2 oxidation state because all O sites are protonated. The interlayer void can be occupied by water molecules and various anionic species like CO_3^{2-}. LDH materials have various applications as catalysts, ion-exchange materials, halogen absorbers, and sorbents.[89] In case of $HCoO_2$, the Co ions are in oxidation state +3 and the layers are connected via hydrogen bridges as in the mineral heterogenite (PDF#00-026-11107).[90] The interlayer distance is significantly shorter than in $Co(OH)_2$ and even shorter than the distance between the kagomé layers of the spinel structure. The hydrogen atoms can be replaced by alkali metal ions like Li^+, and Na^+ which leads to larger interlayer distances with the order H < Li < Na. The ratio between alkali and Co ion determines the mean Co oxidation state via +3+x of $M_{1-x}CoO_2$. Besides their application as catalysts, e.g. layered $Na_{0.5}CoO_2$ is a superconductor at $T>50$ K which was attributed to a zigzag ordering of the Na ions and a charge ordering in the CoO_2 layer.[80] The presence of Co^{4+} ions in the structure is responsible for enhanced electrical conductivity. Co^{4+} ions in lattice of Co_3O_4 as determined by XRD and iodometric titration experiments were discussed to be the origin for enhanced electrical conductivity and catalytic activity.[91-93]

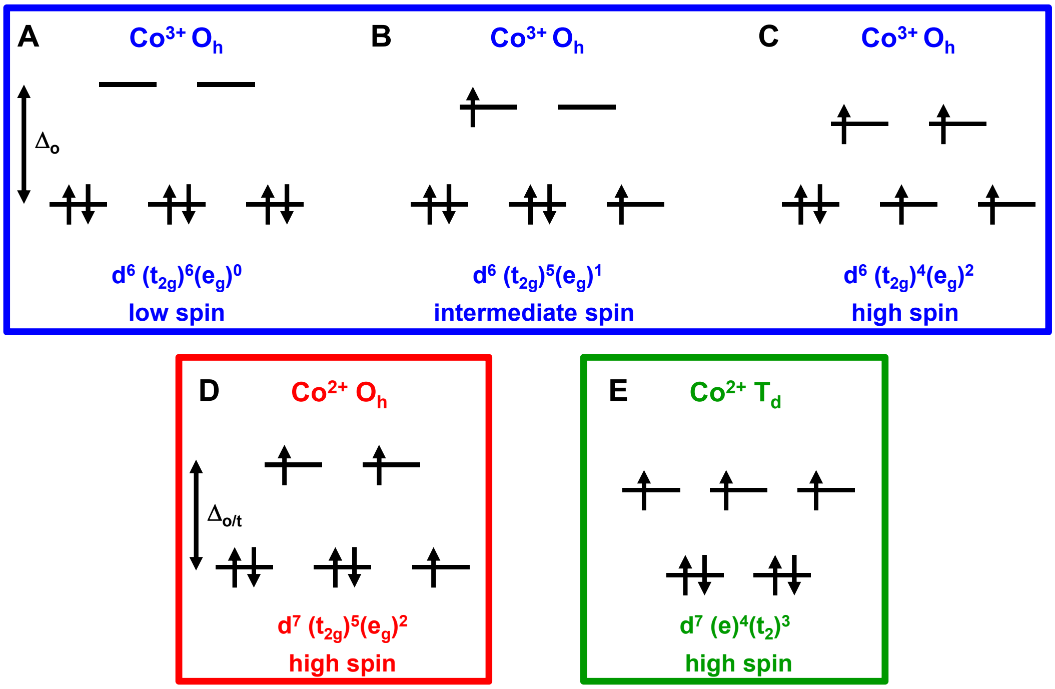

Figure 3: Electronic configuration of 3d orbitals in octahedral Co^{3+} (A-C) as well as octahedral Co^{2+} (D) and tetrahedral Co^{2+} (E). $\Delta_{o/t}$ denotes the crystal field stabilization energy (CFSE) which is lower at intermediate or high spin configuration compared to low spin configuration in octahedral ligand field of Co^{3+}. The same applies for the tetrahedral compared to octahedral ligand field of Co^{2+}. The 3d orbitals are shown as degenerate for clarity. The figure is based on [20, 94-96].

Electronic Structure of Co oxides

The electronic structure of an electrocatalyst can have a significant influence on the catalytic activity as discussed in Section 2.1.3. Figure 3 shows three possible spin configurations for Co^{3+} O_h and two possible spin configurations for Co^{2+}. The low spin configuration of Co^{3+} O_h ions is caused by large crystal field stabilization energy (CFSE) which leads to completely filled 3d t_{2g} and empty e_g orbitals. The t_{2g} orbitals are d_{xy}, d_{xz}, and d_{yz} and the e_g orbitals are $d_{x^2-y^2}$ and d_{z^2}.

The CFSE represents the energetic separation between the t_{2g} and the e_g orbitals due to the ligand field of the adjacent O atoms in the Co oxide structure.[39] A smaller CFSE leads to a higher electron occupancy of e_g states in ground state and thus, to intermediate spin Co^{3+} with $(t_{2g})^5(e_g)^1$ configuration or high spin Co^{3+} with $(t_{2g})^4(e_g)^2$ configuration. In case of Co^{2+} O_h ions, the d^7 configuration leads to three unpaired electrons and therefore, high spin configuration.[97] This configuration is energetically preferred over the completely filled t_{2g} states and only one unpaired electron in the e_g orbitals. In case of the tetrahedral ligand field, the energy of the 3d states is reversed leading to completely filled e orbitals and the three unpaired electrons in the t_2 orbitals. The Co^{2+} T_d ions therefore also exhibit high spin configuration. The density of unoccupied states in the 3d orbitals of Co ions can be specifically identified from Co L_3 X-ray absorption near-edge structure (XANES) spectra.

It is generally accepted that the ground state of the Co^{3+} ions in symmetrical octahedral CoO_6 bonding environment is in low spin configuration.[94-95] This is the case e.g. for bulk Co ions in $LiCoO_2$ and Co_3O_4. However, the spin configuration changes by thermal excitation to high spin which was found to be energetically preferred over intermediate spin state.[94] But the sensitivity of the CFSE for distortions and variations in the CoO_6 bonding environment and symmetry is even more important for electrocatalysts. The local atomic structure of the Co ions has significant influence on the spin state of the Co ions and therefore, on the electronic configuration of the Co oxide.[80, 96]

A tetragonal distortion of the CoO_6 octahedron along z-axis in a brownmillerite-like $Sr_2Co_{1.2}Ga_{0.8}O_5$ was found to split the degenerated e_g orbitals (d_{z^2} and $d_{x^2-y^2}$) which leads to high spin configuration of the Co^{3+} O_h ions.[96] The energy of the d_{z^2} orbital shifts down towards the t_{2g} orbital and the energy of the $d_{x^2-y^2}$ shifts upwards when the Co-O bond along z-direction is elongated. Simultaneously, the energy of the t_{2g} d_{xy} orbital shifts up towards the d_{z^2} e_g orbital. The distortion of the octahedral environment and the resulting lower energy separation of the 3d orbitals leads to occupation of the e_g orbitals on cost of the t_{2g} orbitals and equivalent to the high spin Co^{3+} configuration (see Figure 3). The presence of intermediate spin Co^{3+} ions could not be shown in the $Sr_2Co_{1.2}Ga_{0.8}O_5$ and was explained by the low energetic splitting of the e_g states. The energy separation between the e_g orbitals was ~1 eV for a distortion of +0.3 Å along z-direction.

In case of a pyramidal CoO_5 coordination in a layered perovskite structure of Sr_2CoO_3Cl the high spin configuration was found to be present in ground state.[95] This change in coordination symmetry influences the electronic structure and thus, the Co *L*- and O *K*-edge XANES spectra. In the Co L_3 XANES of the high spin Co^{3+}, a feature at the low energy side was present in contrast to the spectra of low spin Co^{3+}. The missing O atom compared to the octahedral CoO_6 coordination led to a displacement of the Co ion from the basal plane. This yielded in a down-shift of d_{z^2} e_g state by ~1.6 eV towards the unoccupied t_{2g} state and the hybridization of the $d_{x^2-y^2}$ orbitals with the O 2p orbitals decreased. Furthermore, intermediate spin configuration was only energetically preferred when the position of the Co ions was restricted to be in the basal plane.

The Co^{3+} spin states does not only depend on the symmetry of the bonding environment in the bulk but also specific surface terminations influence the spin configuration as calculated for surface Co^{3+} ions of $LiCoO_2$.[98] The structure of $LiCoO_2$ is structurally very similar to the β-CoOOH but the H^+ are replaced by Li^+. The octahedral configuration on the (110) and (104) surfaces is changed to square pyramidal and pseudo-tetrahedral configuration when terminating O atoms were neglected. According to this change in bonding symmetry the Co^{3+} ions exhibit intermediate spin configuration for square pyramidal and high spin for pseudo-tetrahedral coordination. The identification of intermediate spin configuration might be related to a restricted position of the Co^{3+} ion in the basal plane. In the bulk and on the (100) surfaces, the Co^{3+} O_h ions show symmetric octahedral bonding environment with μ_3-oxo bridges and exhibit low spin configuration. Although, in this calculation the presence of terminating O was not taken into account the distortion of the CoO_6 at the special surfaces is likely to retain after adsorption of oxygen species. The contracted metal-oxygen bond length (1.63 Å versus 1.91 Å) at these coordinatively-unsaturated Co sites might lead to an asymmetry in the CoO_6 bonding environment.[66, 99]

Thus, the Co coordination and coordination symmetry significantly influence the electronic configuration of the Co ions. These differences have significant influence on the hybridization of the Co 3d and O 2p orbitals which play an essential role in the charge transfer states and therefore, on various physical properties of the Co oxide as electrocatalysts.

Co Oxide Electrocatalysts for OER in Alkaline Electrolyte

Co oxides were mostly applied as OER electrocatalysts in alkaline electrolyte due to their instability at low pH.[16, 100] The first reports on pure Co-based OER electrocatalysts were published in the late 1970's. Therein, Co oxide coatings with thicknesses in the µm-range were prepared by thermal annealing of precursor solutions on various substrates.[101-102] These electrocatalysts were first prepared on Fe substrates and later the influence of the other metal substrate on the catalytic activity was investigated. It was shown that Fe substrate leads to the best catalytic activity in highly alkaline electrolyte with a Tafel slope of 42 - 46 $mV \cdot dec^{-1}$. But OER accompanies Fe incorporation in the crystalline Co_3O_4 as revealed by sputter depth profiling.

Later, the group of Trasatti extensively investigated the surface electrochemical properties of Co_3O_4 in alkaline electrolyte.[83] It was shown that the preparation of thick Co_3O_4 films on bare Ti fails and an RuO_2 interlayer was applied presumably to enhance the electrical conductivity of the TiO_x interlayer. This RuO_2 interlayer is not affecting the chemical features of the Co_3O_4 surface electrochemistry. One major redox transition was found to precede the catalytic wave and was attributed to the reaction $CoOOH \leftrightarrow CoO_2 + H^+ + e^-$ representing the Co^{3+}/Co^{4+} redox couple. This finding is in agreement with the Pourbaix diagrams.[16, 100]

Approaches to enhance the catalytic activity of Co_3O_4 were aiming at an increase of the electrochemically-active surface area e.g. by hard templating which led to mesoporous Co_3O_4.[103-104] The pore sizes ranges between 3 – 6 nm and the BET surface area between 70 – 150 $m^2 \cdot g^{-1}$. This mesoporous Co_3O_4 was found to significantly increase the mass-based catalytic activity compared to untemplated Co_3O_4 due to its larger surface area.[104] Hierarchically-mesoporous Co_3O_4 were prepared by hard templating and selective leaching of incorporated Mg ions. The selective leaching of the Mg ions substantially increases the surface area from ~100 to ~300 $m^2 \cdot g^{-1}$ and thus, increases the O_2 yield compared to nonhierarchially-mesoporous Co_3O_4.[105] A study of Co_3O_4 nanoparticles with sizes of 6, 21, and 47 nm showed an increasing mass-based catalytic activity with BET surface area in alkaline electrolyte.[106]

Another synthetic route to prepare Co-based electrocatalytic coatings with elevated electrochemical surface area is electrodeposition of Co oxyhydroxides or hydroxides. Electrodeposition especially performed at room temperature leads primarily to X-ray amorphous coatings[107] and is widely used for preparation of electrocatalytic coatings for OER. [74, 108-109]

Similar to the NiFe-based electrocatalysts[72-74] the influence of purification of KOH electrolyte was investigated for CoOOH electrocatalysts.[42] It was found that the Co redox chemistry changed and Tafel slope increases after purification of the electrolyte. The Co^{2+}/Co^{3+} redox transition and the catalytic wave shift anodically. Furthermore, they investigated the OER activity and surface chemistry of electrodeposited $Co_{1-x}Fe_xOOH$ and they also identified an optimal Fe content in CoOOH for OER activity. Catalytic testing for 2h leads to an increase in Tafel slope of ~10 $mV \cdot dec^{-1}$ almost independent from the Fe content. This increase accompanies an increasing fraction of lattice oxygen in the near-surface composition of the $Co_{1-x}Fe_xOOH$. Thus, prolonged oxygen evolution leads to changes in the present oxygen species and to a change in the catalytic processes deteriorating the catalytic activity.

DFT calculations based on the OER mechanism described in Section 2.1.2 were performed for several surface terminations of the β-CoOOH.[25] The high-index (104) surface was found to exhibit the lowest theoretic overpotential for water oxidation of the investigated surfaces whereas the (012) surface is thermodynamically preferred termination at higher overpotential. The high activity of the (104) plane compared to the other planes was explained by the Co^{3+} state as the lowest valency within the catalytic cycle which stands in contrast to Co^{4+} for the other surface terminations. Furthermore, the potential-determining step on (104) surface was found to be the O-O bond formation (ΔG_{OOH}, Eqn. 9). In contrast the potential-determining step on the (012) surface is the healing of O vacancy at the $O_{\mu 2}$ site by water molecule accompanied with deprotonation (ΔG_{O2}, Eqn. 10).

Interestingly, the activation energy for deprotonation of OOH and desorption of O_2 on this $O_{\mu 2}$ site was found to be only 0.03 eV compared to 0.8 eV for the same step from terminating O site on the (104) surface.

Experimental indications for a higher catalytic activity of the high index surface compared to low index surfaces were determined for nanorods of $LiCoO_2$.[110] In alkaline electrolyte the OER activity per oxide surface area was higher for shorter nanorods which led to a larger tip/side area ratio. The sides of the nanorods exhibit (003) termination whereas the tips show (104) termination. Furthermore, the high index surface termination was found to exhibit high or intermediate spin Co^{3+} ions according to DFT calculations[98] and a lower hybridization between the Co 3d and the O 2p orbitals as revealed by electron energy loss spectroscopy (EELS) recorded at the O *K*-edge. In terms of Co oxide redox chemistry the ratio of Co^{2+}/Co^{3+} and Co^{3+}/Co^{4+} transitions seemingly increased due to the shortening of the nanorods. The higher catalytic activity of the tip (at similar Tafel slope) was explained by the facile access of oxygen species and an elevated Co oxide redox chemistry of coordinatively unsaturated Co ions.

CoCat - An Electrocatalysts for OER in Neutral Electrolyte

Water oxidation and oxygen evolution in neutral, phosphate-containing electrolyte received growing attention since 2008. In this year, a cobalt-phosphate OER electrocatalyst, herein denoted as CoCat,[53, 109, 111-117] was reported for the first time. This electrocatalyst is prepared and catalytically active in neutral phosphate-containing electrolyte. One major advantage of this material is its self-repair mechanism as it can be prepared under OER conditions.[116] Therefore, Co^{2+} ions in solution are expected to be redeposited isostructurally as electrocatalyst. The CoCat films consist of octahedrally-coordinated (mainly) Co^{3+} ions which are connected via di-μ-oxo bridges.[111-113] The Co ions are thought to form layer fragments of ~12-14 ions which is in agreement with simulations of pair distribution functions extracted from high energy-X-ray diffraction (HE-XRD) and simulations of EXAFS spectra.[112-113, 118] A cubane-like structural motif was proposed in an early structural investigation but it is difficult to clearly differentiate between the two structural motifs. It has to be noted that the cubane-like structure shows stronger similarity to the thermodynamically-favoured spinel structure in case of missing tetrahedrally-coordinated Co^{2+} ions.

It was found that the deposition conditions influence the CoO_x fragment size. When the synthesis is performed in Cl^- or CH_3COO^--containing electrolyte the domain size is larger than in phosphate-containing electrolyte as measured by the number/confinement of the di-μ-oxo bridges between pairs of Co ions. Simultaneously, the fraction of redox active Co ions and the catalytic current at an overpotential of 433 mV decreased.[53]

The electronic structure and spin state of the Co ions in CoCat was investigated using resonant photoemission spectroscopy at Co L_3- and O K-edge.[119] It was found that these comparably thick films consisted of high-spin Co^{2+} and low-spin Co^{3+} ions which is in agreement with the structural analysis using EXAFS.[114] Additionally, oxygen-to-metal charge-transfer states were identified. The charge transfer state related to the Co^{3+} ions is centred at the Fermi level which also corresponds to the O_2/H_2O redox potential. Thus, low-spin Co^{3+} were assigned to be the active species in contrast to high-spin Co^{2+} ions for which the charge transfer state is more than 1 eV above the O_2/H_2O redox potential.

The influence of catalyst loading on the catalytic activity was extensively characterized and it could be shown that the bulk atomic structure as well as the OER activity per number of Co ions did not depend on the film thickness at low overpotential. The film thickness was varied between 15 nm and 1.5 μm and a linear correlation between deposited Co ions and Co redox charge was found. Thus, the bulk of the CoCat films is electrochemically accessible and active for OER. Furthermore, the catalytic activity was found to depend non-linearly on the pH when different proton-accepting bases are used. The current density at the same overpotential follows pK_a and thus, the proton abstraction capability of the buffered electrolyte.[120]

Recently, an *in situ* investigation of the CoCat was published where oxidation state and structural changes of the Co ions were followed over several redox transitions and during OER.[114] From their results the authors concluded that the electrochemical redox transitions are accompanied by oxidation state changes at ~1.4 V and at ~1.63 V vs. RHE as seen in the *in situ* UV-Vis spectra. Quantification of the oxidation state from Co K-edge XANES spectra showed that the mean oxidation state increases at the two redox features from +2.6 to +3 and further to +3.25. Thus, 40% of the Co^{3+} ions were reducible to Co^{2+} whereas during OER only 25% were identified as Co^{4+}. Simultaneously, the EXAFS coordination number of the Co-O and di-μ-oxo Co-Co distance increased predominantly at the first and second redox transition, respectively. The Co-O distance shortened during oxidation from Co^{3+} to Co^{4+} and simultaneously the Debye-Waller factor of the di-μ-oxo bridged Co ions increased. This behaviour was explained with five-coordinated Co^{2+} ions below 1.4 V which get oxidized to $Co^{3+}O_6$. The oxidation of Co^{3+} O_h ions to Co^{4+} O_h then proceeded via deprotonation of μ-OH bridges and terminating OH and was accompanied by a contraction of the CoO_6 building block.

Thus, various Co oxide based electrocatalysts have been prepared and tested for electrochemical water splitting and oxygen evolution reaction in alkaline electrolyte. The knowledge about oxygen evolution in neutral electrolyte is however limited to the X-ray amorphous Co-Cat catalyst. This work aims *inter alia* at the investigation of mainly crystalline Co oxides as electrocatalysts for OER in neutral, phosphate containing electrolyte and their differences and similarities to the CoCat in terms of structure and electrochemical properties.

2.2.2 Water Oxidation and OER on Mn Oxide Electrocatalysts

"[…] In comparison to Co, the high abundance and low toxicity of manganese render Mn oxides as advantageous materials and make Mn-based catalysts highly favourable.[3] Biologically active Mn-containing water splitting complexes offer a possibly coincidental, yet elegant analogy. In earlier works several Mn oxides varying in structure and oxidation state has been reported to be active for water oxidation, but the catalytic rates often were low and the catalyst remained without real practical application.[122-130] Structure-activity relations of water-oxidizing Mn oxides have been discussed but are clearly insufficiently understood.[123-124, 131]

Like other binary transition metal oxides, manganese dioxides exhibit an exceptional variety of polymorphs relating, *inter alia*, to the small ionic radius for Mn^{4+}. The schematic presentation of Figure 4 shows MnO_2 in layered structures with mainly edge-sharing Mn octahedra such as δ-MnO_2 (Figure 4c) or in tunneled structures (Figure 4a and b) with a combination of corner- and edge-sharing Mn octahedra such as β- and γ-MnO_2 with (1x1), (2x1) tunnels and a combination of both, respectively.[132-134]

A common structural imperfection in tunneled MnO_2 materials is the de Wolff defect – an intergrowth of β-MnO_2 chains in γ-MnO_2 and vice versa.[135-136] Furthermore, MnO_2 can exhibit Mn vacancies which lead to a replacement of Mn^{4+} ions by Mn^{3+} and results in a mean oxidation state of Mn lower than 4.[137-139] The presence of Mn^{3+} ions in the lattice can additionally cause microtwinning – a growth defect of the γ-MnO_2 lattice.[132] Synthetic δ-MnO_2 consists of MnO_6 layers where the interlayer space is filled with Na^+ or K^+ ions surrounded with water molecules. In case of an inhomogeneous distribution of the water molecules and the foreign cations, the MnO_6 layers show a "turbostratic" arrangement and thus, are stacked without ordering.[133]

Manganese oxides have long played a crucial role in battery applications and were structurally well characterized in electrochemical battery environments.[140] For catalytically active Mn oxides both layered and tunnelled structures have been reported.[112-113, 122-123, 139, 141] In nature, water oxidation in PSII proceeds at a metal-oxido manganese-calcium complex.[142] Recently, a synthetic Mn-Ca water oxidation catalyst has been prepared via a chemical synthesis route.[143]

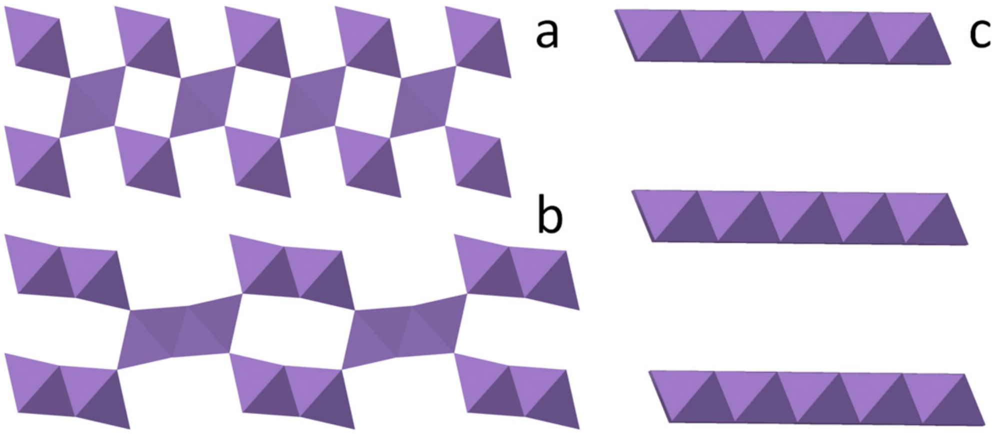

Figure 4: Structures of selected MnO_2 modifications: β-MnO_2 (a), γ-MnO_2 (b), and δ-MnO_2 (c). The MnO_6 coordination octahedra are schematically shown. The structures are extended in the direction perpendicular to the paper plane by rows of edge-sharing octahedra (in a, b, and c). This results in (1x1) tunnels of coordination octahedra (a), in (2x1) tunnels (b), and in a layered manganese oxide (c). In the layered oxides, the interlayer space is filled with water molecules and ions. Figure reproduced from Ref. [121] with permission from the Royal Society of Chemistry.

EXAFS studies revealed that in this amorphous material Mn ions are mainly interconnected via di-$\mu_{2/3}$-oxo-bridges and similarly to δ-MnO_2 form layers, whereas the Ca ions are positioned in the interlayer space forming Mn_3CaO_4 cubanes or compensating the charge deficiency on top of Mn-vacancies. The resulting structural motifs show striking similarities to the natural Mn-Ca complex in PSII.[124] In a subsequent study, it has been shown that other redox-inert cations can be incorporated into the layered MnO_x structure, but the obtained catalytic activity is highest when Ca ions are present.[131]

Recently, an electrolytically-prepared Mn oxide (MnCat) has been presented which does not contain Ca^{2+} ions but which shows electrocatalytic activity towards oxygen evolution in neutral electrolyte. In the structure of this MnCat, together with the extensive di-μ-oxo bridging, a significant fraction of mono-μ-oxo bridged Mn ions was found whereas another MnO_x, electrodeposited from the same media but using different electrochemistry protocol, showed almost exclusively di-μ-oxo bridged Mn ions and had no catalytic activity.[123] It was suggested that Mn ions in lower oxidation state can take the structural (and perhaps also the functional) role of Ca in the catalytically active layered Mn oxides.

A synthetic tetranuclear Mn complex was incorporated into a Nafion® matrix where it decomposes and forms a layered $Mn^{3+/4+}$ oxide.[144-145] Dissociation upon illumination results in disordered Mn^{2+} ions, which could be electrochemically re-oxidized to the layered, water-oxidizing $Mn^{3+/4+}$ oxide. These finding suggest that cycling through various Mn oxidation states may be crucial in water-oxidation by amorphous Mn oxides.

As opposed to the CoCat, the mechanism of water oxidation catalysed by Mn-based catalysts is much less investigated. In 80's the mechanism of electrocatalytic oxygen evolution with Mn oxides in highly acidic and alkaline electrolyte was investigated using Tafel slope analysis, pH titration and a one electron transfer step was argued to be rate-determining.[27, 128, 130] Recently, a mechanistic study of oxygen evolution at δ-MnO_2 in neutral electrolyte suggested that the disproportionation of Mn^{3+} to soluble Mn^{2+} may be a limiting factor of oxygen evolution activity at neutral pH.[146] Increasing pH above 9 was suggested to stabilize Mn^{3+} ions and to lead to a non-Nernstian potential dependence on pH during transition from neutral to alkaline reaction conditions and furthermore, to a higher oxygen evolution activity.[146]

Recently, two nano-structured manganese oxides supported on multi-walled carbon nanotubes have been developed via two novel synthetic routes – symproportionation-deposition reaction and incipient wetness impregnation. These materials showed promising activity and stability for electrochemical water splitting in neutral electrolyte; the initial studies indicated that the two oxides may differ in their atomic structure.[126] […]"[121]

Chapter 3 Experimental

3.1 Physicochemical Characterization

X-ray Diffraction

The crystal structure of catalysts was determined using X-ray diffraction (XRD) in a Bruker D8 Advance. Diffraction pattern of thin films were recorded in grazing-incident mode from 10° to 75°. As primary optics a Göbel mirror with a 2.5° Soller was mounted. Secondary optics consists of a horizontal 0.23° Soller and a scintillation counter as detector. The samples were mounted on a single crystal Si plate. The incident angle was 1° and the step size ranged between 0.04° and 0.06°. The collection time was 140 s. The as-prepared samples were deposited on bare or Ti-coated Si(100) wafers.

Powder X-ray diffraction was conducted in Bragg-Brentano mode with a 1.5° Soller as primary optics as well as Ni filter, 8 mm iris and 1.5° Soller as secondary optics. A position-sensitive detector (LynXEye, Bruker) with an opening angle of 3° were used. Diffraction pattern were recorded between 10° and 75° using a step size of 0.02° and a collection time of 7 s. Divergence and antiscattering slit were adjusted for a constant illuminated area. A low background Si sample holder was used.

SEM

Scanning electron micrographs were recorded using a JEOL 7401F field emission SEM operated at 10 kV in secondary electron mode.

TEM

Transmission electron micrographs were recorded using a FEI Tecnai G^2 20 S-TWIN instrument operated at 200 kV. Metal oxide films were scratched off the substrate using scalpel and transferred onto a lacy carbon-coated copper grid.

ICP-OES

The composition of colloidal solutions, powders and thin films samples was determined using a Varian 715-ES-inductively coupled plasma (ICP) analysis system with optical emission spectroscopy detection (OES). Therefore, the samples were dissolved overnight using a mixture of concentrated nitric acid (AnalaR, NormaPur, VWR) and hydrochloric acid (AnalaR, NormaPur, VWR) in ratio of 1:3. The solution was subsequently diluted using Milli-Q water to match the calibration of the ICP-OES (c_{TM} < 10 mg/l). In case of supported powder catalysts, the solution was filtered prior to the dilution step. The concentration of transition metal ions was determined from the emission lines at 191.446 nm, 257.610 nm, 259.372 nm, 260.568 nm, 279.482 nm, 279.827 nm, 280.108 nm, 293.305 nm, 293.931 nm, 294.921 nm for Mn and 228.615 nm for Co.

X-ray Absorption Spectroscopy at Mn and Co *K*-edge

XANES/EXAFS experiments were carried out at the BESSY II synchrotron radiation source operated by the Helmholtz-Zentrum Berlin (HZB) if not stated differently. The measurements at the Mn and Co *K*-edge were conducted at the KMC-1 bending-magnet beamline at 20 K in a cryostat (Oxford-Danfysik) with a liquid-helium flow system. Further details are given in ref. [123]. Sample preparation for XAS is described in the corresponding chapters.

X-ray Photoelectron Spectroscopy and X-ray Absorption Spectroscopy at Co *L*- and O *K*-edge [68]

X-ray photoemission as well as Co *L*- and O *K*-edge absorption spectra were collected at the ISISS beamline of the synchrotron radiation facility BESSY II of the Helmholtz-Zentrum Berlin (HZB).[147] The kinetic energy of the photoelectrons during XPS was 550 eV. The XANES spectra were recorded in the total electron yield mode. All spectra were recorded under ultra-high vacuum conditions. The O 1s spectra were fitted using three components and a Shirley background was subtracted. The near-surface compositions were extracted from the integrated intensities of the element specific emission spectra. The intensity of Co *L*- and O *K*-edge absorption edge were normalized to a selected X-ray energy significantly above the absorption edge. Sample preparation is described in the corresponding chapters.

3.2 Electrochemical Characterization

Electrochemical measurements were conducted with a three-electrode rotating disk electrode (RDE) setup in a custom-made glass cell using a PINE® rotator and a Biologic SP-200 potentiostat. The reference electrode was commercial reversible hydrogen electrode (RHE, Gaskatel) or saturated calomel electrode (Princeton) for measurements in alkaline electrolyte and mercury/mercury sulphate electrode (MMS, Princeton) or Ag/AgCl (3M KCl, World Precision Instruments) for measurements in neutral electrolyte. The reference electrode was connected via a Haber–Luggin capillary to the working electrode compartment. Independent from pH, platinum gauze acted as a counter electrode which was separated from the working electrode compartment with a glass frit.

Electrochemical experiments were conducted in 0.1M phosphate buffer (KPi) at pH 7 or 0.1M KOH at pH 13. The neutral phosphate buffer was prepared by mixing 0.1M K_2HPO_4 (99.99%, Merck Suprapur and in case of the MnO_x >98%, Sigma-Aldrich) and 0.1M KH_2PO_4 (99.995%, Merck Suprapur and in case of the MnO_x 99%, Merck) aqueous solutions until the desired pH was obtained. Alkaline electrolyte was freshly prepared from KOH (semiconductor grade, 99.99%, Sigma-Aldrich) and Milli-Q water. Prior to electrochemical measurements N_2 was bubbled through the electrolyte for at least 15 min with a huge flow and was switched blanketing flow during electrochemical measurements. The working electrode was rotated at 1600 rpm to ensure a hydrodynamic equilibrium and electrolyte mixing. In case of CoO_x, the N_2 flow was switched to a low flow through the electrolyte during electrochemical measurements and the rotation rate was 400 rpm. Cyclic voltammograms were recorded without rotation. Unless differently stated, all electrode potentials were corrected for Ohmic losses using electrochemical impedance spectroscopy and were referred to RHE. All reference electrodes were calibrated in the corresponding electrolyte using a Pt/H_2 electrode.

For Tafel slope analysis, current density was recorded stepwise in the corresponding potential range in a quasi-stationary mode. The electrode potential was increased with steps of ~20 mV and held for 5 min. In case of MnO_x samples anodic and cathodic data sets were averaged. To determine the Ohmic resistance, impedance spectra were recorded at every potential step between 50 kHz and 100 mHz with modulation amplitude of 10 or 20 mV.

3.3 Experimental Setup for *in situ* X-ray based Structural Analysis

To investigate the structural properties of electrocatalysts under electrochemical reaction conditions an experimental setup was developed in this work to characterize thin film catalysts under potential control using hard X-ray radiation. The setup can be used to apply *in situ* X-ray diffraction, absorption and reflectometry, and is based on the thin layer concept.[148] The setup is described in the following.

Figure 5 shows the schematics of the experimental setup and a picture taken during experiments conducted at the synchrotron facility Bessy II, Berlin. The experimental setup consists of an electrochemical cell in which a three electrode configuration was realized. The reference electrode is an Ag/AgCl (3M KCl, World Precision Instruments) placed in vicinity to the working electrode via polytetrafluoroethene (PTFE) capillary.

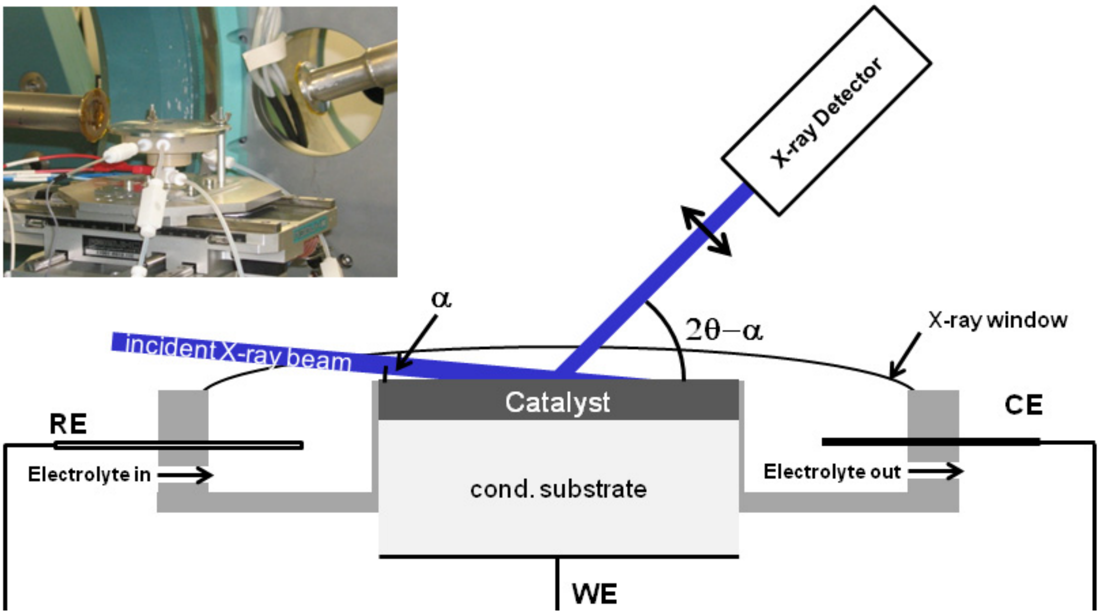

Figure 5: Schematic drawing of experimental setup for in situ X-ray studies at electrocatalysts under electrochemical reaction conditions. The inset shows a photograph of the in situ X-ray setup as operated at Bessy II, Berlin. Therein, the X-ray beam comes from the tube on the left side and the scattered X-ray from the sample are collected at the detector connect to the evacuated tube on the right side. RE, CE, and WE denotes reference, counter, and working electrode, respectively.

Pt wire acts as counter electrode and is placed in the electrolyte outlet of the cell to minimize H_2 concentration in the working electrode compartment. The cell is covered with an X-ray transparent, chemically-inert and -resistant Prolene® foil (Chemplex®, 4 µm).

The electrolyte tubing is realized by PTFE tubes and fittings. The electrochemical cell is made of polychlorotrifluoroethene (PCTFE) which is chemically resistant. The sample is placed on a PCTFE rod and is hold by slight under pressure which ensured by a membrane pump. A demister unit was applied between sample holder and membrane pump to safe the pump from flooding in case of electrolyte leakage. The sealing between sample and sample holder is realized by Viton® O-Ring and the sample is contacted from the backside using a Ti wire.

During *in situ* characterization the electrolyte is pumped through the cell using a peristaltic pump and can be constantly degassed e.g. using N_2 to remove all O_2 and H_2 and ensure constant reaction conditions. The *in situ* electrochemical setup can be operated in two modes – electrochemical mode and X-ray mode as defined by the thickness of the electrolyte layer between sample and foil. To set electrochemical mode which ensures the equilibration of current and catalyst, the thickness of the electrolyte layer can be increased by applying a slight electrolyte overpressure by a larger pump rate or by changing the level of the electrolyte outlet. The X-ray characterization is conducted after electrochemical equilibration at the desired electrode potential in X-ray mode when the thickness of electrolyte layer between sample and X-ray window is minimal. This minimizes the X-ray attenuation and scattering by the water molecules and leads to an optimized photon flux at the sample and detector especially at X-ray energies below 12 keV. The electrochemical cell is designed such that it can be operated with the sample surface horizontally or vertically orientated and grazing-incident X-ray configuration can be performed.

Chapter 4 Correlating Structural Motifs and Catalytic Activity of Layered and 3D Cross-linked MnO_x for OER

“Manganese based precious metal-free electrocatalysts for the oxygen evolution reaction (OER) are promising materials for energy storage systems based on dark or photo-coupled water electrolysis, because they are active, inexpensive and of low toxicity. In this work, atomic scale structure-activity relations of two different nano-structured manganese oxides, MnOx, are established using a combination of X-ray absorption, diffraction and electrochemistry. Prepared by chemical symproportionation (s-MnO_x) and impregnation (i-MnO_x), the s-MnO_x catalyst consisted of a layered structure similar to δ-MnO_2 while the i-MnO_x displayed a mixture of tunnelled, 3D cross-linked β- and a defective γ-MnO_2. During electrocatalytic oxygen evolution the structural motifs of both MnO_x remain largely unchanged, but the oxidation state of Mn increases from 3.5 to 3.9-4. Kinetic parameters of the electrocatalytic oxygen evolution reaction were extracted using Tafel slope analysis and pH titration experiment and the role of the protons abstracted was analyzed. The study uncovers fundamental differences of general importance in the catalytic activity between layered and cross-linked structures. Exclusive presence of di-μ-oxo bridged Mn ions in the layered structure is coupled to a pronounced redox and charge capacity behaviour. This ensured efficient use of surface and bulk active sites, and resulted in a relatively large Tafel slope. Consequently, the intrinsic OER activity is especially high in the s-MnO_x. In contrast, 3D cross-linked structures with both mono- and di-μ-oxo bridged Mn ions resulted in lower intrinsic activity but smaller Tafel slope, and thus favourable activity at technological water-splitting rates. The insights of this comparative study will provide guidance in the structural design and optimization of other non precious metal oxide OER catalysts.” [121]

Chapter 4 and section Appendix A1 were reproduced from Ref. [121] with permission from the Royal Society of Chemistry.

A.B. designed and performed the experiments. I.Z. performed the synchrotron XAS measurements and data evaluation. A.B., I.Z., H.D. and P.S. wrote the manuscript.

4.1 Experimental Details

4.1.1 Synthesis of Catalysts Powders

Carbon-supported manganese oxide has been synthesized via two different preparation methods – symproportionation deposition-precipitation (s-MnOx) and incipient wetness impregnation (i-MnOx).[126] In both cases, multi-walled carbon nanotubes (MWNT, Bayer MaterialScience AG, 95% C) has been pre-treated with concentrated HNO_3 at 100°C for 16 h to remove the residual growth catalyst and amorphous carbon impurities and to functionalize their inner and outer surfaces by oxidation.

s-MnOx has been prepared via impregnation of the carbon support with Mn^{2+} from 0.015M manganese(II) nitrate tetrahydrate/ 0.09M ammonium chloride solution ($Mn(NO_3)_2{\bullet}4H_2O$, Merck) and drop wise addition of an 0.01M aqueous potassium permanganate solution ($KMnO_4$, Roth) under vigorous stirring. A constant pH of 8 was ensured via titration with ammonia. Afterwards, the compound was thoroughly washed, filtered and dried in air at 110 °C for 16 h.

i-MnOx has been prepared via incipient wetness impregnation of the carbon support with a nominal loading of 10 wt.% of Mn^{2+} ions in an aqueous $Mn(NO_3)_2$ solution. The compound was consecutively dried in air for 6 h and 24 h at 60 °C and 110 °C, respectively.

4.1.2 Electrochemical Characterization

Preparation of Electrodes

"[…] The catalytically active MnO_x powders were deposited as thin films on glassy carbon (GC) rotating disk electrodes (Pine Instruments, ø 5 mm). Prior to the deposition, GC electrodes were polished and cleaned stepwise in an ultrasonic bath using Milli-Q water, acetone, and Milli-Q water. 5 mg of catalyst powder was suspended in a mixture of 1.99 ml of ultrapure water, 500 ml of 2-propanol and 10 µl of Nafion® solution (5 wt% of stock solution, Sigma-Aldrich) followed by homogenization using a horn sonicator. Finally, 10 µl of the catalyst suspension was dispersed on the electrode and dried in air at 60 °C for 10 min. Thus, a Mn loading of the GC electrodes of 172.8 nmol cm^{-2} and 178.5 nmol cm^{-2} was achieved for s- and i-MnOx, respectively. […]

Sample Preparation for XAS Characterization

Samples for XAS experiments were prepared on glassy carbon cylinders, in analogy to the electrochemical RDE experiments. Electrochemical treatment in the OER range was conducted at 1.763 V for 3 min. After removal from the electrolyte under potential control, the electrode was dried immediately under air and nitrogen and immersed in liquid nitrogen where it was until XAS measurements.

4.2 Results

4.2.1 Structural Investigations

Long-Range Order and Morphology

Figure 6 shows the powder X-ray diffraction pattern of s-MnOx and i-MnOx recorded between 10 and 75° using Cu K_α radiation. The graphite structure of the $MWNT_{ox}$ causes three strong diffraction peaks at ~25, ~43° and ~53° (Figure A1). For s-MnOx, two asymmetric reflections at ~37° and ~66° are caused by the defective crystal structure of a δ-MnO_2 phase (space group: C1). These two reflections are in good agreement with the reflections arising from regular distances within the layers consisting of edge-sharing Mn octahedra. The reflections can be assigned to the (200)/(110) and (310)/(020) doublets at ~37° and ~66°, respectively. The absence of reflections (h k $l\neq0$), especially the strong (00l), reveals the absence of long-range order of layer stacking. This can be induced by MnO_6 monolayers or variations in the interlayer distance due to “turbostratic” disorder.[133] Reflection shape analysis revealed significant size-induced broadening.

The integral breadth analysis of the MnOx reflections led to a coherence length of the layers of ~6 nm. Thus, s-MnOx is structurally similar to the δ-MnO_2 phase. Xie et al. found a very similar diffraction pattern for the MnO_x-coated MWNT and claimed it to be an ε-MnO_2 phase. This ε-MnO_2 phase can be described as a highly defective MnO_2 phase showing more de Wolff defects and microtwinning than γ-MnO_2 or rather a nearly random distribution of Mn ions in a hexagonally close packed O^{2-} lattice.[149]

In the case of i-MnOx, the diffraction pattern exhibits more than 10 reflections arising from γ-MnO_2 (space group: Pnma; PDF#00-044-0142) and rutile-type β-MnO_2 (space group: $P4_2/mnm$, PDF#01-072-1984) as the major and minor phase, respectively.

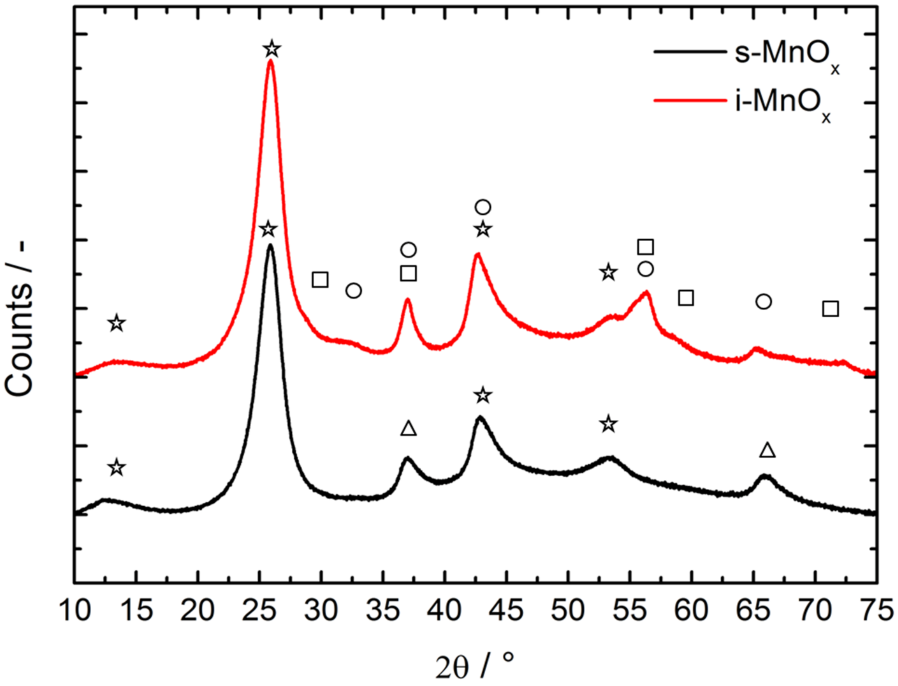

Figure 6: Powder X-ray diffraction pattern of s-MnO$_x$ (black) and i-MnO$_x$ (red) between 10° and 75°, at Cu K$_\alpha$ radiation. Reflections are labeled by squares for β-MnO$_2$, by circles for γ-MnO$_2$, by triangles for the layered MnO$_2$ phase, and by stars for the reflexes caused by the support material. The latter are shown in Figure A1.

Crystallite size analysis from reflection broadening is generally hindered for β- and γ-MnO$_2$ because size-induced broadening is superimposed by defect-induced broadening of the reflections. Furthermore, the limited intensity of the reflections made crystallite size analysis for the γ-MnO$_2$ phase in i-MnOx impossible. In the case of β-MnO$_2$, the (220) reflection at ~59° is not affected by defects in the rutile lattice and could be used to estimate the size of the β-MnO$_2$ crystallites to be below 5 nm.[132] According to the diffraction pattern, the γ-MnO$_2$ phase of i-MnOx exhibits a significant amount of single chains of Mn octahedra in the γ-MnO$_2$ lattice (de Wolff defects) and a minor fraction of twinning faults. The presence of de Wolff defects is visible in the significant shift of the (130) reflection at ~32° with more than 3° from its ideal position. De Wolff defects can reduce the angular separation of γ-MnO$_2$ (110) and (130) from 12 to 7°.[132] However, the γ-MnO$_2$(110) reflection is hidden under the C reflection at ~25°. The presence of any sizeable contribution from α-Mn$_2$O$_3$ in i-MnOx (as a possible origin of the diffraction reflection at ~32°) was excluded from XAFS characterization discussed further below. Microtwinning in the γ-MnO$_2$ lattice could be extracted from the merged (221)/(240) doublet of γ-MnO$_2$ at ~56° but the real fraction of microtwinning is significantly lower because higher degree of microtwinning would lead to a shift of the (130) reflection towards higher diffraction angles, which was not observed in our data.

These findings from X-ray diffraction analysis are in agreement with earlier TEM analysis showing that s- and i-MnOx consist of Mn oxide particles with a size <10 nm attached to the $MWNT_{ox}$.[126]

Manganese Oxidation State from XANES Spectra

To get further insights into the structure of the two catalytically active oxides at the atomic scale, we employed X-ray absorption spectroscopy at the Mn K-edge (Figure 7). The XANES (X-ray absorption near-edge structure) region is particularly sensitive to the average oxidation state and local coordination geometry.[150] In general, the energy of the X-ray absorption edge increases with increasing oxidation states of the absorbing atoms due to the rise in the electron binding energy.[151] On the basis of calibration with Mn compounds with known structures, the average oxidation state of manganese in i-MnOx powder was around 3, while in s-MnOx it was around 3.5. After deposition on the GC electrode the oxidation state in both s-MnOx and i-MnOx was estimated to be around 3.5 (Figure A2 and Figure A3). This indicates that both oxides contain a large fraction of Mn^{4+} already before applying an oxidizing potential, but a significant amount of Mn ions are in a lower oxidation state (+2 or +3). The result for s-MnOx is in good agreement with the previously determined Mn oxidation state by Mn L-edge measurements and temperature-programmed reduction (TPR).[126] The oxidation state for i-MnOx previously obtained from Mn L-edge XAS, however, was +2, explainable by Mn reduction occurring either during the thermal treatment at low oxygen partial pressure and or caused by X-ray irradiation during data collection. In the present study the thermal treatment was performed at 110 °C instead of 80 °C and in ambient air. X-ray photoreduction was avoided in the present study by (i) collecting the XAS spectra at a temperature of 20 K and (ii) using strictly limited periods of X-ray irradiation on a single sample spot.

For transition metal based catalysts, the oxidation state of the metal ion was suggested to depend on the applied potential during electrocatalytic OER.[53, 115, 123, 152] To determine the extent of these changes for the Mn ions in the studied materials, we measured XAS spectra of s- and i-MnOx frozen in liquid nitrogen immediately after applying 1.763 V in 0.1M KPi at pH 7 for 3 min. In both oxides, a clear shift of the edge position in the XANES spectra was observed (Figure A2) corresponding to an increase of the mean Mn oxidation state to almost +4.0. The same shift in the edge position was observed for s-MnOx frozen after 3 min of operation at 1.763 V in 0.1M KOH at pH 13.

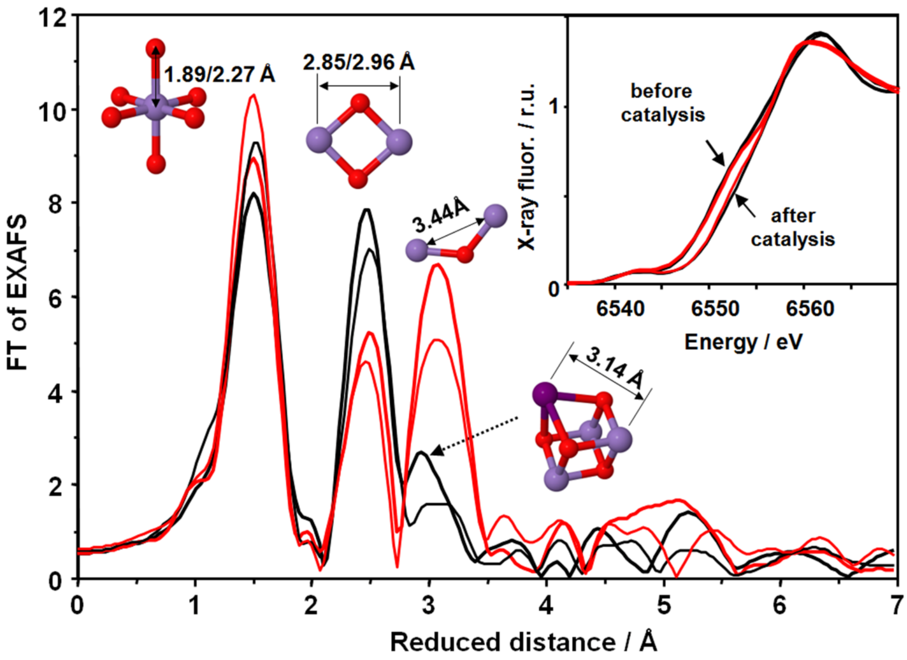

Figure 7: X-ray absorption spectra of s-MnO_x (black) and i-MnO_x (red) deposited on electrodes before and after catalysis. The edge region of the spectra (XANES) is shown in the inset. The average oxidation state of Mn in the two samples directly after deposition on the electrode (thick lines) is around 3.5, while after 3 min of operation at 1.763 V in 0.1 M KPi at pH 7, it increases to 3.9-4.0 (thin lines). The structural motifs considered in the EXAFS simulations are schematically depicted next to the corresponding FT peak and the obtained interatomic distances are indicated. (Mn^{4+} ions are presented as spheres in magenta, Mn^{3+} ions in dark purple, and oxygen as red spheres.)

Despite the similar Mn oxidation state of the two oxides after operation as catalysts, the quasi-*in situ* experiment revealed differences in XAS edge shapes which imply that the coordination geometry of the Mn ions is modified. To address these structural differences, extended X-ray absorption fine structure (EXAFS) spectra were analysed.

Structural Information from EXAFS

The Fourier transforms (FTs) of the EXAFS spectra of s-MnOx and i-MnOx are presented in Figure 7. In the FT, typically each peak corresponds to a specific absorber-backscatterer vector. In our case the absorber is a Mn ion, and the backscattering atoms can be either oxygen atoms or Mn ions surrounding the absorber. The distance between the absorber and backscatterer corresponds to the position of the FT peak plus about 0.4Å.[150] Both s-MnOx and i-MnOx show a first peak at a reduced distance of around 1.5 Å, which is typical for 6-fold oxygen coordinated Mn^{4+} ions and a second peak at around 2.5 Å related to di-μ-oxo-bridged Mn^{4+} ions.[153-154] For i-MnOx there is also a well pronounced third peak, assignable to mono-μ-oxo connected Mn ions (longer Mn–Mn distance).[155] This assignment of the first three peaks can be made by comparison to the FT spectra of Mn oxides with known structures (Figure A4-B†). Visual comparison to the FTs of EXAFS spectra from reference Mn oxides suggests that while s-MnOx has layered δ-MnO_2-like structure composed predominantly of edge-sharing (di-µ-oxo-connected) Mn octahedra (Figure 8), the i-MnOx contains a significant fraction of corner-sharing (mono-µ-oxo-connected) Mn octahedra resulting in formation of tunnels.

To confirm this interpretation and to analyse the structural changes during the electrochemical water oxidation, we simulated seven k^3-weighted EXAFS spectra measured from s-MnOx and i-MnOx (i) as powders, (ii) after deposition on the GC electrode, (iii) and after catalytic operation at 1.763 V at pH 7. The GC electrode covered with s-MnOx was also measured after electrocatalytical operation at pH 13. In the EXAFS simulations, we assumed two Mn–O distances contributing to the first Mn coordination shell: the shorter Mn–O distance is assigned to Mn^{4+}–O vectors and the longer is assignable either to Mn^{3+}–O vectors along the elongated Jahn–Teller axis or to Mn^{2+}–O vectors. The sum of the coordination numbers for these two shells was kept equal to six because the small pre-edge feature of the XANES data suggested that in all samples the majority of the Mn ions are 6-fold coordinated. The other FT peaks were simulated with three shells of Mn backscatterer: a short Mn–Mn vector corresponding to edge-sharing MnO_6 octahedra (second peak), a longer Mn–Mn distance corresponding to corner-sharing MnO_6 octahedra (the third peak visible clearly in i-MnOx samples) and an elongated di-µ-oxo bridge, which could be hidden due to the large third peak in i-MnOx but is visible in s-MnOx. Such an intermediate distance was found in layered Mn oxides before and likely corresponds to Mn_4O_4 cubane motifs formed by the attachment of a Mn ion in an oxidation state lower than +4. Also in other water-oxidizing oxides, formation of a metal-oxo-cubane has been reported.[131, 154] The simulation results shown in Figure A5 confirm the qualitative interpretation given above and specify internuclear distances at high precision. We approached identification of structural changes resulting from application of oxidising potential during operation of the electrocatalyst. In tendency, Mn–O distances were decreased after operation at 1.763 V, confirming the increase of the average Mn oxidation state implied by the XANES data. For the Mn–Mn vectors in the s-MnOx sample, there appears no significant change in the coordination numbers, neither due to attachment to the GC electrode nor due to electrochemical treatment oxidation.

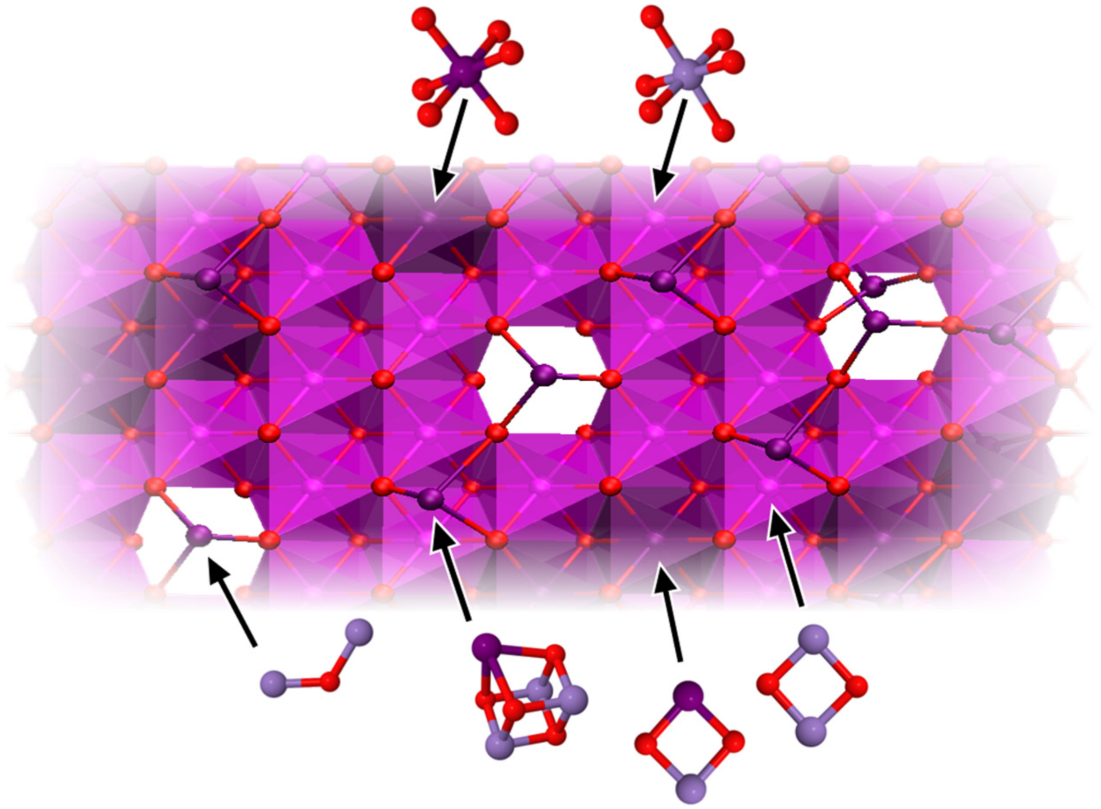

Figure 8: Schematic model for a distorted MnOx layer fragment formed from edge-sharing (di-μ-oxo bridged) $Mn^{4+}O_6$ and $Mn^{3+}O_6$ octahedra. Some Mn ions from the layer are missing (defects), and other Mn ions are bound on top (or below) of the layer resulting in mono-μ-oxo bridges (corner-sharing octahedra). At these defect sites, a row of edge-sharing octahedra could grow perpendicularly to the first one; this eventually may lead to formation of tunnel-like structures. Binding of a Mn^{3+} ions on top of the layer at sites without layer defects results in formation of a (distorted) Mn_4O_4 cubanes. (Mn^{4+} ions in magenta, Mn^{3+} ions in dark purple, O in red.)

For i-MnOx, there is an increase in the EXAFS coordination of the Mn–Mn vectors caused by attachment to the electrode. Interestingly, application of an oxidizing potential decreases the number of Mn–Mn vectors. Although these changes appear to be significant, due to the large error bars an unambiguous statement about the extent and character of the structural changes cannot be made based on these fit results. The EXAFS fit results in a mean Mn–Mn distance of (2.89±0.01) Å between the Mn nuclei of two edge-sharing MnO_6 octahedra. The XANES data show the prevalence of Mn^{4+} but also Mn^{3+} ions may be present. For di-μ-oxo-bridged Mn^{4+} ions, the obtained Mn–Mn is often shorter, namely 2.86 Å.[123, 154-156] Moreover, we find that the Debye–Waller (DW) parameter corresponding to this shell is unusually high (Figure A5-C†) indicating either a broad Gaussian-shaped distance distribution function or a bimodal distribution, both centred around a mean Mn–Mn distance of 2.89 Å.

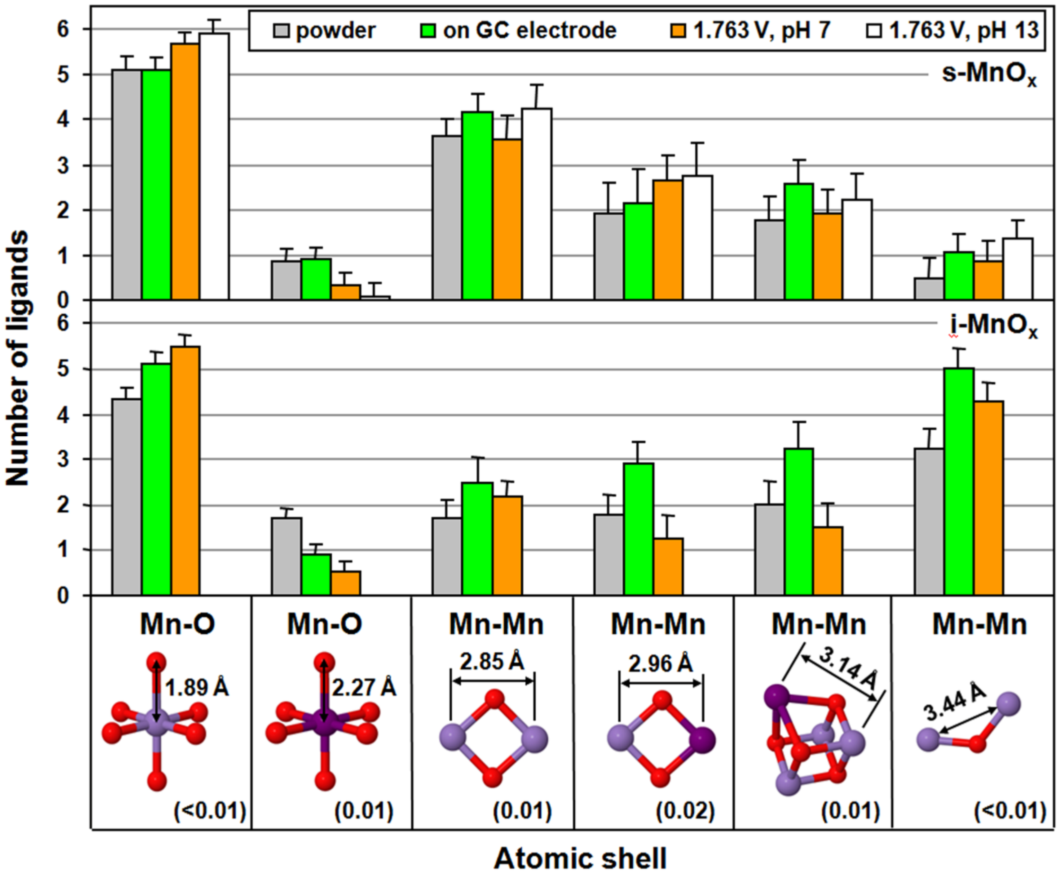

Figure 9: Coordination numbers and interatomic distances obtained by joint simulation of the k^3-weighted EXAFS spectra from s-MnO$_x$ (upper panel) and i-MnO$_x$ (lower panel) before and after operation as water oxidation catalysts in 0.1M KPi (pH 7) or 0.1M KOH (pH 13). The corresponding absorber-backscatter distances were kept equal for all seven spectra and are displayed together with the corresponding structural motif (colour code as in Fig. 2). The error bars represents the 68% confidence interval; the error for the interatomic distances is given in parentheses below the corresponding structural motif. For further details, see Figure A6.

The latter option is clearly more likely and implies that there are two specific Mn–Mn distances which contribute to the second FT peak. The shorter (<2.89 Å) and the longer one (>2.89 Å) may be assignable to Mn^{4+}-(μ-O)$_2$–Mn^{4+} and Mn^{4+}–(μ-O)$_2$–Mn^{3+} motifs, respectively.[131, 155] For more refined analysis, we approached a 'joint-fit' of all seven EXAFS spectra keeping the interatomic distances for the corresponding shells equal in all spectra. The increased significance of the joint-fit approach facilitated, *inter alia*, resolution of two short Mn–Mn distances of 2.85 and 2.96 Å, respectively. The joint-fit results are shown in Figure 9and discussed in the following. In the first Mn coordination sphere, short 1.89 Å Mn–O vectors typical for 6-fold coordinated Mn^{4+} are prevalent. A small fraction of up to 15% longer Mn–O distances of 2.29 Å is consistent with a minor contribution of Mn^{2+} or Mn^{3+} ions (for Mn^{3+} ions such long Mn–O distances are found along the Jahn–Teller axis).[157-158]

The results of the joint-fit approach (Figure 9) confirm the absence of major structural change for s-MnOx. After catalyst operation at 1.763 V, there may be a slight decrease in the number of the out-of-layer Mn^{3+} ions (cubane motifs, 3.14 Å) and a slight increase of the in-layer Mn^{3+} ions (2.96 Å), resulting in larger heterogeneity of the Mn–Mn distances contributing to the second FT peak and thus a decreased peak height. These changes are relatively small and thus close to the error limit. The sum of the two short Mn–Mn vectors is around 6 as expected for perfectly ordered layers of δ-MnO_2.[154] Interestingly, this value appears to increase slightly upon catalyst operation at 1.763 V, possibly explainable by Mn–Mn vectors from out-of-layer Mn^{4+} ions involved in $Mn^{4+}{}_4(\mu O)_4$ cubane formation. When an oxidizing potential is applied to i-MnOx, larger structural rearrangements can be observed (Figure 9). There is a clear decrease of the mono-μ-oxo and di-μ-oxo-vectors with participation of Mn^{3+} ions (2.96 Å and 3.14 Å distances). This decrease in the number of in-layer Mn^{3+} ions (2.96 Å) contrasts the slight increase in s-MnOx. Also the Debye–Waller parameter (distance spread) for the Mn–O distances increases at higher potential for s-MnOx and decreases for i-MnOx (Figure A6), which could reflect different protonation patterns of the oxygen atoms at bridging and terminal positions. The presented results indicate clear differences between the structure of the two oxides in their resting states (XRD, EXAFS) and regarding the structural changes induced by application of an oxidizing potential (EXAFS).

The question arises of whether and how these structural differences relate to the elementary mechanism of the water oxidation and oxygen evolution. To investigate this further, s-MnOx and i-MnOx were characterized electrochemically and indeed, confirmation for different processes involved in water oxidation was found in the different kinetic characteristics of the two materials, as described in the following.

4.2.2 Electrochemical and Electrokinetic Investigations

Electrochemical Characterization

Cyclic voltammetry was used to investigate the redox behaviour of the Mn ions in s- and i-MnOx in 0.1 M KPi at pH 7. Figure 10 shows the first and the 11th potential scan recorded between 1.0 and 1.7 V at a scan rate of 100 $mV \cdot s^{-1}$ with a starting potential of 1.5 V. Both materials exhibited a mainly capacitive voltammogram between 1.0 and 1.6 V caused by the charge storage capability of both the high-surface carbon support and MnOx. The capacitance of s-MnOx is clearly larger than that of i-MnOx, which does exceed the capacitance of the carbon support only marginally (Figure A8). This suggests a higher extent of oxidative charging (by Mn oxidation) in s-MnOx.

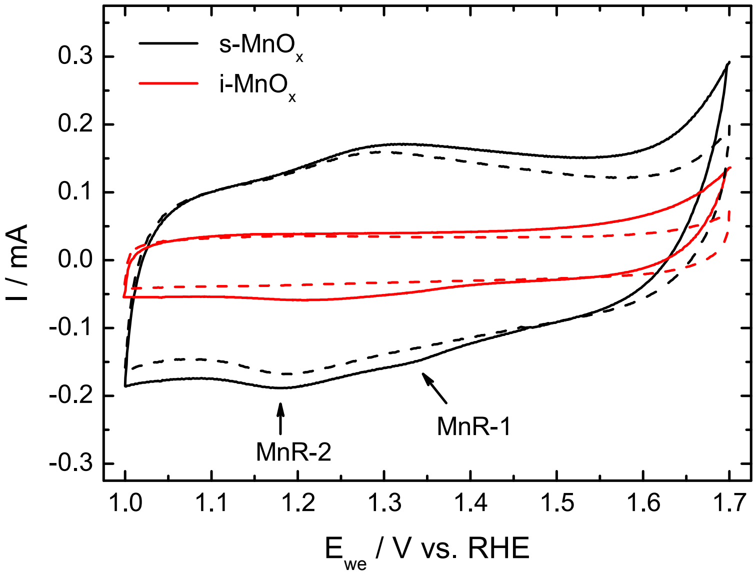

Figure 10: Cyclic voltammograms (CV) of first (solid) and 11th (dashed) scan of s-MnO$_x$ (black) and i-MnO$_x$ (red). The CVs were recorded in 0.1 M KPi at pH 7 with a scan rate of 100 mV s^{-1}. Two minima resolved in the s-MnO$_x$ CV are labeled by MnR-1 and MnR-2, respectively.

At potentials above 1.6 V, the current increases inter alia due to oxygen evolution. Both voltammograms show the differences in the redox behaviour of the Mn ions in MnOx. The first cathodic potential scan of both MnOx exhibits a double reduction feature (MnR-1 and MnR-2) between 1.45 and 1.10 V. During the subsequent anodic scan, s-MnOx exhibits the corresponding oxidation peak whereas no oxidation peak is resolved for i-MnOx. The transferred charge during electrochemical reduction of the Mn ions in i-MnOx is significantly lower.

Comparing the potential of the reduction feature of s- and i-MnOx with literature values might point toward the redox couple of Mn^{2+}/MnO_2.[159] This assignment is in line with the XANES results which show that at an OER potential mainly Mn^{4+} ions are present in the catalyst. However, the presence of a double reduction feature in s- and i-MnOx suggests a two-step electrochemical reduction of Mn^{4+} to Mn^{3+} and further on to Mn^{2+}. In electrodeposited MnOx films, similar redox peaks were successfully connected to changes in the visible light absorption of the oxide and interpreted as Mn oxidation state changes.[123] During continuous potential cycling between 1.0 and 1.7 V, the Mn^{4+} reduction features disappear completely in the case of i-MnOx whereas s-MnOx continues to exhibit both redox features even after 10 potential cycles with only slightly reduced charge. Thus, the Mn ions in i-MnOx passivate irreversibly (but notably not completely) during initial reduction and the voltammogram becomes almost purely capacitive, whereas we observe only little redox passivation in s-MnOx.

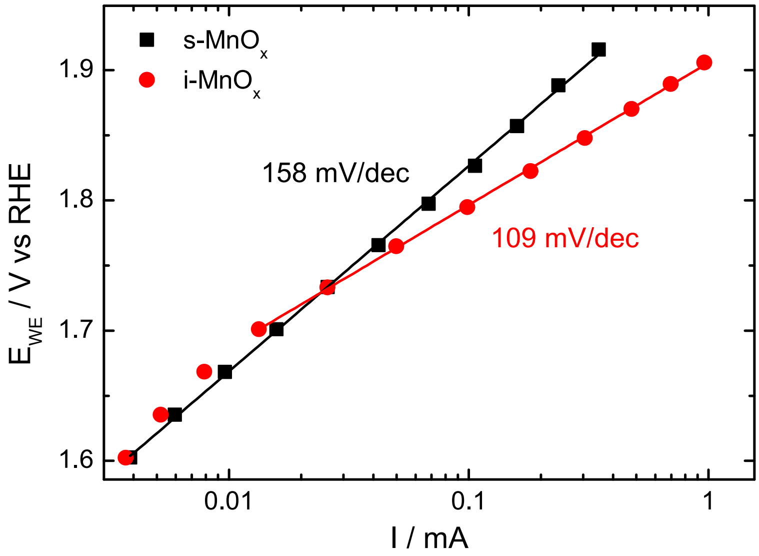

Figure 11: Tafel plot of s-MnO$_x$ (black) and i-MnO$_x$ (red) extracted from quasi-stationary potential-step RDE experiments in 0.1 M KPi at pH 7. All electrode potentials have been iR-corrected. The respective Tafel slopes as determined by linear regression are indicated.

Tafel Slope Analysis

Figure 11 shows Tafel plots for s- and i-MnOx extracted from quasi-stationary experiments in 0.1 M phosphate buffer at pH 7. (In Figure 11 and elsewhere, the detected electrical current is given; the current density per cm^2 is by a factor of about five higher than the indicated current.) Both s- and i-MnOx show a linear E vs. log(I) dependency in the potential range of 1.6–1.9 V and 1.7–1.9 V, respectively. The onset potential for the electrocatalytic oxygen evolution is 100 mV lower for s- than that of i-MnOx. A linear regression of the experimental data within the mentioned potential ranges led to Tafel slopes of 158 and 109 mV·dec^{-1} and thus, experimental anodic transfer coefficients, b, of 0.39 and 0.54 for s- and i-MnOx, respectively.

The exchange current density i_0 of s-MnOx (10^{-3} mA) is significantly higher than that of i-MnOx (10^{-7} mA). Thus, s-MnOx shows a significantly higher intrinsic electrocatalytic activity than that of i-MnOx, whereas at higher electrode potentials the OER activity of i-MnOx is superior. Thus, we conclude conservatively that there are pronounced functional differences between s-MnOx and i-MnOx in the rate-determining process and possibly regarding number and location of active sites.

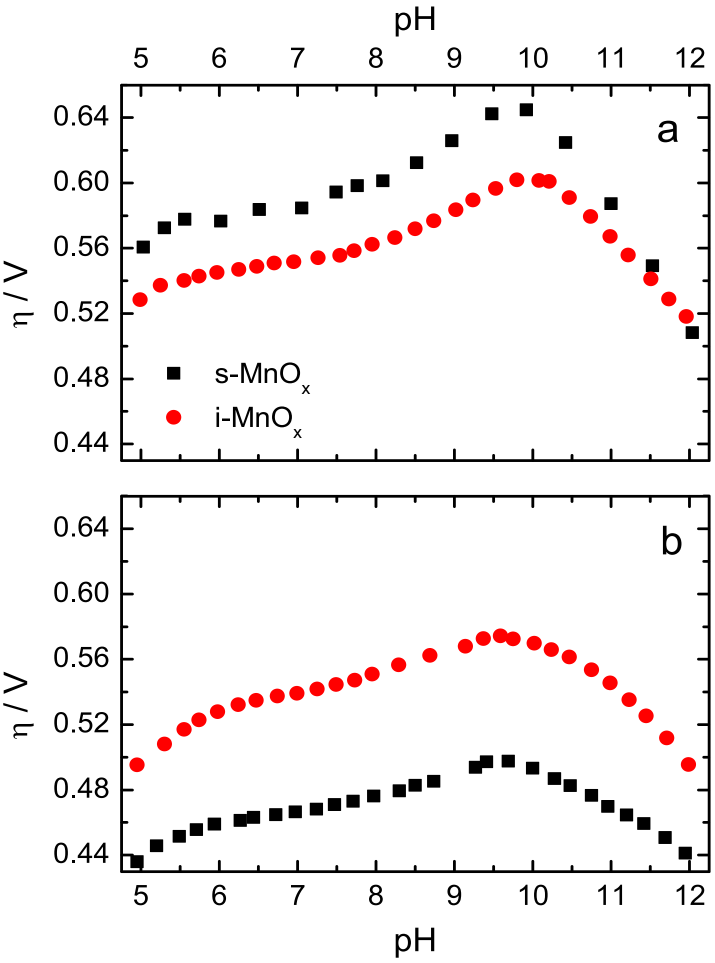

Figure 12: pH dependency of the overpotential (η) of s- and i-MnO$_x$ determined in 0.1 M KPi at constant currents of (a) 50 μA and (b) 20 μA. The overpotential has been calculated according to
$\eta = E_{NHE} + (59\text{mV/pHunit}) \cdot \text{pH} - 1.23\ \text{V}$.

pH Dependence of Current and Overpotential

Figure 12 shows the dependence of the overpotential η on the H^+/OH^- concentration in the electrolyte between pH 5 and 12 at a constant current of 20 μA and 50 μA. At both currents, the η–pH profile for both MnOx can be divided into two regimes.

For example at a constant current of 20 μA (Figure 12b), the overpotential increases between pH 5 and 9.6 for s-MnOx (i-MnOx) from 435 mV (495 mV) to 497 mV (574 mV). Above pH 10, the overpotential decreases to 441 mV (495 mV). Thus at 20 μA, s-MnOx exhibits a lower overpotential over the investigated pH range than i-MnOx, due to its higher intrinsic electrocatalytic activity (higher exchange current density), but the principal pH dependence of the catalytic current of two oxides is the same.

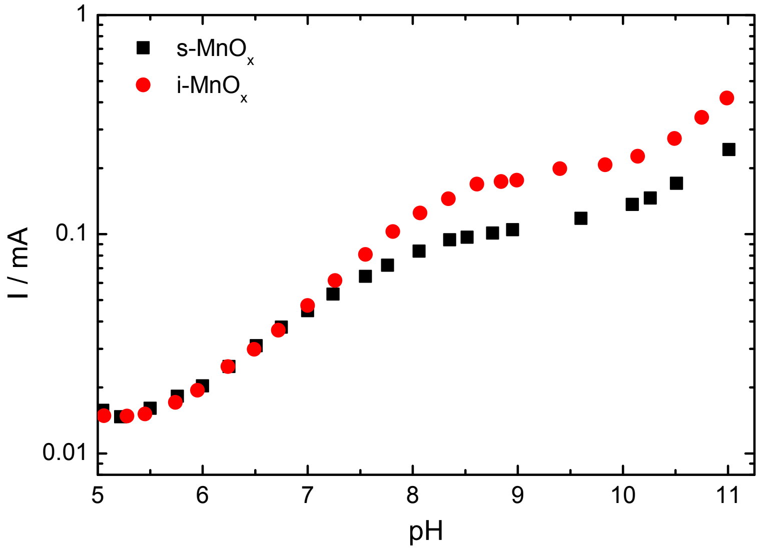

Figure 13: pH dependence of the catalytic current (*I*) determined in 0.1 M KPi at a constant electrode potential of 1.35 V vs. NHE.

At 50 µA (Figure 12a), i-MnOx exhibits a lower overpotential, due to its lower Tafel slope. Yet again, the principal pH dependence of the two oxides is the same.

Thus, we conclude that an intricate coupling of electrocatalysis to (de)protonation reactions is functionally decisive in both oxides. Comparison of the two panels of Figure 12 reveals that the crossover point of the Tafel plot is observable at all investigated pH values implying that at all pH, the exchange current in s-MnOx is higher than that in i-MnOx whereas the Tafel slope always is lower in i-MnOx.

This implies that the functional differences between the two oxides indicated by different Tafel slopes and exchange currents do not relate to differences in the coupling of the rate-determining step to protonation reactions. We also investigated the pH-dependence of the current at a constant catalytic potential of 1.35 V vs. NHE (Figure 13). With increasing pH, a biphasic increase in the catalytic current is observed. The first increase is detected for pH values ranging from 5.7 to 8.7, that is, around the second pK of the phosphate ion ($pK_{2nd} \approx 7.2$, $H_2PO_4^{1-}/HPO_4^{2-} + H^+$); at pH values below 5.7 and above 8.2, plateau levels are reached. Thus, the pH dependence of the catalytic current at a constant potential of 1.35 V vs. NHE resembles the pH titration curve of the phosphate ion.

This finding suggests that stoichiometry or concentrations of [HPO_4^{2-}] and [H2PO4^{1-}] determine catalytic activity. At even higher pH (>10), a further increase is observed, explainable by the increasing availability of OH^- ions at higher pH values.

4.3 Discussion

The oxygen evolution reaction is a complex multi-electron transfer process controlled by macroscopic, microscopic and atomistic parameters, such as the number, accessibility and character of catalytically active sites, the chemical reaction mechanism, the concentration of reactant, electrical and protonic conductivities, and the removal of products. The number of catalytically active sites depends on the number of accessible Mn ions for water molecules, which, in turn, is strongly connected to the structure and the morphology of the electrocatalyst. If no Mn ions of the bulk material were involved in the water splitting, the number of active sites would be (most probably) directly proportional to the surface area of MnOx and thus, particle size. However, in the case of a layered MnO_2 phase, bulk Mn ions are accessible for water molecules and cations alike and thus, the number of accessible active sites is more likely approaching the total number of Mn ions. Furthermore, the local coordination of the Mn ions can critically determine how accessible they are and to what extent they can contribute to the overall catalytic activity. For the two nano-structured Mn oxide catalysts considered herein, there is a clear and important structural difference in the Mn coordination, e.g. there exist nearly exclusively di-μ-oxo bridged Mn ions in s-MnOx, whereas more mono- than di-μ-oxo bridged Mn ions exist in the i-MnOx catalyst. The electrochemical analysis suggests that higher intrinsic onset activity in the low-current regime is associated with the prevalent presence of di-μ-oxo-bridged Mn ions in form of a layered oxide (Figure 4c) coupled with a significantly higher electrochemical capacitance. Thus, we hypothesize that the electrochemical accessibility of catalytically active Mn ions, likely one important controlling factor for OER activity, is higher in the layered s-MnOx structures than in the cross-linked i-MnOx structures. This is consistent with the fact that in layered δ-like MnO_2 structures bulk Mn ions are much better accessible for the reactant molecules and cations through the interlayer space. This is in clear contrast to tunnelled MnO_2 structures which generally show a lower charge storage capacity compared to layered Mn structures and the charge storage capacity is proportional to the void space in the lattice. The (1x1) and (2x1) tunnels in i-MnOx exhibit certain proton conductivity but are not accessible to the water molecules and larger cations.[137, 160] In conclusion, the participation of bulk Mn ions could lead to a larger number of active sites and thus, a higher exchange current density for s-MnOx than i-MnOx. The structural motif of di-μ-oxo-bridged transition metal ions resulting in layers (or layer fragments) of edge-sharing MO_6 octahedra has proven to be a unifying feature of many oxygen-evolving Co and Ni oxide electrocatalysts prepared by electrodeposition.[53, 112-113, 141] Looking at electrodeposited OER catalyst materials, the beneficial effect of layered oxide with the prevalence of di-μ-oxo-bridging between metal ions and their large interlayer space filled by water and further ions becomes obvious: bulk metal ions are able to participate as catalytically active sites.[53] Beyond its favourable intrinsic activity (high exchange current density), Tafel slope analysis showed that layered s-MnOx displayed inferior electrocatalytic behaviour at larger current densities reflected by a larger Tafel slope of 158 mV·dec^{-1} compared to 109 mV·dec^{-1} for i-MnOx. The unfavourably large Tafel slope of s-MnOx likely relates to the high level of order within the layers of edge-sharing MnO_6 octahedra, which is clearly higher than those found in the electrodeposited MnO_x of ref. [123] (a Tafel slope of 90 mV·dec^{-1}) and in water-oxidizing MnO_x particles.[123, 131] Less order implies a higher number of defect sites, e.g. Mn vacancies; the structures of putative defect sites are shown in Figure 8. These defect sites prevent the prevalence of di-μ_3-oxo thereby resulting in more di-μ_2-O(H) bridges between Mn ions as well as in a higher number of terminal water coordination sites; both features likely are crucial for OER activity.[29] And indeed, an inverse relationship between di-μ_3-oxo bridging (low number of di-μ_2-O(H) bridges and defect sites in general) and OER activity has been demonstrated for Co- and Mn-based oxides before,[53, 123, 131] but a comparison of Tafel slopes had not been approached. We now propose that an unfavourably high Tafel slope of the OER reaction can result from a strong prevalence of unreactive di-μ_3-oxo bridges between the first-row transition metal ions of the respective oxide, which is caused by the octahedral cross-linking and/or a level of structural order that is too high. This suggestion is supported by the results of the present investigation and immediately provides a guideline for designing catalytic oxides with a favourably low Tafel slope. We note in passing that di-μ_2-oxo bridges are also present at the ideal β-MnO_2(110) and γ-MnO_2(100) surfaces and so, similar structural motifs could participate in the electrocatalysis of s-MnOx ('internal' surface between oxide fragment and intercalated water) as well as of i-MnOx ('external' oxide-electrolyte surface). Tafel slopes of 120 mV·dec^{-1} have been determined for Mn oxide electrocatalysts and from this, a one-electron transfer step has been concluded to be the *rate-determining step* (rds) in MnO_x.[128] Herein, a lower Tafel slope of 109 mV·dec^{-1} as determined for i-MnOx does not support a simple one-electron transfer step to be rate determining during OER, neither does the value of 158 mV·dec^{-1} in s-MnOx. In line with this conclusion, the detected pH-dependence of overpotential and catalytic current rule out rate-limitation by a simple one-electron transfer step, but point towards a role of proton-coupled electron transfer in the *rds*.

A critical factor determining the OER activity is ion transport, specifically proton removal from the catalytic site and proton transfer into the electrolyte. Relevant factors may be the proton conductivity and uptake capability of the electrolyte. The log(I)–pH profile of Figure 13 reflects the 2nd phosphate pK, thereby illustrating a crucial role of the phosphate protonation state. In the η–pH profile of Figure 12, we find a minimal catalytic activity at a maximal concentration of HPO_4^{2-} equivalent to the minimal buffer strength in the investigated pH range (Figure A12). The buffer strength is the ability to compensate for increasing H^+ concentration by chemical binding of the proton to a base. At pH values above the 2nd phosphate pK ($pK_{2nd} \approx 7.2$), the buffer strength of the $HPO_4^{2-}/H_2PO_4^{1-}$ ion decreases. At higher pH, the hydroxyl ions can significantly contribute to the proton uptake and the buffer strength increases. Both effects are reflected in the η–pH curves of both oxides. The beneficial influence of the phosphate buffer is not related to an increase of the proton conductivity of the bulk solution. Though there are changes in the conductivity of the electrolyte (Figure A11a), the iR-correction does not change the η–pH profile significantly (Figure A11b†). The chemical proton abstraction from the active site by phosphate ions either adsorbed to MnO_x or in solution within the Helmholtz layer appears to be decisive. Thus, Mn based catalyst materials containing sizeable amounts of a proton-accepting base either as an intrinsic constituent – as reported for the 'cobalt-phosphate catalyst'[109] – or formed during operation may be a promising strategy.

4.4 Summary

We have revealed the dominant atomic-scale structural motifs of two distinctly different, either layered or 3D cross-linked, water-oxidizing MnO_x catalysts, and succeeded in correlating these structure motifs with the respective catalytic activity. Such relationships are of general importance, since they enable us to identify critical oxide characteristics controlling electrocatalytic activity. Our investigation suggests that the deliberate formation of activity controlling structural motifs can be controlled by simple conventional liquid metal ion precursor chemistry and is not restricted to electrodeposition methods. The electrokinetic analysis showed that the apparent processes during water oxidation depend on the different octahedral cross-linking in MnOx (with essentially the same mean oxidation state of the Mn ions), as clearly reflected in the two pronouncedly different Tafel slopes. The comparison to the structural data suggests that the atomic structure is a crucial determinant of the apparent processes during OER catalysis. Comparison with electrodeposited electrocatalysts guides towards a general character of MnO_x OER electrocatalysts. The active catalyst states of both MnO_x are closely related to the catalyst “precursor” although the mean Mn oxidation state increases from 3.5 to 4 upon operation at catalytic potential. Specifically, clear indications for Mn–Mn bridging mode changes in i-MnOx upon oxidation of the catalyst are detectable. This important discovery requires further in-depth investigation before its discussion in terms of the mechanism of water oxidation in the Mn oxides can be approached. We also note the interesting structural analogy between out-of-layer Mn ions linked to in-layer Mn ions via mono-μ-oxo-bridges resulting in corner-sharing MnOx octahedra and coordinatively unsaturated sites (cus) metal ion sites in rutile surfaces. It is feasible that coordinative under-saturation of such out-of-layer Mn ions may confer favourable adsorption and catalytic reaction characteristics as found for rutile cus sites.[161-162] Furthermore, our studies unravelled the beneficial effect of the proton uptake capability of the phosphate buffer during water splitting due to buffer strength and OH^- concentration. These findings – and the complex pH dependence in general – illustrate the importance of proton abstraction in OER catalysis by the two herein investigated oxides. However, further studies especially on the interaction between phosphate and MnOx with respect to OER are necessary. In summary, the structure–activity insights from this study provide guidelines to design and control the electrochemical OER behaviour of the complex structural chemistry of non-precious transition metal oxides. The water accessibility of the bulk oxide and the number of defect sites were tentatively identified as determinants of the experimental exchange current density and Tafel slope, respectively. The presented work may pave the way for future investigations which eventually could result in a comprehensive understanding of structure–activity relationships in water-oxidizing Mn oxides at the atomistic level."[121]

Chapter 5 Reversible Amorphization and the Catalytically Active State of Crystalline Co_3O_4 during Oxygen Evolution

“Water splitting catalyzed by earth-abundant materials is pivotal for global-scale production of non-fossil fuels, yet our understanding of catalyst structure and reactivity is still insufficient. Here, we report on the structurally reversible evolution of crystalline Co_3O_4 electrocatalysts during oxygen evolution reaction (OER) using advanced *in situ* X-ray techniques. At electrode potentials facilitating OER catalysis, a sub-nanometer shell of the Co_3O_4 is transformed into an X-ray amorphous $CoO_x(OH)_y$, which comprises di-μ-oxo bridged $Co^{3+/4+}$ ions. Unlike irreversible amorphizations, here, the formation of the catalytic active layer is reversed by re-crystallisation upon return to non-catalytic electrode conditions. The Co_3O_4 material thus combines the stability advantages of a controlled, stable crystalline material with high catalytic activity thanks to the structural flexibility of its active amorphous oxides. We propose that crystalline oxides may be tailored for generating reactive amorphous surface layers at catalytic potentials, just to return to their stable crystalline state under rest conditions.” [68]

Chapter 5 and section Appendix A2 were reproduced from Ref. [68] with permission from the Nature Publishing Group.

A. Bergmann, E. Martinez-Moreno, D. Teschner, P. Chernev, M. Gliech, J. F. d. Araújo, T. Reier, H. Dau, P. Strasser, *Nat. Commun.* **2015**, 6:8625.

A.B., E.M.M., P.C. and D.T. performed the experiments and analyzed the data. J.F.A. performed DEMS experiments, M.G. performed transmission electron microscopy, and T.R. performed scanning electron microscopy and assisted in the synthesis. A.B., H.D., and P.S. designed the experiments and wrote the manuscript.

5.1 Experimental Details

Preparation of Co_3O_4 Thin Films

“Co oxide films were deposited on GC (HTW) plates using spin coating. Before the deposition, the substrates were polished until a mirror-like finish was achieved and cleaned stepwise in an ultrasonic bath using de-ionized water and acetone. The Ti cylinders were treated in HNO_3/H_2O solution for 2 h at 150 °C after polishing. The spin coating solution consisted of 0.25M Cobalt(II) 2,4-pentanedionate (AlfaAesar) in 15 vol.% acetic acid (Sigma-Aldrich, 99.7%), 18 vol.% de-ionized water (>18MΩ) and 67 vol.% ethanol (abs., AnalaR Normapur). The precursor was dissolved using sonification for 10 min. The spin coating was conducted at 2,000 r.p.m. for the GC plates and 5,000 r.p.m. for Ti cylinders. In total three and five layers were deposited on the GC and Ti substrates, respectively. After each layer deposition, the samples were calcined in air for 10 min at 300 °C to decompose the Co precursor. Finally, the samples were calcined for 15 min at 400 °C in air to achieve a crystalline Co oxide. […]

DEMS Measurements

To investigate the reaction products, DEMS was performed. The DEMS apparatus consisted of a home-made dual thin-layer electrochemical flow cell based on a design reported elsewhere61. The flow cell was connected via separation polytetrafluoroethylene (PTFE) membrane to a Prisma quadrupole mass spectrometer (QMS 200, Pfeiffer Vacuum) equipped with two turbomolecular pumps HiPace 80 operating the MS chamber at 10^{-6} mbar. N2-saturated 0.1M KPi at pH 7 acted as electrolyte and the electrolyte flow was adjusted to 5 ml s^{-1}. The reference electrode was a reversible hydrogen electrode and a Pt wire was the counter electrode. Cyclic voltammetry measurements were conducted in the OER regime between 1.1 and 1.675 V versus reversible hydrogen electrode using a sweep rate of 6mVs1. Simultaneously, the ion current for O_2 (m/z=32) and CO_2 (m/z=44) was recorded. All electrode potentials were corrected for Ohmic losses.

in situ GIXRD Measurements

Investigation of crystal structure under electrochemical reaction conditions have been conducted at the MPI-MF beamline at ANKA, Karlsruhe.[163] An home-made *in situ* electrochemical cell for X-ray studies as described above. The electrolyte was constantly circulated using a peristaltic pump and degassed with N_2 during *in situ* GIXRD studies. A Ag/AgCl (3M KCl, World Precision Instruments, freshly calibrated versus a Pt/H_2 electrode) and Pt wire acted as reference electrode and counter electrode, respectively. The working electrode was immersed at +1.0 V and then the electrode potential increased to the desired potential with

6 mV s^{-1}. Prior to X-ray characterization the electrode potential was hold for at least 10 min to ensure stationary conditions. The OER potential was +1.62 V which was determined from current density of 0.5 mA cm^{-2} during the anodic potential scan. After OER the electrode potential was decreased to +1.0 V and the electrode removed under potential control. Peak broadening was determined by fitting the reflections of Co_3O_4(511), Ti(110) and Co_3O_4(440) using pseudo-Voigt profiles. The structural coherence length was calculated using Scherrer equation from the integral breadth of the fitted Co_3O_4 profiles using a shape factor of 0.89. Errors of the structural coherence length were calculated from the estimated standard deviation of the integral breadths.

X-ray Absorption Measurements

Co K-edge experiments were carried out at the BESSY synchrotron radiation source operated by the Helmholtz–Zentrum Berlin. The measurements were conducted at the KMC-1 bending-magnet beamline at 20 K in a cryostat (Oxford-Danfysik) with a liquid-helium flow system. Further details are given in ref. [123]. Electrochemical conditioning was conducted in analogy to the *in situ* GIXRD experiment. After 15 min at the desired electrode potential, the samples were freeze-quenched using liquid N_2 under potential control and stored in liquid N_2 until XAS measurements were conducted. Further information regarding data analysis is given in the caption of Figure A26. […]

5.2 Results

5.2.1 Morphology and Local Structure

Figure 14 shows scanning and transmission electron micrographs of CoO_x films as well as selected area electron diffraction (SAED). The as-prepared films exhibited a homogeneous morphology with a certain porosity leading to increased electrolyte accessibility. The porosity of Co_3O_4 films was ~0.46. (cf. Figure A13 for further details) Thus, OER was not limited to the outer surface of the CoO_x films. The metal loading was ~960 $nmol_{Co}$ cm^{-2} on glassy carbon substrate as determined by ICP-OES. The microstructure consisted of agglomerated crystallites with size of 5-10 nm. The SAED pattern showed a typical ring structure characteristic for polycrystalline materials and agrees well with the normal spinel structure of Co_3O_4.

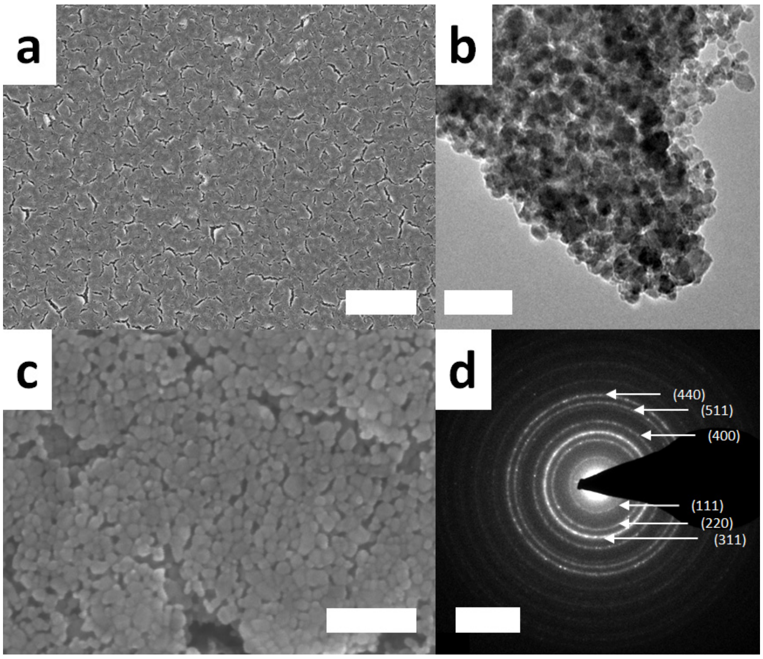

Figure 14: Scanning electron micrographs in low (a) and high magnification (c), transmission electron micrograph (b) and selected area electron diffraction (SAED) pattern (d) of as-prepared Co_3O_4 films. Diffraction rings of Co_3O_4 are indexed in the SAED pattern. The scale bars represent 2 µm, 50 nm, 100 nm, and 5 nm^{-1} in panel a, b, c, and d, respectively.

5.2.2 Electrochemical characterization in neutral, phosphate-containing electrolyte

The electrocatalytic properties and Co oxide redox electrochemistry were investigated in N_2-saturated 0.1 M KP_i at pH 7. Tafel plot and cyclic voltammogram are shown in Figure 15. The electrochemical surface area (ECSA) was determined using potentiostatic impedance spectroscopy following ref. [51]. (cf. Figure A14 for further information). Co_3O_4 films exhibited a pronounced redox feature at ~1.54 V which was preceded by a minor feature at a potential of ~1.4 V. According to the Pourbaix diagram[100] and a previous CoO_x study[114], the redox feature at 1.54 V can be attributed to the Co^{3+}/Co^{4+} redox transition whereas the feature at about 1.4 V is consistent with a Co^{2+}/Co^{3+} transition. Evaluation of the capacitance-corrected reductive charge of the two redox features showed that only ~1.8% of the Co ions change its oxidation state by one equivalent during this cyclic voltammogram.

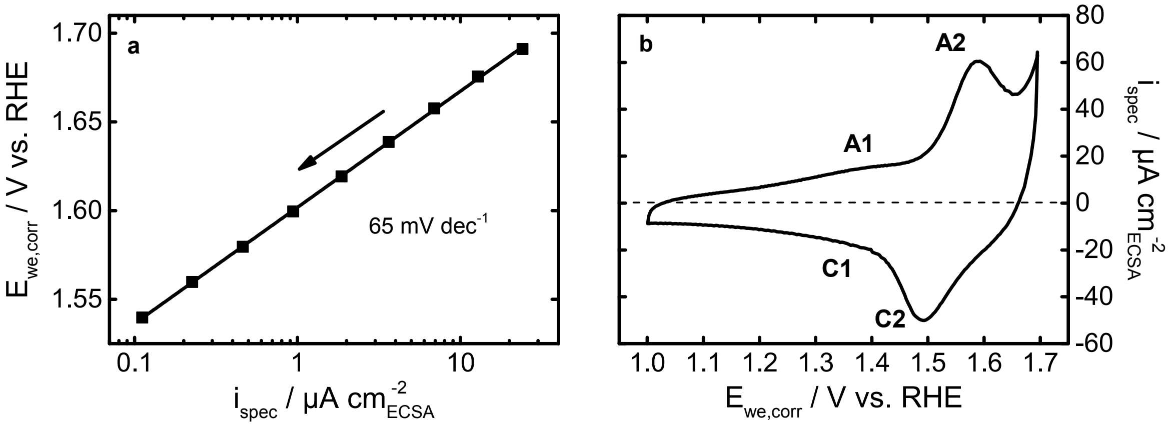

Figure 15: Tafel plot (a) and cyclic voltammogram (b) of Co_3O_4 films deposited on glassy carbon recorded in 0.1 M KP_i at pH 7. The Tafel plot was extracted from cathodic quasi-stationary potential-step rotating disc electrode (RDE) experiments after equilibration for 4 min at each potential; the line corresponds to a Tafel slope and an exchange current density of 65 mV/dec and $2.26 \cdot 10^{-9}$ mA cm^{-2}_{ECSA}, respectively. The cyclic voltammogram was recorded with a scan rate of 100 mV s^{-1} and shows a minor and major Co redox feature at ~1.4 V (A1/C1) and ~1.54 V (A2/C2), respectively. The capacitance-corrected reductive charge of the two redox features showed that only ~1.8% of the Co ions change its oxidation state by one equivalent. Electrode potentials were corrected for Ohmic losses and current was normalized using electrochemical surface area (ECSA) as determined by potentiostatic electrochemical impedance spectroscopy.[51] The electrochemical surface roughness was 26.4.

Thus, we conclude that only Co ions primarily from the surface participate in the Co oxide redox chemistry under this dynamic condition. The Co_3O_4 films exhibited a linear E—log(i) behaviour between 1.54 and 1.7 V with a Tafel slope of 65 mV dec^{-1} in N_2-saturated electrolyte.

The Tafel slope as determined at anodic polarization was slightly higher than that determined from cathodic quasi-stationary potential step experiment (cf. Figure A15, Figure A16, Figure A20). The Tafel slope of crystalline Co_3O_4 was found to be very similar compared to the one of electrodeposited Co oxide films which exhibit ≥60 mV dec^{-1} in 0.1M KP_i.[53, 56, 117] We note that catalytic activity and Co oxide redox behaviour showed very good stability (Figure A15 - Figure A21). Furthermore, OER does not influence morphology and Co loading (Figure A22 and Figure A23).

To verify electrocatalytical oxygen evolution of Co_3O_4 in neutral, phosphate-containing electrolyte we performed differential electrochemical mass-spectrometry (DEMS) experiments. Figure A24 shows a cyclic voltammogram of Co_3O_4 in the OER range and the corresponding ion current of m/z=32 and 44 as a measure of the evolution of oxygen and carbon dioxide, respectively.

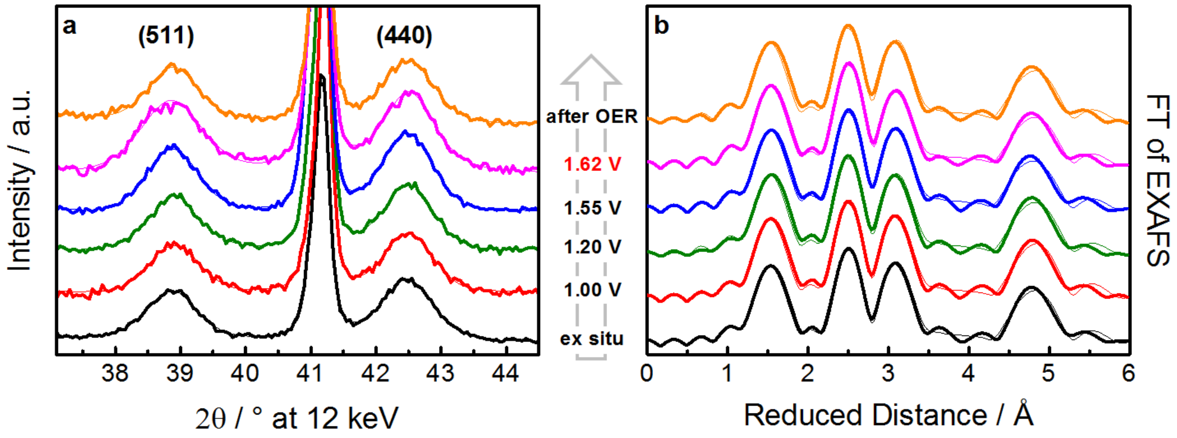

Figure 16: *In situ* X-ray diffraction patterns (a) and Fourier-transforms (FT) of (quasi-)in situ EXAFS spectra collected at the Co K-edge (b) of Co_3O_4 catalyst films. Experimental data and fitted profiles are shown in bold and thin lines, respectively. The diffraction patterns were recorded using grazing-incident excitation at α=0.3° and 12 keV. The electrode potential was increased stepwise from +1.0 V to +1.62 V vs. RHE, the latter representing the catalytically-active catalyst state, in 0.1 M KPi at pH 7. (cf. Figure 15a and Figure A24) The state after OER is a dry state for which the electrode was removed from electrolyte at +1.0 V rinsed with de-ionized water and dried in N_2 flow. The Miller indices of selected Co_3O_4 reflections are indicated; the diffraction patterns were background corrected for better visualization. Fitting was performed using pseudo-Voigt profiles. Samples for XAS were freeze-quenched under potential control using liquid N_2 after 15 min at 1.62 V in 0.1M KP_i.

The onset potential of O_2 evolution agreed well with the Co^{3+}/Co^{4+} redox potential and O_2 evolution followed the rise of the current density with electrode potential. Thus, we conclude that the Co_3O_4 films showed significant oxygen evolution activity above the Co^{3+}/Co^{4+} redox couple at ~1.54 V in neutral, phosphate-containing electrolyte and exhibit typical Co oxide redox behaviour.

5.2.3 Long-range Order of Co_3O_4 under Electrochemical Reaction Conditions

To examine atomic structure and crystallinity of Co_3O_4 films at different electrochemical potentials including the OER, we conducted *in situ* grazing-incident X-ray diffraction (GIXRD) experiments. Diffraction patterns of Co_3O_4 films deposited on Ti in the as-prepared state, at selected electrode potentials and after *in situ* characterization are shown in Figure A25 and Figure 16a. Besides the reflections from the Ti substrate, Co_3O_4 (Space group: Fd-3m, PDF#00-042-1467) was the only detectable crystalline phase prior to and during electrochemical reaction conditions. Thus, the catalyst film essentially retained its Co_3O_4 structure under the entire electrochemical potential range considered.

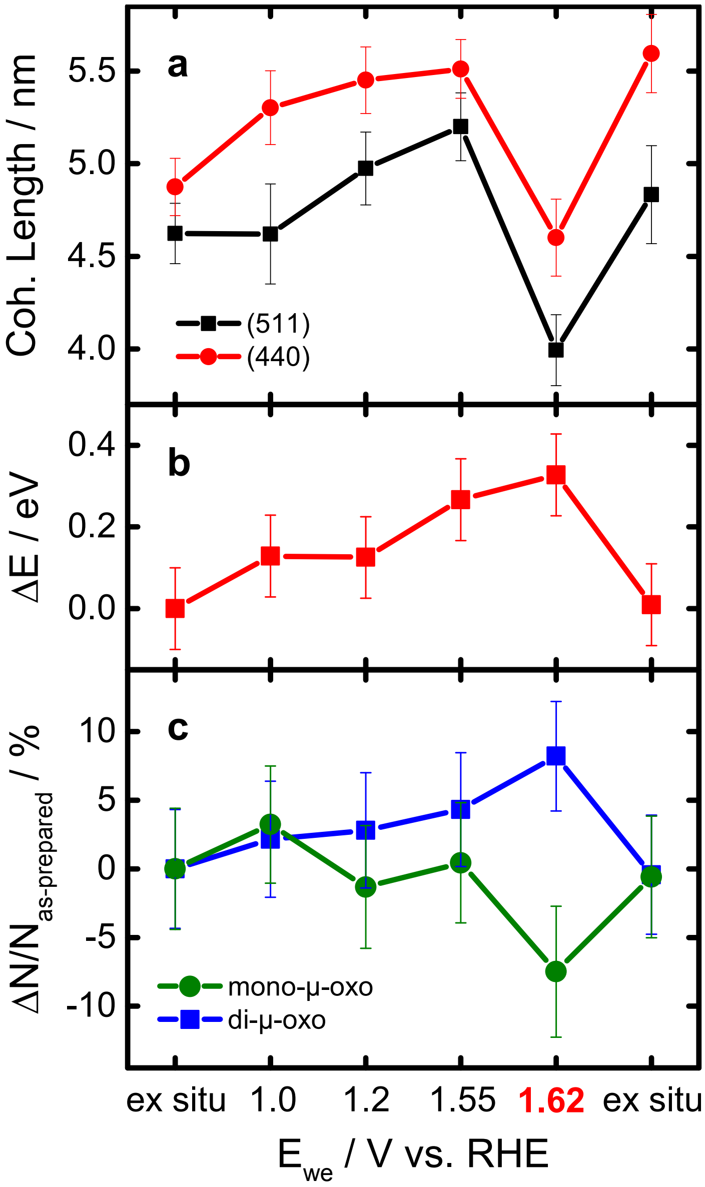

Figure 17: Structural coherence length of Co_3O_4 (a), shift of the Co X-ray absorption K-edge (b), change in EXAFS coordination number of di- and mono-μ-oxo bridges between Co ions (c) with respect to the as-prepared state. The state at +1.62 V corresponds to the catalytically active oxygen evolution state (cf. Figure 15 and Figure A24). Electrode potentials in this particular experiment are not corrected for Ohmic losses but we note that Ohmic correction decreased the electrode potential at +1.62 V by less than ~1 mV in the quasi-stationary experiment. The structural coherence length was calculated using the Scherrer equation from the integral breadth of the Co_3O_4(511) and (440) reflections.[164] A shape factor k of 0.89 was used. The error of the structural coherence length was calculated from the estimated standard deviation of the fitted integral breadth. The likely error of the shift of the Co K edge was estimated to be ±0.1 eV. The coordination numbers were determined by simulations of k^3-weighted EXAFS spectra. The error ranges of the EXAFS fit parameters were estimated from the covariance matrix of the fit and represent the 68% confidence intervals. Further details on data analysis are given in the caption of Table 7 and Table 8

However, a closer analysis of the broadening of selected Co_3O_4 reflections (Figure 17a, Table 7) showed that the mean structural coherence length of the crystalline domains had changed. The structural coherence length increased after immersion into the electrolyte at +1.0 V and then increased further with more positive electrode potential. The largest structural coherence length was found at the onset of OER at +1.55 V, just anodic of the Co redox features (Figure 15). As the electrode potential was increased further to +1.62 V, the structural coherence length of the Co_3O_4 domains decreased by almost 10 Å. In the dry state after OER the structural coherence length recovered to the identical value as before OER at +1.2 V.

Our observations can be plausibly explained by an initial irreversible growth of Co_3O_4 crystallites up to an electrode potential of +1.2 V, likely due to Ostwald ripening and/or coalescence,[165-166] combined with a reversible structural transformation of Co_3O_4 detectable at an electrode potential of +1.62 V, where catalytic oxygen evolution proceeded at elevated rates (cf. Figure A24). At the onset of OER (+1.55 V), the Co_3O_4 exhibited its largest structural coherence length. Thereafter, further increasing the oxygen evolution rate at more anodic electrode potentials resulted in a reversible structural transformation leading to a lower degree of crystallinity. This structural transformation can be explained with the formation of a CoO_x shell on the crystalline Co_3O_4 domains which are in contact with the electrolyte. This CoO_x did not give rise to additional Bragg reflections due to its sub-nm size and is thus X-ray amorphous. On the reverse cathodic scan, upon leaving the potential range of sustained catalytic oxygen evolution associated with electrochemical reduction, the amorphous shell recrystallized to Co_3O_4. To our knowledge, this is the first time that such a reversible structural transformation of a shell on Co_3O_4 crystallites from crystalline to amorphous and back has been reported. We further emphasize that this unusual reversible amorphization of Co oxide appears to be linked to an elevated catalytic oxygen evolution rate.

5.2.4 Co Oxidation State and Local Atomic Structure under Electrochemical Reaction Conditions

To determine the local atomic structure and oxidation state of the Co ions in Co_3O_4 under electrochemical reaction conditions and especially the Co coordination in the X-ray amorphous CoO_x present during OER, we performed X-ray absorption spectroscopy at the Co *K*-edge for Co_3O_4 films which were deposited on glassy carbon and freeze-quenched at selected electrode potential.

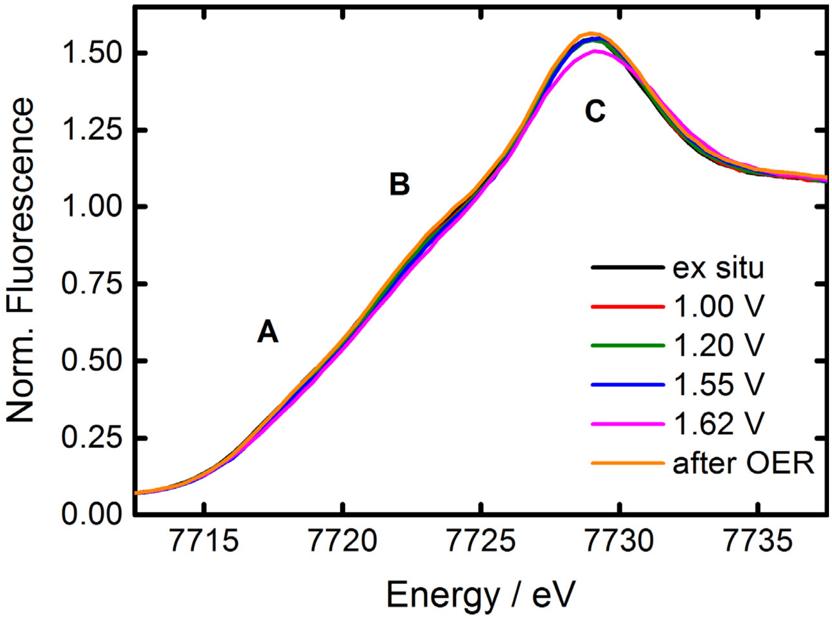

Figure 18: Fluorescence-detected quasi-in situ XANES spectra of Co_3O_4 films in various catalyst states. For increasingly positive potentials, the Co K-edge absorption edge shifted reversibly to higher energies suggesting oxidation of 10-15% of the cobalt ions under stationary oxygen evolution conditions. Under OER conditions, the XANES profile exhibited an almost linear increase due to significantly weaker shoulders marked with (A) and (B). The intensity at the principal edge-maximum at (C) was clearly reduced only in the oxygen evolving active state (at +1.62 V). Samples were freeze-quenched under potential control using liquid N_2 after 15 min at 1.62 V in 0.1M KPi and stored in liquid N2 until XAS measurements were conducted.

In previous work we have verified that the protocol of this experiment[114] facilitates the collection of high-quality, extended-range EXAFS data that remain unaffected by radiation-induced modifications of the solvent-exposed catalyst material.

Figure 18 shows the XANES spectra recorded at the Co *K*-edge of Co_3O_4 films at selected catalyst states. The energy of the Co K absorption edge of the as-prepared catalyst agreed well with a mean Co oxidation state between +2 and +3, as expected for Co_3O_4. With increasing electrode potential the Co absorption edge shifted slightly to higher energies which is indicative for a higher mean oxidation state of the Co ions.[150]

During OER, the XANES profile exhibited an almost linear increase due to significantly weaker shoulders at about 7718 (A) and 7723 eV (B); moreover, a clearly reduced intensity at the principal edge-maximum at about 7729 eV (C) was observed only in the OER-active state (at +1.62 V). These spectroscopic differences indicate significant structural differences in the local atomic and electronic structure of the amorphous CoO_x shell formed during catalysis (at

+1.62 V) as compared to the crystalline Co_3O_4 structure prevalent before and after catalysis. However, as expected from the *in situ* GIXRD results, the majority of Co ions remained in their initial state within the crystalline Co_3O_4.

The local atomic structure of the absorbing Co ions could be assessed qualitatively from the Fourier-transformed EXAFS and quantitatively by EXAFS simulations (Table 8). In Figure 17 three major peaks representing absorber-backscatterer distances are visible for the Co_3O_4 films in all catalyst states. The first peak corresponds to the convolution of two Co-O distances stemming from tetrahedral and octahedral Co coordination (mean distance of ~1.91 Å). The second and third peak is consistent with the Co-Co distances for pairs of Co ions connected via di-μ-oxo (2.85 Å) and mono-μ-oxo (3.36 Å) bridges, respectively. Di-μ-oxo bridges represent edge-sharing Co octahedra whereas the mono-μ-oxo bridges reflect corner-sharing Co octa- and tetrahedra. (cf. Figure 19a) Comparing the magnitude of the second and third FT-peak, significant changes in the Co coordination during oxygen evolution could be identified, in particular the shift toward more di-μ-oxo bridged, octahedrally coordinated Co ion in the OER-active state (at +1.62 V).

Figure 17b shows the energy shift of the Co K edge compared to the as-prepared state for various catalyst states. The edge position was identical at +1.0 and +1.2 V but was shifted by +0.1 eV compared to the as-prepared state. At +1.55 V the edge position was +0.3 eV higher and the determined shift was maximal at high OER activity. After OER, the edge position of the Co_3O_4 agreed well with the as-prepared state. Thus, the evolution of the Co oxidation state is a reversible process and the mean oxidation state for electrode potentials at +1.0 V and above is higher than in under dried conditions.

Simulations of k^3-weighted EXAFS spectra were conducted to determine the Co coordination in Co_3O_4 under electrochemical reaction conditions and especially of the X-ray amorphous CoO_x present during OER (Figure A26 and Table 8). Figure 17c shows the relative changes in the coordination numbers assignable either to di- or mono-μ-oxo bridges at selected catalyst states. In agreement with the evolution of the structural coherence length, the number of di- and mono-μ-oxo bridges remained constant within the experimental error between the as-prepared state and +1.55 V. The reversible amorphization at elevated oxygen evolution rate, however, was accompanied with a change from mono- towards di-μ-oxo bridged Co ions; the *ex situ* state after OER resembled the as-prepared state in terms of μ-oxo Co linking.

In summary, the X-ray absorption data suggest that in the OER-active state with elevated levels of oxygen evolution (at +1.62 V), tetrahedrally coordinated, mono-μ-oxo bridged Co^{2+} ions are reversibly converted into octahedrally coordinated, di-μ-O(H) bridged $Co^{3+/4+}$ ions.

Analysis of the X-ray diffraction data reveals a simultaneous coherence-length reduction by 5-10 Å suggesting a smaller crystalline Co_3O_4 core in the OER active state. Both phenomena, the increased amount of di-µ-O(H) bridged $Co^{3+/4+}$ octahedra and the reduced size of the crystalline Co_3O_4 core, are reversed upon returning to the resting state of the catalyst. These observations are consistently explainable by a reversible transformation of part of the Co_3O_4 core into a $CoO_x(OH)_y$ surface shell, as discussed in more detail further below.

5.2.5 Surface Chemistry and Electronic Structure

For further insights in the elemental composition, atomic and electronicstructure of the near-surface of the Co_3O_4 crystallites at the electrode/electrolyte interface before and after OER, we conducted synchrotron-based X-ray photoemission (XPS) and XANES spectroscopy at Co *L*- and O *K*-edge on the Co_3O_4 films. Figure A29a,b shows Co 2p XPS and the Co L_3 XANES spectra of Co_3O_4 films, respectively. Both spectra support the notion of a Co oxide containing mainly Co_3O_4 in the near-surface of the crystallites.[167] We note that because of the more pronounced fine structure at the low-energy side of the Co L_3 absorption peak, the presence of a minor fraction of Co^{2+} O_h in the near-surface is possible (cf. Figure A31). The O 1 s XPS showed that the near-surface of the as-prepared state incorporated protonated oxygen atoms in addition to lattice oxygen (cf. Figure A29c and Figure A32). The strong pre-edge feature of the O *K*-edge XANES spectrum revealed significant hybridization of Co 3d and O 2p orbitals (cf. Figure A29d).[36] After OER, the near-surface of the Co_3O_4 crystallites was largely unchanged; XPS and XANES spectra showed almost identical profiles when compared with the as-prepared catalyst material. Minor differences can be accounted for by adsorption of phosphate ions during operation of the catalyst film in the phosphate-containing electrolyte (cf. Figure A30). We conclude that the identified reversibility of the structural transformation observed by X-ray diffraction and X-ray absorption spectroscopy at the Co *K*-edge is fully supported by our surface-sensitive spectroscopic data (see Appendix A2 for details).

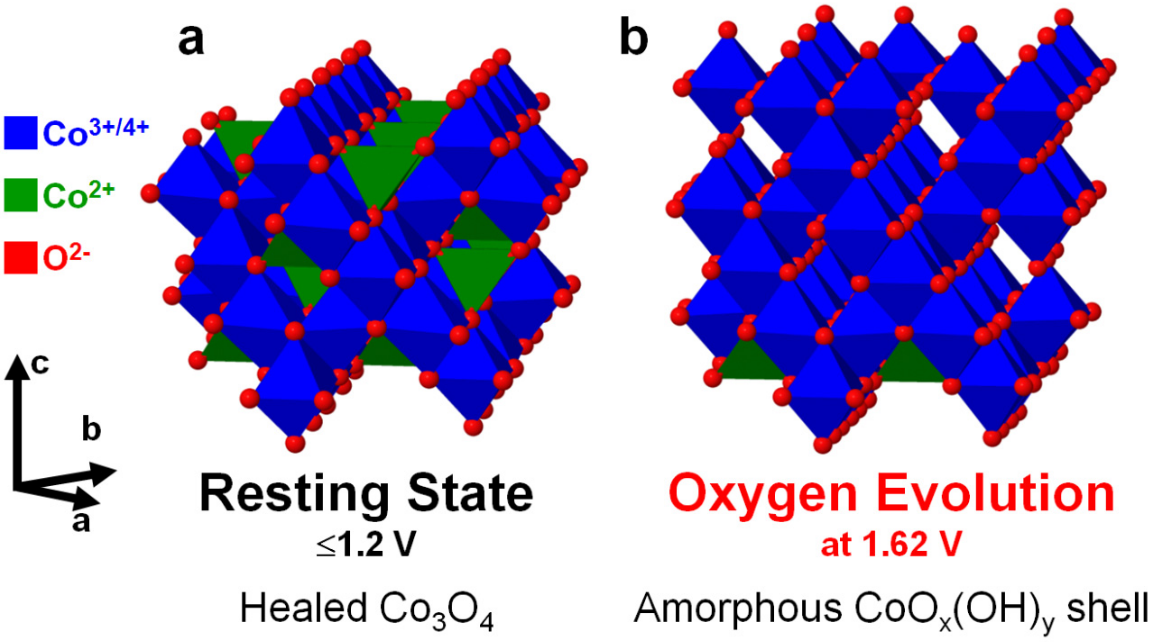

Figure 19: Possible near-surface structures on crystalline Co_3O_4 core under electrochemical conditions. At potentials below Co redox features, Co_3O_4 is in a healed state at which defects in the near-surface are oxidized. At elevated O2 evolution, the CoOx(OH)y grows into the crystalline Co_3O_4 core leading to a reversible amorphization of a sub-nm shell. This amorphous $CoO_x(OH)_y$ shell consists of di-μ-oxo bridged $Co^{3+/4+}$ ions with arbitrary site occupancy in the ideal-cubic close-packed O^{2-} lattice. Hydrogen atoms and phosphates are not shown.

5.3 Discussion

We have investigated the structural evolution of crystalline Co_3O_4 films under electrochemical potential control and during OER in neutral, phosphate-containing electrolyte in detail using *in situ* GIXRD and quasi-*in situ* XAS. For the first time, we uncover a reversible decrease in structural coherence length at electrochemical potentials facilitating elevated oxygen evolution which is coupled to Co oxidation and a change in Co coordination from tetrahedral towards octahedral symmetry. In line with the reversibility, composition and electronic structure of the Co_3O_4 in the bulk volume and in the crystallites near-surface zone remained nearly identical when comparing the catalyst material before and after OER.

To explain this reversible process, we propose that the changes in Co coordination at elevated oxygen evolution rate are caused by formation of a 3D cross-linked $CoO_x(OH)_y$ structure. Figure 19 sketches the structural transformation of the near-surface structure of the crystallites between the resting state (below the Co redox features) and the catalytically active state (at

+1.62 V). At potentials below the Co redox features (at about +1.2 V), the Co_3O_4 is in a healed state with slightly higher mean oxidation state than in the dry state. Reduced Co sites caused by defects in the near-surface of the as-prepared state are oxidized to Co_3O_4. At potentials above of the Co redox features at the onset of OER Co_3O_4 is partially oxidized to a $CoO_x(OH)_y$ without changing crystallinity and local atomic coordination. Thus, the oxidation is presumably limited to the outermost surface of the crystallites.

The formation of a layered CoOOH in the near-surface can be excluded because it would diminish the structural isotropy to the Co_3O_4 core and thus, lead to a lower structural coherence length already at +1.55 V. Bulk oxidation of Co_3O_4 appears to be kinetically hindered and oxidation is thus limited to the surface of the crystallites at +1.55 V. Therefore, we conclude that the onset of the electrocatalytic oxygen evolution occurs on crystalline Co_3O_4, which is oxidized to $CoO_x(OH)_y$ at the outermost surface (initial active surface). We propose this $CoO_x(OH)_y$ represents the reaction zone of OER. At elevated oxygen evolution rate the crystallinity decreases and local atomic structure of Co ions in the near-surface changes. We explain this amorphization with the growth of the $CoO_x(OH)_y$ reaction zone from the surface into the crystalline Co_3O_4 core.

With increasing electrode potential and oxygen evolution rate, the Co^{2+} T_d ions of the crystalline Co_3O_4 in the near-surface get oxidized to +3 and change their coordination from tetrahedral to octahedral. Co^{4+} ions can be isostructurally incorporated in the $CoO_x(OH)_y$ via deprotonation of di-μ-OH bridges.[114] To undergo this change in coordination, Co ions have to move inside the ccp O^{2-} lattice to vacant O_h sites in the reaction zone of the $CoO_x(OH)_y$. Site occupancy of the Co ions can be arbitrary and dynamic under the constraints of an appropriate O/Co ratio and sustained prevalence of the di-μ-oxo Co bridging motif. As a consequence of the unified Co coordination and thus, unified Co-O and Co-Co distances in the $CoO_x(OH)_y$ a slight rearrangement of the O^{2-} lattice towards an ideal ccp arrangement occurs. These structural changes diminish the structural isotropy to the crystalline Co_3O_4 core and lead to the identified amorphization. After oxygen evolution the reaction zone transforms back to the thermodynamically favoured spinel structure.

The origin of the structural transformation of the near-surface described above can furthermore be described by participation of lattice oxygen in the OER mechanism in which the temporary presence of O vacancies in the $CoO_x(OH)_y$ also induce structural disorder in the reaction volume.[54-56] In this scheme, prior to OER the $CoO_x(OH)_y$ surface gets oxidized but is thermodynamically frustrated when oxidation equivalents are accumulated at higher electrode potentials. Above a critical concentration of oxidation equivalents OER starts possibly under participation of lattice oxygen. The formation of oxygen vacancies then initiates structural relaxation which leads to the described change in Co coordination and amorphization in the reaction zone. The short life-time of the O vacancies precludes the reduced Co sites from identification using quasi-*in situ* XANES.(cf. Figure 17 and Figure 18)

3D cross-linked Co oxides form also from Co_3O_4 during Li insertion which underlines the flexibility of Co ions within the ccp O^{2-} lattice under electrochemical conditions.[168-169] Under oxygen evolving conditions, octahedral Co coordination and a mean oxidation state of higher than +3 appears to be a general structural motif as it has been also found for the CoCat[114-115] and layered $CoO_x(OH)_y$[33, 90]. The 3D cross-linked $CoO_x(OH)_y$ appears also structurally similar to the rutile-type oxides such as RuO_2, IrO_2 and β-MnO_2.[26, 121, 170-172] Both structures exhibit octahedral chains of di-μ-oxo bridged metal ions and tunnels in the oxide lattice.

We note that the uncovered amorphization of the near-surface is likely to have significant, beneficial influence on the electrocatalysis. An amorphous metal oxide provides an enhanced degree of structural flexibility, a higher number of special coordination sites possibly under participation of several metal centres and enables elevated accumulation of oxidation equivalents in the reaction zone. *Vice versa*, perfect crystalline order seems to prevent efficient oxygen evolution. The reported OER activity of several crystalline oxide materials may relate directly to reversible surface amorphization 'templated' by the crystalline core of the material.[172-174] Thus, a reversible formation of an amorphous termination layer on a stable crystalline core points towards a unified common oxygen-evolving state of Co oxide (but also other) electrocatalysts – independent of its initial degree of order. This may provide a new approach towards a unified understanding of heterogeneous water oxidation catalysis. Furthermore, we propose that the design of more active and stable electrocatalysts by preparation of core-shell nanostructures in which near-surface amorphization (under electrochemical conditions) is enhanced and simultaneously the crystalline metal oxide core stabilizes the electrocatalyst from elevated metal ion dissolution.

5.4 Summary

In conclusion, using *in situ* X-ray diffraction and (quasi-)*in situ* X-ray absorption spectroscopy as well as XPS and XANES at Co *L*- and O *K*-edge before and after oxygen evolution reaction (OER) in neutral electrolyte, we identified the existence of a reversible structural transformation of Co_3O_4 which accompanies elevated catalytic oxygen evolution. Below the Co redox features the bulk structure of the Co_3O_4 is in a stable rest state with larger size of the crystalline core compared to the dry state. At the onset of the OER catalysis, the Co oxidation state increases within the pseudo-ccp O^{2-} lattice of the reaction zone under retention of the Co coordination. As a result of this, the $CoO_x(OH)_y$ structure remains limited to the surface of the crystallites. However, this catalytic reaction zone increases into the crystalline Co_3O_4 core at more anodic electrode potentials and enhanced oxygen evolution. This is linked to the (reversible) amorphization of a sub-nm shell. The amorphization is accompanied by a higher Co oxidation state and a partial change in Co coordination from tetrahedral to octahedral and can be explained by arbitrary site occupancy of $Co^{3+/4+}$ ions within a slightly rearranged ccp O^{2-} lattice. On the reverse cathodic electrode potential scan, more negative of the active catalytic regime, the amorphous shell crystallizes back to its initial state.

Structurally, we propose that the formation of an $CoO_x(OH)_y$ with di-µ-oxo bridged $Co^{3+/4+}$ O_h ions at the surface is *sine qua non* for oxygen evolution activity on Co_3O_4. At elevated oxygen evolution the amorphous 3D cross-linked $CoO_x(OH)_y$ offers the structural flexibility that enables and enhances catalytic activity. The crystalline Co_3O_4 combines the advantages of a controlled and stable crystalline material in resting state with the required structural flexibility facilitated by a non-crystalline oxide under OER conditions. The notion of and first evidence for a reversible amorphization mechanism, in which electrocatalysts move reversibly between crystalline and amorphous regimes as a response to externally applied electrode potentials, is a new and potentially very important design concept for catalyst."[68]

Chapter 6 Linking Near-surface Structure, Redox Chemistry and Oxygen Evolution of Co Oxides and Their Catalytically Active State

In this chapter the results of the investigation on the influence of the initial Co coordination environment and oxidation state in Co oxide electrocatalysts on their redox chemistry, electrocatalytic properties and the structure of the catalytically active state are described. Therefore, Co oxides consisting of only Co^{2+} O_h, Co^{2+} T_d, or Co^{3+} O_h as transition metal ions as well as the mixed-valent Co_3O_4 were synthesized and tested for oxygen evolution reaction in neutral and alkaline electrolyte. The physicochemical properties of the Co oxide electrocatalysts were extensively investigated in the as-prepared and in the OER-conditioned state. The crystal structure and morphology were determined using X-ray diffraction as well as electron microscopy and diffraction. The local atomic structure and Co oxidation state were identified using (*in situ*) X-ray absorption spectroscopy (XAS) recorded at the Co *K*-edge. The near-surface composition, chemistry and electronic structure were investigated using synchrotron-based X-ray photoelectron spectroscopy (XPS) and XAS at the Co L_3- and O *K*-edge. Additionally, the local atomic structure of the catalytically active state of Co oxide was determined using *in situ* XAS during OER. The results of these investigations show a strong beneficial influence of the local atomic structure and spin state of the Co ions in the near-surface on the Co oxide reducibility and on the OER electrocatalysis. Structural disorder decreases the fraction of low-spin Co^{3+} ions with symmetrical octahedral bonding environment and this decrease is considered to be highly beneficial for the OER activity in neutral electrolyte. Thus, important insights into structure-activity correlations were unravelled which lead to a substantially improved understanding of oxygen evolution on Co oxide electrocatalysts in neutral electrolyte.

This chapter was prepared in collaboration with Detre Teschner, Manuel Gliech, and Tobias Reier.

D.T. performed XPS and XANES Co *L*- and O *K*-edge experiments and data analysis. M.G. performed transmission electron microscopy. T.R. performed scanning electron microscopy and assisted in the synthesis.

6.1 Experimental Details

6.1.1 Synthesis of Co Oxides

Co_3O_4 and rocksalt-CoO Thin Films

Films of Co_3O_4 and rocksalt-CoO (rs-CoO) consisting respectively of Co^{3+} O_h and Co^{2+} T_d as well as Co^{2+} O_h have been prepared using spin-coating as described in Chapter 5. Glassy carbon plates and Si(100) wafers were used as substrates. Prior to the spin coating the substrates were stepwise cleaned using Milli-Q water, acetone, and ethanol in ultrasonic bath and subsequently dried under nitrogen flow. For further details see Chapter 5.[68]

After the deposition of one layer of Co^{2+}, the samples were transferred to the furnace to thermally decompose the Co precursor and form CoO_x thin films. In case of Co_3O_4 films, the samples were calcined for 15 min at 400 °C in air applying a temperature ramp of 10 K min^{-1}. Films of rs-CoO were formed in a two-step process. First, the precursor was decomposed at 300 °C in air using a ramp of 10 K min^{-1}. The samples were taken out of the furnace after 10 min and let cool down to room temperature. In the second step the formed CoO_x was reduced in 5 vol% H_2/Ar atmosphere for 15 min at 400 °C using a ramp of 10 K min^{-1}. The sample remained in this reducing atmosphere until the furnace cooled down to room temperature.

Wurtzite-CoO

The wurtzite-CoO (w-CoO) consisting of only Co^{2+} T_d was prepared using a colloidal, microwave-assisted synthesis and the subsequent drop-coating of GC and Si(110) substrates with a desired Co loading of 322 nmol·cm^{-2}. The colloidal synthesis is based on a published route.[87] For the synthesis, 3.61 mg Co(acetylacetonate)$_3$ (Alfa Aesar, 99.8%) per 1 g oleylamine (>98%, Sigma-Aldrich) was mixed in a 30 ml microwave reaction tube. A typical synthesis consisted of ~10 g oleylamine. Prior to the reaction, the precursor/solvent mixture was degassed using N_2 for at least 60 min, and then immediately closed and transferred to the microwave reactor. The microwave routine consisted of two steps, first the suspension was heated to 135 °C with a heating rate of ~ 70 K min^{-1}. After 5 min at this temperature, the suspension was heated to 200 °C with the same heating rate and kept at this temperature for 30 min. Subsequently, the microwave reaction tube was cooled to 55 °C in N_2 flow. After reaction a green solution has formed which did not precipitate within few days.

The colloidal solution was stepwise washed to remove oleylamine. First, the solution was diluted using 10 ml toluol (99.5%, Sigma-Aldrich) and 30 ml ethanol (AnalaR, NormaPur, VWR) per 10 ml oleyamine and centrifuged at 3000 rpm for 15 min. The supernatant was removed and the precipitate was redispersed in ethanol within 10 min of sonification and mechanical agitation. Subsequently, the solution was again centrifuged. This procedure was repeated twice and the final solution was stored at ~7 °C.

For the preparation of the electrodes, a volume corresponding to a Co loading of 322 $nmol\cdot cm^{-2}$ was drop coated onto the substrate and dried at 60 °C in air. Subsequently, the samples were heat treated for 15 min at 225 °C in Ar atmosphere to remove oleylamine residues.

CoOOH

Thin films of Co oxide consisting of only Co^{3+} O_h ions were prepared using electrodeposition based on a published routine.[108] The films were galvanostatically deposited from a solution of 0.01M $Co(NO_3)_2$ (Alfa-Aesar, 99.999%) in 0.1M NaOAc (Sigma-Aldrich, 99%) at 0.1 mA/cm^2 for 322 s. The electrodeposition was conducted in a two-electrode arrangement in a single compartment cell. The films were deposited on GC plates (~10x10 mm) and a Ti-coated Si(100) wafer. The Si(100) wafer were coated with a Ti layer with a nominal thickness of ~100 nm using electron beam evaporation. A GC plate was placed parallel to the working electrode in less than 1 cm distance and acted as counter electrode. The potential difference between working and counter electrode was ~1.7 V at steady-state. After deposition, the electrodes were extensively washed using Milli-Q water to remove residues from the electrodeposition solution and dried under nitrogen flow.

6.1.2 *in situ* X-ray Absorption Measurements

Investigation of Co oxidation state and local atomic structure under electrochemical reaction conditions have been conducted at the I811 beamline of the synchrotron facility Maxlab, Lund (Sweden).[163] A custom-made *in situ* electrochemical cell for X-ray studies as described in Section 3.3 was used. During *in situ* XAS studies the electrolyte was constantly circulated using a peristaltic pump and degassed with N_2. An Ag/AgCl (3M KCl, World Precision Instruments, freshly calibrated versus a Pt/H_2 electrode) acted as reference and a Pt wire was used as counter electrode. After *ex situ* XAS characterization of the as-prepared state, the working electrode was immersed at +1.62 V and the electrocatalysts conditioned at this OER potential for 15 min. Each electrode potential during *in situ* characterization was approached using linear sweep voltammetry with 6 mV·s^{-1} and maintained for at least 10 min to ensure stationary conditions prior to the *in situ* XAS measurement. The OER potential was determined as the potential required to reach a current density of 0.5 mA cm^{-2} during the anodic potential scan with 6 mV·s^{-1}.

The absorption spectra were recorded in fluorescence mode using a 50 mm^2 Vortex silicon-drift detector and at an incident X-ray angle of ~2°. The fluorescence signal was normalized using incident X-ray intensity and the post-edge intensity. The beamline energy was adjusted to the absorption edge of a Co foil by aligning the first inflection point of the Co *K*-edge absorption spectra to 7709 eV.[175] The step size of the XANES region was 0.4 eV and 0.05 Å^{-1} in the EXAFS region.

Fitting of the k^3-weighted EXAFS spectra was performed in k-space between 2.0 and 12 Å^{-1} for rs- and w-CoO as well as 3 to 12 Å^{-1} for CoOOH. The amplitude-reduction factor S_0^2 was 0.75. A joint-fit approach was used, where the coordination numbers (*N*) were determined independently but the distances (*R*) and Debye-Waller factors (σ) had partially the same values for each sample; Fitting was performed using the software package SimX after calculation of the phase functions with the FEFF program[176-177] (version 8.4, self-consistent field option activated). The error ranges of the fit parameters were estimated from the covariance matrix of the fit and represent the 68% confidence intervals.[141]

6.2 Results

In this section first the results of the physicochemical characterization of the Co oxides in the as-prepared state will be presented. The morphology of the electrocatalysts was determined from electron microscopy and the crystal structure of the desired Co oxide phases from GIXRD. The local atomic structure was extracted from XANES and EXAFS spectra recorded at the Co *K*-edge. The near-surface composition of the Co oxides was determined from X-ray photoemission spectra and the electronic structure from XANES spectra recorded at the Co L_3- and O *K*-edge. Second, the Co surface redox electrochemistry and the electrocatalytic OER activity of the Co oxides were determined from cyclic voltammograms and quasi-stationary potential step experiments in neutral, phosphate-containing electrolyte and alkaline, phosphate-free electrolyte. Third, the physicochemical properties of the as-prepared catalyst state are compared with the conditioned catalyst state after oxygen evolution in neutral, phosphate-containing electrolyte. Fourth, the local atomic structure and mean Co oxidation state of the catalytically active state as determined from *in situ* XANES and EXAFS are presented. Finally, the properties of the OER-conditioned Co oxides in terms of Co surface redox electrochemistry, electronic structure and electrocatalytic properties are related to each other and structure-activity correlations are identified.

6.2.1 Physicochemical Characterization of As-prepared Co oxides

Crystal Structure and Crystallinity

The crystal structure of the as-prepared Co oxides were investigated using GIXRD and Figure 20 shows the diffraction patterns of the Co oxide catalysts in the as-prepared state as deposited on Si(100) wafer. The Si(100) wafers were Ti-coated in case of the electrodeposited CoOOH.

All Co oxides, except CoOOH, showed Bragg reflections of only one Co oxide phase. The reflections of Co_3O_4, rs-CoO, w-CoO agreed well with the database references of the Co_3O_4 (Space group: Fd-3m, PDF#00-042-1467), rocksalt-CoO (Space group: Fm-3m, PDF#01-078-0431) and wurtzite-CoO (Space group: $P6_3mc$, PDF#01-089-2803), respectively. In case of CoOOH the diffraction pattern showed only Bragg reflections of the Ti (Space group: $P6_3/mmc$, PDF#01-089-5009) from the substrate. No Bragg reflections from Co oxide phases were detectable which shows that the crystalline domains were either too small to be detected using GIXRD or the Co oxide was completely amorphous.

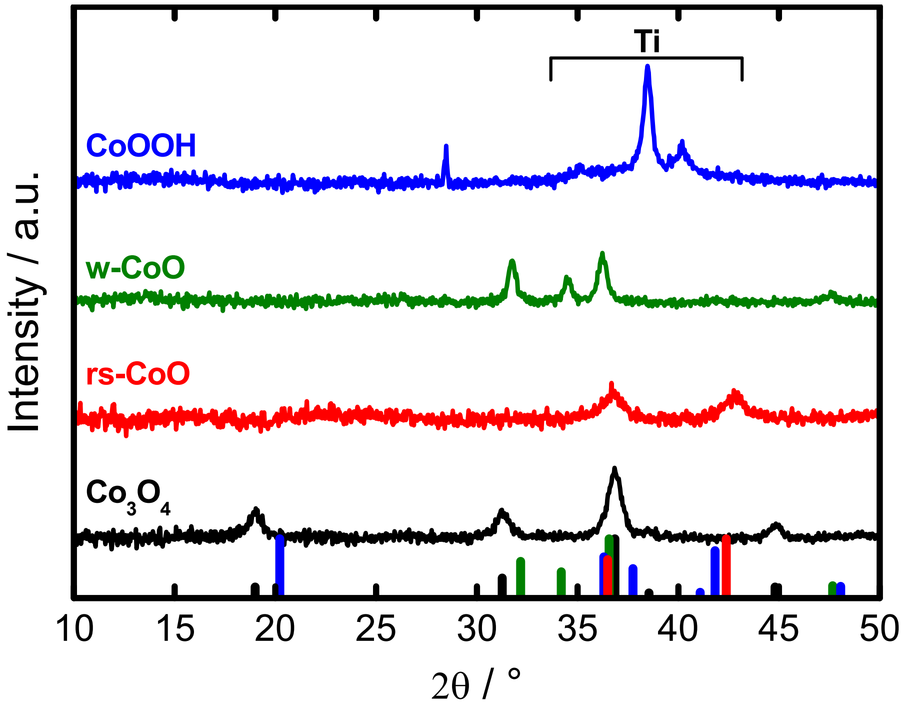

Figure 20: GIXRD patterns of the as-prepared state of Co_3O_4(black), rs-CoO(red), w-CoO(green) deposited on Si(100) substrate, and CoOOH(blue) on Ti-coated Si(100) substrate recorded at an incident angle of 1° using parallel Cu Kα radiation. The diffraction patterns were background corrected for better visualization. The reflections for the database references are shown as bars. Co_3O_4 (black, PDF#00-042-1467), rocksalt-CoO (red, PDF#01-078-0431), wurtzite-CoO (green, PDF#01-089-2803), and Heterogenite (blue, PDF#00-026-11107) are shown. The uncorrected patterns are shown in the Figure A33.

Table 1 shows the results from a Rietveld refinement of the diffraction pattern of the crystalline CoO_x. The Rietveld refinement was conducted assuming the presence of only Co^{2+} ions in w- and rs-CoO as well as Co^{3+} and Co^{2+} at the octahedral and tetrahedral sites of the spinel structure of Co_3O_4, respectively. The refined diffraction patterns are shown in Figure A33.

In case of rs-CoO, an ideal rock salt structure does not agree with the recorded diffraction pattern because the intensity ratio between the CoO(200) at ~42.7° and CoO(111) reflections at ~36.7° is lower than that of the database reference. This deviation from the ideal rocksalt structure can be induced by crystal defects which reduce the symmetry along one unit cell axis, e.g. by tetragonal distortion of the Co octahedra which can be induced by cationic vacancies and the accompanied charge compensation. A better fit result was achieved when the position of the O atom in the unit cell was refined according to a tetragonal distortion of the CoO_6 octahedra (see Figure A33 for further details).

Table 1: Results of Rietveld refinements of the GIXRD patterns of Co_3O_4, rs-CoO and w-CoO as shown in Figure 20 and the refined patterns are shown in Figure A33.

Sample	Lattice constant		Crystallite size / nm
	a / Å	c / Å	
Co_3O_4	8.089±0.001	–	~9
rs-CoO	4.233±0.002	–	~7
w-CoO	3.251±0.001	5.198±0.001	~22

To achieve charge neutrality in the lattice, the lack of positive charge had to be compensated by protonation of the adjacent O sites or changes in the Co oxidation state leading to a distortion of the octahedral coordination environment and additional electronic states within the band gap.[84] Thus, rs-CoO in the as-prepared state might exhibit a slight fraction of defects in the oxide lattice e.g. induced by tetragonal distortion of the CoO_6 octahedra and/or cationic vacancies. The presence of cationic vacancies can also explain a contraction of the oxide lattice and thus, the shorter lattice parameter was observed for rs-CoO ($\Delta a = -1.1$ pm) compared to the PDF references. In contrast, the refined lattice parameters of w-CoO showed a contraction along the c axis and an elongation of the lattice parameter a ($\Delta a = 4.1$ pm, $\Delta c = -4.2$ pm). This distortion indicates either a decrease in bond angles of the CoO_4 tetrahedron or the presence of one shorter Co-O distances along the c-axis and three longer Co-O per Co T_d ion in the crystal lattice spanning the (001) plane of the unit cell. The lattice constant of Co_3O_4 differed only by 0.02 pm from the reference which agreed well with a low degree of crystal defects and/or cationic vacancies.

In addition to the properties of the unit cell, the volume-weighted structural coherence length of the crystalline Co oxides was extracted from the integral breadth of the reflections by Scherrer equation with the shape factor k=1. The structural coherence lengths are denoted in Table 1. The structural coherence length of the Co oxide was largest for the w-CoO (~22 nm) which was more than two times larger than that of Co_3O_4 (~9 nm) and more than three times larger than that of rs-CoO (~7 nm). These differences in the degree of crystallinity and crystal structure indicate differences in the morphology of these Co oxides which are described in the next section.

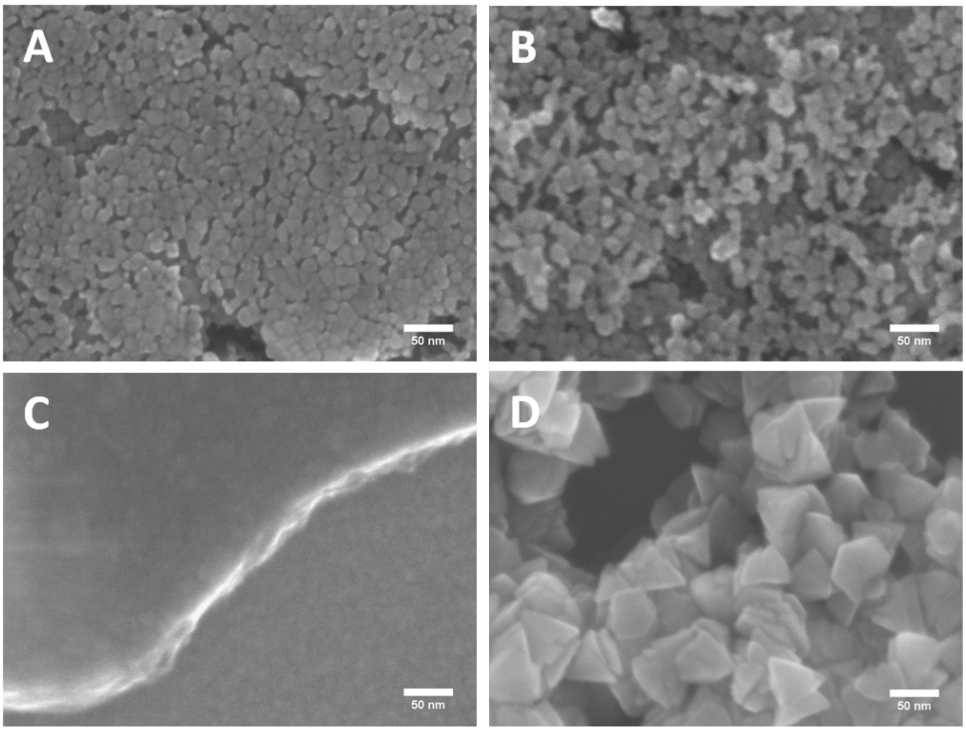

Figure 21: SEM micrographs of the as-prepared state of Co_3O_4(A), rs-CoO(B), CoOOH(C), and w-CoO(D).

Morphology and Local Crystal Structure

The morphology of the Co oxides films has been determined from scanning and transmission electron micrographs as shown in Figure 21 and Figure 22, respectively. Co_3O_4 and rs-CoO coatings exhibited a homogeneous morphology with a certain porosity leading to increased electrolyte accessibility. The film of rs-CoO is more porous compared to the Co_3O_4 film leading to a higher physical surface area. Both films of rs-CoO and Co_3O_4 consisted of agglomerated nanocrystallites which exhibited in a first approximation spherical shape. The crystallites shape can also be obtained from the TEM micrographs (Figure 22). Therein, the size of the crystallites agreed well with the structural coherence length as determined from the diffraction pattern.

Furthermore, the crystalline nature of the Co oxide domains can be seen from the lattice planes in Figure 22. The w-CoO also consisted of agglomerated nanocrystallites. The shape of the nanocrystallites of w-CoO was pyramidal with a hexagonal base. This morphology is in agreement to the shape of wurtzite-CoO nanoparticles reported in literature.[87] The size of the crystallites is significantly larger than that of Co_3O_4 and rs-CoO which is in agreement with the results from Rietveld refinements (see Table 1). Their base diameter is larger than 20 nm.

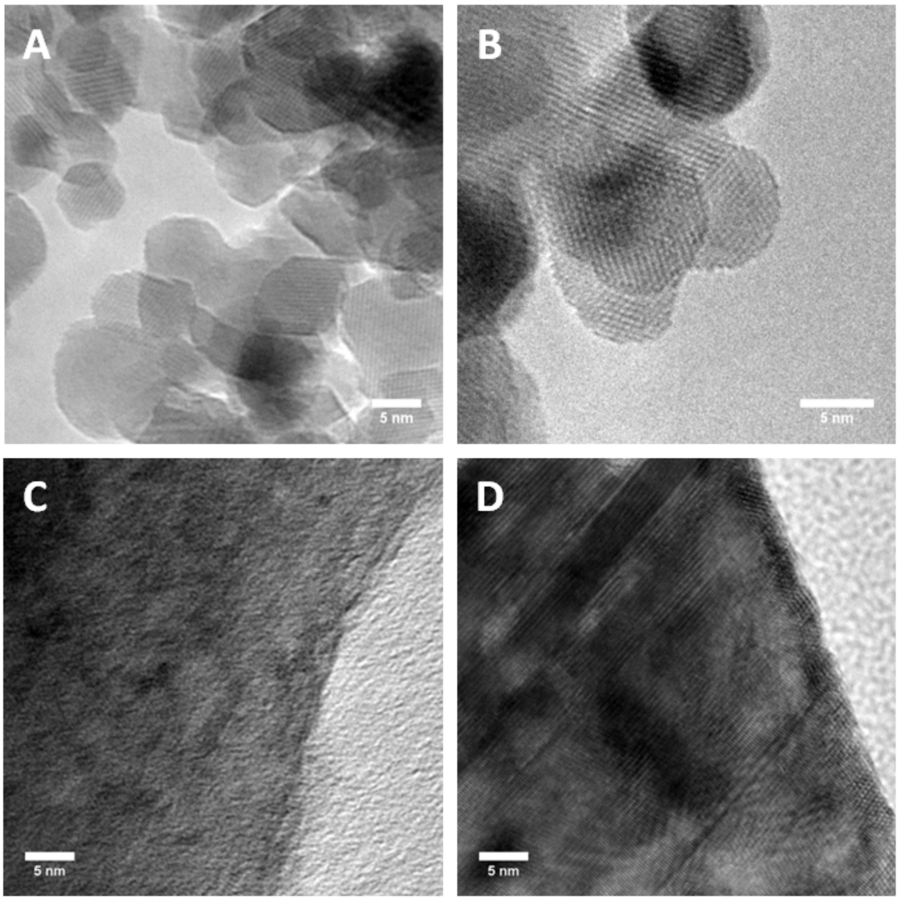

Figure 22: HRTEM micrographs of the as-prepared state of Co_3O_4(A), rs-CoO(B), CoOOH(C), and w-CoO(D).

The TEM micrograph of w-CoO shows the lattice planes in the bulk and on the surface of crystallites. The CoOOH film exhibited a dense, almost featureless morphology with cracks of up to 500 nm width. Even at higher magnification in the TEM micrographs, the domains of CoOOH are not discriminable and no lattice planes are visible. This furthermore shows the high degree of structural disorder and the amorphous nature of the CoOOH.

The local structure of the Co oxides was determined by selected-area electron diffraction (SAED) as shown in Figure 23. All Co oxides exhibited features in the electron diffraction pattern referable to Co oxide phases. The diffraction pattern of the crystalline Co oxides showed ring structures consisting of bright diffraction spots caused by the crystalline Co oxide domains. The ring structure of the crystalline Co oxides agreed well with the database references and with the structural analysis performed with GIXRD. Surprisingly, the CoOOH which appeared to be X-ray amorphous exhibited a diffuse ring structure. Thus, the CoOOH showed partial crystalline order but at a very low degree due to the small domain size. The electron diffraction pattern of CoOOH exhibited a pattern similar to rs-CoO.

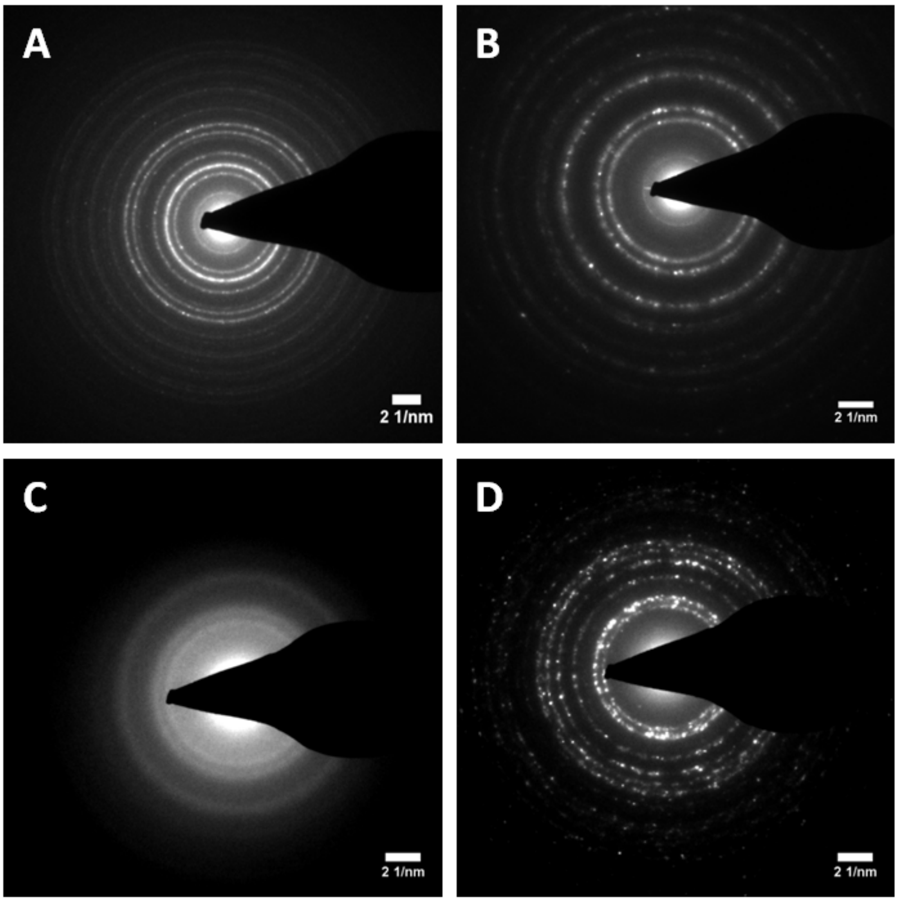

Figure 23: SAED pattern of the as-prepared state of Co_3O_4(A), rs-CoO(B), CoOOH(C), and w-CoO(D).

Thus, the crystalline domains of the CoOOH might possibly be described as a 3D cross-linked $CoO_x(OH)_y$ instead of a layered CoOOH. This 3D cross-linked $CoO_x(OH)_y$ might be present as structure similar to the structure of the near-surface as found for the oxygen-evolving state of Co_3O_4.[68]

In the next section, the Co oxidation state and the local atomic structure are described as extracted from XANES and EXAFS analysis and related to the structure of the crystalline domains as extracted from diffraction experiments. This is especially important to identify the structure of the X-ray amorphous CoOOH.

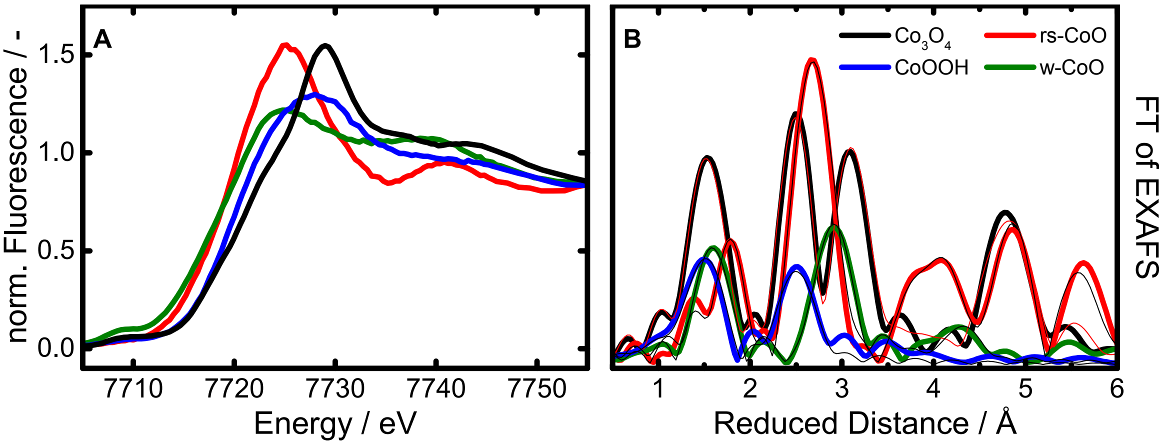

Figure 24: XANES and FT of EXAFS spectra of the as-prepared state of Co_3O_4(black), rs-CoO(red), w-CoO(green), and CoOOH(blue) recorded at the Co K-edge. Experimental curves are shown as bold, simulated as thin lines. See Chapter 5 for experimental details of Co_3O_4. The k^3-weighted EXAFS spectra are shown in Figure A34.

Local Atomic Structure and Co Oxidation State

The local atomic structure and Co oxidation state of the Co oxides have been investigated using XANES and EXAFS as extracted from XAS recorded at the Co *K*-edge. Figure 24A shows the XANES spectra of the Co oxides in the as-prepared state. It can be seen that the edge position and XANES profiles differ strongly between the Co oxides which indicates differences in mean Co oxidation state and coordination environment.

As extracted from half-rise of the absorption edge it was found that the edge position increases in the order w-CoO < rs-CoO < CoOOH < Co_3O_4 with 7716.7, 7717.3, 7718.7, and 7719.3 eV, respectively. If the position of absorption edge was determined via the integral method[151], the oxidation state followed the same trend w-CoO < rs-CoO < CoOOH < Co_3O_4 with 7717.2, 7717.5, 7719.0, and 7719.9 eV. Thus, rs- and w-CoO exhibited the lowest mean Co oxidation state. The Co ions in the CoOOH exhibited a lower mean oxidation state than the Co ions in the Co_3O_4 indicating a higher fraction of Co^{2+} ions in the structure of the sample CoOOH.

The local atomic structure of the absorbing Co ions was determined qualitatively from the Fourier-transformed EXAFS spectra (Figure 24B) and quantitatively by EXAFS simulations (Table 2 and Figure A34). The GIXRD results (Figure 20 and Table 1) already showed substantial structural differences in the crystal structure which lead to differences in the Co-O distances and the Co-Co distances of the Co oxides. In general, the Co-O bond length is expected to increase from Co^{3+} to Co^{2+} O_h which can be explained by the increasing ionic radius due to decreasing electron repulsion with decreasing number of electrons. Simultaneously, the decreased spatial overlap of the electron density between Co and O ions decreases the bond strength. Thus, tetrahedrally-coordinated transition metal ions exhibit a lower ionic radius than octahedrally-coordinated with same oxidation state because the "same number of orbitals shared between fewer bonds will make each bond stronger and therefore shorter".[39]

As shown in Chapter 5, Co_3O_4 exhibited three major distances from the absorbing Co ion of which the first peak in the FT-EXAFS corresponds to the mean Co-O distance of ~1.91 Å. The second and third peak is consistent with the distances between pairs of Co ions connected via di-μ-oxo (~2.85 Å) and mono-μ-oxo bridges (~3.36 Å), respectively. In contrast, the other three Co oxides exhibited only two peaks below a reduced distance of 3.5 Å caused by the Co-O distance and Co-Co distances. The peak position of the Co-O distances increased in the order $CoOOH \approx Co_3O_4 <$ w-CoO $<$ rs-CoO whereas the order of the shortest Co-Co is different with $CoOOH \approx Co_3O_4 <$ rs-CoO $<$ w-CoO. Table 2 shows the results from simulation of the EXAFS spectra which confirm the increasing length of the mean Co-O distance from CoOOH and Co_3O_4 to w-CoO and rs-CoO and the increasing length of the shortest Co-Co distance from CoOOH and Co_3O_4 to rs-CoO and w-CoO.

The Co-O and Co-Co distances found for CoOOH agreed well with Co^{3+} O_h ions which are connected via di-μ-oxo bridges. This structural motif is typical for layered transition metal (oxyhydr)oxides such as δ-MnO_2, NiOOH and FeOOH as well as for the CoCat. However, there was no evidence from the structural analysis that hexagonal CoO_6 layers connected via hydrogen bonds had formed. The typical and strong (00l) reflections which reflect the spacing between the layers in the layered (oxyhydr)oxide structures were absent in the diffraction pattern either due to the low domain size or due to the absence of this structural motif. Alternatively, a 3D cross-linked $CoO_x(OH)_y$ with only di-μ-oxo bridged Co ions could have formed which was in agreement with the results from the structural simulation. This structure would also agree with the electron diffraction pattern showing the presence of a rocksalt-like $CoO_x(OH)_y$ structure. In addition, a significant fraction of reduced Co sites were present in the CoOOH as determined from the XANES spectra. Interestingly, the reduced Co sites did not significantly influence the Co-O bonding environment and Co-Co cross-linking. This finding is in analogy to the CoCat which exhibits an oxidation state which is lower than +3 when prepared under similar conditions but the Co-O bonding environment is typical for a Co^{3+}-containing structure.[114, 119, 178]

Table 2: Results of simulation of the EXAFS spectra of Co_3O_4, rs-CoO, w-CoO, and CoOOH in the as-prepared state. The experimental and simulated spectra are shown in Figure A34 and the complete results shown in Table 9.

Distance	Sample	N	R / Å	Debye-Waller factor σ / Å
Co-O	Co_3O_4	5.3 ± 0.2	1.908 ± 0.001	0.046 ± 0.002
	rs-CoO	0.4 ± 0.4 4.4 ± 0.6	1.985 ± 0.020 2.135 ± 0.008	0.067 ± 0.012
	w-CoO	3.2 ± 0.6	1.971 ± 0.016	0.070 ± 0.010
	CoOOH	3.0 ± 2.0	1.887 ± 0.048	0.048 ± 0.010
Co-Co 1	Co_3O_4	4.6 ± 0.2	2.851 ± 0.001	0.052 ± 0.001
	rs-CoO	12.2 ± 0.3	3.003 ± 0.002	0.077 ± 0.110
	w-CoO	6.3 ± 2.5	3.228 ± 0.014	0.077 ± 0.017
	CoOOH	1.6 ± 2.8	2.825 ± 0.045	0.048 ± 0.058
Co-Co 2	Co_3O_4	6.8 ± 0.3	3.357 ± 0.001	0.052 ± 0.001
	rs-CoO	1.7 ± 0.6 4.8 ± 0.0	3.985 ± 0.012 4.357 ± 0.006	0.032 ± 0.014

In case of rs-CoO, the low Co oxidation state and the length of the shortest Co-Co distance (3.00 Å) agrees well with a Co oxide in which primarily Co^{2+} O_h are connected via di-μ-oxo bridges. However, the best fit was achieved when the Co-O distance was simulated using a shorter (1.98 Å) and a longer distance (2.13 Å) which could be caused by distorted Co-O octahedra e.g. in the vicinity of cationic vacancies. The presence of an elongated Co-O compensating the contracted Co-O distance within the oxide lattice was not simulated due to the superposition with the Co-Co distance. This explanation is in agreement with *ab initio* DFT calculations of CoO in which different degrees of cationic vacancies led to distortions in the CoO_6 octahedra in vicinity.[84] The convolution of shorter and longer Co-O distance led to a shorter mean distance than in ideal rs-CoO. The results from the EXAFS simulation were thus, in good agreement with the results from the Rietveld refinement which already indicated a distortion in the rocksalt-structure (see Table 1). The presence of Co^{3+} and di-μ-oxo bridges between pairs of Co^{3+} ions was not detected. In agreement with the multiple Co-O distance, the second Co-Co distance (mono-μ-oxo bridged Co ions) was also simulated using two distances with 3.99 and 4.35 Å corresponding to shortened and elongated mono-μ-oxo bridges in the crystal lattice, respectively.

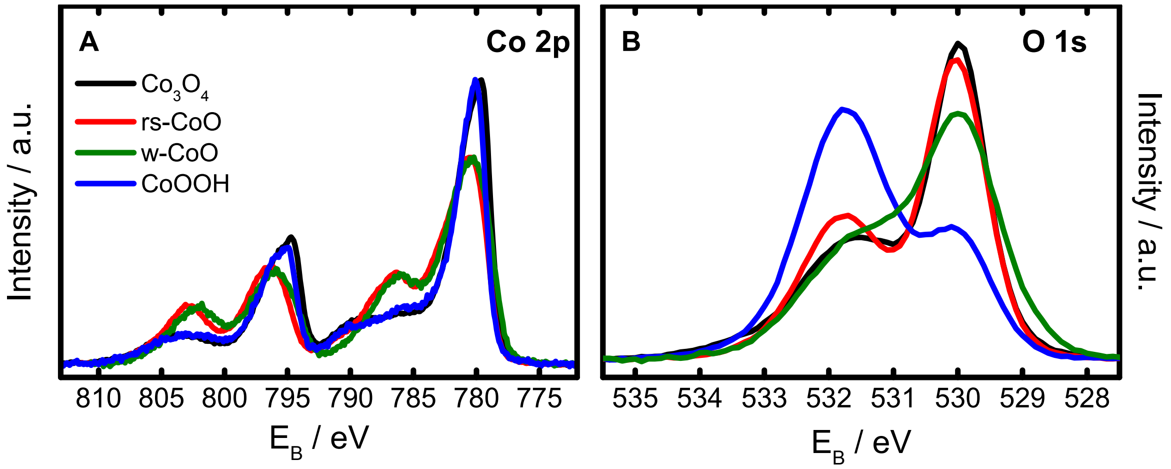

Figure 25: Co 2p (A) and O 1s (B) photoelectron spectra of the as-prepared state of Co_3O_4(black), rs-CoO(red), w-CoO(green), and CoOOH(blue) recorded at a kinetic energy of the photoelectrons of 550 eV.

In case of w-CoO, the low Co *K*-edge position, the length of Co-O and of the shortest Co-Co distance of 1.97 Å and 3.23 Å, respectively, agreed well with a CoO in which only Co^{2+} T_d are connected via mono-μ-oxo bridges.[80-82] The mean Co-O distance is longer than expected for an ideal, undistorted wurtzite-like CoO which would be 1.94 Å. The elongated Co-O distance determined by Rietveld refinement is 1.98 Å. Thus, the EXAFS results reflect well the distorted crystal structure of w-CoO as determined by the Rietveld refinement of the GIXRD data (see Table 1). In an undistorted hexagonal lattice, the Co-Co distance corresponds to the lattice parameter *a*.

Thus, the Co oxidation state and local atomic structure of the crystalline Co oxides as determined from XANES spectra and EXAFS analysis were in good agreement with the crystal structures determined by GIXRD and Rietveld refinement (see Figure 20). Furthermore, the X-ray amorphous CoOOH exhibited a structure with a typical Co^{3+} octahedral bonding environment but a lower mean Co oxidation state was found. In the next section, the determined bulk structure of the Co oxides is compared with the composition and the electronic structure of the near-surface.

Near-Surface Chemical State and Composition

The near-surface chemistry and composition of the Co oxides was investigated using synchrotron-based X-ray photoelectron emission spectroscopy (XPS). Figure 25A and B show the Co 2p and O 1s spectra of the four Co oxides in their as-prepared state. The Co 2p spectra are split by spin-orbit coupling and the two main lines appeared at ~780 and ~796 eV corresponding to Co $2p_{3/2}$ and Co $2p_{1/2}$ states, respectively. The presence of Co^{2+} and Co^{3+} ions in the near-surface can be determined from satellite features at ~786 eV and ~790 eV, respectively.[33]

In case of rs- and w-CoO, the Co 2p spectra exhibited a distinct satellite feature at ~786 eV and negligible contributions at ~790 eV and thus, the near-surface of these two oxides consisted of mainly Co^{2+} ions. In case CoOOH and Co_3O_4, the satellite feature at ~790 eV corresponding to Co^{3+} was present and the Co^{2+} satellite feature exhibited low intensity. The intensity of the Co^{2+} satellite feature in CoOOH was higher than in Co_3O_4. Thus, these two Co oxides exhibited mainly Co^{3+} ions in the near-surface but CoOOH possibly exhibited a slightly higher fraction of Co^{2+} ions in the near-surface. The significant degree of reduced Co ions of the bulk was not found in the near-surface.

The O 1s spectra in Figure 25B showed contributions of at least three different oxygen species in the near-surface of the Co oxides. The O ions incorporated in the oxide lattice, surface hydroxyl groups and chemisorbed water led to peaks at ~530 eV, 531.5 eV, and 533 eV, respectively.[33]

Table 3: Surface composition of Co_3O_4, rs-CoO, w-CoO, and CoOOH in the as-prepared state as extracted from peak fitting and integration of XPS Co 2p and O 1s spectra.

Sample	O/Co	Fraction of Lattice O	Lattice-O / Co
Co_3O_4	1.48	0.54	0.83
rs-CoO	1.15	0.59	0.68
w-CoO	1.20	0.59	0.71
CoOOH	2.40	0.27	0.65

The surface composition of the Co oxides as extracted from peak fits (see Figure A35) is shown in Table 3. The fraction of lattice oxygen referred to all O atoms was ~0.54-0.59 for the Co^{2+} oxides and Co_3O_4 whereas the CoOOH exhibited a fraction of lattice oxygen of 0.27. Thus, the crystalline Co oxides exhibited a higher fraction of lattice oxygen species in the as-prepared state than the X-ray amorphous CoOOH. The ratio of O/Co of the near-surface represents to a certain extent the oxidation state of the Co ions. Except for the CoOOH, the O/Co ratio increased in parallel to the mean Co oxidation state (see Figure 24).

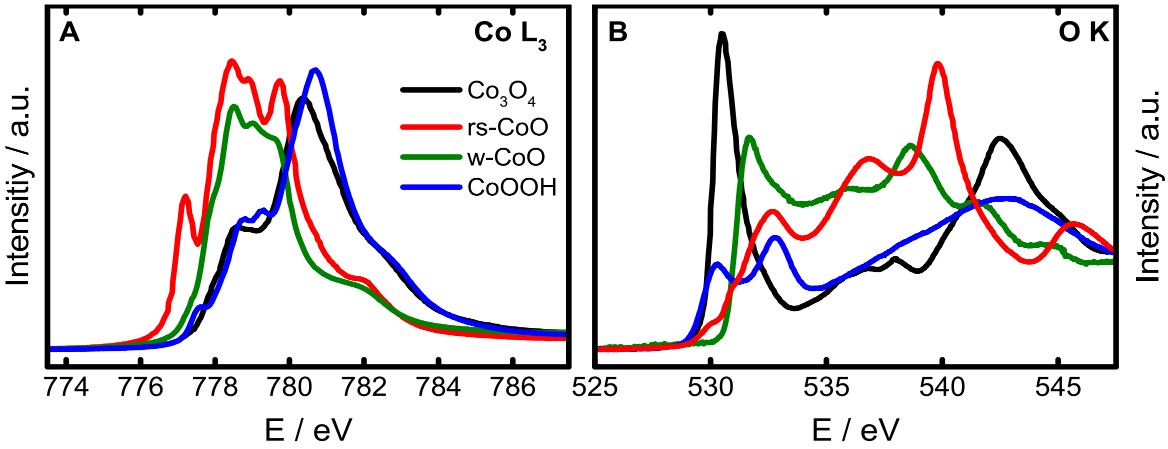

Figure 26: Co L_3 (A) and O K (B) XANES spectra of the as-prepared state of Co_3O_4(black), rs-CoO(red), w-CoO(green), and CoOOH(blue) recorded in total electron yield mode.

The O/Co ratio of CoOOH was with 2.4 significantly higher than the position of the Co *K*-edge position suggested but fits to the bonding environment as extracted from EXAFS analysis and to the Co 2p spectra. The significant degree of protonated O sites and chemisorbed water molecules in the near-surface of the CoOOH can explain the lower mean Co oxidation state and elevated the O/Co ratio.

Electronic Structure

In contrast to XPS, the XANES spectra recorded at the Co L_3- and O *K*-edge probes unoccupied near-surface electronic states in the 3d- and 2p-orbitals of the Co and O ions, respectively. Figure 26A and B shows the XANES spectra of the four Co oxides in the as-prepared state recorded at Co L_3- and O *K*-edge, respectively. The peak position of the Co L_3 XANES spectra depended analogous to the *K*-edge on the Co oxidation state.

The energy of the principal maximum of Co L_3 XANES spectra increased from rs- and w-CoO to Co_3O_4 and CoOOH and thus, followed the O/Co ratio as determined from XPS. The Co L_3 XANES spectra of rs-CoO and Co_3O_4 were in very good agreement with reference spectra.[179] CoOOH exhibited a profile which was similar to the Co L_3 XANES spectra recorded of the CoCat which contained mainly Co^{3+} O_h ions.[180-181] Thus, the Co electronic structure of CoOOH agreed well with the bonding environment of Co^{3+} O_h ions which was identified by EXAFS. But the presence of Co^{2+} T_d ions was revealed by peak fitting (see Figure A38). In addition, the CoOOH spectrum showed a minor pre-feature (at ~777.6 eV for CoOOH).

In case of rs-CoO, the strong pre-feature at 777.2 eV is typical for Co^{2+} O_h ions which are in high spin configuration and thus, exhibit an unoccupied t_{2g} state in the 3d orbitals which is probed in this pre-feature of the Co L_3 XANES spectrum. Thus, in case of CoOOH this feature could be caused by Co O_h ions in high spin configuration leading to unoccupied t_{2g} states. The Co^{2+} O_h feature was absent in the spectrum of w-CoO due to the tetrahedral coordination. In this case, the energy of the t_2 and e states is reversed and the e states are fully occupied but formally the Co^{2+} T_d ions exhibit high spin configuration. Thus, the tetrahedral coordination of the Co ions in the bulk of w-CoO could be proven for the near-surface.

The O *K* XANES spectra of the as-prepared Co oxides can be divided into two regions – below and above the main edge at ~534 eV. The main absorption edge and the features above are commonly assigned to electron transitions from the O 1s to hybridized orbitals of O 2p with Co 4s/4p states.[36, 182] The features below the main absorption edge (pre-edge features) are caused by electron transitions into hybridized Co 3d - O 2p orbitals.[36, 182] As shown in Figure 26B, all four Co oxides exhibited pre-edge features between 529 eV and 534 eV but revealed significant differences its shape. The position of the principal maximum of the pre-edge increased in the order Co_3O_4 < w-CoO < rs-CoO ≈ CoOOH.

In total, three major O states were identified from the pre-edge features of the O *K*-edge spectra of the four Co oxides. The lowest state at ~530.3 eV was found for Co_3O_4 and CoOOH and was thus assigned to electron transitions into states involving 3d orbitals of Co^{3+} O_h. A higher O state was found for the w-CoO at ~531.7 eV and was thus assigned to electron transitions into states involving 3d orbitals of Co^{2+} T_d ions. This state could also contribute to the pre-edge feature of Co_3O_4 which also contains Co^{2+} T_d ions. The highest O state was found at ~532.7 eV for rs-CoO and CoOOH and was thus assigned to electron transitions into states involving 3d orbitals of Co^{2+} O_h ions. Additionally, rs-CoO exhibited an intermediate O state at ~531 eV and also a slight contribution at 530.3 eV. These contributions to the pre-edge feature might be caused by distorted Co octahedra in the CoO lattice as determined from structural analysis and is in agreement with DFT+U calculations on the electronic structure of defective CoO.[84]

The assignment of the electron transitions into orbitals involving Co^{3+} O_h ions is in agreement with DFT calculations of the O K XANES spectrum of a crystalline CoOOH consisting only of Co^{3+} O_h ions.[181] These calculations showed that the pre-edge feature was composed of electron transitions into three O states in which only Co 3d e_g states were involved. The O states were spread over ~1.5 eV. The highest intensity was found for the lowest energy state involving Co $d_{x^2-y^2}$ and d_{z^2} states. The energetically highest O state involved only $d_{x^2-y^2}$ states.

The position of O states as extracted from the local maxima increases with the mean Co-O bond length of the Co oxides as determined by EXAFS analysis and was thus, inversely correlated to the Co-O bond strength. The O states of the Co^{2+} oxides in this study were shifted to higher energies compared to Co^{3+} and the energy of the main O state in w-CoO is lower than in rs-CoO.

In summary, the near-surface and the bulk of the synthesized Co oxide catalysts exhibited the desired Co coordination and bonding environment. The Co oxide showed substantial differences in the electronic structure which could be related to the Co-O bonding environment. However, extensive DFT calculations could be helpful to verify the assignments of the electronic states but this would exceed the scope of this work. In the next section, the results from the electrochemical and –catalytic characterization in neutral and alkaline electrolyte are presented.

6.2.2 OER Electrocatalysis and Redox Electrochemistry of Co oxide

Electrochemical Characterization in Neutral Electrolyte

The surface Co oxide redox chemistry and the electrocatalytic properties of the four Co oxide catalysts in neutral electrolyte were tested using cyclic voltammetry and quasi-stationary potential-step experiments as shown in Figure 27A and B, respectively. All four Co oxides showed a linear potential–log(i) dependence between 1.57 V and 1.70 V representing a catalytic reaction following Butler-Volmer kinetics. Interestingly, the geometric current density at low overpotentials was very similar for the investigated Co oxides.

The Co oxides thus, exhibited similar mass activity for OER due to the same Co loading. At higher electrode potential the catalytic current differed strongly between the Co oxides. The current density of CoOOH at ~1.7 V was twice the current of Co_3O_4. These differences were furthermore quantified using the Tafel slope which was maximal for Co_3O_4 with 86 $mV \cdot dec^{-1}$ and minimal for CoOOH with 68 $mV \cdot dec^{-1}$. The two Co^{2+} oxides catalysts exhibited a similar Tafel slope with 74 and 76 $mV \cdot dec^{-1}$ for rs- and w-CoO, respectively, and represented intermediate electrocatalytic behaviour between the CoOOH and Co_3O_4. Thus, it can be concluded that the X-ray amorphous CoOOH showed superior electrocatalytic properties.

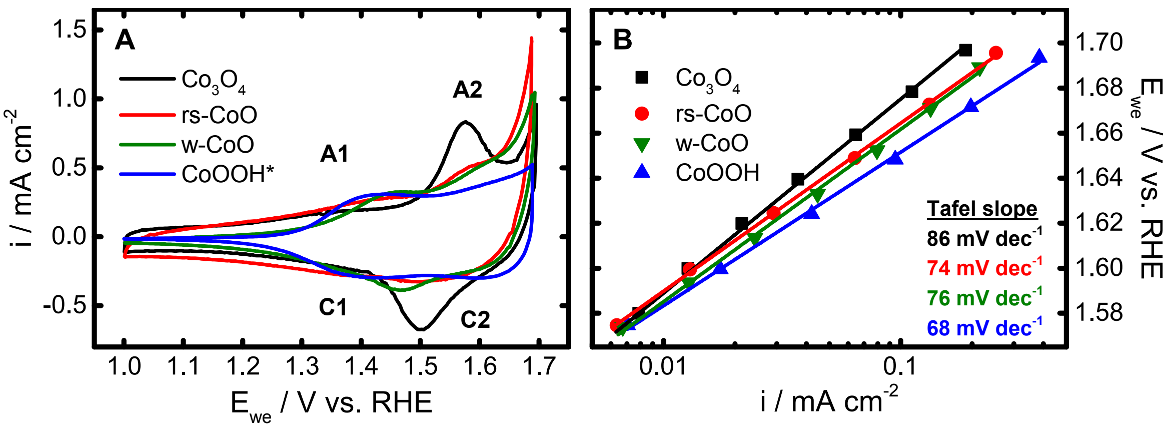

Figure 27: Cyclic voltammograms (A) and Tafel plot (B) of Co_3O_4(black), rs-CoO(red), w-CoO(green), and CoOOH(blue) deposited on glassy carbon recorded in N_2-saturated 0.1 M KPi at pH 7. The Tafel plots were extracted from anodic quasi-stationary potential step experiments. The cyclic voltammograms were recorded with a sweep rate of 200 mV·s^{-1}. The Co loading was identical for all samples with 322 nmol·cm^{-2}. *The current of CoOOH in the cyclic voltammogram was divided by 5 for better visualisation.

Commonly, a Tafel slope of 59 mV·dec^{-1} for OER in neutral, phosphate containing electrolyte is attributed to a chemical *rate-determining step* preceded by a proton-coupled electron transfer step in equilibrium as found for the CoCat.[56, 183] The larger Tafel slope of the investigated Co oxides corresponds to an additional overpotential and energy loss mechanism present during OER on these Co oxides which might superimpose the *rate-determining step* of the electrocatalytic reaction.

To investigate possible similarities and differences in the Co oxide redox chemistry and to link this with the structural and electrocatalytic properties a series of cyclic voltammograms was recorded in neutral, phosphate-containing electrolyte. The CVs shown in Figure 27A were recorded after two potential cycles in the OER region and prior to the quasi-stationary potential step experiments and thus, represented an OER-conditioned catalyst state. The CVs of all four Co oxides exhibited two redox transitions, namely A1/C1 with a redox potential of E_{redox}~1.4 V and A2/C2 of E_{redox}>1.54 V which were assigned to the Co^{2+}/Co^{3+} and Co^{3+}/Co^{4+} redox transitions, respectively.[100, 114] (see Figure 15a) CoOOH exhibited the highest redox potential of A2/C2 with $E_{A2/C2}$>1.6 V and no significant peak splitting was detected. But the oxidative and reductive peaks were broad compared to the A2/C2 redox transition of Co_3O_4. The other three Co oxides exhibited a similar redox potential of A2/C2 (~1.54 V) and the peak splitting was ~80 mV for rs-CoO and Co_3O_4 as well as ~140 mV for w-CoO. No differences in redox potential of A1/C1 were observed for the Co oxides. Peak splitting of redox features is induced by transfer processes of electrons, protons or molecules from/to the redox sites whereas the redox potential is a measure of the thermodynamics of the redox reaction.[17, 184] The observed differences in the Co redox features can be explained by worse electron transfer properties in w-CoO compared to the other three Co oxides. Furthermore, the oxidation of a Co^{3+} ion to Co^{4+} at the surface of CoOOH exhibited a higher redox potential but the onset potential of OER is comparable to the other three Co oxides. Thus, the oxidation of Co^{3+} to Co^{4+} might be energetically more demanding which can be explained by the lower mean Co^{3+}-O bond length of CoOOH compared to e.g. Co_3O_4 (see Table 2). This indicates that the stronger bond strength influences the thermodynamics of the redox processes. The broadness of these redox peaks might be related to the lower degree of confinement of the Co bonding environment in CoOOH due to the X-ray amorphous nature. This induces a broader distribution in the energy of the redox transition in contrast to redox transitions on single crystal surfaces.[185]

The density of electrochemically-accessible Co sites of the Co oxides can be compared using the total charge transferred during a cathodic scan between 1.0 V and the zero-crossing at $E > 1.6$ V. The geometric density of redox active Co sites decreased in the order CoOOH >> Co_3O_4 > w-CoO > rs-CoO. The difference in surface charge between the Co^{2+} oxides and Co_3O_4 was mainly caused by the difference in A2/C2 which was significantly more pronounced for Co_3O_4. The significantly higher density of redox-active Co sites of CoOOH which should lead to a higher current density at the same overpotential was partially compensated by the anodic shift of the Co^{3+}/Co^{4+} redox couple and led to a comparable OER activity with respect to geometric surface area.

The differences in the Co oxide redox chemistry were quantified using the ratio of peak currents of C1 (at 1.35 V or rather 1.43 V for CoOOH) and C2 (at the local minimum above 1.45 V) as shown in Figure A36. This ratio was maximal for CoOOH with $C1/C2 \approx 0.99$ and was minimal for Co_3O_4 with $C1/C2 \approx 0.19$. The initially Co^{2+} oxides exhibited an intermediate state between Co_3O_4 and CoOOH with $C1/C2 \approx 0.68$ and ≈ 0.51 for rs- and w-CoO, respectively. For all investigated Co oxides, the number of reducible Co^{3+} sites is seemingly never higher than the number of oxidizable Co^{3+} sites. (see Figure 27) Thus, the Co oxide redox chemistry was influenced by the initial crystal structure of the Co oxides and by the Co coordination and oxidation state in the as-prepared state. The Co ions at the surface of the initially crystalline Co oxides exhibited a reduced amount of Co sites leading to feature A1/C1 whereas the X-ray amorphous CoOOH had a similar number of Co sites causing features A1/C1 and A2/C2.

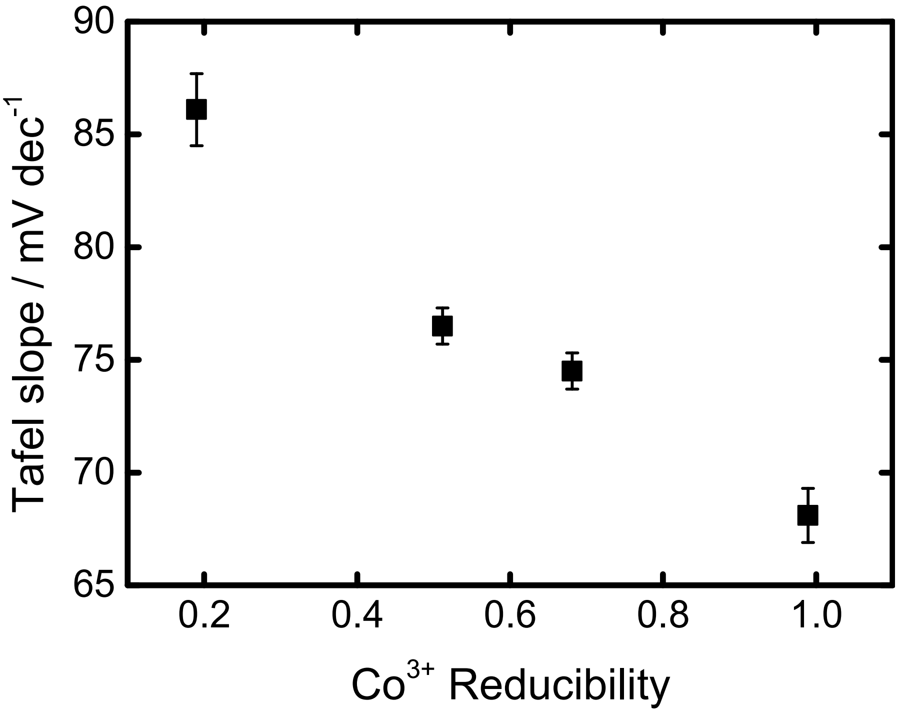

Figure 28: Tafel slope of Co oxides as function of the electrochemical reducibility of the Co^{3+} sites. Reducibility was determined from the peak current ratio of C1 and C2 as extracted from cyclic voltammograms recorded with a sweep rate of 200 mV s^{-1} in 0.1M KP$_i$ at pH7. The potential of C1 was 1.35 V in case of rs-, w-CoO and Co_3O_4 as well as 1.43 V for CoOOH. The potential of C2 was chosen by the local current minimum above a potential of 1.45 V. Tafel slope was determined from anodic quasi-stationary potential step experiments in the same electrolyte. See Figure A36 for further details.

Following this assignment, the reduction of Co^{3+} ions at the surface of Co_3O_4, rs- and w-CoO was hampered compared to CoOOH. In CoOOH almost all Co^{3+} sites that could be oxidized to Co^{4+} can also be reduced to Co^{2+}. These differences in the Co oxide redox electrochemistry can be related to electronic and local atomic structure. It has to be noted that the determined differences in the Co oxide redox behaviour cannot be caused by the participation of Co ions from the bulk of the $CoO_x(OH)_y$ domains. The determined cathodic charges during cyclic voltammograms showed that only up to 5% of the Co ions deposited on the electrode are actually redox active. Therefore, the redox features of CoOOH (and of the other three Co oxides) are predominantly caused by Co oxide surface sites.

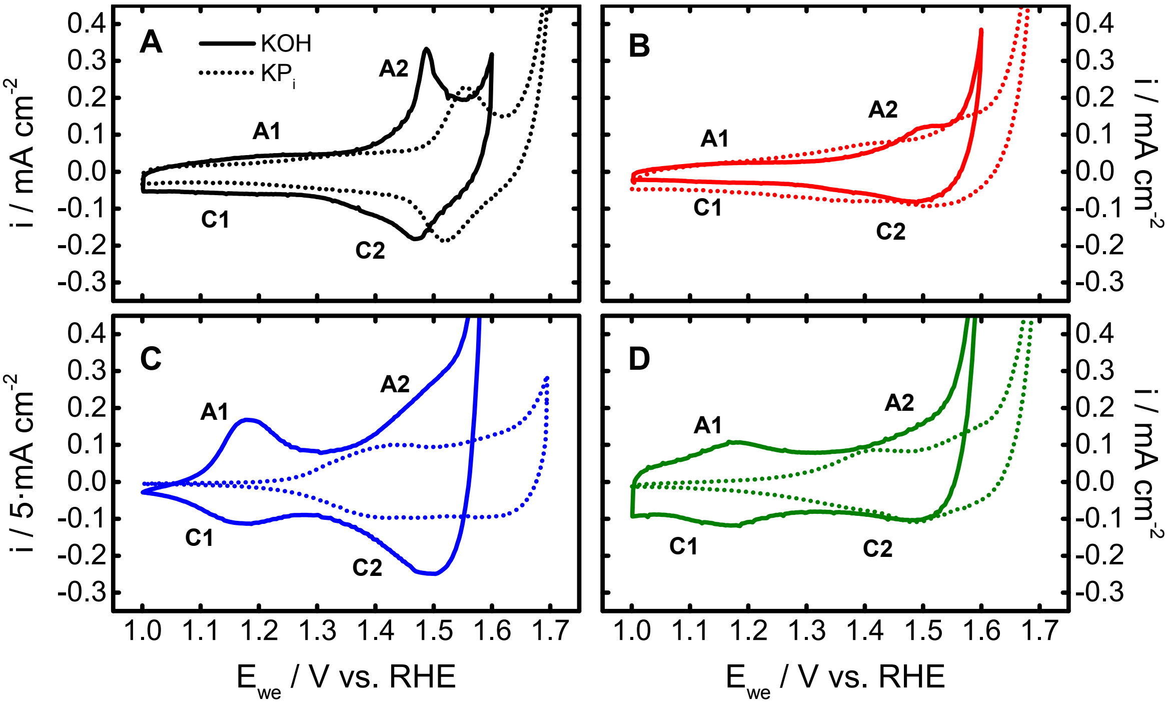

Figure 29: Cyclic voltammograms of Co_3O_4(A), rs-CoO(B), CoOOH(C), and w-CoO(D) recorded with a sweep rate of 200 mV s^{-1} in N_2-saturated 0.1 M KOH (solid) and 0.1M KPi at pH 7 (dashed).

Comparing the Co oxide redox electrochemistry with the electrocatalytic properties showed a correlation between the redox features A2/C2, A1/C1 and the Tafel slope. The onset of OER on Co oxides was linked to the oxidation of the Co^{3+} ions; if Co^{4+} are present a linear potential-log(i) behaviour can be seen. Thus, the formation of Co^{4+} is necessary to achieve catalytic OER current. (see also Figure A24).

The electrocatalytic properties were found to benefit significantly as the Tafel slope decreases with increasing ratio of C1/C2 as shown in Figure 28. The largest C1/C2 ratio and the lowest Tafel slope were determined for CoOOH whereas the lowest C1/C2 ratio was found for Co_3O_4 accompanied by the highest Tafel slope of the investigated Co oxides. Thus, a high fraction of electrochemically-reducible Co^{3+} sites at the surface is highly beneficial for OER activity. The beneficial influence of these reducible Co^{3+} sites is furthermore shown when the Co surface redox electrochemistry of the Co oxides in neutral electrolyte is compared with the OER activity determined in alkaline electrolyte as it is discussed in the next section.

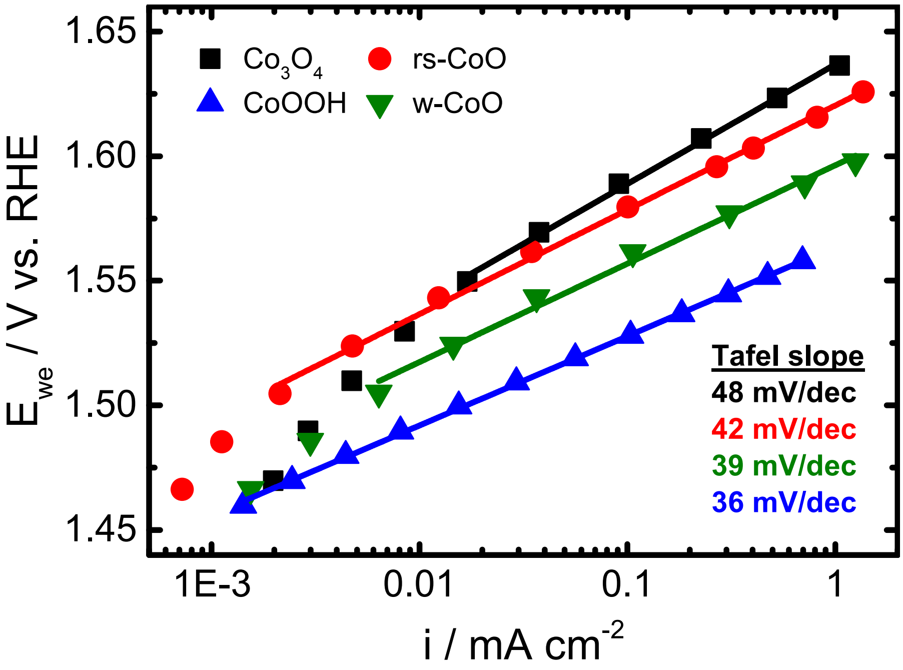

Figure 30: Tafel plots of Co_3O_4 (black), rs-CoO (red), CoOOH (blue) and w-CoO (green) recorded in N_2-saturated 0.1 M KOH. The solid lines represent the given Tafel slope 48, 42, 39, and 36 mV·dec^{-1} for Co_3O_4, rs-CoO, CoOOH, and w-CoO, respectively.

Electrochemical Characterization in Alkaline Electrolyte

Figure 29 shows cyclic voltammograms of the four Co oxides recorded in 0.1M KOH and in neutral electrolyte in 0.1M KP_i at pH 7. In the alkaline electrolyte, all four Co oxides exhibited two Co oxide redox transitions in analogy to the behaviour in neutral electrolyte. However, the redox potentials of both transitions were shifted cathodically. Redox transition A2/C2 was found at E_{redox}> 1.48 V and A1/C1 at ~1.15 V. Thus, the determined shift of A1/C1 was significantly larger (~200 mV) than that of A2/C2 (<100 mV) and the potential difference between Co^{2+}/Co^{3+} and Co^{3+}/Co^{4+} transition was more than 100 mV larger in alkaline than neutral electrolyte.

To determine the electrocatalytic properties of the Co oxides in alkaline electrolyte, quasi-stationary potential step experiments in 0.1M KOH were performed and the experimental data are shown in Figure 30. The Tafel slopes of all Co oxides were lower than in neutral electrolyte. CoOOH exhibited the lowest (36 mV·dec^{-1}) and Co_3O_4 the highest Tafel slope (48 mV·dec^{-1}). rs- and w-CoO showed an intermediate electrocatalytic behaviour. The Tafel plot of Co_3O_4 furthermore exhibited a larger Tafel slope at low overpotentials. The overpotential at maximal current density of the quasi-stationary potential step experiment follows the same order as the Tafel slope. Thus, both electrokinetic figures benefit from a higher charge of the Co^{2+}/Co^{3+} redox peak.

An influence of the redox electrochemistry of the Co oxides on their electrocatalytic properties was also seen in case of alkaline electrolyte. Firstly, the onset potential of OER shifted cathodically similar to the redox potential of the Co^{3+}/Co^{4+} transition. The electrocatalytic activity in alkaline electrolyte benefited strongly from the geometric density of reducible Co^{3+} sites whereas the Tafel slope decreased only slightly.

Furthermore, the lower Tafel slope of the Co oxides in alkaline electrolyte was accompanied by an increased potential difference between Co^{2+}/Co^{3+} and Co^{3+}/Co^{4+} redox transitions. This increased potential difference led to a significantly higher rate of oxidation of possibly formed Co^{2+} ions during OER which can be beneficial for the electrocatalysis due to elevated electrochemical healing of oxygen vacancies (see section 2.1.2 and 2.1.4-5). This step is possibly potential-determining for OER as found by DFT calculations for water oxidation on (012) surface of CoOOH.[25] However, the rate-determining step involves most likely O-O bond formation which can be formed via nucleophilic attack of adsorbed O by OH^- ions in alkaline electrolyte. To correlate the differences in redox electrochemistry and OER electrocatalysis determined for the Co oxides with their structural and electronic properties of the near-surface and of the bulk it is necessary to investigate the Co oxides after OER conditioning. Co^{2+} oxides are likely to undergo irreversible changes during the OER with its inherent oxidizing reaction conditions.

In the next section, the extensive characterization of the morphology, local crystal and atomic structure as well as the near-surface composition and electronic structure are described for the Co oxides catalysts after OER conditioning in the neutral, phosphate-containing electrolyte. Thereby, irreversible changes of the physicochemical properties of the bulk and of the near-surface are identified and are related the electrochemical and electrocatalytic properties.

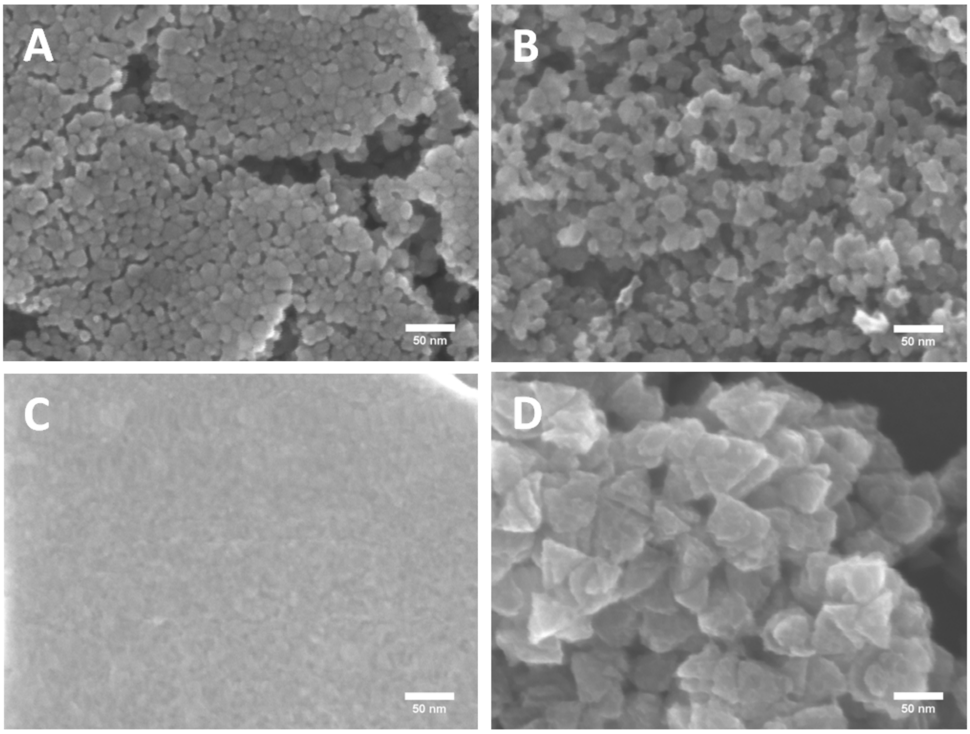

Figure 31: SEM micrographs of the OER-conditioned state of Co_3O_4(A), rs-CoO(B), CoOOH(C), and w-CoO (D) deposited on glassy carbon. OER conditioning was performed for 15 min at 1.62 V in N_2-saturated 0.1M KP_i.

6.2.3 Physicochemical characterization of OER-conditioned Co oxides

Morphology and Local Crystal Structure

The morphology of the Co oxides in the OER-conditioned state was investigated using scanning and transmission electron microscopy as shown in Figure 31 and Figure 32. OER conditioning was performed for 15 min at 1.62 V in N_2-saturated 0.1M KP_i at pH 7 and the OER-conditioned materials are denoted as e.g. Co_3O_4-OER. Comparing the morphology of the OER-conditioned state with the as-prepared state (Figure 21 and Figure 22) it becomes apparent that the OER conditioning did not severely change the morphology of the Co oxides. However, the surface of the Co oxides crystallites changed (significantly) on the nanometre scale, as apparent from the TEM images (see Figure 32).

The films of Co_3O_4-OER and rs-CoO-OER retained their homogeneity and porosity. The crystallites of Co_3O_4 did not change irreversibly in shape, size and local crystal structure as shown in Chapter 5.

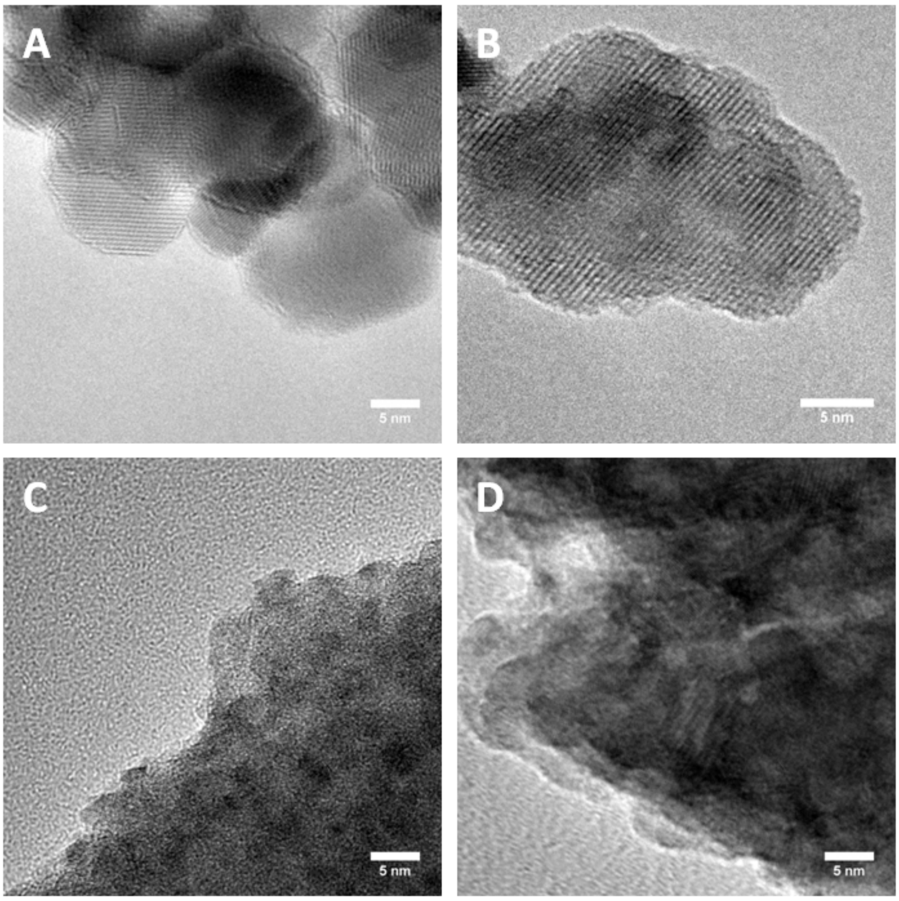

Figure 32: HRTEM micrographs of the OER-conditioned state of Co_3O_4(A), rs-CoO(B), CoOOH(C), and w-CoO (D). OER conditioning was performed for 15 min at 1.62 V in N_2-saturated 0.1M KP_i at pH 7.

In case of rs-CoO-OER, the surface of the film seemed slightly rougher and the crystallite boundaries merged. This shows a restructuring of the surface of the film and/or crystallites. The TEM micrographs reveals that the crystallites of rs-CoO partially lost their spherical shape and transformed towards a more ellipsoidal shape with a rougher surface as shown in Figure 32B. This finding indicates an irreversible structural change of rs-CoO during OER. In contrast, the film of the CoOOH appeared more structured, defined and rougher after OER conditioning. The TEM micrograph shows that the bulk of the CoOOH-OER film incorporated darker regions compared to as-prepared state which indicates beginning crystallization and/or restructuring of the amorphous CoOOH. However, the size of the domains of the CoOOH-OER was still less than 2 nm and thus, the OER-conditioned state of CoOOH is highly disordered.

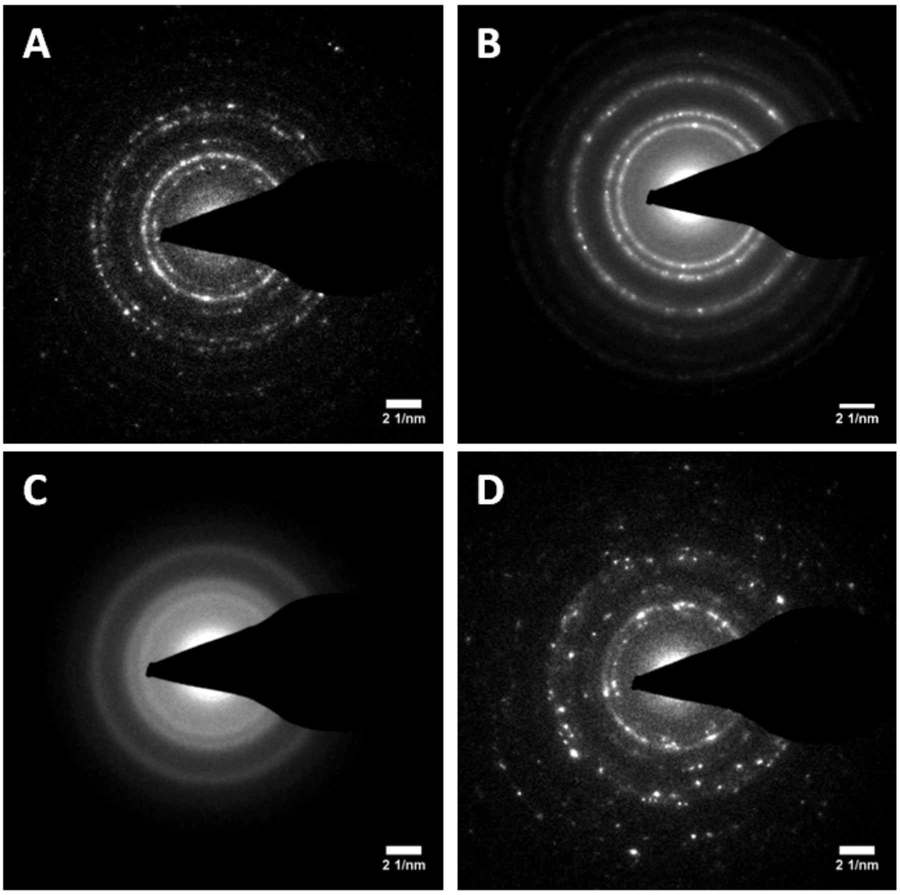

Figure 33: SAED pattern of the OER-conditioned state of Co_3O_4(A), rs-CoO(B), CoOOH(C), and w-CoO (D). The SAED patterns were recorded at lower magnification than the TEM micrographs shown in Figure 32.OER conditioning was performed for 15 min at 1.62 V in N_2-saturated 0.1M KP_i at pH 7.

The strongest change in morphology due to OER was determined for the crystallites of w-CoO. Although the crystallites of w-CoO-OER retained their pyramidal shape, the facets got significantly roughened after OER electrocatalysis. This roughening can be traced in the SEM and TEM micrographs shown in Figure 31D and Figure 32D, respectively. The smooth facets of the w-CoO crystallites of the as-prepared state transformed to a conglomerate of smaller domains in w-CoO-OER. The lattice planes of the as-prepared state were hardly visible in the w-CoO-OER (see Figure 23D). Thus, the OER led to an irreversible loss of crystallinity and restructuring of the near-surface of w-CoO.

The crystal structure of the Co oxides after OER conditioning was investigated using SAED as shown in Figure 33. The crystal structure of Co_3O_4, rs-CoO and CoOOH did not change after OER conditioning as shown in Figure 33A-C. rs-CoO-OER and CoOOH-OER exhibited a rocksalt-like structure.

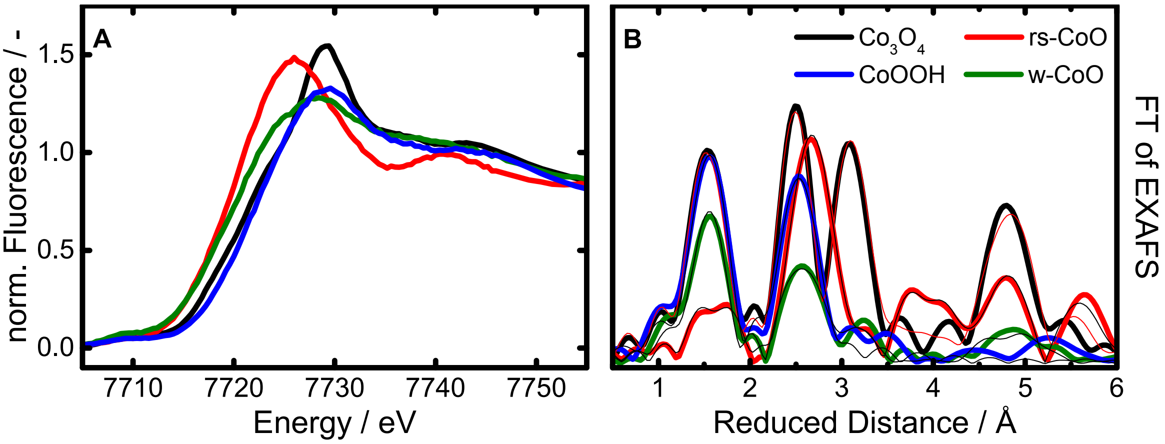

Figure 34: XANES (A) and FT of EXAFS (B) spectra of Co_3O_4(black), rs-CoO(red), w-CoO(green), and CoOOH(blue) after OER recorded at the Co *K*-edge. Experimental curves are shown in bold, simulated in thin lines. The OER-conditioned state was investigated under *in situ* conditions at 1.2 V in N_2-saturated 0.1M KP_i at pH 7. OER conditioning was performed for 15 min at 1.62 V in the same electrolyte. The Co_3O_4 show the dry state after OER conditioning as shown in Figure 16 and Figure 18.[68] The k^3-weighted EXAFS spectra are shown in Figure A34.

In case of rs-CoO-OER, single diffraction spots could be seen whereas the electron diffraction pattern of CoOOH-OER exhibited a diffuse ring structure. This furthermore shows the higher degree of order and larger domain size of rs-CoO compared to CoOOH also after OER conditioning. In case of w-CoO-OER, the roughening and restructuring of the near-surface of the w-CoO-OER crystallites were accompanied with significant changes in the crystal structure of the pyramidal crystallites (see Figure 33D). The crystal structure transformed from a wurtzite-like crystal structure of the as-prepared state to a structure similar to Co_3O_4 in the OER-conditioned state.

The determined irreversible changes in the morphology and crystal structure of the Co oxides due to OER conditioning indicated irreversible changes in the local atomic structure and Co oxidation state which are identified in the next section using *in situ* XANES and EXAFS analysis of the OER-conditioned Co oxides in the resting state.

Local Atomic Structure and Co Oxidation State

The local atomic structure and mean Co oxidation state of the Co oxides after OER conditioning were investigated at 1.2 V using *in situ* XANES and EXAFS as extracted from XAS measurements recorded at the Co *K*-edge. The XANES spectra of the OER-conditioned Co oxides (Figure 34A) showed that the edge position increased for the rs-, w-CoO and CoOOH. Co_3O_4-OER did not change irreversibly due to OER. The strongest edge shift was determined for CoOOH-OER with +1.7 eV (by the integral method). The absorption edge of w-CoO-OER and rs-CoO-OER shifted by +0.9 and +0.3 eV, respectively. The determined edge shift represents a partial, irreversible oxidation of Co^{2+} to Co^{3+} ions in the Co oxides. The formation of Co^{4+} can be ruled out due to the short lifetime of these states. For Co_3O_4-OER, the mean Co oxidation state did not change.

The irreversible increase of the Co oxidation state of rs-, w-CoO and CoOOH were accompanied by changes in Co bonding environment as determined qualitatively from the FT of the EXAFS spectra (Figure 34B) and quantitatively from the results of simulation of the EXAFS spectra (Table 4 and Figure A34). In case of CoOOH-OER, the strong edge shift was accompanied by a significant increase in intensity of the Co-O and Co-Co peaks in the FT of EXAFS spectra.

Table 4: Results of simulation of the EXAFS spectra of Co_3O_4, rs-CoO, w-CoO, and CoOOH at 1.2 V after OER-conditioning. The differences between as-prepared state and the state at 1.2 V are given. In case of rs-, w-CoO and CoOOH after OER conditioning was perform prior to the XAS experiments. The experimental and simulated spectra are shown in Figure A34 and the complete fitting results in Table 10.

Distance	Sample	N	ΔN	R / Å	ΔR_{mean} / Å	σ / Å
Co-O	Co_3O_4	5.4 ± 0.2	+0.1	1.908 ± 0.001	0	0.046 ± 0.002
	rs-CoO	1.7 ± 0.4 2.0 ± 0.4	+1.3 -2.4	1.985 ± 0.020 2.135 ± 0.008	-0.02	0.061 ± 0.007
	w-CoO	3.9 ± 0.6	+0.7	1.932 ± 0.014	-0.04	0.049 ± 0.010
	CoOOH	5.0 ± 2.1	+1.4	1.906 ± 0.023	+0.02	0.03 ± 0.03
Co-Co 1	Co_3O_4	4.7 ± 0.2	±0.0	2.851 ± 0.001	±0.00	0.052 ± 0.001
	rs-CoO	1.4 ± 0.4 10.6 ± 0.6	+1.4 -1.6	2.875 ± 0.009 3.003 ± 0.002	-0.01	0.032 ± 0.016 0.077 ± 0.009
	w-CoO	2.6 ± 1.7 3.0 ± 2.3	+2.6 -3.3	2.840 ± 0.020 3.185 ± 0.080	-0.20	0.077 ± 0.017
	CoOOH	4.2 ± 3.1	+2.6	2.840 ± 0.023	+0.02	0.060 ± 0.030
Co-Co 2	Co_3O_4	7.0 ± 0.3	±0.0	3.357 ± 0.001		0.052 ± 0.001
	rs-CoO	0.0 ± 0.7	±0.0	3.350 ± 0.000		0.077 ± 0.009
	w-CoO	3.6 ± 3.4	+3.6	3.351 ± 0.048		0.071 ± 0.010

This increase can be explained by an increase of the coordination numbers of Co-O and di-μ-oxo bridges from 3.0 to 5.0 and, respectively, 1.6 to 4.2. The length of the two distances did not change significantly and was the shortest of the investigated Co oxides also in the conditioned state.

Thus, the Co bonding environment showed an even stronger confinement to Co^{3+} O_h ions after OER conditioning which was in agreement with the higher mean Co oxidation state and the beginning crystallization of the CoOOH-OER as determined by TEM. However, CoOOH-OER remained an X-ray amorphous $CoO_x(OH)_y$ with mainly di-μ-oxo bridged Co^{3+} O_h ions. Furthermore, it has to be noted that the structural analysis was performed under *in situ* conditions cathodic of the Co^{2+}/Co^{3+} redox transition and thus, a reversible structural change of the bulk between a layered CoOOH to a layered $Co(OH)_2$ can be ruled out.

In case of the rs-CoO-OER, only slight irreversible changes in the Co oxidation state and local atomic structure could be determined. After OER conditioning, the number of shorter Co^{3+}-O increased and di-μ-oxo Co^{3+}-Co^{3+} distances had formed while the number of the Co^{2+}-O distances with 2.13 Å and di-μ-oxo bridges between pairs of Co^{2+} O_h with 3.00 Å decreased. Thus, only a slight fraction of the Co^{2+} ions in rs-CoO-OER got irreversibly oxidized during OER conditioning and thus, led to a slight fraction of di-μ-oxo bridged Co^{3+} O_h ions. Generally, the low degree of changes in coordination number of the two shorter distances and the comparably low shift of the Co *K*-edge showed that only a slight fraction of the Co ions in rs-CoO-OER changed.

In case of w-CoO-OER, the position and intensity of the peaks representing the Co-O and Co-Co distance changed significantly due to OER conditioning. The Co-O distance was simulated using a single distance representing the mean length of the Co-O bond. This distance shifted by approx. -4 pm to 1.93 Å after OER conditioning. The first Co-Co distance was found at ~2.84 Å which is typical for di-μ-oxo bridged Co^{3+} O_h ions. However, not all Co^{2+} T_d ions in w-CoO-OER got oxidized and changed their coordination because mono-μ-oxo bridged Co^{2+} T_d ions retained and the mean Co-O distance remained longer in the OER-conditioned state than found for pure Co^{3+} O_h structures e.g. in CoOOH-OER and Co_3O_4-OER. Furthermore, the Co *K*-edge of w-CoO-OER shifted by less than 2 eV which would have been the case if all Co ions had increased their oxidation state by +1. Thus, the majority of the Co^{2+} T_d ions in w-CoO-OER transformed irreversibly to Co^{3+} O_h ions.

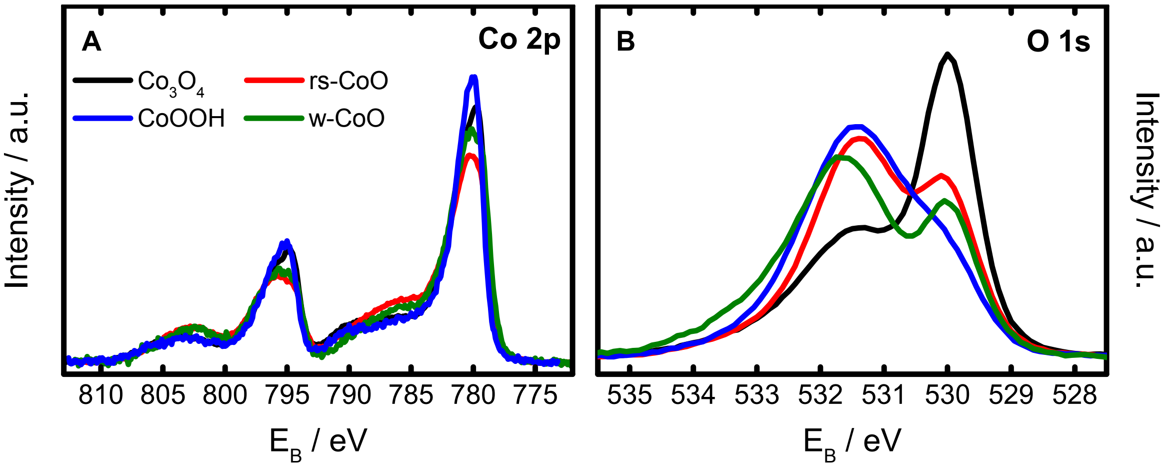

Figure 35: Co 2p (A) and O 1s (B) X-ray photoelectron spectra of the OER-conditioned state of Co_3O_4(black), rs-CoO(red), w-CoO(green), and CoOOH(blue) recorded at a kinetic energy of the photoelectrons of 550 eV. OER conditioning was performed for 15 min at 1.62 V in N_2-saturated 0.1M KP_i at pH 7.

In addition, the presence of Co-Co distances with ~3.35 Å indicated Co^{2+} T_d ions incorporated in the normal spinel structure. However, no clear statement regarding the presence of a spinel phase could be made from the EXAFS simulations due to the large fit error. The local atomic structure of the bulk of w-CoO-OER was similar to Co_3O_4 as seen in SAED pattern (see Figure 33D).

Thus, the irreversible changes in the Co oxidation state and in the local atomic structure of the initially Co^{2+} oxides and of the CoOOH led to structures similar to a $CoO_x(OH)_y$ with primarily di-μ-oxo bridged Co^{3+} O_h ions although to a very different degree. At 1.2 V, CoOOH-OER exhibited almost ideal Co oxyhydroxide structure; w-CoO-OER exhibited primarily the $Co^{3+}O_x(OH)_y$ structure whereas in case of rs-CoO-OER only a slight fraction of the material changed. In case of the w-CoO-OER, a $CoO_x(OH)_y$ similar to the spinel structure possibly with only very limited occupancy of the tetrahedral sites could have been formed. In the next section, the determined bulk structure of the OER-conditioned Co oxides are compared with structure and composition of the near-surface of the Co oxides.

Near-Surface Chemical State and Composition

Figure 35A and B shows the XP spectra in the Co 2p and O 1s region of the OER-conditioned state of the four Co oxides. The Co 2p spectra showed two main peaks at ~780 and ~795 eV corresponding to the Co $2p_{3/2}$ and Co $2p_{1/2}$ spin-orbit split states, respectively. The presence of

Co^{2+} and Co^{3+} ions in the near-surface can be estimated from satellite features at ~786 eV and ~790 eV, respectively.[33]

The oxidation and structural change of the initially Co^{2+} oxides determined in the bulk was also present in the near-surface region. In case of rs- and w-CoO-OER, the distinct satellite feature at ~786 eV in the as-prepared state decreased significantly in the OER-conditioned state although it did not disappear completely. Co_3O_4-OER did not show a change in Co 2p spectra induced by OER whereas for CoOOH-OER the slight Co^{2+} satellite feature present in the as-prepared state decreased. Thus, the chemical state of the Co ions the near-surface region of the Co oxides in the OER-conditioned state unified to a stronger degree than it was found for the bulk local atomic structure.

The O 1s spectra in Figure 35B showed the presence of at least three different oxygen species in the near-surface region of the Co oxides after OER conditioning. All four Co oxides exhibited a decrease in lattice oxygen peak height compared to the as-prepared state although the decrease in lattice oxygen of Co_3O_4-OER was very low.

Table 5: Surface composition of Co_3O_4, rs-CoO, w-CoO, and CoOOH in the as-prepared and OER-conditioned state as extracted from peak fitting of XPS Co 2p, O 1s, and P 2p spectra. OER conditioning was performed for 15 min at 1.62 V in 0.1M KP_i.

Sample	O/Co ratio		Fraction of Lattice-O		Lattice-O/Co ratio		P/Co ratio
	ASP	OER	ASP	OER	ASP	OER	OER
Co_3O_4	1.48	1.57	0.54	0.50	0.83	0.79	0.05
rs-CoO	1.15	2.00	0.59	0.28	0.68	0.56	0.43
w-CoO	1.20	2.33	0.59	0.23	0.71	0.54	0.39
CoOOH	2.40	2.68	0.27	0.14	0.65	0.40	0.28

Simultaneously, the peak height of hydroxyl contribution increased due to OER. The surface composition of the Co oxides was extracted from peak fits (see Figure A37) and is shown in Table 5. Firstly, the O/Co ratio increased slightly for Co_3O_4-OER and CoOOH-OER and significantly for rs- and w-CoO-OER. This increase was caused *inter alia* by the increased Co oxidation state in the near-surface, by the smaller domain size in case of w-CoO-OER compared to its as-prepared state, and by O-containing adsorbates. Furthermore, the fraction of lattice oxygen decreased to 0.50 and 0.14 for Co_3O_4-OER and CoOOH-OER, respectively.

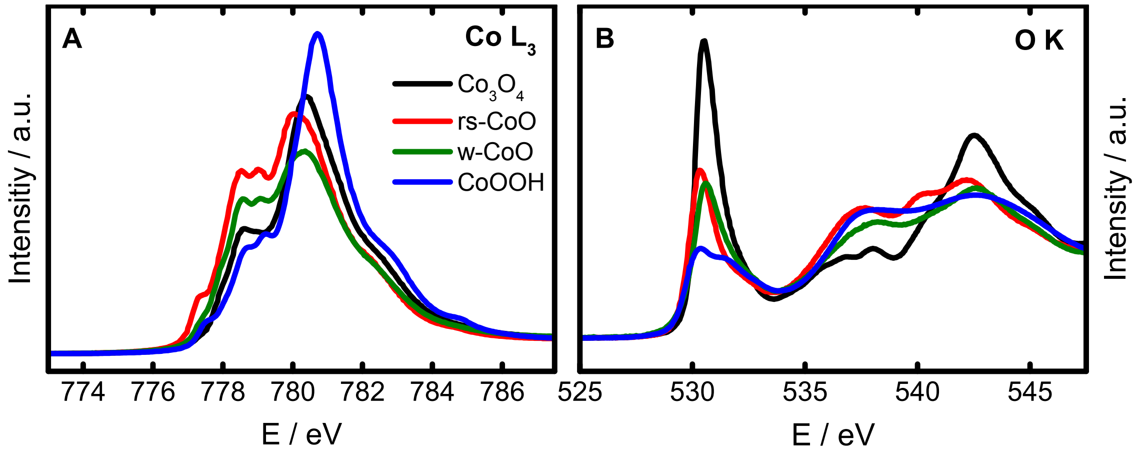

Figure 36: Co L_3 (A) and O K (B) XANES spectra of the OER-conditioned state of Co_3O_4(black), rs-CoO(red), w-CoO(green), and CoOOH(blue) recorded in total electron yield mode. OER conditioning was performed for 15 min at 1.62 V in N_2-saturated 0.1M KP_i at pH 7.

For w- and rs-CoO-OER, the fraction of lattice oxygen decreased significantly from 0.59 to 0.23 and 0.28, respectively. The decrease in lattice oxygen was accompanied by an increase of protonated oxygen ions. The formation of protonated O sites can be caused by three effects: surface hydroxylation, increase of cationic defects leading to charge compensation via protonation of adjacent O sites and by incorporation/adsorption of phosphates.

Table 5 shows that the P/Co ratio in the near-surface after OER conditioning depended on the initial Co oxidation state and coordination. The binding energy of P 2p was in agreement with P ions in phosphate groups.[33] For Co_3O_4-OER, the P/Co ratio is less than 0.1 whereas for rs- and w-CoO-OER the P/Co ratio was significantly larger with ~0.4. CoOOH-OER exhibited a P/Co ratio of 0.28 but a higher K/Co ratio (0.14) compared to the other Co oxides indicating that remnant electrolyte caused the higher P/Co ratio and the strong decrease in fraction of lattice-O species rather than adsorbed phosphates.

It has to be noted that the determined increase in O/Co ratio cannot directly be related to the increase in Co oxidation state because it is unlikely that all oxygen atoms from the phosphate groups are linked to Co ions. Thus, complementary investigations using XANES recorded at the Co L_3- and O K-edge were necessary to investigate the influence of structural transformation on the surface chemical state of Co and O ions.

Electronic Structure

Figure 36A and B show the XANES spectra of the four Co oxides in the OER-conditioned state recorded at the Co L_3- and O K-edge, respectively. In line with the results from XPS the Co L_3-edge position increased for rs- and w-CoO-OER whereas it did not change for

Co_3O_4-OER and CoOOH-OER. The peak positions in the Co L_3 XANES spectra in the OER-conditioned state are rather similar, the lowest was observed for rs-CoO-OER with 780 eV and the highest for CoOOH-OER with 780.7 eV. w-CoO-OER and Co_3O_4-OER exhibited their maximum at 780.35 and 780.4 eV, respectively. The position of the typical Co^{2+} O_h feature increased by ~0.2 eV and decreased slightly in intensity for CoOOH-OER and strongly for rs-CoO-OER. This indicated the (reduced) presence of high spin $Co^{2+/3+}$ ions in the near-surface of rs-CoO and CoOOH after OER conditioning. In case of w-CoO, the typical Co^{2+} O_h feature was absent in the as-prepared and OER-conditioned state.

Linear combination fitting of the Co L_3 XANES spectra of rs-CoO-OER and w-CoO-OER with reference spectra revealed that in both cases Co^{2+} with their initial coordination were still present in the near-surface. The spectrum of the as-prepared Co_3O_4 was chosen as secondary fit component although this does not necessarily reflect the local atomic structure. This leads to a composition of rs-CoO-OER of 50.5% Co ions in Co_3O_4, 15.4% CoOOH, 23.7% Co^{2+} O_h and 10.3% Co^{2+} T_d and w-CoO-OER consisted of 70% Co ions in Co_3O_4 and 30% Co^{2+} T_d. In case of CoOOH-OER, a composition of 80% as-prepared CoOOH and 20% Co ions in Co_3O_4 was determined (see Figure A38).

The O *K* XANES spectra of the Co oxides after OER conditioning are shown in Figure 36B. Obviously, the unified coordination and oxidation state of the Co ions in the near-surface after OER conditioning led to a unification of the pre-edge feature of their O *K* XANES spectra. The pre-edge feature of all four Co oxides exhibited a principal maximum between 530.3 and 530.6 eV which was previously assigned to electronic transitions into O states in which Co^{3+} O_h ions in low-spin configuration are involved.

The intensity of the principal maximum increased from CoOOH-OER via w- and rs-CoO-OER to Co_3O_4-OER. The strong contributions from O states related to Co^{2+} O_h and T_d ions decreased significantly but all Co oxides showed secondary contributions above the principal maximum. The strongest secondary contribution was present in the pre-edge of CoOOH-OER in which a shoulder ~1 eV above the maximum was present. The position of this state is too low to be caused by electron transitions in which Co^{2+} ions were involved and is thus, also assigned to electronic states related to Co^{3+} O_h ions. The origin of this state is discussed later in more detail. This additional state was also seen in the as-prepared state of rs-CoO (see Figure 26B) and might also be present in Co_3O_4, rs-, and w-CoO-OER but at low intensity. The contribution above 532 eV might involve O orbitals hybridized with Co^{2+} 3d or P orbitals.[181]

Below 530 eV, a tailing of the pre-edge feature can be seen which is lowest for Co_3O_4 and follows the presence of the high spin Co O_h as determined form the Co L_3 XANES spectra of the other three Co oxides (see Figure 36A and Figure A39).

Peak fitting of the O K pre-edge feature was performed to quantify the differences in O states and orbital hybridization. In the fit procedure, four Gaussian components were used and a linear rise of the pre-edge background assumed (see Figure A40). The peak at lowest energy had to be fitted by two components between 530.1 and 530.8 eV. The third component was located approximately ~1 eV higher whereas the 4th component was located between 532.2 and 532.8 eV. Applying the assignment of peaks in pre-edge of the O *K* XANES spectra of the as-prepared state with the spectra of the OER-conditioned state showed that Peak 1 and 2 are caused by electron transition into orbitals involving Co^{3+} O_h ions in low spin configuration. Thus, the degree of orbital hybridization between low-spin Co^{3+} O_h ions and O ions was estimated from the area of peak 1+2 and it decreased in the order Co_3O_4-OER > w-CoO-OER > rs-CoO-OER > CoOOH-OER. The degree of orbital hybridization of low spin Co^{3+} and O ions can be seen (in analogy to the lattice-O/Co ratio) as a measure of structural order.

Thus, the investigation of the electronic structure of the OER-conditioned Co oxides revealed a strong unification. This finding was in agreement with the structural analysis showing the irreversible formation of very similar structural motifs due to OER in neutral, phosphate-containing electrolyte. The irreversible changes indicate a common OER-active state of the four Co oxides in neutral, phosphate-containing electrolyte. Furthermore, it could be seen that the fraction of low-spin Co^{3+} ions in the near-surface differ strongly between the Co oxides. In the next section, the results regarding the local atomic structure and Co oxidation state during OER are presented.

6.2.4 Local Atomic Structure and Co Oxidation State during OER

To determine the local atomic structure and the Co oxidation state of the catalytically active catalyst state after OER conditioning, *in situ* X-ray absorption spectroscopy under OER conditions was performed. Figure 37A shows the Co *K* XANES spectra of the four Co oxides during OER. The edge position, determined via the integral method during OER, was higher for all four Co oxides than that in the resting state at 1.2 V. CoOOH exhibited the largest edge shift with +0.6 eV whereas the absorption edge of the initially Co^{2+} oxides shifted by only +0.1 eV. Co_3O_4 showed an edge position shift of +0.3 eV.

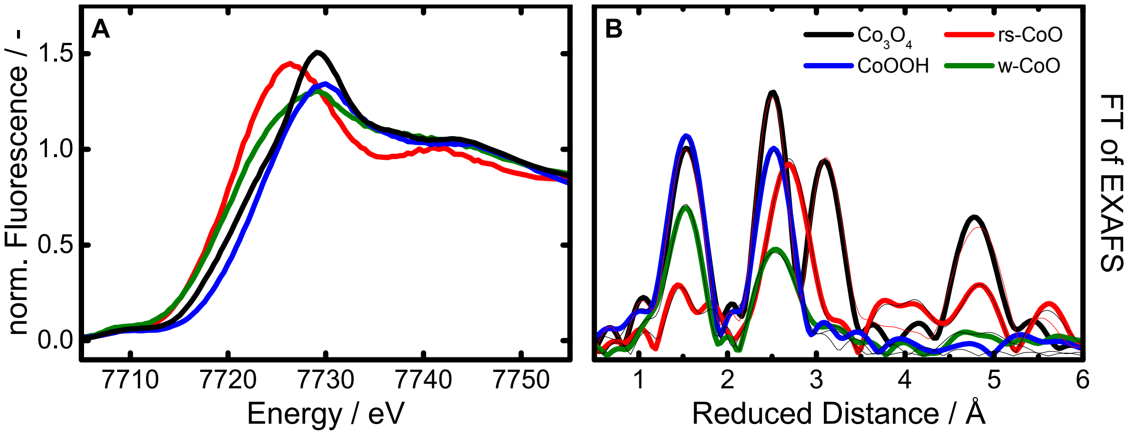

Figure 37: *in situ* XANES (A) and FT of EXAFS (B) spectra of Co_3O_4(black), rs-CoO(red), w-CoO(green), and CoOOH(blue) during OER recorded at the Co K-edge. Experimental curves are shown in bold, simulated in thin lines. The catalytically active state was investigated under *in situ* conditions in N_2-saturated 0.1M KPi at pH 7. The electrode potential was chosen to a current density of 0.5 $mA\cdot cm^{-2}$. Prior an OER conditioning was performed for 15 min at 1.62 V in the same electrolyte. See Chapter 5 for experimental details of Co_3O_4.[68] The k^3-weighted EXAFS spectra are shown in Figure A34.

Thus, the mean Co oxidation state increased strongest for CoOOH and remained rather unchanged for rs- and w-CoO during OER compared to the OER-conditioned state. This behaviour was explained by the different number of redox active Co ions as determined by the cyclic voltammograms (Figure 27A). The charge transferred during CV is directly related to the number of redox active Co ions.

Combining these results, the transferred charge corresponding to electrochemical Co oxidation followed the same trend as the mean Co oxidation state during transition from resting state at 1.2 V to the catalytically active state. During OER anodic of the Co^{3+}/Co^{4+} transition, the presence of Co^{4+} is thermodynamically possible, therefore the increased Co oxidation state during OER could be caused by the presence of Co^{4+} ions.

The determined changes in the Co oxidation state were accompanied by changes in the Co local atomic structure of the four Co oxides during OER as determined qualitatively from the FT of EXAFS spectra (Figure 37B) and quantitatively from simulation of EXAFS spectra (Table 6 and Figure A34). In case of Co_3O_4 the near-surface region of the crystallites was found to transform reversibly to a 3D $CoO_x(OH)_y$ during OER due to change of Co coordination from Co^{2+} T_d to $Co^{3+/4+}$ O_h (see Chapter 5).[68] In case of the other three Co oxides, the Co-O distance was found to decrease after transition to the catalytically active state by ~0.02 Å but the coordination numbers hardly increased above the fit error.

Table 6: Results of simulation of the EXAFS spectra of the catalytically active state of Co_3O_4, rs-CoO, w-CoO, and CoOOH. The spectra were recorded after OER conditioning and the differences between the catalytically active state during OER and the state at 1.2 V are given. The experimental and simulated spectra are shown in Figure A34 and the complete results shown in Table 11. See Chapter 5 for experimental details of Co_3O_4.[68]

Distance	Sample	N	ΔN	R / Å	ΔR_{mean} / Å	σ / Å
Co-O	Co_3O_4	5.4 ± 0.2	±0	1.908 ± 0.001	-	0.046 ± 0.002
	rs-CoO	2.0 ± 0.3 2.4 ± 0.4	+0.3 +0.4	1.950 ± 0.014 2.135 ± 0.008	-0.03 ±0.00	0.067 ± 0.012
	w-CoO	4.0 ± 0.7	+0.1	1.910 ± 0.014	-0.02	0.049 ± 0.010
	CoOOH	5.6 ± 2.2	+0.5	1.887 ± 0.022	-0.02	0.045 ± 0.027
Co-Co	Co_3O_4	5.0 ± 0.2	+0.3	2.851 ± 0.001	-	0.052 ± 0.001
	rs-CoO	1.7 ± 0.4 10.2 ± 0.7	+0.4 -0.4	2.862 ± 0.008 3.003 ± 0.002	-0.01 ±0.00	0.032 ± 0.016 0.077 ± 0.009
	w-CoO	3.2 ± 1.9 2.3 ± 2.1	+0.6 -0.7	2.833 ± 0.022 3.185 ± 0.080	-0.04	0.077 ± 0.017
	CoOOH	4.6 ± 3.0	+0.4	2.830 ± 0.021	-0.01	0.058 ± 0.028
Co-Co	Co_3O_4	6.0 ± 0.3	-1.0	3.357 ± 0.001	-	0.052 ± 0.001
	rs-CoO	0.5 ± 2	+0.5	3.350 ± 0.000	-	0.077 ± 0.009
	w-CoO	2.8 ± 2.9	-0.8	3.351 ± 0.050	-	0.077 ± 0.017

Furthermore, the length of the di-μ-oxo bridges between pairs of $Co^{3+/4+}$ ions decreased during OER for rs-, w-CoO, and CoOOH. Thus, the oxidative conditions during OER led to changes in the Co bonding environment. As already shown for Co_3O_4 the mean oxidation state is higher during OER due to the electrochemical oxidation of the Co ions, possibly up to Co^{4+}. This electrochemical oxidation is accompanied by a decrease in the Co^{3+}-O and Co^{3+}-Co^{3+} distances. This effect was only seen for rs-, w-CoO and CoOOH and thus, for the Co oxide electrocatalysts that exhibited a near-surface with low degree of order after OER conditioning.

In the next section, the results of the extensive characterization of the morphology, local crystal and local atomic structure as well as the near-surface composition and electronic structure of the OER-conditioned state are related to the Co oxide redox electrochemistry. Furthermore, these correlations are referred to the electrocatalytic OER properties of the Co oxides and conclusions drawn guiding towards the identification of the active site and the mechanism of OER on Co oxides.

6.3 Discussion

In this chapter four Co oxide OER electrocatalysts were prepared by spin coating, drop coating of a colloid solution as well as electrodeposition and were extensively investigated with respect to their morphology, crystal and local atomic structure, their Co oxidation state and near-surface properties such as composition and electronic structure. The as-prepared structure differed substantially ranging from crystalline Co^{2+} oxides consisting of either octahedrally or tetrahedrally-coordinated Co ions to the crystalline normal spinel with octahedrally-coordinated Co^{3+} and tetrahedrally-coordinated Co^{2+} ions and an X-ray amorphous CoOOH consisting of Co ions in a Co^{3+} O_h bonding environment. These Co oxides were characterized in the as-prepared state, after OER conditioning and additionally, the structure of the catalytically active state was determined using *in situ* X-ray absorption spectroscopy. The Co oxide redox electrochemistry and its electrocatalytic OER properties were determined in neutral, phosphate-containing and alkaline, phosphate-free electrolyte.

In Chapter 5 a reversible, structural transformation and amorphization of the near-surface of Co_3O_4 crystallites during OER was identified.[68] In this chapter an irreversible structural transformation of the Co^{2+} oxides and the CoOOH during OER towards an amorphous $CoO_x(OH)_y$ consisting of primarily Co^{3+} O_h was determined. The CoOOH showed an as-prepared state with a significant fraction of Co^{2+} ions which were irreversibly oxidized to Co^{3+} during OER conditioning. The Co-O coordination environment and Co-Co cross-linking of the Co^{2+} oxides after OER conditioning was similar to the X-ray amorphous CoCat and CoOOH which can be referred to as a phosphate-free analogue of the CoCat. The degree of structural transformation of the initially Co^{2+} oxides was stronger in the near-surface than in the bulk and was significantly stronger for the wurtzite-like w-CoO compared to rs-CoO exhibiting a defective rocksalt crystal structure in the as-prepared state. The latter crystal structure was found to resist bulk oxidation in the investigated time scale. However, no conclusion regarding long-term resistance against bulk oxidation can be made on the basis of the results of this work. But structural investigation of Co^{2+}-based electrocatalysts after long-time OER in neutral electrolyte points towards a complete oxidation and structural transformation towards the CoCat.[186]

During OER in neutral electrolyte, the structure of all four Co oxides seems to exhibit a universal, catalytically active state although to a different degree. The catalytically active state is independent from the crystalline or amorphous nature of the as-prepared state and consists of predominantly di-μ-oxo bridged $Co^{3+/4+}$ O_h ions and an elevated degree of structural disorder. The Co bonding environment of the Co^{3+} O_h ions in rs-, w-CoO and CoOOH contracts during OER compared to the resting state at 1.2 V. This slight contraction can be explained by the oxidation of the Co^{3+} to Co^{4+} ions during oxygen evolution presumably via deprotonation of μ-OH bridges. This finding is in agreement with the catalytically active state of the amorphous and thus, structurally-flexible CoCat.[114]

Although the Co oxides exhibited unified structural motifs in the catalytically active state, substantial differences in their electrocatalytic properties and Co oxide redox chemistry were found. The Tafel slope and the ratio of the two Co redox features differed substantially between the Co oxides. The beneficial influence of reducible Co^{3+} sites on the Tafel slope was revealed by the electrochemical characterization in neutral and alkaline electrolyte. In neutral electrolyte, the highest fraction of reducible Co^{3+} sites was found in the CoOOH which exhibited a redox behaviour and Tafel slope very similar to the CoCat. In contrast, Co_3O_4 exhibited the lowest fraction of reducible Co^{3+} sites and the highest Tafel slope. rs- and w-CoO exhibited intermediate Tafel slopes and fractions of reducible Co^{3+} sites.

The Tafel slope determined in alkaline electrolyte was found to be significantly lower than in neutral electrolyte. However, it also benefited from a larger number of reducible Co^{3+} sites. The lower Tafel slope in alkaline electrolyte compared to neutral electrolyte is accompanied by an increased overpotential of the onset of OER versus the Co^{2+}/Co^{3+} redox potential. These findings indicate differences in the rate-determining step between neutral and alkaline electrolyte. The higher concentration of OH^- significantly enhances proton abstraction from the OH and OH_2 adsorbates (see Figure A12). Furthermore, the O-O bond formation via nucleophilic attack by OH^- ions might become energetically favoured over the preferred (geminal) coupling of adsorbed O ions as found for neutral electrolytes.[69] However, Fe impurities, commonly found in alkaline electrolytes, are discussed to have significant influence on the OER on Co and Ni oxides and (oxy)hydroxides.[20, 43, 72] It has been shown that the removal of Fe impurities increases the Tafel slope of Co oxyhydroxides in alkaline electrolyte to $\sim 60\ mV \cdot dec^{-1}$. The alkaline electrolyte used in this work was not purified but in contrast to other reports XPS did not reveal accumulation of Fe ions in the near-surface after alkaline OER conditioning.

To reveal the relation between the local atomic and the electronic structure of the near-surface with the OER electrocatalysis in neutral electrolyte the fraction of reducible Co^{3+} sites and the degree of order/structural integrity after OER conditioning were compared. The Co_3O_4 which was crystalline at non-catalytic conditions exhibited the lowest ratio of reducible Co^{3+} sites whereas the X-ray amorphous CoOOH exhibited the highest ratio; w- and rs-CoO showed an intermediate behaviour with an intermediate state of structural disorder and/or restructuring in the near-surface.The degree of structural disorder in the near-surface can also be related to the degree of hybridization between 3d orbitals of low-spin Co^{3+} and 2p orbitals of the O ions of the OER-conditioned Co oxides as determined from the pre-edge feature of the O *K* XANES spectra.

Figure 38 shows that the electrochemical reducibility is anticorrelated and the Tafel slope is correlated to the presence of electronic states related to low-spin Co^{3+} ions. The presence of low-spin Co^{3+} ions is related to the presence of undistorted CoO_6 octahedra in the near-surface and thus, to structural order. Vice versa, this finding points towards the importance of structural disorder leading to the reducible Co^{3+} sites at the surface and to preferable OER electrocatalytic properties. The elevated degree of disorder in the $CoO_x(OH)_y$ domains is related to a lower domain size and to a higher number of defects such as cationic vacancies. Both phenomena decrease the fraction of $O_{\mu 3}$ sites to terminating O and $O_{\mu 2}$ sites and therefore, induce a structural distortion of the CoO_6 bonding symmetry. Bonds between surface Co ions and terminating O are shorter than bonds between Co and bridging O[66, 99] and μ_2-hydroxo bridges between Co^{3+} ions are longer than μ_3-oxo bridges.[70] A symmetrical CoO_6 bonding environment is thus, primarily present in the bulk and on special surface planes such as CoOOH(001) and Co_3O_4(111) surfaces as well as within the CoO_6 layer fragments of the CoCat. The distortion of the CoO_6 bonding environment has significant influence on the electronic structure because it splits the energy of the degenerate e_g states of Co ions as found by combined experimental and computational studies.[96, 98] This splitting changes the Co^{3+} spin state from low to intermediate or high spin configuration and can also explain the splitting of the O *K* pre-edge feature of the X-ray amorphous CoOOH (see Figure 36). The significant contribution of an electronic state which is present ~1 eV above the dominant O state related to low spin Co^{3+} ions can be explained by the higher state of the energetically separated e_g orbitals. An intermediate contribution of low-spin Co^{3+} ions was found for rs- and w-CoO-OER.

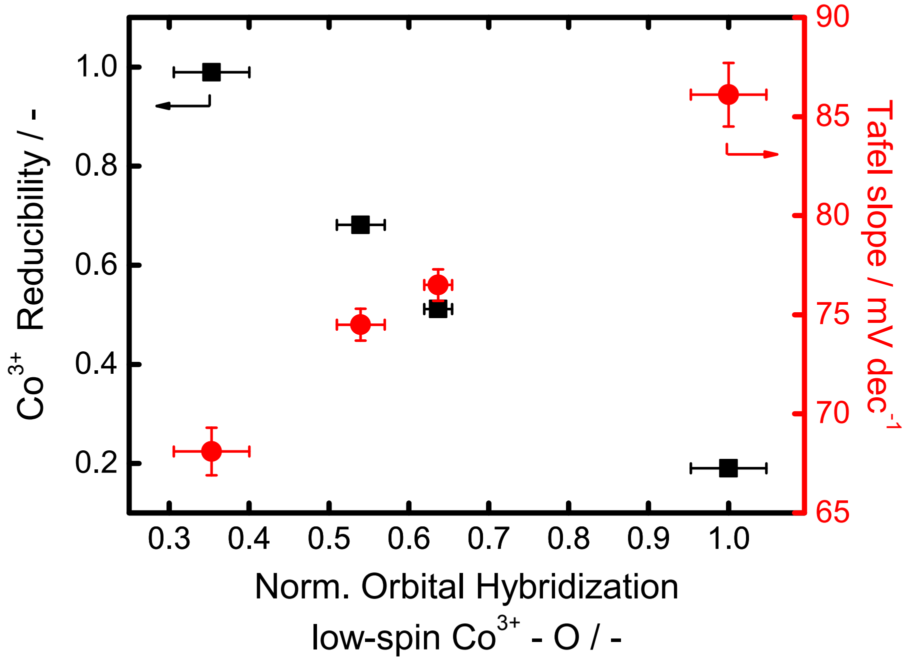

Figure 38: Co oxide reducibility (black squares) and Tafel slope (red circles) in 0.1M KP_i at pH 7 as function of the normalized of hybridization between the 3d orbitals of low-spin Co^{3+} O_h ions and O 2p orbitals. The reducibility of the Co oxides was determined from the peak current ratio of C1 and C2 as extracted from the cyclic voltammograms as shown in Figure 27A and Figure A36. The Tafel slope was determined from quasi-stationary anodic potential step experiments as shown in Figure 27B. The normalized degree of orbital hybridization was estimated from area of the O *K* pre-edge feature according to electron transitions at ~530.5 eV and normalized with the peak area of Co_3O_4. The peak area was determined by fits as shown in Figure A40.

Furthermore, the tailing of the low energy side of O *K* pre-edge feature indicates the presence of unoccupied t_{2g} states of high-spin Co^{3+} ions. The low hybridization of the O 2p with low spin Co^{3+} 3d orbitals and the different spin configuration cannot be explained by a layered CoOOH because the crystalline, layered $LiCoO_2$ exhibited a similar pre-edge feature as the crystalline Co_3O_4 of this work.[187] Simultaneously, the participation of Co sites within the bulk and layers cannot explain the elevated reducibility because crystalline, layered $Co(OH)_2$ exhibited similar redox behaviour in neutral electrolyte as the crystalline Co_3O_4 with primarily one redox couple at ~1.6 V.[188-189]

However, the direct quantification of the Co^{3+} O_h ions in intermediate or high spin configuration on the surface is difficult due to the presence of remnant Co^{2+} ions, (adsorbed) phosphates and an elevated information depth of up to 10 nm. Furthermore, extensive DFT calculations of the O *K* XANES spectra of bulk and surface Co and O ions are necessary to completely understand the electronic structure. But the data of this work show that the reducibility of the Co^{3+} ions is correlated to a lower number of O sites related to low-spin Co^{3+} ions and thus, to a special CoO_6 configuration which can be explained to a higher degree of structural disorder in the catalytically-relevant near-surface.

The electrochemical reducibility of Co^{3+} ions can also be related to their CoO_6 bonding environment and a higher number of terminating O (O^T) sites. The intermediate and high spin Co^{3+} ions are specially coordinated and thus, reducible in contrast to the low spin Co^{3+} O_h ions with ideal octahedral bonding symmetry. The low-spin Co^{3+} O_h ions are connected via di-μ_3-O(H) bridges as shown in Figure 2. These Co^{3+} sites can be oxidized via deprotonation of the μ_3-OH bridges but are not electrochemically reducible to Co^{2+} via secondary protonation of μ_3-oxo bridges. In contrast, the intermediate and high spin Co^{3+} sites can be electrochemically reduced via protonation of the μ_2-oxo bridges and protonation of O^T sites leading to surface hydroxyls. These special coordinated Co sites are present at edges and steps of the surface planes of the $CoO_x(OH)_y$ domains.

The electrochemical reducibility of these special coordinated Co^{3+} sites has a beneficial influence on the OER electrocatalysis. These sites can possibly act as catalytically active site for OER as described in the following. Due to the high fraction of terminating O these surface Co ions exhibit (multiple) adsorption sites for H_2O which is the reagent of oxygen evolution in acidic and neutral electrolyte. Furthermore, the presence of multiple terminating O ions is highly beneficial for O-O bond formation via geminal coupling of adsorbed O ions and O_2 release. Geminal coupling of adsorbed O atoms has been found to be energetically preferred over nucleophilic attack on Co oxide in neutral electrolyte especially if more than one terminating O site per Co ion is present.[69] The *rate-determining step* of OER on Co oxide in neutral electrolyte is thought to be a chemical step which is preceded by a coupled proton/electron transfer step in equilibrium.[56, 183] Thus, O-O bond formation (or O_2 release) is the *rate-determining step* and in this mechanistic framework an ideal Tafel slope of ~59 $mV \cdot dec^{-1}$ is found. The deviation of the Tafel slope obtained for the Co oxides from this value (determined from anodic potential step experiments) can be related to the fraction of bridging O in the near-surface. A larger fraction of bridging O and lower fraction of terminating O lead to a higher Tafel slope because bridging O have to participate in the OER mechanism especially at elevated oxygen evolution rates. But O_2 evolution from bridging O is slower e.g. due to the higher formation energy of O vacancies at the surface because the formation energy increases from O^T via $O_{\mu 2}$ to $O_{\mu 3}$ sites.[67] Thus, the *rate-determining step* is hampered which leads to a higher Tafel slope with increasing degree of structural order. This additional process cannot be caused by charge transfer processes following Ohm's law because it depends on the overpotential exponentially and not linearly. According to Butler-Volmer equation, a higher number of active sites would not lead to a lower Tafel slope but would only change the exchange current density. Furthermore, O vacancies in the reaction zone can induce structural transformation of the near-surface of Co oxides as found by DFT calculations[67] and as shown by the growth of the $CoO_x(OH)_y$ reaction zone into the crystalline Co_3O_4.[68] Thus, the Tafel slope as determined from anodic potential step experiments might (also) reflect the degree of structural transformation of the near-surface induced by participation of bridging O in OER and thus, the formation of the disordered reaction zone for OER. The Tafel slope as determined from cathodic potential step experiments has been found to be lower for the crystalline Co_3O_4 which can be explained by the formation of a larger reaction zone at higher oxygen evolution rates leading to almost optimal Tafel slope within this mechanistic framework. (see Figure A24)

Thus, fast and slow OER sites are present at the surface of the $CoO_x(OH)_y$. At the fast OER sites the surface Co ion are reducible and predominantly terminating O atoms participate in the reaction mechanism. At slow OER sites, the Co^{3+} ions might be irreducible and/or bridging O are needed to form O_2. This finding is in agreement with the presence of two surface species on a Co_3O_4 during photocatalytic water oxidation in neutral, phosphate-containing electrolyte which exhibit different kinetics.[62] The authors concluded from *in situ* step-scan FTIR spectra that two adjacent, electronically-coupled Co^{4+} sites exhibit fast OER kinetics. The slow kinetics were attributed to single Co sites leading to $Co^{4+}{=}O$ at which formation of O_2 molecules is hampered. However, the authors did not specify how and in which ratio these sites are present on the catalyst surface. Following the results of the near-surface structure, the Co oxide redox electrochemistry and electrocatalysis in the same electrolyte the fast OER site can be assigned to the reducible, μ_2-oxo bridged Co^{3+} sites with possibly more than one O^T sites at which the O-O bond formation via (geminal) coupling is possible. The slow site might be assigned to the irreducible Co^{3+} sites at which O-O bond formation is hampered (or impossible under photocatalytic conditions) due to the necessity of bridging O participation in the OER mechanism.

Furthermore, the spin state of surface Co ions in $LaCoO_3$ and in the layered $LiCoO_2$ has been identified as significant parameter in the evolution of O_2 in electrochemical processes.[110, 190]

It has been argued that the intermediate or high spin state is accompanied by a weaker Co-O bond which leads to elevated O_2 evolution. The lower bond strength enhances desorption of molecular O_2 as discussed above for the O^T and $O_{\mu 2}$ sites. In case of $LiCoO_2$, a higher Co spin state was found for the high-index surface termination (104) which exhibited a higher catalytic activity in alkaline electrolyte according to experimental and computational results.[25, 110]

This finding is also in agreement with the results of this work in which the near-surface structure with elevated degree of structural disorder and higher Co spin state and increased the Co oxide reducibility was found to significantly enhance the OER activity on Co oxide electrocatalysts.

6.4 Summary

In this chapter, structure-activity correlations of Co-based OER electrocatalysts were unravelled using an array of microscopic, diffraction and spectroscopic methods. Therefore, four distinctly-different Co oxides and oxyhydroxides were synthesized and their physicochemical properties extensively investigated in as-prepared state and after OER. Additionally, the local atomic structure of the OER-conditioned and catalytically active state was determined using *in situ* X-ray absorption spectroscopy.

A strong correlation between the near-surface (electronic) structure, the Co oxide redox electrochemistry and the electrocatalytic properties was unravelled. The presence of electrochemically-reducible Co^{3+} sites is highly beneficial for the OER electrocatalysis in neutral and alkaline electrolyte. These Co sites in the near-surface of the $CoO_x(OH)_y$ domains exhibit distinct differences in their electronic structure which can be explained by a distortion of the octahedral bonding environment. This distortion is due to differences in the Co-O bond length of terminating O sites and μ_2-(hydr)oxo bridges. The identification of their electrochemical and spectroscopic fingerprints allows the discrimination against the electrochemically-irreducible Co^{3+} ions which exhibit symmetric octahedral bonding environment and are connected via μ_3-oxo bridges. The presence of these reducible Co^{3+} sites is related to the degree of structural disorder e.g. cationic vacancies and low domain size and their catalytic function could be integrated into a mechanistic framework.

In addition, a strong irreversible structural transformation of the Co^{2+} crystallites during OER towards an amorphous $CoO_x(OH)_y$ with a universal structural motif of di-μ-oxo bridged Co^{3+} O_h ions was identified. The oxygen-evolving state of the Co oxide electrocatalysts is stronger oxidized and exhibits a contracted CoO_6 bonding environment. This contraction is expected to be beneficial for the O-O bond formation via (geminal) coupling of adsorbed O atoms during OER. This structure is expected to be related to the structure of the near-surface of the Co_3O_4 crystallites under OER conditions (see Chapter 5).

Thus, universal structural motifs of the catalytically active state of Co-based OER electrocatalysts were determined. Furthermore, important activity-determining properties of Co-based OER electrocatalysts and their electrochemical and spectroscopic fingerprints were successfully identified. These findings might be also valid for other OER electrocatalysts although they still have to be unravelled. These new insights of this work lead to a better understanding of the OER electrocatalysis on 3d transition metal-based electrocatalysts and will therefore help to develop improved electrocatalysts for efficient water electrolysis.

Chapter 7 Summary and Outlook

The aim of this work was to identify structure-activity correlations and the structure of the catalytically active state of 3d transition metal (TM)-based electrocatalysts for oxygen evolution reaction (OER). These TM oxides and oxyhydroxides are promising candidates to realize inexpensive water electrolysis devices for the efficient generation of molecular hydrogen in neutral and alkaline reaction conditions. This hydrogen can serve as chemical storage medium for electricity generated by intermittent renewable energy sources and thus, can enhance the industrial transformation towards a nuclear-free and CO_2-neutral primary energy supply.

In this work structurally-different Co- and Mn-based electrocatalysts were synthesized and extensively characterized in the as-prepared and OER-conditioned state to correlate their physicochemical with their electrochemical and -catalytic properties. These investigations led to the identification of a special TM coordination in the near-surface for elevated OER activity in neutral and alkaline electrolyte. Spectroscopic and electrochemical fingerprints of this activity-determining property were identified. Additionally, an electrochemical setup for *in situ* X-ray studies was realized and applied to determine the local atomic and crystal structure of the catalytically active state of the 3d TM electrocatalysts. The local atomic structure and the crystallinity in the oxygen-evolving state differ from that in the catalytically-silent and/or in the as-prepared state and transform (reversibly) towards di-μ-oxo bridged $TM^{3+/4+}$ ions in an amorphous near-surface. Thus, the results of this work significantly increase the understanding of OER electrocatalysis and emphasize the importance of *in situ* structural investigations.

Specifically, strong similarities in structure-activity correlations of Mn- and Co-based electrocatalysts in neutral electrolyte are illustrated. The importance of special coordination TM sites and octahedral cross-linking is shown for Mn- and Co-based electrocatalysts. These sites are related to TM sites with special coordination in ground state similar to the so-called coordinatively unsaturated (*cus*) sites. It is shown that a Mn oxide with 3D octahedral cross-linking and a crystal structure leading to *cus* sites at selected surface planes exhibits superior OER activity compared to a crystalline layered MnO_x (see Chapter 4). The OER activity of the Co-based electrocatalysts does also benefit from a higher fraction of these special coordinated Co sites in the near-surface (see Chapter 6). The fraction of these sites increases with structural disorder e.g. cationic vacancies and lower domain size leading to a higher fraction of kinks and edges which connect differently terminated surface planes. The importance of these special coordination TM sites for OER is in agreement with findings for other OER catalysts and for other oxidation reactions.[110, 161-162]

The beneficial influence of these special coordination Co sites was found as their electrochemical and spectroscopic fingerprints were identified and compared to their OER activity. These sites excel in their electrochemical reducibility from Co^{3+} state as revealed by their cyclic voltammograms and exhibit pronounced differences in the electronic structure as identified by their O *K* X-ray absorption spectra. Both features are correlated with the catalytic activity as determined by the Tafel slope and therefore, allow the discrimination against the irreducible and presumably catalytically-inactive Co surface sites (see Chapter 6). In case of MnO_x the redox features are not as specific which inhibits the identification of correlations between redox electrochemistry and catalytic activity (see Chapter 4).

These special coordinated sites and their catalytic function can be integrated into a mechanistic framework as they can act as adsorption sites for the OER reagents in the reaction zone of the catalyst. The μ_2-oxo bridges in vicinity enable (or enhance) deprotonation of the reaction intermediates as they are better proton acceptors than μ_3-oxo bridges. Multiple terminating O sites might furthermore enhance the rate-determining step, either O-O bond formation or O_2 release. The importance of proton abstraction by the electrolyte during OER has been exemplarily shown in this work for Mn oxide catalysts (see Chapter 4). At large proton uptake capability (near the acid dissociation constants pK_a's of the buffered electrolyte and at high OH^- concentrations) the proton abstraction is fast and does not hamper the OER rate. But at low buffer capacity (between the pK_a's of the buffer) the proton abstraction is slow and can limit the OER rate. Thus, the proton abstraction by the anions of electrolyte is crucial but does not deteriorate the OER under conventional reaction conditions at high pH and near the pK_a's of the buffered electrolyte.

Furthermore, the results of this work show that the (near-surface) structure of the catalytically-silent or as-prepared state of TM-based electrocatalysts does not necessarily reflect the structure of the oxygen-evolving state. Irreversible changes in TM coordination and cross-linking after OER occur and are induced by the electrochemical oxidation of the TM ions leading to Co^{3+} and Mn^{4+} ions in octahedral coordination. The near-surface of pure Co^{2+} oxides transforms towards $CoO_x(OH)_y$ with elevated degree of structural disorder and di-μ-oxo bridged Co^{3+} O_h ions (see Chapter 6). In case of the 3D cross-linked MnO_x the μ-oxo bridging of the Mn ions partially changes from mono- to di-μ-oxo bridges after OER. Thus, the investigated TM-based electrocatalysts exhibit universal structural motifs with octahedrally-coordinated and di-μ-oxo bridged TM ions and an oxidation state of +3 in case of Co and +4 in case of Mn.

In addition to these irreversible changes, this work unravels structural changes during transition from a catalytically-silent to an oxygen-evolving state. In case of the amorphous

$CoO_x(OH)_y$ domains a contraction of the CoO_6 bonding environment compared to the catalytically-silent state was identified during OER (see Chapter 6) and is in agreement with the structure of the catalytically active state of the CoCat. This contraction is expected to be beneficial for the O-O bond formation from two adsorbed O atoms at the same Co ion. In case of crystalline Co_3O_4 a reversible amorphization of the near-surface of the crystallites was identified at elevated OER rate (see Chapter 5). This structural transformation is accompanied by an electrochemical oxidation as well as by a change in Co coordination from tetrahedral to octahedral. It can be explained by the participation of bridging O from the oxide in the OER mechanism. Thus, OER leads to an amorphous reaction zone on the crystalline core and this effect might represent a universal phenomenon for crystalline OER electrocatalysts. These findings highlight the importance of *in situ* structural investigations of OER electrocatalysts to identify the structure of the oxygen-evolving state as well as to correlate this to the structure of the catalytically-silent and of the as-prepared state.

In summary, the insights of this work lead to a better understanding of the OER electrocatalysis on 3d transition metal-based electrocatalysts, to a new approach towards a unified understanding of heterogeneous water oxidation catalysis and will help to develop improved electrocatalysts for efficient water electrolysis.

However, further investigations on the activity-determining properties and on the catalytically active state of highly-active and –stable OER electrocatalysts are necessary. Especially, the direct confirmation of the TM coordination and electronic structure in the near-surface under operating conditions is a cornerstone in understanding (electrochemical) water splitting and oxygen evolution. Therefore, surface-sensitive X-ray photoelectron and absorption spectroscopy experiments have to be conducted in presence of adsorbed water/electrolyte and under electrode potential control. Several groups are currently working on this topic and first results have already been published.[191-192] These studies could be supported by the application of *in situ* electrochemical TEM which also is under development.[193] The combined *in situ* X-ray diffraction and absorption experiments should be extended to other highly-active and crystalline electrocatalysts like NiFe layered double hydroxides or Ru- and IrO_2 to confirm the universal character of an amorphous reaction zone of crystalline OER catalysts.

Furthermore, the role of lattice O in the OER mechanism has to be deeply investigated to specifically determine the structure of the active site. Therefore, an extensive study on the overpotential-dependent composition of the reaction products during operation in isotope-labelled electrolyte should be conducted for Co- and Mn-based electrocatalysts in neutral electrolyte.[61] The O atoms at the active site would be exchanged by ^{18}O atoms and their spectroscopic identification would lead to further insights into the structure and properties of the active sites. The role of the anionic species in the electrolyte like PO_4^-, SO_4^- on the catalytic mechanism and its interaction with the surface of the electrocatalyst remained largely unknown. The interaction between catalyst and these anions can be determined by *in situ* vibrational spectroscopy studies under catalytic conditions.[194]

The design of improved electrocatalysts has to aim at the formation of a large fraction of these special coordinated TM sites. This can be *inter alia* realized by the introduction of templating agents such as foreign metal ions which can be selectively removed by chemical or electrochemical methods. This dissolution will lead to cationic vacancies and therefore, lead to elevated fraction of active sites[65] or enhance the near-surface amorphization of e.g. Co_3O_4.

Generally, the investigation of the catalysts stability is highly important as it represents another key barrier for their application in commercial electrolyzers. Thus, the structural stabilization of active sites and reduced metal dissolution rate at high catalytic activity is necessary. To realize this property ternary metal oxides have to be considered and possibly new synthesis concepts have to be developed.

Bibliography

[1] T. F. Stocker, D. Qin, G.-K. Plattner, L. V. Alexander, S. K. Allen, N. L. Bindoff, F.-M. Bréon, J. A. Church, U. Cubasch, S. Emori, P. Forster, P. Friedlingstein, N. Gillett, J. M. Gregory, D. L. Hartmann, E. Jansen, B. Kirtman, R. Knutti, K. K. Kumar, P. Lemke, J. Marotzke, V. Masson-Delmotte, G. A. Meehl, I. I. Mokhov, S. Piao, V. Ramaswamy, D. Randall, M. Rhein, M. Rojas, C. Sabine, D. Shindell, L. D. Talley, D. G. Vaughan, S.-P. Xie, in *Climate Change 2013: The Physical Science Basis. Contribution of Working Group I to the Fifth Assessment Report of the Intergovernmental Panel on Climate Change* (Eds.: T. F. Stocker, D. Qin, G.-K. Plattner, M. Tignor, S. K. Allen, J. Boschung, A. Nauels, Y. Xia, V. Bex, P. M. Midgley), Cambridge University Press, Cambridge, United Kingdom and New York, NY, USA., **2013**

[2] *BP Statistical Review of World Energy June 2015*, **2015**.

[3] P. C. K. Vesborg, T. F. Jaramillo, *RSC Advances* **2012**, *2*, 7933-7947.

[4] M. Meinshausen, N. Meinshausen, W. Hare, S. C. B. Raper, K. Frieler, R. Knutti, D. J. Frame, M. R. Allen, *Nature* **2009**, *458*, 1158-1162.

[5] H. B. Gray, *Nature Chemistry* **2009**, *1*, 7-7.

[6] N. S. Lewis, D. G. Nocera, *Proceedings of the National Academy of Sciences* **2006**, *103*, 15729-15735.

[7] F. Díaz-González, A. Sumper, O. Gomis-Bellmunt, R. Villafáfila-Robles, *Renewable and Sustainable Energy Reviews* **2012**, *16*, 2154-2171.

[8] M. Carmo, D. L. Fritz, J. Mergel, D. Stolten, *International Journal of Hydrogen Energy* **2013**, *38*, 4901-4934.

[9] O. Gröger, H. A. Gasteiger, J.-P. Suchsland, *Journal of The Electrochemical Society* **2015**, *162*, A2605-A2622.

[10] R. de Levie, *Journal of Electroanalytical Chemistry* **1999**, *476*, 92-93.

[11] U. Bossel, *The Birth of the Fuel Cell*, European Fuel Cell Forum, Oberrohrdorf, **2000**.

[12] J. Larminie, A. Dicks, *Fuel Cell Systems Explained*, John Wiley & Sons, Ltd,. **2013**.

[13] S. Cherevko, A. R. Zeradjanin, A. A. Topalov, N. Kulyk, I. Katsounaros, K. J. J. Mayrhofer, *ChemCatChem* **2014**, *6*, 2219-2223.

[14] H. B. Beer, *Journal of The Electrochemical Society* **1980**, *127*, 303C-307C.

[15] S. Trasatti, *Electrochimica Acta* **2000**, *45*, 2377-2385.

[16] M. Pourbaix, *Atlas d'équilibres électrochimiques*, Gauthier-Villars, Paris, **1963**.

[17] C. H. Hamann, W. Vielstich, *Elektrochemie*, 4th ed., Wiley-VCH, Weinheim, **2005**.

[18] E. Gileadi, *Electrode kinetics for Chemists, Chemical Engineer and Material Scientists*, VCH, **1993**.

[19] A. G. Scheuermann, J. D. Prange, M. Gunji, C. E. D. Chidsey, P. C. McIntyre, *Energy & Environmental Science* **2013**, *6*, 2487-2487.

[20] W. T. Hong, M. Risch, K. A. Stoerzinger, A. Grimaud, J. Suntivich, Y. Shao-Horn, *Energy & Environmental Science* **2015**, *8*, 1404-1427.

[21] J. Rossmeisl, A. Logadottir, J. K. Nørskov, *Chemical Physics* **2005**, *319*, 178-184.

[22] J. Rossmeisl, Z. W. Qu, H. Zhu, G. J. Kroes, J. K. Nørskov, *Journal of Electroanalytical Chemistry* **2007**, *607*, 83-89.

[23] I. C. Man, H.-Y. Su, F. Calle-Vallejo, H. A. Hansen, J. I. Martínez, N. G. Inoglu, J. Kitchin, T. F. Jaramillo, J. K. Nørskov, J. Rossmeisl, *ChemCatChem* **2011**, *3*, 1159-1165.

[24] M. García-Mota, M. Bajdich, V. Viswanathan, A. Vojvodic, A. T. Bell, J. K. Nørskov, *The Journal of Physical Chemistry C* **2012**, *116*, 21077-21082.

[25] M. Bajdich, M. Garcia-Mota, A. Vojvodic, J. K. Norskov, A. T. Bell, *Journal of the American Chemical Society* **2013**, *135*, 13521-13530.

[26] S. Trasatti, *Electrochimica Acta* **1984**, *29*, 1503-1512.

[27] J. O. Bockris, T. Otagawa, *The Journal of Physical Chemistry* **1983**, *87*, 2960-2971.

[28] P. Rüetschi, P. Delahay, *The Journal of Chemical Physics* **1955**, *23*, 556-560.

[29] H. Dau, C. Limberg, T. Reier, M. Risch, S. Roggan, P. Strasser, *ChemCatChem* **2010**, *2*, 724-761.

[30] N. B. Halck, V. Petrykin, P. Krtil, J. Rossmeisl, *Physical Chemistry Chemical Physics* **2014**, *16*, 13682-13688.

[31] J. Rossmeisl, K. Dimitrievski, P. Siegbahn, J. K. Nørskov, *The Journal of Physical Chemistry C* **2007**, *111*, 18821-18823.

[32] L. C. Seitz, T. J. P. Hersbach, D. Nordlund, T. F. Jaramillo, *The Journal of Physical Chemistry Letters* **2015**, *6*, 4178-4183.

[33] B. S. Yeo, A. T. Bell, *Journal of the American Chemical Society* **2011**, *133*, 5587-5593.

[34] R. Frydendal, M. Busch, N. B. Halck, E. A. Paoli, P. Krtil, I. Chorkendorff, J. Rossmeisl, *ChemCatChem* **2015**, *7*, 149-154.

[35] J. Suntivich, K. J. May, H. A. Gasteiger, J. B. Goodenough, Y. Shao-Horn, *Science* **2011**, *334*, 1383-1385.

[36] J. Suntivich, W. T. Hong, Y.-L. Lee, J. M. Rondinelli, W. Yang, J. B. Goodenough, B. Dabrowski, J. W. Freeland, Y. Shao-Horn, *The Journal of Physical Chemistry C* **2014**, *118*, 1856-1863.

[37] R. Subbaraman, D. Tripkovic, K.-C. Chang, D. Strmcnik, A. P. Paulikas, P. Hirunsit, M. Chan, J. Greeley, V. Stamenkovic, N. M. Markovic, *Nature Materials* **2012**, *11*, 550-557.

[38] P. Strasser, S. Koh, T. Anniyev, J. Greeley, K. More, C. Yu, Z. Liu, S. Kaya, D. Nordlund, H. Ogasawara, M. F. Toney, A. Nilsson, *Nature Chemistry* **2010**, *2*, 454-460.

[39] P. A. Cox, *Transition Metal Oxides - An Introduction into their Electronic Structure and Properties, Vol. 27*, Oxford University Press, Oxford, **1995**.

[40] Y. Matsumoto, E. Sato, *Materials Chemistry and Physics* **1986**, *14*, 397-426.

[41] J. van Elp, J. L. Wieland, H. Eskes, P. Kuiper, G. A. Sawatzky, F. M. F. de Groot, T. S. Turner, *Physical Review B* **1991**, *44*, 6090-6103.

[42] M. S. Burke, M. G. Kast, L. Trotochaud, A. M. Smith, S. W. Boettcher, *Journal of the American Chemical Society* **2015**, *137*, 3638-3648.

[43] M. S. Burke, S. Zou, L. J. Enman, J. E. Kellon, C. A. Gabor, E. Pledger, S. W. Boettcher, *The Journal of Physical Chemistry Letters* **2015**, *6*, 3737-3742.

[44] D. N. Mueller, M. L. Machala, H. Bluhm, W. C. Chueh, *Nature Communications* **2015**, *6:6097*.

[45] K. S. W. Sing, D. H. Everett, R. A. W. Haul, L. Moscou, R. A. Pierotti, J. Rouquerol, T. Simieniewska, *Pure and Applied Chemistry* **1985**, *57*, 603-619.

[46] N. R. Sahraie, U. I. Kramm, J. Steinberg, Y. Zhang, A. Thomas, T. Reier, J.-P. Paraknowitsch, P. Strasser, *Nature Communications* **2015**, *6:8618*.

[47] P. Chartier, C. Hitz, J.-F. Koenig, *Electrochimica Acta* **1997**, *42*, 3471-3475.

[48] P. Nkeng, S. Marlier, J.-F. Koenig, P. Chartier, G. Poillerat, J.-L. Gautier, *Electrochimica Acta* **1998**, *43*, 893-898.

[49] T. Binninger, E. Fabbri, R. Kotz, T. J. Schmidt, *Journal of the Electrochemical Society* **2013**, *161*, H121-H128.

[50] S. Rudi, C. Cui, L. Gan, P. Strasser, *Electrocatalysis* **2014**, *5*, 408-418.

[51] C. C. L. McCrory, S. Jung, J. C. Peters, T. F. Jaramillo, *Journal of the American Chemical Society* **2013**, *135*, 16977-16987.

[52] C. Angelinetta, S. Trasatti, L. D. Atanososka, R. T. Atanasoski, *Journal of Electroanalytical Chemistry and Interfacial Electrochemistry* **1986**, *214*, 535-546.

[53] M. Risch, K. Klingan, F. Ringleb, P. Chernev, I. Zaharieva, A. Fischer, H. Dau, *ChemSusChem* **2012**, *5*, 542-549.

[54] J. Willsau, O. Wolter, J. Heitbaum, *Journal of Electroanalytical Chemistry* **1985**, *195*, 299-306.

[55] M. Wohlfahrt-Mehrens, J. Heitbaum, *Journal of Electroanalytical Chemistry* **1987**, *237*, 251-260.

[56] Y. Surendranath, M. W. Kanan, D. G. Nocera, *Journal of the American Chemical Society* **2010**, *132*, 16501-16509.

[57] D. B. Hibbert, *Journal of the Chemical Society, Chemical Communications* **1980**, 202-203.

[58] D. B. Hibbert, C. R. Churchill, *Journal of the Chemical Society, Faraday Transactions 1: Physical Chemistry in Condensed Phases* **1984**, *80*, 1965-1975.

[59] R. Kötz, S. Stucki, D. A. Scherson, D. M. Kolb, *Journal of Electroanalytical Chemistry* **1984**, *172*, 211-219.

[60] S. Fierro, T. Nagel, H. Baltruschat, C. Comninellis, *Electrochemistry Communications* **2007**, *9*, 1969-1974.

[61] K. Macounova, M. Makarova, P. Krtil, *Electrochemistry Communications* **2009**, *11*, 1865-1868.

[62] M. Zhang, M. de Respinis, H. Frei, *Nature Chemistry* **2014**, *6*, 362-367.

[63] T. Binninger, R. Mohamed, K. Waltar, E. Fabbri, P. Levecque, R. Kotz, T. J. Schmidt, *Scientific reports* **2015**, *5*, 12167.

[64] N. Danilovic, R. Subbaraman, K.-C. Chang, S. H. Chang, Y. J. Kang, J. Snyder, A. P. Paulikas, D. Strmcnik, Y.-T. Kim, D. Myers, V. R. Stamenkovic, N. M. Markovic, *The Journal of Physical Chemistry Letters* **2014**, *5*, 2474-2478.

[65] T. Reier, Z. Pawolek, S. Cherevko, M. Bruns, T. Jones, D. Teschner, S. Selve, A. Bergmann, H. N. Nong, R. Schlögl, K. J. J. Mayrhofer, P. Strasser, *Journal of the American Chemical Society* **2015**, *137*, 13031-13040.

[66] Y. D. Kim, A. P. Seitsonen, S. Wendt, J. Wang, C. Fan, K. Jacobi, H. Over, G. Ertl, *The Journal of Physical Chemistry B* **2001**, *105*, 3752-3758.

[67] F. Zasada, W. Piskorz, Z. Sojka, *The Journal of Physical Chemistry C* **2015**, *119*, 19180-19191.

[68] A. Bergmann, E. Martinez-Moreno, D. Teschner, P. Chernev, M. Gliech, J. F. d. Araújo, T. Reier, H. Dau, P. Strasser, *Nature Communications* **2015**, 6:8625.

[69] G. Mattioli, P. Giannozzi, A. Amore Bonapasta, L. Guidoni, *Journal of the American Chemical Society* **2013**, *135*, 15353-15363.

[70] G. Mattioli, M. Risch, A. Amore Bonapasta, H. Dau, L. Guidoni, *Physical Chemistry Chemical Physics* **2011**, *13*, 15437-15441.

[71] U. Diebold, *Surface Science Reports* **2003**, *48*, 53-229.

[72] L. Trotochaud, J. K. Ranney, K. N. Williams, S. W. Boettcher, *Journal of the American Chemical Society* **2012**, *134*, 17253-17261.

[73] L. Trotochaud, S. L. Young, J. K. Ranney, S. W. Boettcher, *Journal of the American Chemical Society* **2014**, *136*, 6744-6753.

[74] D. Friebel, M. W. Louie, M. Bajdich, K. E. Sanwald, Y. Cai, A. M. Wise, M. J. Cheng, D. Sokaras, T. C. Weng, R. Alonso-Mori, R. C. Davis, J. R. Bargar, J. K. Norskov, A. Nilsson, A. T. Bell, *Journal of the American Chemical Society* **2015**, *137*, 1305-1313.

[75] K. J. May, C. E. Carlton, K. A. Stoerzinger, M. Risch, J. Suntivich, Y.-L. Lee, A. Grimaud, Y. Shao-Horn, *The Journal of Physical Chemistry Letters* **2012**, *3*, 3264-3270.

[76] M. Risch, A. Grimaud, K. J. May, K. A. Stoerzinger, T. J. Chen, A. N. Mansour, Y. Shao-Horn, *The Journal of Physical Chemistry C* **2013**, *117*, 8628-8635.

[77] A. Grimaud, K. J. May, C. E. Carlton, Y.-L. Lee, M. Risch, W. T. Hong, J. Zhou, Y. Shao-Horn, *Nature Communications* **2013**, *4:2439.*

[78] M. H. Miles, Y. H. Huang, S. Srinivasan, *Journal of The Electrochemical Society* **1978**, *125*, 1931-1934.

[79] M. Grzelczak, J. Zhang, J. Pfrommer, J. Hartmann, M. Driess, M. Antonietti, X. Wang, *ACS Catalysis* **2013**, *3*, 383-388.

[80] B. Raveau, M. Seikh, *Cobalt Oxides: From Crystal Chemistry to Physics*, Wiley-VCH, Weinheim, **2012**.

[81] W. L. Smith, A. D. Hobson, *Acta Crystallographica Section B Structural Crystallography and Crystal Chemistry* **1973**, *29*, 362-363.

[82] K. E. Sickafus, J. M. Wills, N. W. Grimes, *Journal of the American Chemical Society* **1999**, *82*, 3279-3292.

[83] R. Boggio, A. Carugati, S. Trasatti, *Journal of Applied Electrochemistry* **1987**, *17*, 828-840.

[84] U. D. Wdowik, K. Parlinski, *Physical Review B* **2008**, *77*, 115110.

[85] M. J. Han, J. Yu, *Journal of the Korean Physical Society* **2006**, *48*, 1496-1500.

[86] A. S. Risbud, L. P. Snedeker, M. M. Elcombe, A. K. Cheetham, R. Seshadri, *Chemistry of Materials* **2005**, *17*, 834-838.

[87] W. S. Seo, J. H. Shim, S. J. Oh, E. K. Lee, N. H. Hur, J. T. Park, *Journal of the American Chemical Society* **2005**, *127*, 6188-6189.

[88] K. R. Kittilstved, W. K. Liu, D. R. Gamelin, *Nature Materials* **2006**, *5*, 291-297.

[89] A. I. Khan, D. O'Hare, *Journal of Materials Chemistry* **2002**, *12*, 3191-3198.

[90] M. H. Hey, *Mineralogical magazine* **1962**, *32*, 253-259.

[91] M. Casas-Cabanas, G. Binotto, D. Larcher, A. Lecup, V. Giordani, J. M. Tarascon, *Chemistry of Materials* **2009**, *21*, 1939-1947.

[92] G. Godillot, L. Guerlou-Demourgues, L. Croguennec, K. M. Shaju, C. Delmas, *The Journal of Physical Chemistry C* **2013**, *117*, 9065-9075.

[93] F. Tronel, L. Guerlou-Demourgues, M. Ménétrier, L. Groguennec, L. Goubault, P. Bernard, C. Delmas, *Chemistry of Materials* **2006**, *18*, 5840-5851.

[94] M. W. Haverkort, Z. Hu, J. C. Cezar, T. Burnus, H. Hartmann, M. Reuther, C. Zobel, T. Lorenz, A. Tanaka, N. B. Brookes, H. H. Hsieh, H. J. Lin, C. T. Chen, L. H. Tjeng, *Physical Review Letters* **2006**, *97*.

[95] Z. Hu, H. Wu, M. W. Haverkort, H. H. Hsieh, H. J. Lin, T. Lorenz, J. Baier, A. Reichl, I. Bonn, C. Felser, A. Tanaka, C. T. Chen, L. H. Tjeng, *Physical Review Letters* **2004**, *92*.

[96] S. Y. Istomin, O. A. Tyablikov, S. M. Kazakov, E. V. Antipov, A. I. Kurbakov, A. A. Tsirlin, N. Hollmann, Y. Y. Chin, H. J. Lin, C. T. Chen, A. Tanaka, L. H. Tjeng, Z. Hu, *Dalton Transactions* **2015**, *44*, 10708-10713.

[97] N. Hollmann, Z. Hu, M. Valldor, A. Maignan, A. Tanaka, H. H. Hsieh, H. J. Lin, C. T. Chen, L. H. Tjeng, *Physical Review B* **2009**, *80*.

[98] D. Qian, Y. Hinuma, H. Chen, L.-S. Du, K. J. Carroll, G. Ceder, C. P. Grey, Y. S. Meng, *Journal of the American Chemical Society* **2012**, *134*, 6096-6099.

[99] K. Shojaee, A. Montoya, B. S. Haynes, *Computational Materials Science* **2013**, *72*, 15-25.

[100] J. Chivot, L. Mendoza, C. Mansour, T. Pauporté, M. Cassir, *Corrosion Science* **2008**, *50*, 62-69.

[101] A. Honji, C. Iwakura, H. Tamura, *Chemistry Letters* **1979**, 1153-1156.

[102] A. Honji, H. Tamura, *Electrochimica Acta* **1981**, *26*, 1319-1326.

[103] H. Tüysüz, M. Comotti, F. Schuth, *Chemical Communications* **2008**, 4022-4024.

[104] H. Tüysüz, Y. J. Hwang, S. B. Khan, A. M. Asiri, P. Yang, *Nano Research* **2012**, *6*, 47-54.

[105] J. Rosen, G. S. Hutchings, F. Jiao, *Journal of the American Chemical Society* **2013**, *135*, 4516-4521.

[106] A. J. Esswein, M. J. McMurdo, P. N. Ross, A. T. Bell, T. D. Tilley, *The Journal of Physical Chemistry C* **2009**, *113*, 15068-15072.

[107] G. H. A. Therese, P. V. Kamath, *Chemistry of Materials* **2000**, *12*, 1195-1204.

[108] D. Friebel, M. Bajdich, B. S. Yeo, M. W. Louie, D. J. Miller, H. Sanchez Casalongue, F. Mbuga, T.-C. Weng, D. Nordlund, D. Sokaras, R. Alonso-Mori, A. T. Bell, A. Nilsson, *Physical Chemistry Chemical Physics* **2013**, *15*, 17460-17467.

[109] M. W. Kanan, D. G. Nocera, *Science* **2008**, *321*, 1072-1075.

[110] B. Han, D. Qian, M. Risch, H. Chen, M. Chi, Y. S. Meng, Y. Shao-Horn, *The Journal of Physical Chemistry Letters* **2015**, *6*, 1357-1362.

[111] P. Du, O. Kokhan, K. W. Chapman, P. J. Chupas, D. M. Tiede, *Journal of the American Chemical Society* **2012**, *134*, 11096-11099.

[112] M. Risch, V. Khare, I. Zaharieva, L. Gerencser, P. Chernev, H. Dau, *Journal of the American Chemical Society* **2009**, *131*, 6936-6937.

[113] M. W. Kanan, J. Yano, Y. Surendranath, M. Dinca, V. K. Yachandra, D. G. Nocera, *Journal of the American Chemical Society* **2010**, *132*, 13692-13701.

[114] M. Risch, F. Ringleb, M. Kohlhoff, P. Bogdanoff, P. Chernev, I. Zaharieva, H. Dau, *Energy & Environmental Science* **2015**, *8*, 661-674.

[115] J. G. McAlpin, Y. Surendranath, M. Dinca, T. A. Stich, S. A. Stoian, W. H. Casey, D. G. Nocera, R. D. Britt, *Journal of the American Chemical Society* **2010**, *132*, 6882-6883.

[116] D. A. Lutterman, Y. Surendranath, D. G. Nocera, *Journal of the American Chemical Society* **2009**, *131*, 3838-3839.

[117] M. Risch, K. Klingan, I. Zaharieva, H. Dau, in *Molecular Water Oxidation Catalysis*, John Wiley & Sons, Ltd, **2014**, pp. 163-185.

[118] C. L. Farrow, D. K. Bediako, Y. Surendranath, D. G. Nocera, S. J. L. Billinge, *Journal of the American Chemical Society* **2013**, *135*, 6403-6406.

[119] M. Richter, D. Schmeißer, *Applied Physics Letters* **2013**, *102*, 253904-253904.

[120] K. Klingan, F. Ringleb, I. Zaharieva, J. Heidkamp, P. Chernev, D. Gonzalez-Flores, M. Risch, A. Fischer, H. Dau, *ChemSusChem* **2014**, *7*, 1301-1310.

[121] A. Bergmann, I. Zaharieva, H. Dau, P. Strasser, *Energy & Environmental Science* **2013**, *6*, 2745-2755.

[122] Y. Gorlin, T. F. Jaramillo, *Journal of the American Chemical Society* **2010**, *132*, 13612-13614.

[123] I. Zaharieva, P. Chernev, M. Risch, K. Klingan, M. Kohlhoff, A. Fischer, H. Dau, *Energy & Environmental Science* **2012**, *5*, 7081-7089.

[124] I. Zaharieva, M. M. Najafpour, M. Wiechen, M. Haumann, P. Kurz, H. Dau, *Energy & Environmental Science* **2011**, *4*, 2400-2408.

[125] V. B. R. Boppana, F. Jiao, *Chemical Communications* **2011**, *47*, 8973-8975.

[126] K. Mette, A. Bergmann, J.-P. Tessonnier, M. Hävecker, L. Yao, T. Ressler, R. Schlögl, P. Strasser, M. Behrens, *ChemCatChem* **2012**, *4*, 851-862.

[127] F. Jiao, H. Frei, *Chemical Communications* **2010**, *46*, 2920-2922.

[128] M. Morita, C. Iwakura, H. Tamura, *Electrochimica Acta* **1977**, *22*, 325-328.
[129] M. Morita, C. Iwakura, H. Tamura, *Electrochimica Acta* **1979**, *24*, 639-643.
[130] M. Morita, C. Iwakura, H. Tamura, *Electrochimica Acta* **1979**, *24*, 357-362.
[131] M. Wiechen, I. Zaharieva, H. Dau, P. Kurz, *Chemical Science* **2012**, *3*, 2330-2339.
[132] Y. Chabre, J. Pannetier, *Progress in Solid State Chemistry* **1995**, *23*, 1-130.
[133] J. H. Albering, in *Handbook of Battery Materials* (Ed.: J. O. Besenhard), Wiley-VCH Verlag GmbH, **1999**, pp. 85-112.
[134] J. E. Post, *Proceedings of the National Academy of Sciences* **1999**, *96*, 3447-3454.
[135] P. de Wolff, *Acta Crystallographica* **1959**, *12*, 341-345.
[136] S. Turner, P. R. Buseck, *Nature* **1983**, *304*, 143-146.
[137] P. Rüetschi, *Journal of The Electrochemical Society* **1984**, *131*, 2737-2744.
[138] P. Rüetschi, *Journal of The Electrochemical Society* **1988**, *135*, 2657-2663.
[139] P. Rüetschi, R. Giovanoli, *Journal of The Electrochemical Society* **1988**, *135*, 2663-2669.
[140] Y. Mo, Y. Hu, I. T. Bae, B. Miller, M. R. Antonio, D. A. Scherson, *Journal of The Electrochemical Society* **1997**, *144*, 1598-1603.
[141] M. Risch, K. Klingan, J. Heidkamp, D. Ehrenberg, P. Chernev, I. Zaharieva, H. Dau, *Chemical Communications* **2011**, *47*, 11912-11914.
[142] H. Dau, I. Zaharieva, M. Haumann, *Current Opinion in Chemical Biology* **2012**, *16*, 3-10.
[143] M. M. Najafpour, T. Ehrenberg, M. Wiechen, P. Kurz, *Angewandte Chemie* **2010**, *122*, 2281-2285.
[144] R. Brimblecombe, A. Koo, G. C. Dismukes, G. F. Swiegers, L. Spiccia, *Journal of the American Chemical Society* **2010**, *132*, 2892-2894.
[145] R. K. Hocking, R. Brimblecombe, L.-Y. Chang, A. Singh, M. H. Cheah, C. Glover, W. H. Casey, L. Spiccia, *Nature Chemistry* **2011**, *3*, 461-466.
[146] T. Takashima, K. Hashimoto, R. Nakamura, *Journal of the American Chemical Society* **2012**, *134*, 1519-1527.
[147] A. Knop-Gericke, E. Kleimenov, M. Hävecker, R. Blume, D. Teschner, S. Zafeiratos, R. Schlögl, V. I. Bukhtiyarov, V. V. Kaichev, I. V. Prosvirin, A. I. Nizovskii, H. Bluhm, A. Barinov, P. Dudin, M. Kiskinova, in *Advances in Catalysis, Vol. 52* (Eds.: B. C. Gates, H. Knözinger), Burlington: Academic Press, **2009**, pp. 213-272.
[148] F. U. Renner, PhD thesis, Universität Stuttgart (Stuttgart), **2004**.
[149] X. Xie, L. Gao, *Carbon* **2007**, *45*, 2365-2373.
[150] J. E. Penner-Hahn, *Coordination Chemistry Reviews* **1999**, *190-192*, 1101-1123.
[151] H. Dau, P. Liebisch, M. Haumann, *Anal. Bioanal. Chem.* **2003**, *376*, 562-583.
[152] D. K. Bediako, B. Lassalle-Kaiser, Y. Surendranath, J. Yano, V. K. Yachandra, D. G. Nocera, *Journal of the American Chemical Society* **2012**, *134*, 6801-6809.
[153] A.-C. Gaillot, D. Flot, V. A. Drits, A. Manceau, M. Burghammer, B. Lanson, *Chemistry of Materials* **2003**, *15*, 4666-4678.
[154] T. G. Spiro, J. R. Bargar, G. Sposito, B. M. Tebo, *Accounts of Chemical Research* **2010**, *43*, 2-9.
[155] S. M. Webb, B. M. Tebo, J. R. Bargar, *American Mineralogist* **2005**, *90*, 1342-1357.
[156] I. Saratovsky, P. G. Wightman, P. A. Pasten, J.-F. Gaillard, K. R. Poeppelmeier, *Journal of the American Chemical Society* **2006**, *128*, 11188-11198.
[157] S. Geller, *Acta Crystallographica Section B* **1971**, *27*, 821-828.
[158] R. E. Pacalo, E. K. Graham, *Physics and Chemistry of Minerals* **1991**, *18*, 69-80.
[159] D. R. Lide*, Vol. 82*, CRC-Press, **2001**.
[160] O. Ghodbane, J.-L. Pascal, F. Favier, *ACS Applied Materials & Interfaces* **2009**, *1*, 1130-1139.

[161] H. Over, *Chemical Reviews* **2012**, *112*, 3356-3426.

[162] H. Over, *Electrochimica Acta* **2013**, *93*, 314-333.

[163] A. Stierle, A. Steinhäuser, A. Rühm, F. U. Renner, R. Weigel, N. Kasper, H. Dosch, *Review of Scientific Instruments* **2004**, *75*, 5302-5307.

[164] Z. Zhang, F. Zhou, E. J. Lavernia, *Metallurgical and Materials Transactions A* **2003**, *34*, 1349-1355.

[165] W. Ostwald, *Zeitschrift für physikalische Chemie* **1897**, *22*, 289-330.

[166] R. Borup, J. Meyers, B. Pivovar, Y. S. Kim, R. Mukundan, N. Garland, D. Myers, M. Wilson, F. Garzon, D. Wood, P. Zelenay, K. More, K. Stroh, T. Zawodzinski, J. Boncella, J. E. McGrath, M. Inaba, K. Miyatake, M. Hori, K. Ota, Z. Ogumi, S. Miyata, A. Nishikata, Z. Siroma, Y. Uchimoto, K. Yasuda, K.-i. Kimijima, N. Iwashita, *Chemical Reviews* **2007**, *107*, 3904-3951.

[167] NIST X-ray Photoelectron Spectroscopy Database, Version 4.1 http://srdata.nist.gov/xps/.

[168] V. Pralong, *Progress in Solid State Chemistry* **2009**, *37*, 262-277.

[169] M. M. Thackeray, S. D. Baker, K. T. Adendorff, J. B. Goodenough, *Solid State Ionics* **1985**, *17*, 175-181.

[170] T. Reier, M. Oezaslan, P. Strasser, *ACS Catalysis* **2012**, *2*, 1765-1772.

[171] M. Bernicke, E. Ortel, T. Reier, A. Bergmann, J. Ferreira de Araujo, P. Strasser, R. Kraehnert, *ChemSusChem* **2015**, *8*, 1908-1915.

[172] T. Reier, D. Teschner, T. Lunkenbein, A. Bergmann, S. Selve, R. Kraehnert, R. Schlögl, P. Strasser, *Journal of the Electrochemical Society* **2014**, *161*, F876-F882.

[173] H. N. Nong, H.-S. Oh, T. Reier, E. Willinger, M.-G. Willinger, V. Petkov, D. Teschner, P. Strasser, *Angewandte Chemie* **2015**, *127*, 3018-3022.

[174] H. N. Nong, L. Gan, E. Willinger, D. Teschner, P. Strasser, *Chemical Science* **2014**, *5*, 2955-2963.

[175] J. A. Bearden, A. F. Burr, *Reviews of Modern Physics* **1967**, *39*, 125-142.

[176] A. L. Ankudinov, B. Ravel, J. J. Rehr, S. D. Conradson, *Physical Review B* **1998**, *58*, 7565-7576.

[177] J. J. Rehr, R. C. Albers, *Reviews of Modern Physics* **2000**, *72*, 621-654.

[178] M. Richter, D. Schmeißer, *ECS Transactions* **2013**, *50*, 113-126.

[179] S. Zafeiratos, T. Dintzer, D. Teschner, R. Blume, M. Hävecker, A. Knop-Gericke, R. Schlögl, *Journal of Catalysis* **2010**, *269*, 309-317.

[180] M. Risch, D. Shevchenko, M. F. Anderlund, S. Styring, J. Heidkamp, K. M. Lange, A. Thapper, I. Zaharieva, *International Journal of Hydrogen Energy* **2012**, *37*, 8878-8888.

[181] M. Risch, PhD thesis, Freie Universität Berlin (Berlin), **2011**.

[182] F. de Groot, M. Grioni, J. Fuggle, J. Ghijsen, G. Sawatzky, H. Petersen, *Physical Review B* **1989**, *40*, 5715-5723.

[183] J. B. Gerken, J. G. McAlpin, J. Y. C. Chen, M. L. Rigsby, W. H. Casey, R. D. Britt, S. S. Stahl, *Journal of the American Chemical Society* **2011**, *133*, 14431-14442.

[184] R. S. Nicholson, *Analytical Chemistry* **1965**, *37*, 1351-1355.

[185] R. M. Arán-Ais, M. C. Figueiredo, F. J. Vidal-Iglesias, V. Climent, E. Herrero, J. M. Feliu, *Electrochimica Acta* **2011**, *58*, 184-192.

[186] D. González-Flores, I. Sánchez, I. Zaharieva, K. Klingan, J. Heidkamp, P. Chernev, P. W. Menezes, M. Driess, H. Dau, M. L. Montero, *Angewandte Chemie* **2015**, *127*, 2502-2506.

[187] W.-S. Yoon, K.-B. Kim, M.-G. Kim, M.-K. Lee, H.-J. Shin, J.-M. Lee, J.-S. Lee, C.-H. Yo, *The Journal of Physical Chemistry B* **2002**, *106*, 2526-2532.

[188] Y. Zhang, B. Cui, Z. Qin, H. Lin, J. Li, *Nanoscale* **2013**, *5*, 6826-6833.

[189] Y. Zhang, B. Cui, C. Zhao, H. Lin, J. Li, *Physical Chemistry Chemical Physics* **2013**, *15*, 7363-7369.

[190] W. T. Hong, M. Gadre, Y.-L. Lee, M. D. Biegalski, H. M. Christen, D. Morgan, Y. Shao-Horn, *The Journal of Physical Chemistry Letters* **2013**, *4*, 2493-2499.

[191] R. Arrigo, M. Havecker, M. E. Schuster, C. Ranjan, E. Stotz, A. Knop-Gericke, R. Schlögl, *Angewandte Chemie International Edition* **2013**, *52*, 11660-11664.

[192] D. Mierwaldt, S. Mildner, R. Arrigo, A. Knop-Gericke, E. Franke, A. Blumenstein, J. Hoffmann, C. Jooss, *Catalysts* **2014**, *4*, 129-145.

[193] S. Raabe, D. Mierwaldt, J. Ciston, M. Uijttewaal, H. Stein, J. Hoffmann, Y. Zhu, P. Blöchl, C. Jooss, *Advanced Functional Materials* **2012**, *22*, 3378-3388.

[194] C. Luengo, M. Brigante, J. Antelo, M. Avena, *Journal of Colloid and Interface Science* **2006**, *300*, 511-518.

[195] A. Hulanicki, *Reactions of acids and bases in analytical chemistry*, Ellis Horwood Ltd., **1987**.

Acronyms

BEP	Brønsted or Bell-Evans-Polanyi
BET	Brunauer-Emmet-Teller
ccp	cubic close-packed
CFSE	Crystal field stabilization energy
Cus	Coordinatively unsaturated site
CV	Cyclic voltammogram
DEMS	Differential electrochemical mass-spectrometry
DFT	Density functional theory
DSA	Dimensionally-stable anode
DW	Debye-Waller factor
ECSA	Electrochemical surface area
EELS	Electron energy loss spectroscopy
EXAFS	Extended X-ray absorption fine structure
FT	Fourier transform
GC	Glassy carbon
GIXRD	Grazing-incidence X-ray diffraction
hcp	hexagonal close-packed
HE-XRD	High energy X-ray diffraction
Hupd	Hydrogen underpotential deposition
HZB	Helmholtz-Zentrum Berlin
ICP-OES	Inductively-coupled plasma – optical emission spectroscopy
KPi	Potassium phosphate buffer
LDH	Layered double hydroxide
MMS	Mercury/Mercury sulphate
MS	Mass spectrometry
MWNT	Multi-walled carbon nanotubes
NHE	Normal hydrogen electrode
OER	Oxygen evolution reaction
PCET	Proton-coupled electron transfer
PCTFE	Polychlorotrifluoroethene
PEIS	Potentiostatic electrochemical impedance spectroscopy
PTFE	Polytetrafluoroethene
RDE	Rotating disk electrode
rds	Rate-determining step
RHE	Reversible hydrogen electrode
SAED	Selected-area electron diffraction
TM	Transition metal
TOF	Turnover frequency
TPR	Temperature-programmed reduction
XANES	X-ray absorption near-edge structure
XPS	X-ray photoelectron spectroscopy
XRD	X-ray diffraction

List of Tables

Table 1: Results of Rietveld refinements of the GIXRD patterns of Co_3O_4, rs-CoO and w-CoO as shown in Figure 20 and the refined patterns are shown in Figure A33. 91

Table 2: Results of simulation of the EXAFS spectra of Co_3O_4, rs-CoO, w-CoO, and CoOOH in the as-prepared state. The experimental and simulated spectra are shown in Figure A34 and the complete results shown in Table 9. 97

Table 3: Surface composition of Co_3O_4, rs-CoO, w-CoO, and CoOOH in the as-prepared state as extracted from peak fitting and integration of XPS Co 2p and O 1s spectra. 99

Table 4: Results of simulation of the EXAFS spectra of Co_3O_4, rs-CoO, w-CoO, and CoOOH at 1.2 V after OER-conditioning. The differences between as-prepared state and the state at 1.2 V are given. In case of rs-, w-CoO and CoOOH after OER conditioning was perform prior to the XAS experiments. The experimental and simulated spectra are shown in Figure A34 and the complete fitting results in Table 10. 113

Table 5: Surface composition of Co_3O_4, rs-CoO, w-CoO, and CoOOH in the as-prepared and OER-conditioned state as extracted from peak fitting of XPS Co 2p, O 1s, and P 2p spectra. OER conditioning was performed for 15 min at 1.62 V in 0.1M KP_i. 116

Table 6: Results of simulation of the EXAFS spectra of the catalytically active state of Co_3O_4, rs-CoO, w-CoO, and CoOOH. The spectra were recorded after OER conditioning and the differences between the catalytically active state during OER and the state at 1.2 V are given. The experimental and simulated spectra are shown in Figure A34 and the complete results shown in Table 11. See Chapter 5 for experimental details of Co_3O_4.[68] 121

Table 7: Fit results for Co_3O_4(511) and Co_3O_4(440) reflections of the *in situ* X-ray diffraction of thin films as function of catalyst state. Fitting was performed using pseudo-Voigt profiles. The error of the fit parameters represents one estimated standard deviation. The structural coherence length was determined from the integral breadth in the Scherrer equation. A shape factor of 0.89 was used. 166

Table 8: Simulation results for the fits of the k^3-weighted EXAFS spectra of Co_3O_4 thin films as a function of catalyst state. The error ranges of the fit parameters were estimated from the covariance matrix of the fit and represent the 68% confidence intervals.[141] 167

Table 9: Results of simulation of the EXAFS spectra of rs-CoO, w-CoO, and CoOOH in the as-prepared state. The experimental and simulated spectra are shown in Figure A34. 173

Table 10: Results of simulation of the EXAFS spectra of rs-CoO, w-CoO, and CoOOH at 1.2 V after OER-conditioning. The differences between as-prepared state and the state at 1.2 V in case of rs-, w-CoO and CoOOH after OER conditioning are given. The experimental and simulated spectra are shown in Figure A34. 174

Table 11: Results of simulation of the EXAFS spectra of rs-CoO, w-CoO, and CoOOH during OER. The experimental and simulated spectra are shown in Figure A34. 175

List of Figures

Figure 1: Schematic diagram of Gibbs free energy of reactive species and intermediates as function of reaction coordinate within the four step mechanistic framework considered by Rossmeisl.[21-25] The educt, reaction intermediates and product as well as the activation energies for the reaction intermediates are denoted. In case of an ideal catalyst (black) all activation energies are equally large. On a real catalyst (red) one reaction step defines the lowest overpotential at which all reaction steps are energetically downhill and thus, occur spontaneously. See Eqns. 7-10 and the next section. Figure adapted from Dau et.al.[29] and Hong et.al.[20]. 23

Figure 2: Ideal structures of selected Co oxides and Co oxyhydroxides: Co_3O_4 (a), rocksalt-CoO (b), CoOOH (c) and wurtzite-CoO (d). The CoO_6 coordination octahedra and CoO_4 coordination tetrahedra are shown. Co^{3+}, Co^{2+} octahedra and Co^{2+} tetrahedra are shown in blue, red, and green, respectively. Hydrogen atoms are shown in white. 34

Figure 3: Electronic configuration of 3d orbitals in octahedral Co^{3+} (A-C) as well as octahedral Co^{2+} (D) and tetrahedral Co^{2+} (E). $\Delta_{o/t}$ denotes the crystal field stabilization energy (CFSE) which is lower at intermediate or high spin configuration compared to low spin configuration in octahedral ligand field of Co^{3+}. The same applies for the tetrahedral compared to octahedral ligand field of Co^{2+}. The 3d orbitals are shown as degenerate for clarity. The figure is based on [20, 94-96]. 36

Figure 4: Structures of selected MnO_2 modifications: β-MnO_2 (a), γ-MnO_2 (b), and δ-MnO_2 (c). The MnO_6 coordination octahedra are schematically shown. The structures are extended in the direction perpendicular to the paper plane by rows of edge-sharing octahedra (in a, b, and c). This results in (1x1) tunnels of coordination octahedra (a), in (2x1) tunnels (b), and in a layered manganese oxide (c). In the layered oxides, the interlayer space is filled with water molecules and ions. Figure reproduced from Ref. [121] with permission from the Royal Society of Chemistry. 43

Figure 5: Schematic drawing of experimental setup for in situ X-ray studies at electrocatalysts under electrochemical reaction conditions. The inset shows a photograph of the in situ X-ray setup as operated at Bessy II, Berlin. Therein, the X-ray beam comes from the tube on the left side and the scattered X-ray from the sample are collected at the detector connect to the evacuated tube on the right side. RE, CE, and WE denotes reference, counter, and working electrode , respectively. 48

Figure 6: Powder X-ray diffraction pattern of s-MnO_x (black) and i-MnO_x (red) between 10° and 75°, at Cu K_α radiation. Reflections are labeled by squares for β-MnO_2, by circles for γ-MnO_2, by triangles for the layered MnO_2 phase, and by stars for the reflexes caused by the support material. The latter are shown in Figure A1. 54

Figure 7: X-ray absorption spectra of s-MnO_x (black) and i-MnO_x (red) deposited on electrodes before and after catalysis. The edge region of the spectra (XANES) is shown in the inset. The average oxidation state of Mn in the two samples directly after deposition on the electrode (thick lines) is around 3.5, while after 3 min of operation at 1.763 V in 0.1 M KPi at pH 7, it increases to 3.9-4.0 (thin lines). The structural motifs considered in the EXAFS simulations are schematically depicted next to the corresponding FT peak and the obtained interatomic distances are indicated. (Mn^{4+} ions are presented as spheres in magenta, Mn^{3+} ions in dark purple, and oxygen as red spheres.) 56

Figure 8: Schematic model for a distorted MnOx layer fragment formed from edge-sharing (di-μ-oxo bridged) $Mn^{4+}O_6$ and $Mn^{3+}O_6$ octahedra. Some Mn ions from the layer are missing (defects), and other Mn ions are bound on top (or below) of the layer resulting in mono-μ-oxo bridges (corner-sharing octahedra). At these defect sites, a row of edge-sharing octahedra could grow perpendicularly to the first one; this eventually may lead to formation of tunnel-like structures. Binding of a Mn^{3+} ions on top of the layer at sites without layer defects results in formation of a (distorted) Mn_4O_4 cubanes. (Mn^{4+} ions in magenta, Mn^{3+} ions in dark purple, O in red.) 58

Figure 9: Coordination numbers and interatomic distances obtained by joint simulation of the k^3-weighted EXAFS spectra from s-MnO_x (upper panel) and i-MnO_x (lower panel) before and after operation as water oxidation catalysts in 0.1M KPi (pH 7) or 0.1M KOH (pH 13). The corresponding absorber-backscatter distances were kept equal for all seven spectra and are displayed together with the corresponding structural motif (colour code as in Fig. 2). The error bars represents the 68% confidence interval; the error for the interatomic distances is given in parentheses below the corresponding structural motif. For further details, see Figure A6. 59

Figure 10: Cyclic voltammograms (CV) of first (solid) and 11th (dashed) scan of s-MnO_x (black) and i-MnO_x (red). The CVs were recorded in 0.1 M KPi at pH 7 with a scan rate of 100 mV s^{-1}. Two minima resolved in the s-MnO_x CV are labeled by MnR-1 and MnR-2, respectively. 61

Figure 11: Tafel plot of s-MnO_x (black) and i-MnO_x (red) extracted from quasi-stationary potential-step RDE experiments in 0.1 M KPi at pH 7. All electrode potentials have been iR-corrected. The respective Tafel slopes as determined by linear regression are indicated. 62

Figure 12: pH dependency of the overpotential (η) of s- and i-MnO_x determined in 0.1 M KPi at constant currents of (a) 50 μA and (b) 20 μA. The overpotential has been calculated according to $\eta = E_{NHE} + (59mV/pHunit) \cdot pH - 1.23$ V. 63

Figure 13: pH dependence of the catalytic current (*I*) determined in 0.1 M KPi at a constant electrode potential of 1.35 V vs. NHE. 64

Figure 14: Scanning electron micrographs in low (a) and high magnification (c), transmission electron micrograph (b) and selected area electron diffraction (SAED) pattern (d) of as-prepared Co_3O_4 films. Diffraction rings of Co_3O_4 are indexed in the SAED pattern. The scale bars represent 2 μm, 50 nm, 100 nm, and 5 nm^{-1} in panel a, b, c, and d, respectively. 72

Figure 15: Tafel plot (a) and cyclic voltammogram (b) of Co_3O_4 films deposited on glassy carbon recorded in 0.1 M KP_i at pH 7. The Tafel plot was extracted from cathodic quasi-stationary potential-step rotating disc electrode (RDE) experiments after equilibration for 4 min at each potential; the line corresponds to a Tafel slope and an exchange current density of 65 mV/dec and $2.26 \cdot 10^{-9}$ mA $cm^{-2}{}_{ECSA}$, respectively. The cyclic voltammogram was recorded with a scan rate of 100 mV s^{-1} and shows a minor and major Co redox feature at ~1.4 V (A1/C1) and ~1.54 V (A2/C2), respectively. The capacitance-corrected reductive charge of the two redox features showed that only ~1.8% of the Co ions change its oxidation state by one equivalent. Electrode potentials were corrected for Ohmic losses and current was normalized using electrochemical surface area (ECSA) as determined by potentiostatic electrochemical impedance spectroscopy.[51] The electrochemical surface roughness was 26.4. 73

Figure 16: *In situ* X-ray diffraction patterns (a) and Fourier-transforms (FT) of (quasi-)in situ EXAFS spectra collected at the Co K-edge (b) of Co_3O_4 catalyst films. Experimental data and fitted profiles are shown in bold and thin lines, respectively. The diffraction patterns were recorded using grazing-incident excitation at α=0.3° and 12 keV. The electrode potential was increased stepwise from +1.0 V to +1.62 V vs. RHE, the latter representing the catalytically-active catalyst state, in 0.1 M KPi at pH 7. (cf. Figure 15a and Figure A24) The state after OER is a dry state for which the electrode was removed from electrolyte at +1.0 V rinsed with de-ionized water and dried in N_2 flow. The Miller indices of selected Co_3O_4 reflections are indicated; the diffraction patterns were background corrected for better visualization. Fitting was performed using pseudo-Voigt profiles. Samples for XAS were freeze-quenched under potential control using liquid N_2 after 15 min at 1.62 V in 0.1M KP_i. 74

Figure 17: Structural coherence length of Co_3O_4 (a), shift of the Co X-ray absorption K-edge (b), change in EXAFS coordination number of di- and mono-μ-oxo bridges between Co ions (c) with respect to the as-prepared state. The state at +1.62 V corresponds to the catalytically active oxygen evolution state (cf. Figure 15 and Figure A24). Electrode potentials in this particular experiment are not corrected for Ohmic losses but we note that Ohmic correction decreased the electrode potential at +1.62 V by less than ~1 mV in the quasi-stationary experiment. The structural coherence length was calculated using the Scherrer equation from the integral breadth of the Co_3O_4(511) and (440) reflections.[164] A shape factor k of 0.89 was used. The error of the structural coherence length was calculated from the estimated standard deviation of the fitted integral breadth. The likely error of the shift of the Co K edge was estimated to be ±0.1 eV. The coordination numbers were determined by simulations of k^3-weighted EXAFS spectra. The error ranges of the EXAFS fit parameters were estimated from the covariance matrix of the fit and represent the 68% confidence intervals. Further details on data analysis are given in the caption of Table 7 and Table 8 75

Figure 18: Fluorescence-detected quasi-in situ XANES spectra of Co_3O_4 films in various catalyst states. For increasingly positive potentials, the Co K-edge absorption edge shifted reversibly to higher energies suggesting oxidation of 10-15% of the cobalt ions under stationary oxygen evolution conditions. Under OER conditions, the XANES profile exhibited an almost linear increase due to significantly weaker shoulders marked with (A) and (B). The intensity at the principal edge-maximum at (C) was clearly reduced only in the oxygen evolving active state (at +1.62 V). Samples were freeze-quenched under potential control using liquid N_2 after 15 min at 1.62 V in 0.1M KPi and stored in liquid N2 until XAS measurements were conducted. 77

Figure 19: Possible near-surface structures on crystalline Co_3O_4 core under electrochemical conditions. At potentials below Co redox features, Co_3O_4 is in a healed state at which defects in the near-surface are oxidized. At elevated O2 evolution, the CoOx(OH)y grows into the crystalline Co_3O_4 core leading to a reversible amorphization of a sub-nm shell. This amorphous $CoO_x(OH)_y$ shell consists of di-μ-oxo bridged $Co^{3+/4+}$ ions with arbitrary site occupancy in the ideal-cubic close-packed O^{2-} lattice. Hydrogen atoms and phosphates are not shown. 80

Figure 20: GIXRD patterns of the as-prepared state of Co_3O_4(black), rs-CoO(red), w-CoO(green) deposited on Si(100) substrate, and CoOOH(blue) on Ti-coated Si(100) substrate recorded at an incident angle of 1° using parallel Cu Kα radiation. The diffraction patterns were background corrected for better visualization. The reflections for the database references are shown as bars. Co_3O_4 (black, PDF#00-042-1467), rocksalt-CoO (red, PDF#01-078-0431), wurtzite-CoO (green, PDF#01-089-2803), and Heterogenite (blue, PDF#00-026-11107) are shown. The uncorrected patterns are shown in the Figure A33. 90

Figure 21: SEM micrographs of the as-prepared state of Co_3O_4(A), rs-CoO(B), CoOOH(C), and w-CoO(D). 92

Figure 22: HRTEM micrographs of the as-prepared state of Co_3O_4(A), rs-CoO(B), CoOOH(C), and w-CoO(D). 93

Figure 23: SAED pattern of the as-prepared state of Co_3O_4(A), rs-CoO(B), CoOOH(C), and w-CoO(D). 94

Figure 24: XANES and FT of EXAFS spectra of the as-prepared state of Co_3O_4(black), rs-CoO(red), w-CoO(green), and CoOOH(blue) recorded at the Co K-edge. Experimental curves are shown as bold, simulated as thin lines. See Chapter 5 for experimental details of Co_3O_4. The k^3-weighted EXAFS spectra are shown in Figure A34. 95

Figure 25: Co 2p (A) and O 1s (B) photoelectron spectra of the as-prepared state of Co_3O_4(black), rs-CoO(red), w-CoO(green), and CoOOH(blue) recorded at a kinetic energy of the photoelectrons of 550 eV. 98

Figure 26: Co L_3 (A) and O K (B) XANES spectra of the as-prepared state of Co_3O_4(black), rs-CoO(red), w-CoO(green), and CoOOH(blue) recorded in total electron yield mode. 100

Figure 27: Cyclic voltammograms (A) and Tafel plot (B) of Co_3O_4(black), rs-CoO(red), w-CoO(green), and CoOOH(blue) deposited on glassy carbon recorded in N_2-saturated 0.1 M KPi at pH 7. The Tafel plots were extracted from anodic quasi-stationary potential step experiments. The cyclic voltammograms were recorded with a sweep rate of 200 $mV \cdot s^{-1}$. The Co loading was identical for all samples with 322 $nmol \cdot cm^{-2}$. *The current of CoOOH in the cyclic voltammogram was divided by 5 for better visualisation. 103

Figure 28: Tafel slope of Co oxides as function of the electrochemical reducibility of the Co^{3+} sites. Reducibility was determined from the peak current ratio of C1 and C2 as extracted from cyclic voltammograms recorded with a sweep rate of 200 mV s^{-1} in 0.1M KP_i at pH7. The potential of C1 was 1.35 V in case of rs-, w-CoO and Co_3O_4 as well as 1.43 V for CoOOH. The potential of C2 was chosen by the local current minimum above a potential of 1.45 V. Tafel slope was determined from anodic quasi-stationary potential step experiments in the same electrolyte. See Figure A36 for further details. 105

Figure 29: Cyclic voltammograms of Co_3O_4(A), rs-CoO(B), CoOOH(C), and w-CoO(D) recorded with a sweep rate of 200 mV s^{-1} in N_2-saturated 0.1 M KOH (solid) and 0.1M KPi at pH 7 (dashed). 106

Figure 30: Tafel plots of Co_3O_4 (black), rs-CoO (red), CoOOH (blue) and w-CoO (green) recorded in N_2-saturated 0.1 M KOH. The solid lines represent the given Tafel slope 48, 42, 39, and 36 $mV \cdot dec^{-1}$ for Co_3O_4, rs-CoO, CoOOH, and w-CoO, respectively. 107

Figure 31: SEM micrographs of the OER-conditioned state of Co_3O_4(A), rs-CoO(B), CoOOH(C), and w-CoO (D) deposited on glassy carbon. OER conditioning was performed for 15 min at 1.62 V in N_2-saturated 0.1M KP_i. 109

Figure 32: HRTEM micrographs of the OER-conditioned state of Co_3O_4(A), rs-CoO(B), CoOOH(C), and w-CoO (D). OER conditioning was performed for 15 min at 1.62 V in N_2-saturated 0.1M KP_i at pH 7. 110

Figure 33: SAED pattern of the OER-conditioned state of Co_3O_4(A), rs-CoO(B), CoOOH(C), and w-CoO (D). The SAED patterns were recorded at lower magnification than the TEM micrographs shown in Figure 32.OER conditioning was performed for 15 min at 1.62 V in N_2-saturated 0.1M KP_i at pH 7. 111

Figure 34: XANES (A) and FT of EXAFS (B) spectra of Co_3O_4(black), rs-CoO(red), w-CoO(green), and CoOOH(blue) after OER recorded at the Co *K*-edge. Experimental curves are shown in bold, simulated in thin lines. The OER-conditioned state was investigated under *in situ* conditions at 1.2 V in N_2-saturated 0.1M KP_i at pH 7. OER conditioning was performed for 15 min at 1.62 V in the same electrolyte. The Co_3O_4 show the dry state after OER conditioning as shown in Figure 16 and Figure 18.[68] The k^3-weighted EXAFS spectra are shown in Figure A34. 112

Figure 35: Co 2p (A) and O 1s (B) X-ray photoelectron spectra of the OER-conditioned state of Co_3O_4(black), rs-CoO(red), w-CoO(green), and CoOOH(blue) recorded at a kinetic energy of the photoelectrons of 550 eV. OER conditioning was performed for 15 min at 1.62 V in N_2-saturated 0.1M KP_i at pH 7. 115

Figure 36: Co L_3 (A) and O *K* (B) XANES spectra of the OER-conditioned state of Co_3O_4(black), rs-CoO(red), w-CoO(green), and CoOOH(blue) recorded in total electron yield mode. OER conditioning was performed for 15 min at 1.62 V in N_2-saturated 0.1M KP_i at pH 7. 117

Figure 37: *in situ* XANES (A) and FT of EXAFS (B) spectra of Co_3O_4(black), rs-CoO(red), w-CoO(green), and CoOOH(blue) during OER recorded at the Co K-edge. Experimental curves are shown in bold, simulated in thin lines. The catalytically active state was investigated under *in situ* conditions in N_2-saturated 0.1M KPi at pH 7. The electrode potential was chosen to a current density of 0.5 $mA\cdot cm^{-2}$. Prior an OER conditioning was performed for 15 min at 1.62 V in the same electrolyte. See Chapter 5 for experimental details of Co_3O_4.[68] The k^3-weighted EXAFS spectra are shown in Figure A34. 120

Figure 38: Co oxide reducibility (black squares) and Tafel slope (red circles) in 0.1M KP_i at pH 7 as function of the normalized of hybridization between the 3d orbitals of low-spin Co^{3+} O_h ions and O 2p orbitals. The reducibility of the Co oxides was determined from the peak current ratio of C1 and C2 as extracted from the cyclic voltammograms as shown in Figure 27A and Figure A36. The Tafel slope was determined from quasi-stationary anodic potential step experiments as shown in Figure 27B. The normalized degree of orbital hybridization was estimated from area of the O *K* pre-edge feature according to electron transitions at ~530.5 eV and normalized with the peak area of Co_3O_4. The peak area was determined by fits as shown in Figure A40. 125

List of Publications

These publications were published during within the course of PhD.

[1] **A. Bergmann**, E. Martinez-Moreno, D. Teschner, P. Chernev, M. Gliech, J. Ferreira de Araújo, T. Reier, H. Dau, P. Strasser, Reversible amorphization and the catalytically active state of crystalline Co_3O_4 during oxygen evolution. Nat. Commun., 6:8625 (2015).

[2] T. Reier, Z. Pawolek, S. Cherevko, M. Bruns, T. Jones, D. Teschner, S. Selve, **A. Bergmann**, H. N. Nong, R. Schlögl, K. J. J. Mayrhofer, P. Strasser, Molecular Insight in Structure and Activity of Highly Efficient, Low-Ir Ir–Ni Oxide Catalysts for Electrochemical Water Splitting (OER). Journal of the American Chemical Society 137, 13031-13040 (2015).

[3] M. Bernicke, E. Ortel, T. Reier, **A. Bergmann**, J. Ferreira de Araujo, P. Strasser, R. Kraehnert, Iridium Oxide Coatings with Templated Porosity as Highly Active Oxygen Evolution Catalysts: Structure-Activity Relationships. ChemSusChem 8, 1908-1915 (2015).

[4] E. Ortel, J. Polte, D. Bernsmeier, B. Eckhardt, B. Paul, **A. Bergmann**, P. Strasser, F. Emmerling, R. Kraehnert, Pd/TiO_2 coatings with template-controlled mesopore structure as highly active hydrogenation catalyst. Applied Catalysis A: General 493, 25-32 (2015)

[5] T. N. Huan, E. S. Andreiadis, J. Heidkamp, P. Simon, E. Derat, S. Cobo, G. Royal, **A. Bergmann**, P. Strasser, H. Dau, V. Artero, M. Fontecave, From molecular copper complexes to composite electrocatalytic materials for selective reduction of CO_2 to formic acid. Journal of Materials Chemistry A 3, 3901-3907 (2015).

[6] T. Reier, D. Teschner, T. Lunkenbein, **A. Bergmann**, S. Selve, R. Kraehnert, R. Schlögl, P. Strasser, Electrocatalytic Oxygen Evolution on Iridium Oxide: Uncovering Catalyst-Substrate Interactions and Active Iridium Oxide Species. Journal of the Electrochemical Society 161, F876-F882 (2014).

[7] P. W. Menezes, A. Indra, N. R. Sahraie, **A. Bergmann**, P. Strasser, M. Driess, Cobalt–Manganese-Based Spinels as Multifunctional Materials that Unify Catalytic Water Oxidation and Oxygen Reduction Reactions. ChemSusChem 8, 164-171 (2014).

[8] A. Indra, P. W. Menezes, N. R. Sahraie, **A. Bergmann**, C. Das, M. Tallarida, D. Schmeißer, P. Strasser, M. Driess, Unification of Catalytic Water Oxidation and Oxygen Reduction Reactions: Amorphous Beat Crystalline Cobalt Iron Oxides. Journal of the American Chemical Society 136, 17530-17536 (2014).

[9] **A. Bergmann,** I. Zaharieva, H. Dau, and P. Strasser, Electrochemical water splitting by layered and 3D cross-linked manganese oxides: correlating structural motifs and catalytic activity. Energy & Environmental Science 6, 2745-2755 (2013).

[10] K. Mette, **A. Bergmann**, J.-P. Tessonnier, M. Hävecker, L. Yao, T. Ressler, R. Schlögl, P. Strasser, M. Behrens, Nanostructured Manganese Oxide Supported on Carbon Nanotubes for Electrocatalytic Water Splitting. ChemCatChem 4, 851-862 (2012).

Appendix

A1 Supplementary Information to Chapter 4[121]

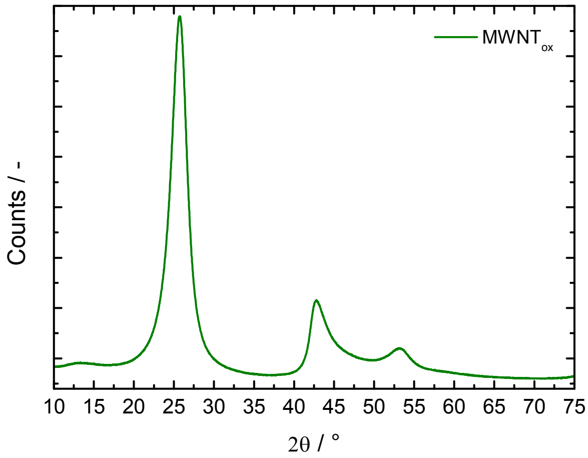

Figure A1: Powder x-ray diffraction pattern of MWNT$_{ox}$ between 10° and 75° at Cu K$_\alpha$ radiation.

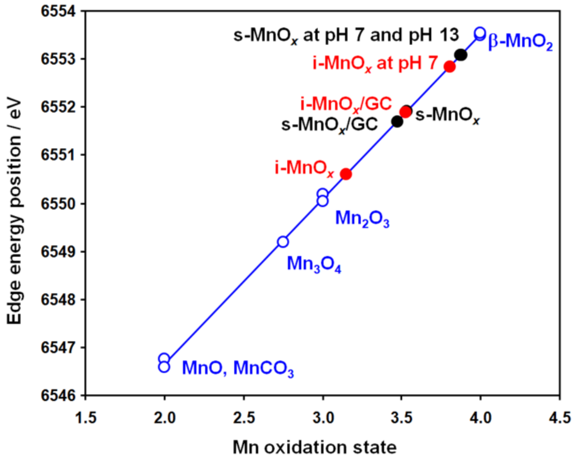

Figure A2: Calibration line based on Mn compounds with known structure and oxidation state (in blue). Black symbols and labels indicate the edge position and estimated mean Mn oxidation state for s-MnOx powder before (s-MnOx) and after (s-MnOx/GC) deposition on the electrode, and after electrocatalytic operation at 1.763 V vs. RHE for 3 min at pH 7 (0.1 M KPi) or pH 13 (0.1 M KOH). Red symbols and label represent the corresponding values for the i-MnOx.

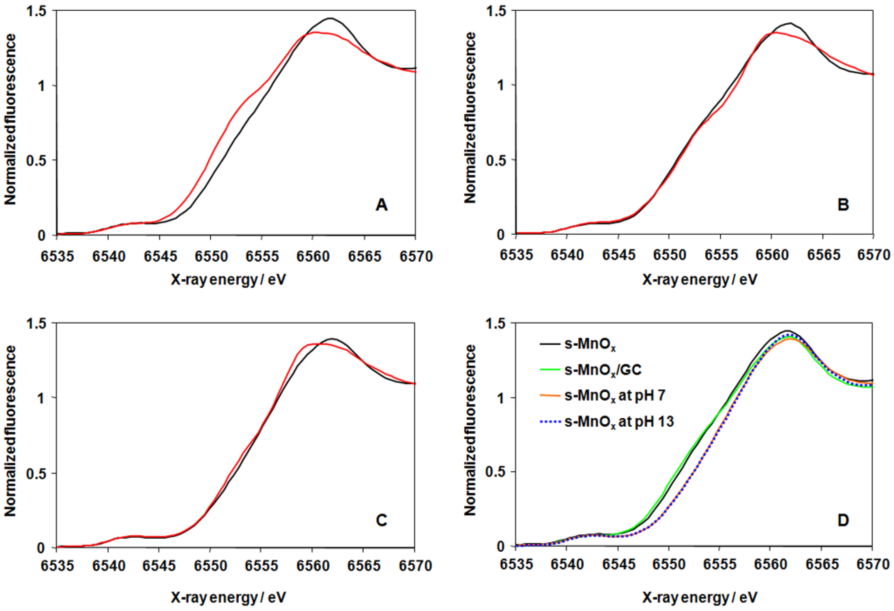

Figure A3: XANES spectra of s-MnOx (in black) and i-MnOx (in red) after synthesis (A), after deposition on GC electrode (B), and after operating for 3 min at 1.763 V vs. RHE in 0.1 M KPi, pH 7 (C). In (D) is shown a comparison of the XANES spectra recorded from s-MnOx at different stages of catalyst preparation.

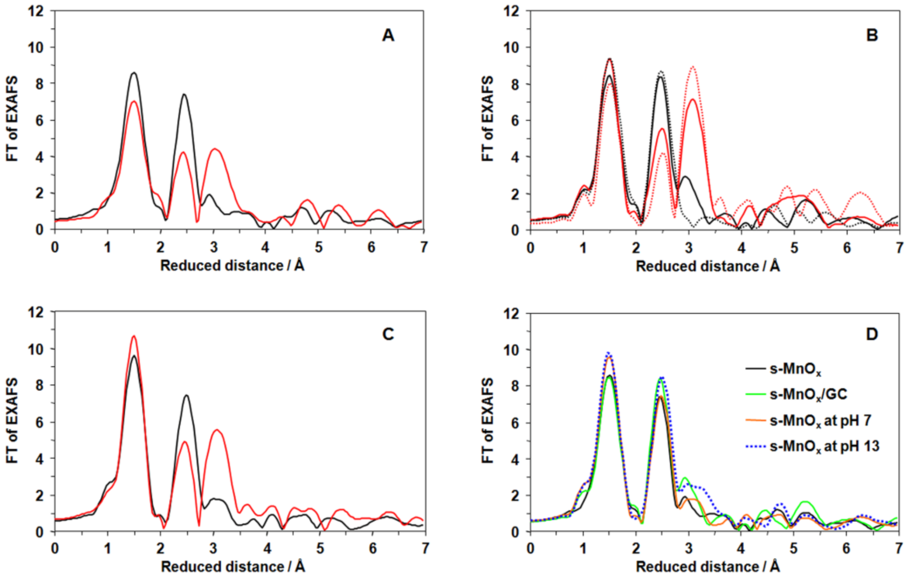

Figure A4: Fourier-transformed EXAFS spectra of s-MnOx (black solid lines) and i-MnOx (red solid lines) after synthesis (A), after deposition on GC electrode (B), and after operating for 3 min at 1.763 V vs. RHE in 0.1 M phosphate buffer, pH 7 (C). In (B) the spectra from δ-MnO2 and b-MnO2 reference compounds are shown using black and red dotted lines, respectively. In (D) a comparison of the Fourier-transformed EXAFS spectra recorded from s-MnOx at different stages of catalyst preparation is shown.

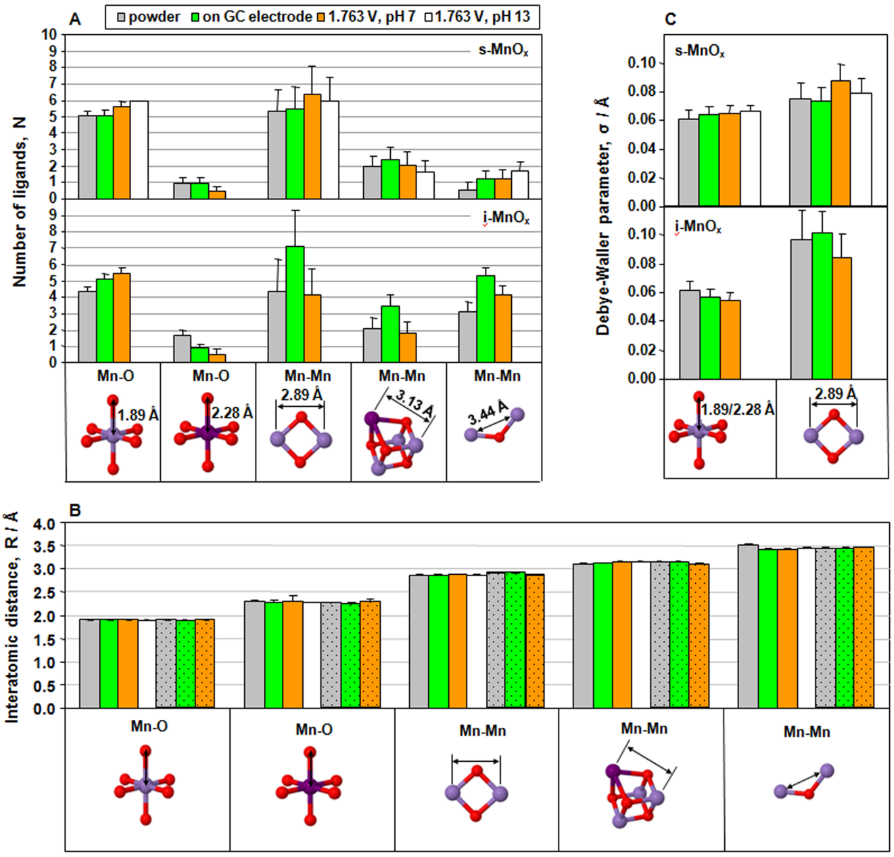

Figure A5: Simulation results for the independent fits of the k3-weighted EXAFS spectra from s-MnOx and i-MnOx before and after operation as water oxidation catalysts in 0.1 M KPi (pH 7) or 0.1 M KOH (pH 13). (A) – EXAFS coordination numbers, (B) – interatomic distances, (C) – Debye-Waller parameters. During the simulation, the sum of the coordination numbers for the two oxygen shells was kept equal to six and the same Debye-Waller parameter was used for each of the two oxygen shells. The Debye-Waller parameters for the last two Mn-Mn shells were fixed to 0.063 Å. The errors represent a 68% confidence interval.

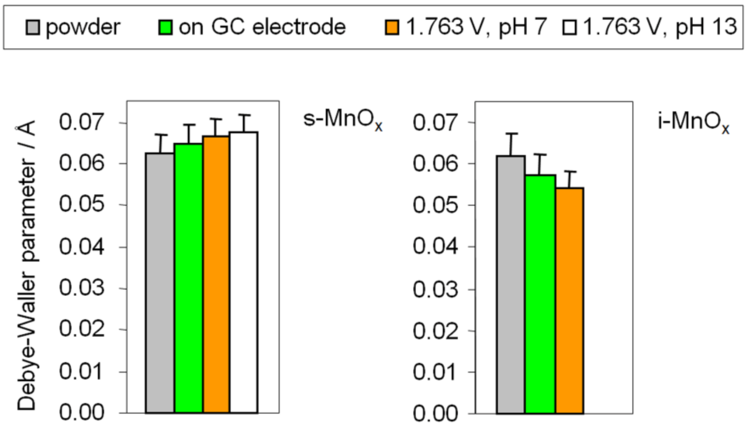

Figure A6: Debye-Waller parameters for the oxygen shell of backscattering atoms. The other fit parameters are presented in Fig. 3 in the main text.

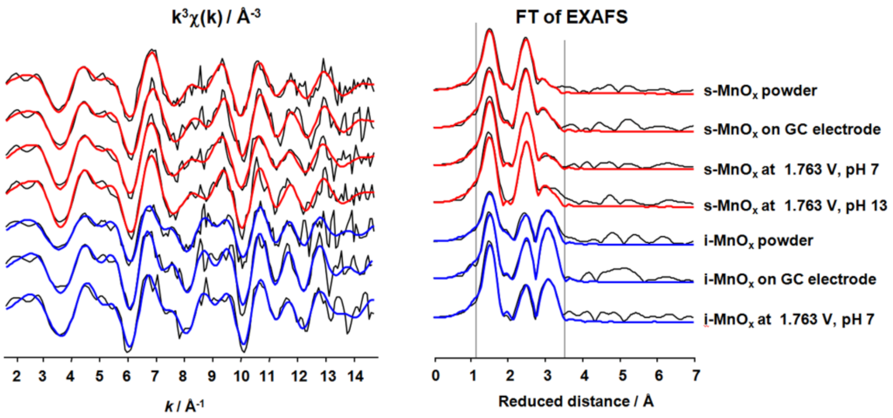

Figure A7: k^3-weighted experimental EXAFS spectra of the studied Mn oxides (thin black lines) and the joint-fit simulation result (red lines for s-MnOx, blue for the i-MnOx). The fit parameters are given in Fig. 3 of the main manuscript. The grey vertical lines indicate the range used to calculate the RF error factor. The averaged RF-values equalled 15.1% for the joint-fit simulation approach and 13.6% for simulations with independently variable interatomic distances

.

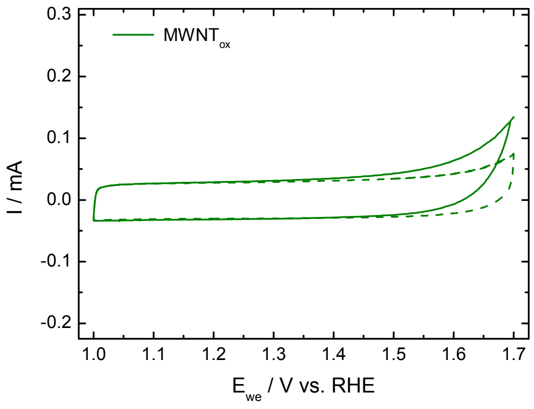

Figure A8: First (solid) and 11th (dashed) voltammogram of MWNTox (without catalyst) recorded in 0.1 M KPi at pH 7 with a scan rate of 100 mV s^{-1}.

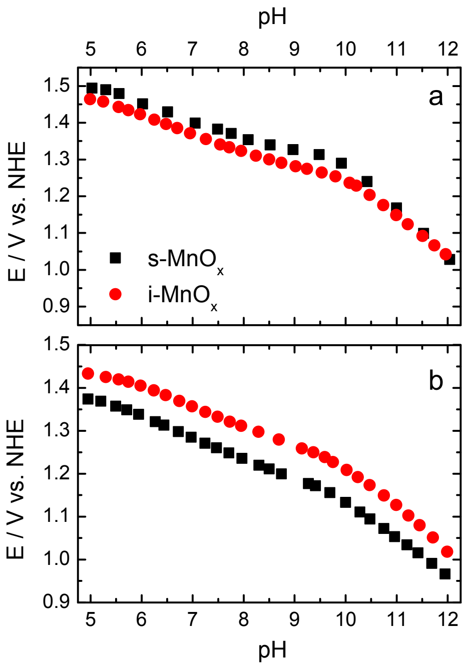

Figure A9: pH dependence of the electrode potential vs. NHE at a constant current of (a) 50 µA and (b) 20 µA recorded during titration of aliquots of 40 wt.% KOH into 0.1 M KPi increasing the pH between 5 and 12. At each pH values the corresponding potential was detected after equilibration for 3 min.

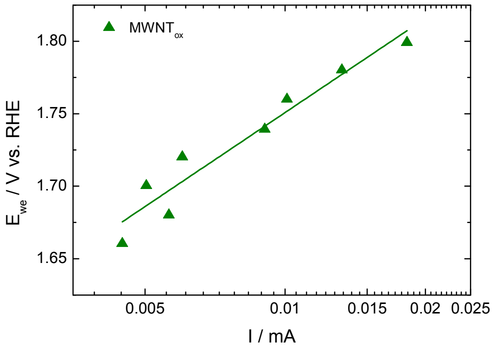

Figure A10: Background current of MWNTox without deposited catalysts. The Tafel plot of MWNT$_{ox}$ in 0.1 M KPi at pH 7 was extracted from quasi-stationary potential-step RDE experiments at a rotation speed of 1600 rpm. All electrode potentials have been iR-corrected. We note that the current values are significantly lower than the corresponding figures in the presence of the investigated Mn oxide catalysts. The Tafel slope was determined to 216 mV dec-1 from linear regression between 1.675 and 1.8 V.

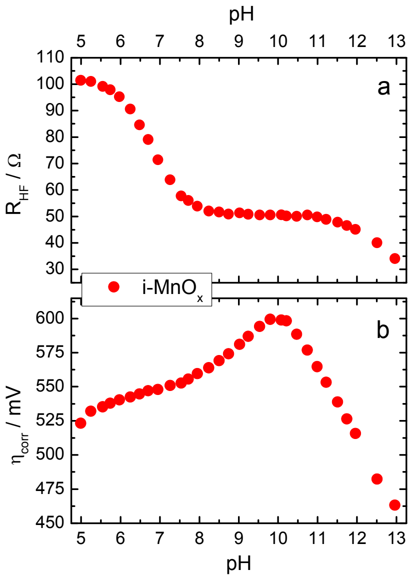

Figure A11: pH dependence of electrolyte resistance (a) and η-pH profile after correction for ohmic losses (iR correction) (b). In (a), the high frequency resistance RHF of the bulk electrolyte has been determined via electrochemical impedance spectroscopy at 1.35 V vs. NHE. The pH was adjusted via titration of aliquots of 40 wt.% KOH.

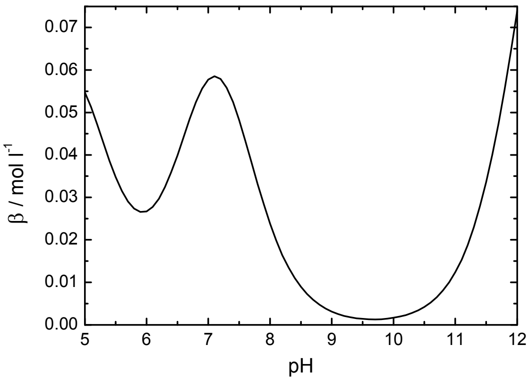

Figure A12: pH dependence of the calculated buffer strength (β). For a concentration of the potassium phosphate buffer of 0.1 M, the buffer strength was calculated as described in ref.[195]

A2 Supplementary Information to Chapter 5[68]

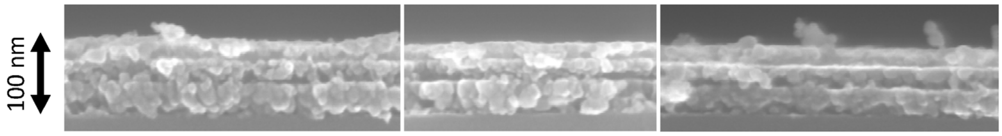

Figure A13: Cross-section scanning electron micrographs of as-prepared Co_3O_4 films deposited on Si (100) wafer. Film thickness is 85 ± 8 nm. The Co loading of the same sample is 294 ± 14 $nmol_{Co} \cdot cm^{-2}$ as determined from ICP-OES. The porosity of the Co_3O_4 films is 0.46 by assuming ideal Co_3O_4 with a molecular weight of 240.7956 $g \cdot mol^{-1}$ and a density ρ of 6.07 $g \cdot cm^{-3}$.

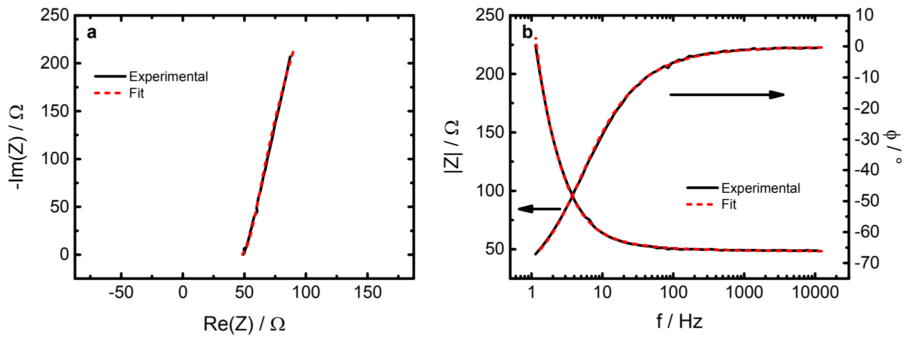

Figure A14: Potentiostatic electrochemical impedance spectra of Co_3O_4 films deposited on glassy carbon recorded at 1.0 V. Impedance spectra were fitted using an equivalent electrical circuit consisting of a serial connection of an Ohmic resistance, RC circuit and a constant phase element. A specific capacitance of 35 μF cm^{-2} was used to calculate ECSA from the determined capacitance.[51]

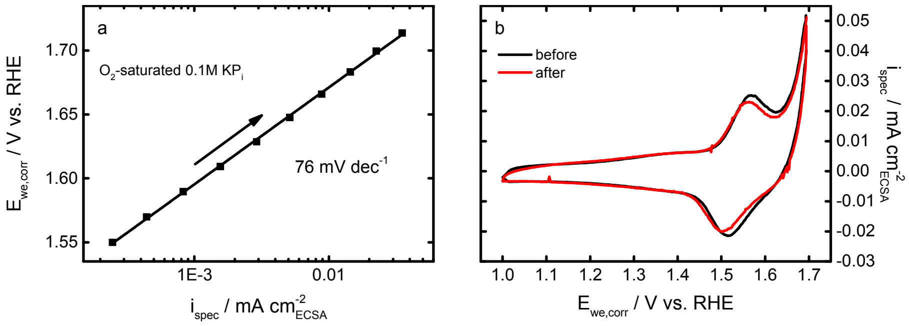

Figure A15: Quasi-stationary anodic potential step experiment of Co_3O_4 films performed in O_2-saturated 0.1M KP_i (a) and cyclic voltammograms (b) recorded at 50 mV/s in N_2-saturated 0.1M KPi at pH 7 before (black) and after (red) the quasi-stationary cathodic potential step experiment performed in O_2-saturated electrolyte. The Tafel slope is 76 mV/dec while the exchange current density is $1.52 \cdot 10^{-8}$ $mA \cdot cm^{-2}_{ECSA}$. Current was normalized using the initial ECSA as determined by PEIS. Electrode potentials were corrected for Ohmic losses using PEIS.

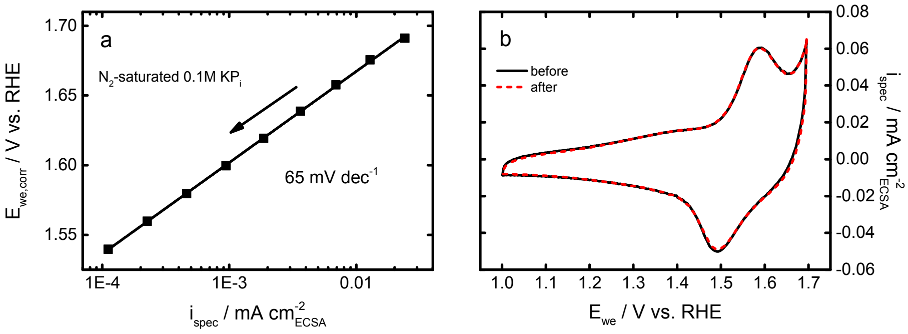

Figure A16: Quasi-stationary cathodic potential step experiment of Co_3O_4 films performed in N_2-saturated 0.1M KP_i (a) and cyclic voltammograms (b) recorded at 100 mV/s in N_2-saturated 0.1M KPi at pH 7 before (black) and after (red, dashed) the quasi-stationary cathodic potential step experiment. The Tafel slope is 65 mV dec^{-1} while the exchange current density is $2.09 \cdot 10^{-9}$ mA cm$^{-2}_{ECSA}$. Current was normalized using the initial ECSA as determined by PEIS. Electrode potentials were corrected for Ohmic losses using PEIS.

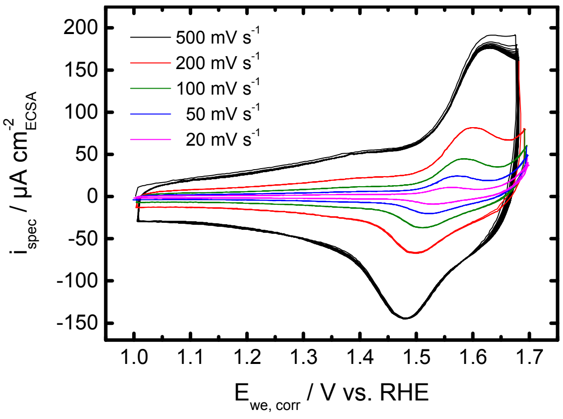

Figure A17: Series of cyclic voltammograms of Co_3O_4 thin films recorded at the given sweep rates in N_2-sat. 0.1M KPi at pH 7. The cyclic voltammograms were recorded after two initial CVs recorded with a sweep rate of 6 mV s^{-1} between 1.0 and 1.76 V as shown in Figure A18. Current was normalized using the initial ECSA as determined by PEIS. Electrode potentials were corrected for Ohmic losses using PEIS.

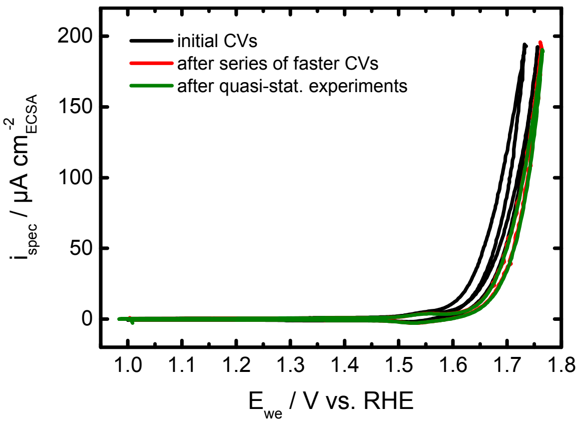

Figure A18: Cyclic voltammograms of Co_3O_4 thin films recorded at 6 mV s^{-1} in N_2-saturated 0.1M KPi at pH 7 at different stages of the electrochemical characterization protocol. The initial irreversible loss of current can be explained by the electrochemical oxidation of organic, carbonaceous residues adsorbed on the Co_3O_4 surface. Current was normalized using the initial ECSA as determined by PEIS prior to OER. Electrode potentials were corrected for Ohmic losses using PEIS.

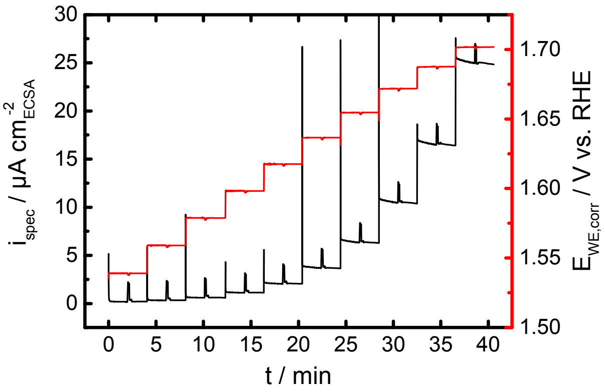

Figure A19: Current and potential vs. time profile of quasi-stationary potential step experiments of Co_3O_4 films recorded in anodic direction in N_2-saturated 0.1M KPi at pH 7. Each electrode potential was hold for ~4 min and an electrochemical impedance spectra (current spikes) was recorded at each potential step. Current was normalized using the initial ECSA as determined by PEIS. Electrode potentials were corrected for Ohmic losses using PEIS.

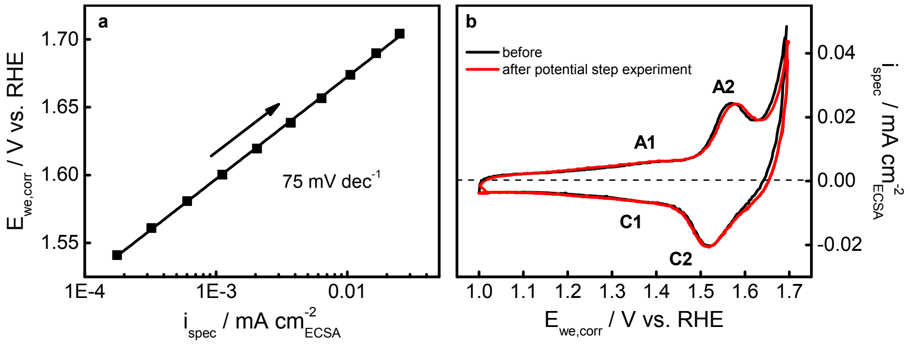

Figure A20: Tafel plot (a) and cyclic voltammograms (b) of Co_3O_4 thin films recorded at 50 mV s^{-1} in N_2-saturated 0.1M KPi at pH 7 before and after the quasi-stationary anodic potential step experiment. Current was normalized using the initial ECSA as determined by PEIS. Electrode potentials were corrected for Ohmic losses using PEIS.

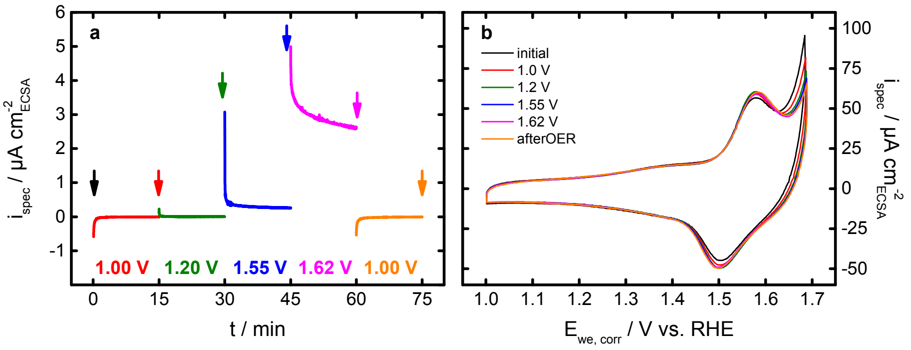

Figure A21: Current-time profile (a) of potential step experiments at the electrode potentials selected for in situ characterization and cyclic voltammograms (b) recorded with 100 mV s^{-1} after 15 min at the corresponding electrode potentials. The 10th cycle is shown. N_2-saturated 0.1M KPi at pH 7 acted as electrolyte. Current was normalized using the initial ECSA as determined by PEIS. Electrode potentials were corrected for Ohmic losses using PEIS.

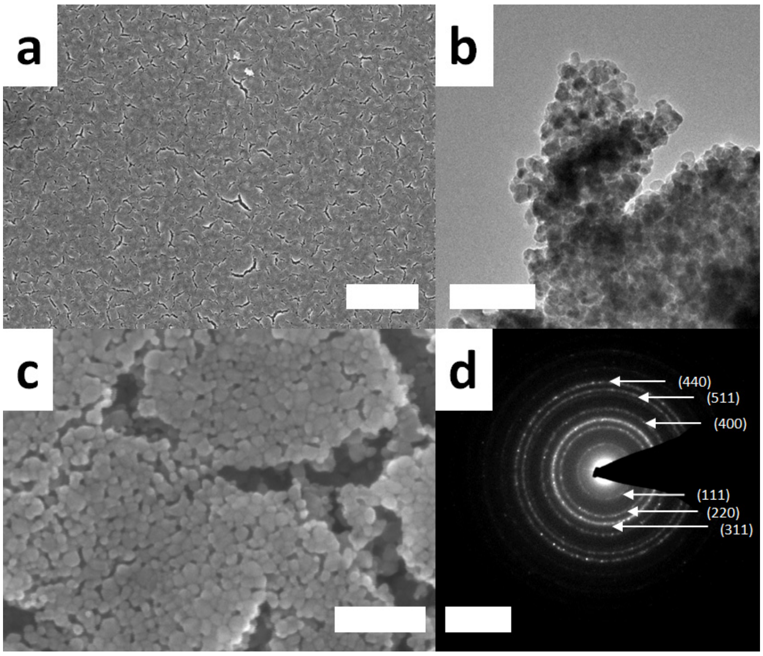

Figure A22: Scanning electron micrographs in low (A) and high magnification (C), transmission electron micrograph (B) and selected area electron diffraction (SAED) pattern (D) of Co_3O_4 films after OER. Diffraction rings of Co_3O_4 are indexed in the SAED pattern. Micrographs and diffraction pattern were recorded after 15 min of OER at 1.62 V in 0.1M KP_i. After 15 min of OER at 1.62 V in 0.1M KPi approximately 1% of the initial Co loading was dissolved in the electrolyte. The scale bars represent 2 µm, 50 nm, 100 nm, and 5 nm^{-1} in panel a, b, c, and d, respectively.

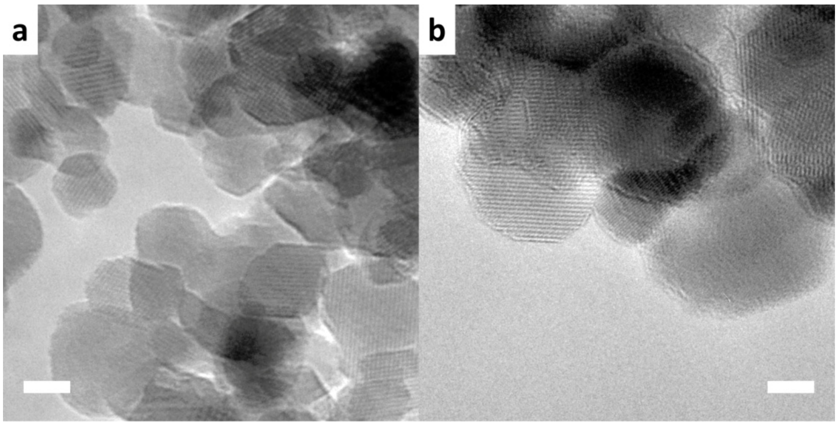

Figure A23: Transmission electron micrograph of Co_3O_4 films (a) in the as-prepared state and (b) after 15 min at 1.62 V in 0.1M KPi at pH 7 without electrochemical reduction after electrocatalysis in the left and right panel, respectively. Transmission electron micrographs recorded after OER show no presence of a restructuring in the near-surface due to cationic redistribution but some defects in the outermost surface layer of the Co_3O_4 crystallites. The scale bars represent 5 nm.

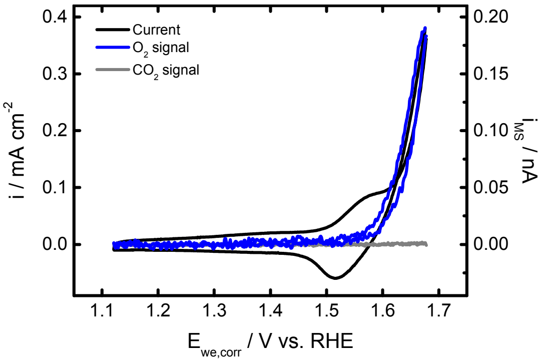

Figure A24: Cyclic voltammogram (black) of Co_3O_4 film deposited on glassy carbon recorded at 6 mV s^{-1} in 0.1M KPi at pH 7 as well as the corresponding signals of m/z=32 (blue) and m/z=44 (grey) corresponding to the signals of O_2 and CO_2, respectively. The electrode potential was corrected for Ohmic losses using PEIS and current was normalized using geometrical sample area.

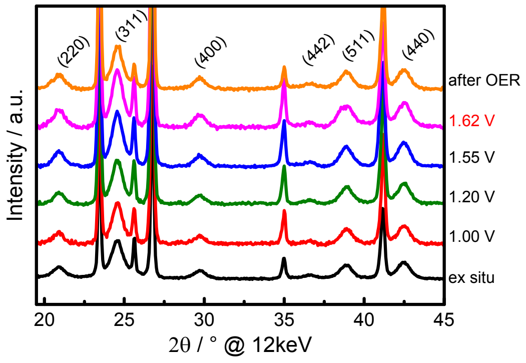

Figure A25: *in situ* X-ray diffraction patterns of Co_3O_4 catalyst films. The diffraction patterns were recorded using grazing-incident excitation at α=0.3° and 12 keV. The electrode potential was increased stepwise from 1.0 V to 1.62 V vs. RHE, the latter representing the catalytically active state, in 0.1 M KPi at pH 7. The state after OER is a dry state for which the electrode was removed from electrolyte at 1.0 V rinsed with de-ionized water and dried in N_2 flow. The Miller indices of selected Co_3O_4 reflections are indicated. Diffraction pattern were background corrected for better visualization.

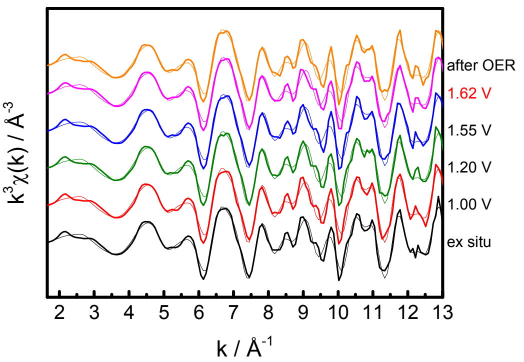

Figure A26: quasi-*in situ* k^3-weighted EXAFS spectra of Co_3O_4 thin films recorded at Co *K*-edge as a function of catalyst state. Experimental and simulated spectra are shown in bold and thin, respectively. Samples were freeze-quenched using liquid N_2 under electrochemical potential control after electrochemical conditioning for 15 min at the given potential in 0.1M KPi at pH 7.

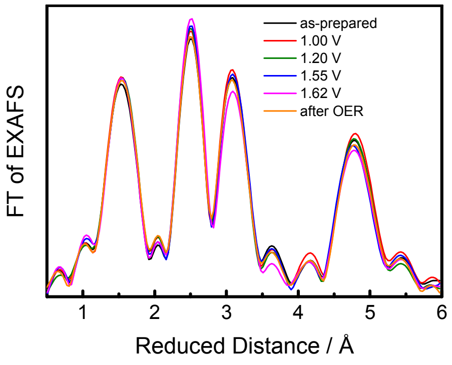

Figure A27: quasi-*in situ* FT of EXAFS spectra of Co_3O_4 films recorded at Co *K*-edge as function of catalyst state. Samples were freeze-quenched using liquid N_2 under electrochemical potential control after electrochemical conditioning for 15 min at the given potential in 0.1M KPi at pH 7.

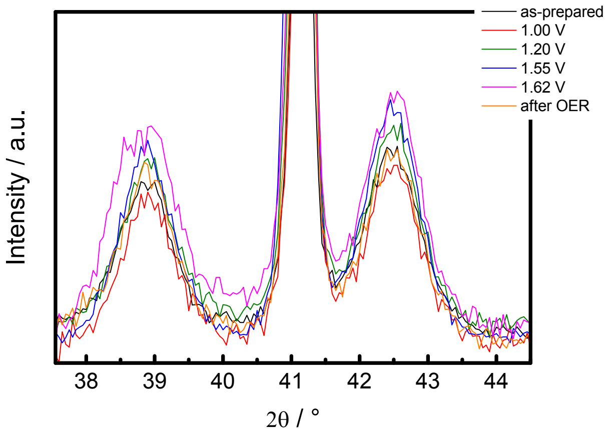

Figure A28: *in situ* X-ray diffraction patterns of Co_3O_4 catalyst films. The diffraction patterns were recorded using grazing-incident excitation at α=0.3° and 12 keV. The electrode potential was increased stepwise from 1.0 V to 1.62 V vs. RHE, the latter representing the catalytically active state, in 0.1 M KPi at pH 7. The state after OER is a dry state for which the electrode was removed from electrolyte at 1.0 V rinsed with de-ionized water and dried in N_2 flow. Diffraction pattern were background corrected for better visualization.

Table 7: Fit results for Co_3O_4(511) and Co_3O_4(440) reflections of the *in situ* X-ray diffraction of thin films as function of catalyst state. Fitting was performed using pseudo-Voigt profiles. The error of the fit parameters represents one estimated standard deviation. The structural coherence length was determined from the integral breadth in the Scherrer equation. A shape factor of 0.89 was used.

Co_3O_4(511)	**as-prepared**	**1.00V**	**1.20V**	**1.55V**	**1.62V**	**after OER**
2θ / °	38.861	38.906	38.900	38.878	38.859	38.885
Error	0.005	0.009	0.007	0.006	0.01	0.008
d / Å	1.5511	1.5494	1.5494	1.5505	1.5512	1.5502
Error	4E-4	7E-4	7E-4	5E-4	7E-4	7E-4
Height/ cts	123	70	73	86	99	74
Error	2	2	1	1	2	2
Area/ cts·°	2969	1691	1638	1846	2767	1709
Error	56	50	42	43	76	47
FWHM / °	0.936	0.95	0.91	0.943	1.13	0.91
Error	0.018	0.02	0.02	0.019	0.03	0.02
IB / °	1.20	1.20	1.12	1.07	1.39	1.15
Error	0.04	0.07	0.04	0.03	0.06	0.06
CL_{IB} / nm	4.62	4.6	4.97	5.19	3.99	4.8
Error	0.16	0.2	0.19	0.18	0.19	0.2

Co_3O_4(440)	**as-prepared**	**1.00V**	**1.20V**	**1.55V**	**1.62V**	**after OER**
2θ / °	42.48	42.495	42.493	42.484	42.504	42.491
Error	0.005	0.007	0.006	0.005	0.008	0.008
d / Å	1.424	1.4238	1.4239	1.4242	1.4236	1.4240
Error	3E-4	5E-4	4E-4	3E-4	7E-4	5E-4
Height/ cts	147	81	88	105	112	82
Error	2	1	1	1	2	1
Area/ cts·°	3405	1742	1823	2151	2749	1655
Error	61	43	39	41	75	42
FWHM / °	0.949	0.91	0.893	0.910	0.97	0.92
Error	0.015	0.02	0.018	0.015	0.02	0.02
IB / °	1.15	1.06	1.03	1.02	1.22	1.00
Error	0.03	0.03	0.03	0.02	0.05	0.03
CL_{IB} / nm	4.87	5.30	5.45	5.51	4.6	5.5
Error	0.15	0.19	0.17	0.15	0.2	0.2

Table 8: Simulation results for the fits of the k^3-weighted EXAFS spectra of Co_3O_4 thin films as a function of catalyst state. The error ranges of the fit parameters were estimated from the covariance matrix of the fit and represent the 68% confidence intervals.[141]

Shell	**Sample**	**ASP**	**1.00V**	**1.20V**	**1.55V**	**1.62V**	**after OER**
Co-O	*N*	5.30	5.44	5.45	5.42	5.40	5.34
R = 1.908 +/- 0.001 Å	Error of *N*	0.2	0.2	0.2	0.2	0.2	0.2
σ = 0.046 +/- 0.002 Å							
Co-Co	*N*	4.63	4.73	4.76	4.83	5.01	4.61
R = 2.851 +/- 0.001 Å	Error of *N*	0.2	0.2	0.2	0.2	0.2	0.2
σ = 0.052 +/- 0.001 Å							
Co-Co	*N*	6.81	7.03	6.72	6.84	6.3	6.77
R = 3.357 +/- 0.001 Å	Error of *N*	0.3	0.3	0.3	0.3	0.3	0.3
σ = 0.052 +/- 0.001 Å							
Co-Co	*N*	7.73	7.37	7.7	7.98	7.27	7.29
R = 4.986 +/- 0.003 Å	Error of *N*	0.9	0.9	0.9	0.9	0.9	0.9
σ = 0.052 +/- 0.001 Å							
Co-Co	*N*	10.98	12.14	10.85	9.28	9.98	10.62
R = 5.315 +/- 0.002 Å	Error of *N*	1.1	1.1	1.1	1.1	1.1	1.1
σ = 0.052 +/- 0.001 Å							
Co-Co-Co, multiple scattering from di-µ-oxo bridged Co on a straight line	*N*	1.17	1.3	1.09	1.09	1.11	1.09
	Error of *N*	0.4	0.4	0.4	0.4	0.4	0.4
R = 5.703 +/- 0.002 Å							
σ = 0.052 +/- 0.001 Å							
Rf		10.95	12.38	12.7	12.19	12.39	13.16

Surface chemistry and electronic structure

For further insight in the elemental composition, atomic and electronic structure of the near-surface of the Co_3O_4 crystallites at the electrode/electrolyte interface before and after OER, we conducted synchrotron-based XPS and XANES at Co *L*- and O *K*-edge experiments on the Co_3O_4 films. Figure A29a and b show Co 2p XPS and the Co L_3 XANES spectra of Co_3O_4 films, respectively. The Co 2p spectrum of the Co_3O_4 shows two peaks at 779.7 and 794.7 eV arising from Co $2p_{3/2}$ and Co $2p_{1/2}$ states, respectively. The main $2p_{3/2}$ satellite at ~789 eV and the weaker satellite at ~786 eV are characteristic for a Co oxide containing mainly Co_3O_4 in the near-surface. Both spectra support the notion of a Co oxide containing mainly Co_3O_4 in the near-surface of the crystallites.[33] We note that due to the more pronounced fine structure at the low energy side of the Co L_3 absorption peak, the presence of a minor fraction of Co^{2+} O_h in the near-surface is possible (cf. Figure A31). The oxygen 1s XPS showed that the near-surface of the as-prepared state incorporated protonated oxygen atoms in addition to lattice oxygen. (cf. Figure A29c and Figure A32) Oxygen ions incorporated in the crystal lattice give rise to a peak at 530 eV, whereas the broad shoulder at ~531.5 eV is mainly caused by hydroxylated O.[33] Additionally, traces of adsorbed water are present leading to a contribution at ~533 eV.[33] The strong pre-edge feature of oxygen *K*-edge XANES spectrum revealed significant hybridization of Co 3d and O 2p orbitals. The main absorption edge and the features above are assigned to electron transitions from the O 1s to hybridized orbitals of O 2p with Co 4s/4p states.[36, 182] (cf. Figure A29d) Thus, the near-surface of the as-prepared state consists of primarily Co_3O_4 with possible minor contribution of additional Co^{2+} O_h ions. The O/Co ratio (at photoelectron kinetic energy of 550 eV) is 1.48 and the fraction of lattice O is 54.4%.

After OER, the near-surface of the Co_3O_4 crystallites was largely unchanged; XPS and XANES spectra showed almost identical profiles when compared to the as-prepared catalyst material. Minor differences can be accounted for by adsorption of phosphate ions (P/Co=0.05) during operation of the catalyst film in the phosphate-containing electrolyte.(cf. Figure A30) The presence of the phosphate ions in the near-surface after OER also influences the O 1s spectrum (increased intensity at ~531 eV[33]) and the O K-edge absorption spectrum (additional feature between 535 and 540 eV).[180] We conclude that the increase of the O/Co ratio to 1.57 is thus primarily caused by the presence of the phosphate ions. We conclude that the identified reversibility of the structural transformation observed by X-ray diffraction and X-ray absorption spectroscopy at the Co *K*-edge is fully supported by our surface-sensitive spectroscopic.

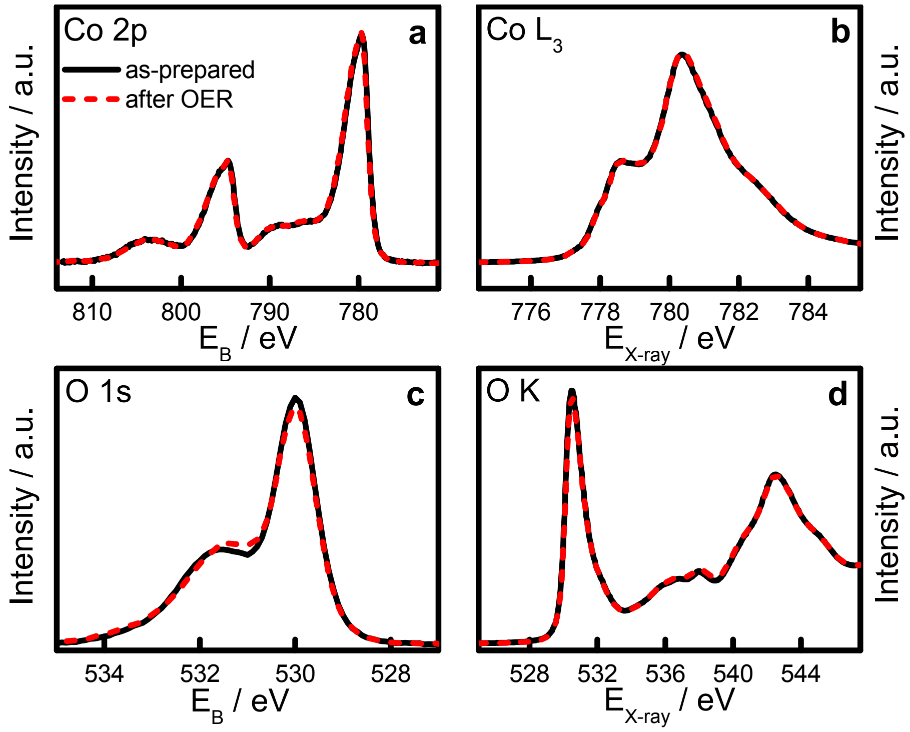

Figure A29: X-ray photoelectron spectra of Co 2p (a), O 1s (c) as well as XANES spectra recorded at Co L_3-(b) and O K-edge (d) of Co_3O_4 thin films prepared on GC. XPS spectra were recorded at photoelectron kinetic energy of 550 eV. XANES spectra were recorded in total-electron yield mode.

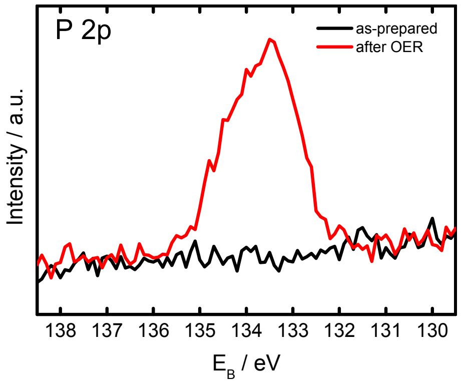

Figure A30: X-ray photoelectron spectra of P 2p recorded using as prepared Co_3O_4 thin films as prepared on glassy carbon and after 15 min of OER at 1.62 V in 0.1M KPi at pH 7. XPS spectra were recorded at photoelectron kinetic energy of 550 eV.

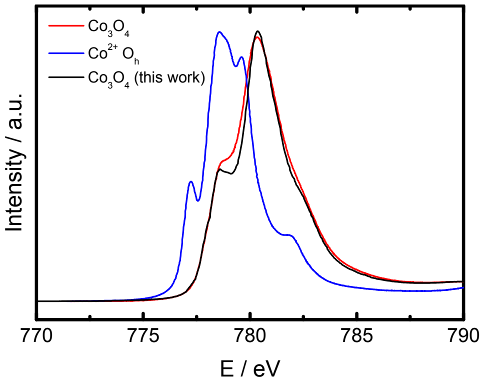

Figure A31: Co L_3-XANES spectra of Co_3O_4 thin films in the as-prepared state as well as of Co_3O_4 and Co^{2+} O_h references.[179] XANES spectra were recorded in total-electron yield mode.

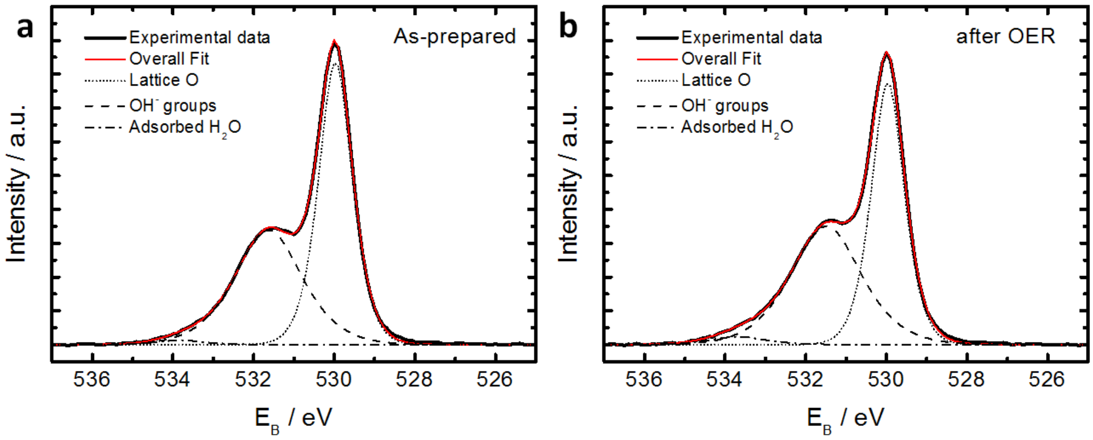

Figure A32: Fits of O 1s spectra of Co_3O_4 thin films as-prepared (a) and after oxygen evolution (b). XPS spectra were recorded at photoelectron kinetic energy of 550 eV. The fit of hydroxyl groups includes also contributions from oxygen species in phosphate molecules.

A3 Supplementary Information to Chapter 6

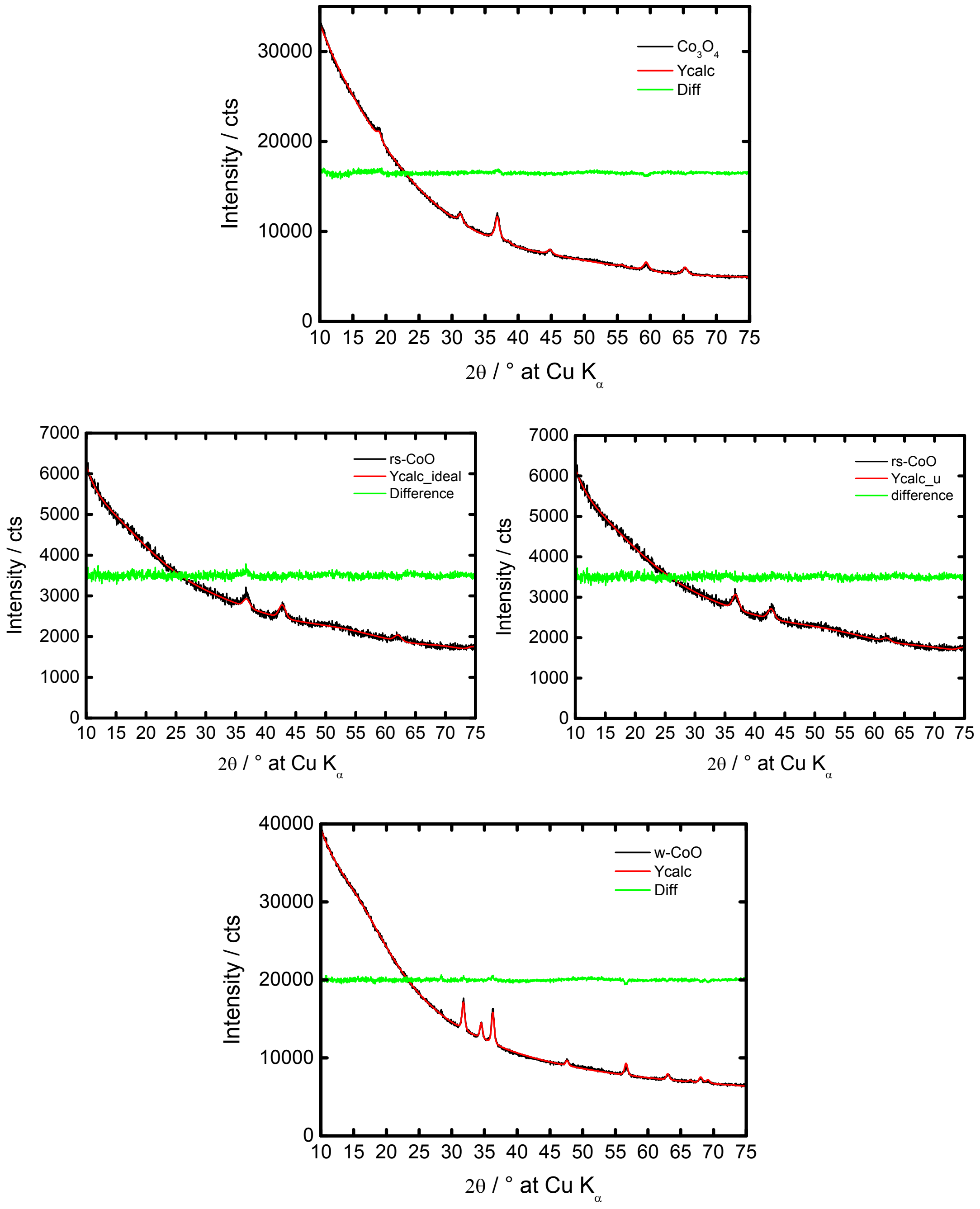

Figure A33: Results of the Rietveld Refinement of Co_3O_4, rs-CoO and w-CoO in the upper, middle and lower panel, respectively. Experimental data are shown in black, calculated patterns (Ycalc) in red, and difference (Diff) in green. $R_{wp'}$ = 2.92, 73.92, 9.38, and 1.43 for Co_3O_4, rs-CoO with ideal occupancy and symmetrical Co^{2+} octahedra, rs-CoO with ideal occupancy and asymmetrical Co^{2+} octahedra, and w-CoO, respectively. The symmetry of the Co^{2+} octahedra were refined via the O position u in the unit cell leading to $u_x = u_y = 0.505$ and $u_z = 0.46 \pm 0.03$ in contrast to the ideal case in which $u_x = u_y = u_z = 0.5$.

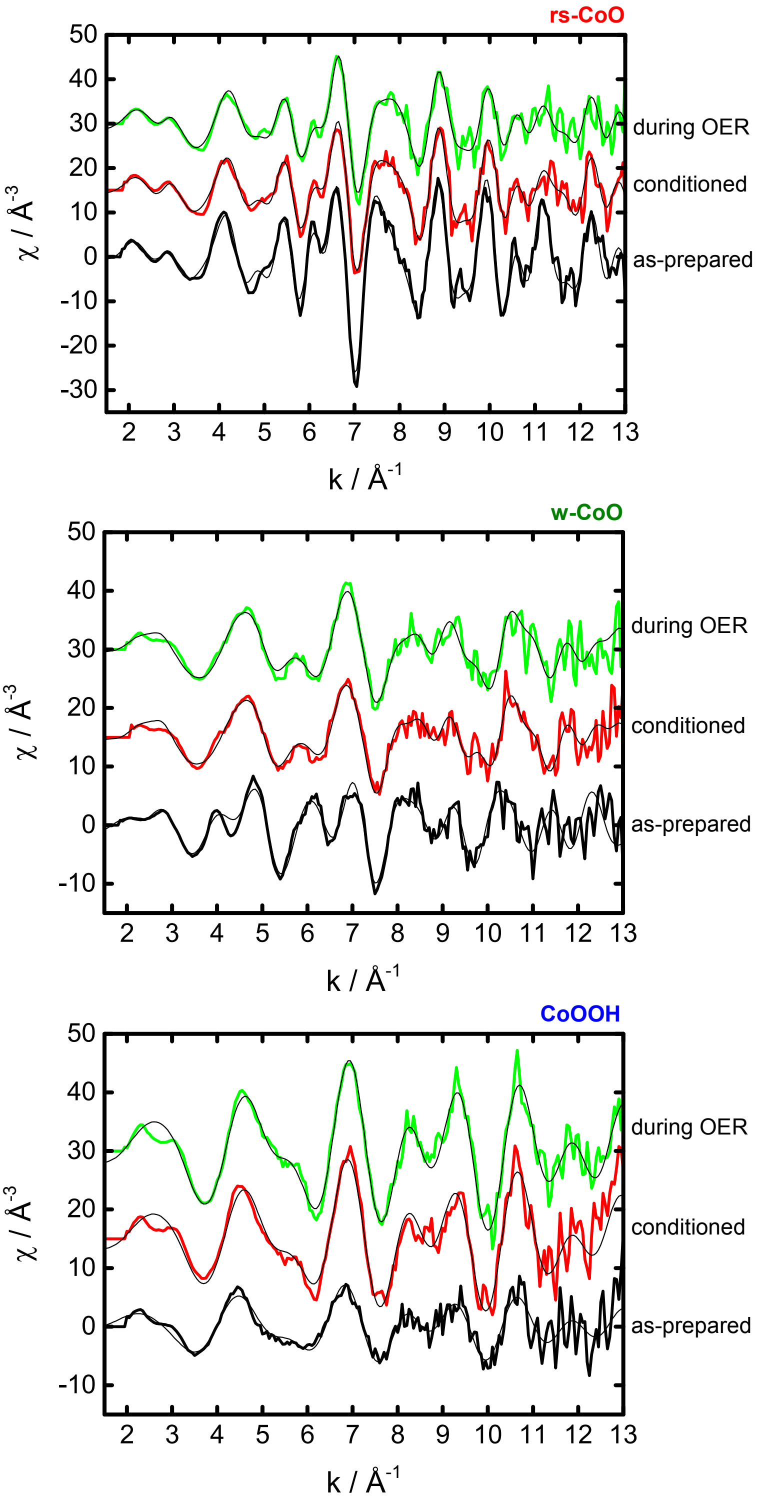

Figure A34: EXAFS spectra of rs-CoO, w-CoO, and CoOOH in the upper, middle and lower panel, respectively. Experimental data of the as-prepared state, the OER-conditioned state and during OER are shown in black, red, and green, respectively. The simulated spectra are shown in thin black lines. Fitting of the k^3-weighted data was done in k-space between 2.0 and 12 Å^{-1} for rs- and w-CoO as well as 3 to 12 Å^{-1} for CoOOH. The fit results are shown in Table 9 - Table 11.

Table 9: Results of simulation of the EXAFS spectra of rs-CoO, w-CoO, and CoOOH in the as-prepared state. The experimental and simulated spectra are shown in Figure A34.

Rs-CoO	**Co-O**	**Co-O**	**Co-Co**	**Co-O**	**Co-Co**	**Co-Co**	**Co-Co**	**Co-Co**	**Co-Co**	**Co-Co**
R / Å	2.135	1.984	3.003	3.707	3.985	4.357	4.821	5.142	5.274	5.823
error	0.008	0.02	0.002	0.028	0.012	0.006	0.018	0.049	0.033	0.006
σ / Å	0.067	0.067	0.077	0.067	0.032	0.032	0.032	0.077	0.077	0.077
error	0.012	0.012	0.12	0.012	0.014	0.014	0.014	0.011	0.011	0.011
N	4.45	0.394	12.1	2.92	1.77	4.73	2.32	16.6	31.1	28
error	0.61	0.5	0.32	1.6	0.61	0	1.3	8.3	9.6	6.8
Rf	**13.38**									

w-CoO	**Co-O**	**Co-Co**	**Co-O**	**Co-Co**
R / Å	1.971	3.228	3.746	4.563
error	0.016	0.014	0.043	0.033
σ / Å	0.0489	0.0774	0.0489	0.0774
error	0.01	0.017	0.01	0.017
N	3.2	6.38	5.99	4.7
error	0.6	2.5	3	3.1
Rf	**14.2**			

CoOOH	**Co-O**	**Co-Co**
R / Å	1.887	2.825
error	0.048	0.045
σ / Å	0.0588	0.0481
error	0.041	0.058
N	3.64	1.65
error	2.7	2.8
Rf	**22.08**	

Table 10: Results of simulation of the EXAFS spectra of rs-CoO, w-CoO, and CoOOH at 1.2 V after OER-conditioning. The differences between as-prepared state and the state at 1.2 V in case of rs-, w-CoO and CoOOH after OER conditioning are given. The experimental and simulated spectra are shown in Figure A34.

Rs-CoO	**Co-O**	**Co-O**	**Co-Co**	**Co-Co**	**Co-Co**	**Co-O**	**Co-Co**	**Co-Co**	**Co-Co**	**Co-Co**	**Co-Co**	**Co-Co**
R / Å	2.135	1.984	2.875	3.003	3.35	3.707	4.821	3.985	4.357	5.137	5.274	5.823
error	0.008	0.02	0.009	0.002	-	0.020	0.018	0.012	0.006	0.04	0.03	0.006
σ / Å	0.067	0.067	0.032	0.077	0.077	0.067	0.032	0.032	0.032	0.077	0.077	0.077
error	0.012	0.012	0.016	0.12	0.12	0.012	0.014	0.014	0.014	0.011	0.011	0.011
N	1.9	1.7	1.3	10.6	0.04	4.5	2.9	1.6	3.1	11	18	18
error	0.4	0.3	0.3	0.6	0.71	1.9	1.1	0.5	0.7	5	7	5
Rf	**8.301**											

w-CoO	**Co-O**	**Co-Co**	**Co-Co**	**Co-Co**	**Co-Co**	**Co-Co**
R / Å	1.932	2.839	3.185	5.26	3.351	5.014
error	0.014	0.029	0.08	0.042	0.048	0.037
σ / Å	0.0489	0.0771	0.0774	0.0771	0.0771	0.0771
error	0.01	0.025	0.017	0.025	0.025	0.025
N	3.9	2.61	3	6.03	3	5.3
error	0.6	1.7	2	7	3	6.3
Rf	**12.88**					

CoOOH	**Co-O**	**Co-Co**
R / Å	1.906	2.84
error	0.023	0.023
σ / Å	0.0385	0.0609
error	0.03	0.03
N	5.09	4.22
error	2.1	3.1
Rf	**9.812**	

Table 11: Results of simulation of the EXAFS spectra of rs-CoO, w-CoO, and CoOOH during OER. The experimental and simulated spectra are shown in Figure A34.

Rs-CoO	**Co-O**	**Co-O**	**Co-Co**	**Co-Co**	**Co-Co**	**Co-O**	**Co-Co**	**Co-Co**	**Co-Co**	**Co-Co**	**Co-Co**	**Co-Co**
R / Å	2.135	1.95	2.862	3.003	3.35	3.707	3.985	4.357	4.821	5.13	5.27	5.823
error	0.008	0.014	0.008	0.002	-	0.028	0.012	0.006	0.018	0.04	0.03	0.006
σ / Å	0.067	0.067	0.032	0.07	0.07	0.067	0.032	0.032	0.032	0.077	0.077	0.077
error	0.012	0.012	0.016	0.12	0.12	0.012	0.014	0.014	0.014	0.011	0.011	0.011
N	2.4	2.0	1.7	10.2	0.4	3.0	0.8	3.0	2.6	7	15	14
error	0.4	0.3	0.4	0.7	1.9	1.9	0.4	0.7	0.9	5	4	3
Rf	**10.1**											

w-CoO	**Co-O**	**Co-Co**	**Co-Co**	**Co-Co**	**Co-Co**	**Co-Co**
R / Å	1.91	2.833	3.185	5.26	3.351	5.014
error	0.014	0.022	0.08	0.042	0.048	0.037
σ / Å	0.0489	0.077	0.077	0.077	0.077	0.077
error	0.01	0.025	0.017	0.025	0.025	0.025
N	3.99	3.22	2.37	4.55	2.82	4.95
error	0.65	1.9	2.1	6.2	2.9	5.7
Rf	**11.48**					

CoOOH	**Co-O**	**Co-Co**
R / Å	1.887	2.830
error	0.022	0.021
σ / Å	0.0456	0.0584
error	0.027	0.028
N	5.63	4.61
error	2.2	3
Rf	**5.368**	

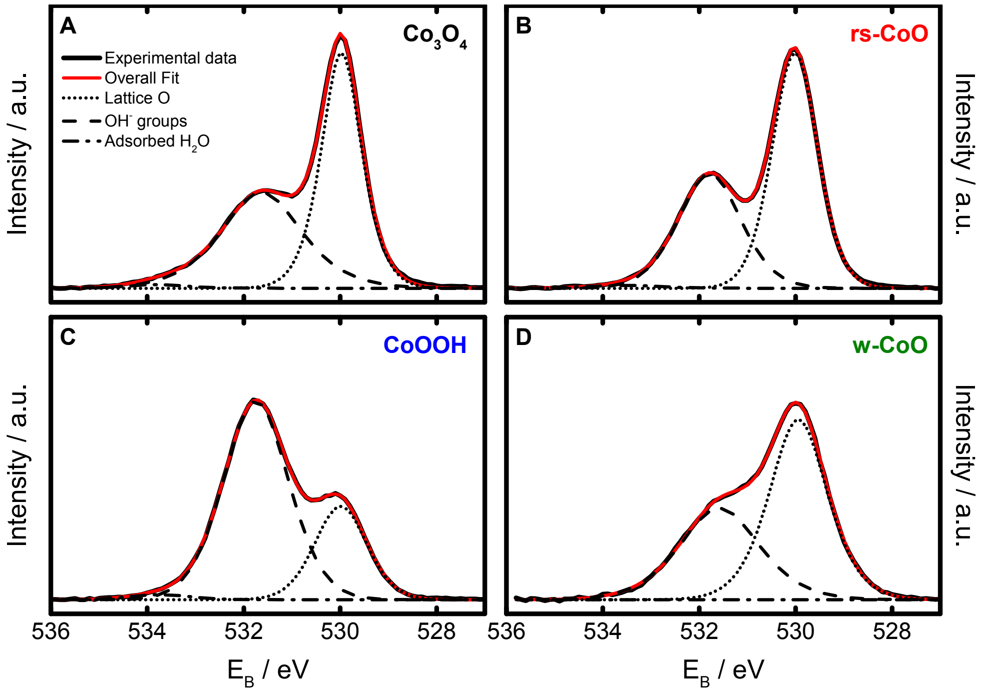

Figure A35: Fits of the O 1s spectra of Co_3O_4(A), rs-CoO(B), CoOOH(C) and w-CoO(D) in the as-prepared state. The spectra were recorded at a kinetic energy of the electrons of 550 eV.

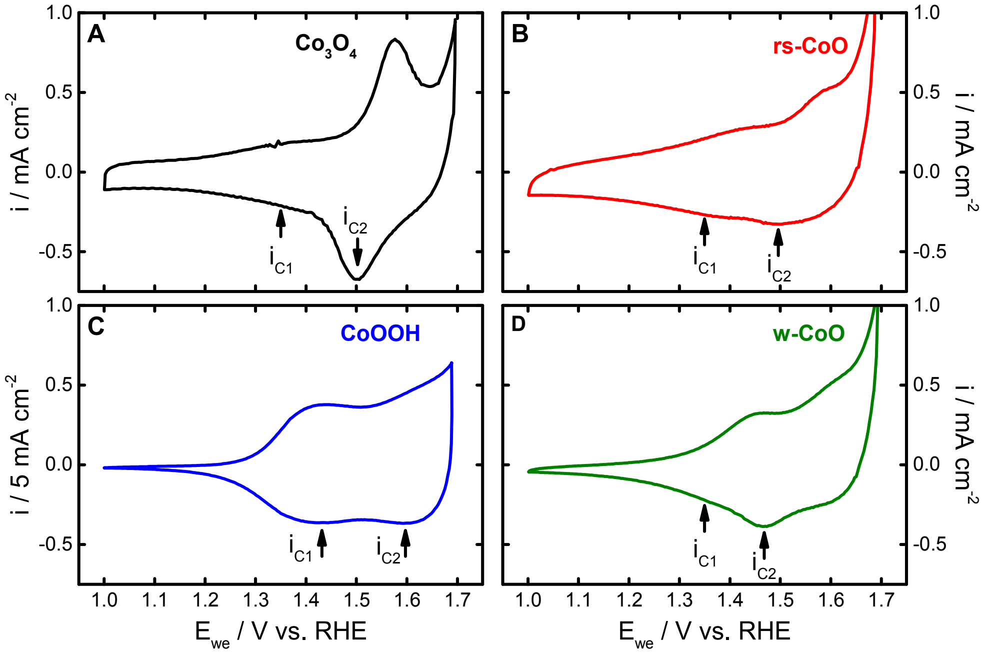

Figure A36: Cyclic voltammograms of Co_3O_4(A), rs-CoO(B), CoOOH(C) and w-CoO(D) recorded with a sweep rate of 200 mV s^{-1} in 0.1M KPi at pH7 after OER conditioning. The potentials where the reductive current of C1 and C2 was extracted are denoted.

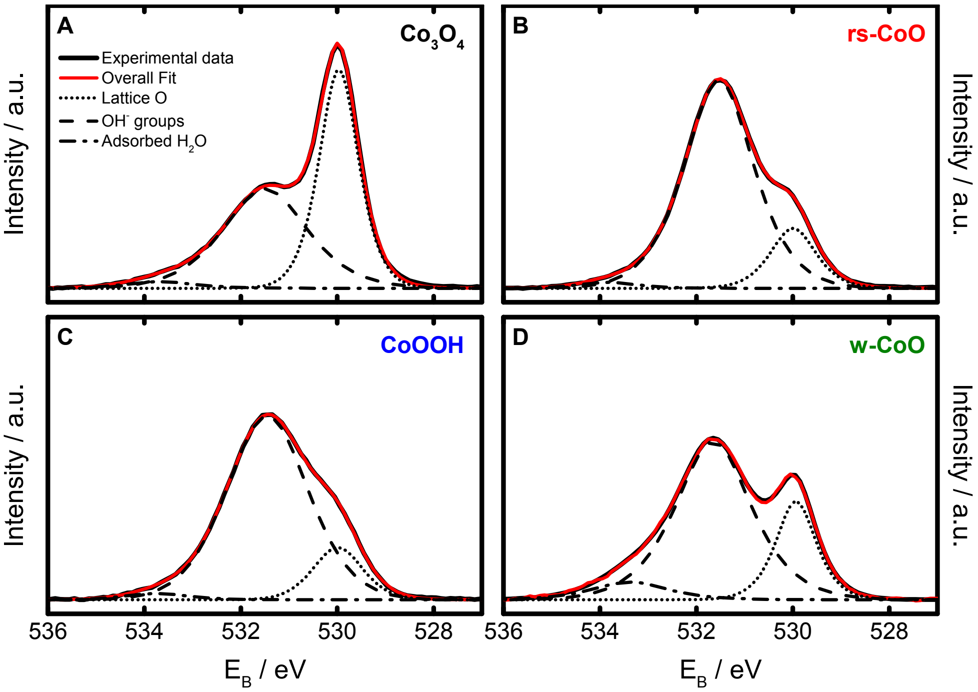

Figure A37: Fits of the O 1s spectra of Co_3O_4(A), rs-CoO(B), CoOOH(C) and w-CoO(D) after OER conditioning for 15 min at 1.62 V in 0.1M KPi at pH 7. The spectra were recorded at a kinetic energy of the electrons of 550 eV.

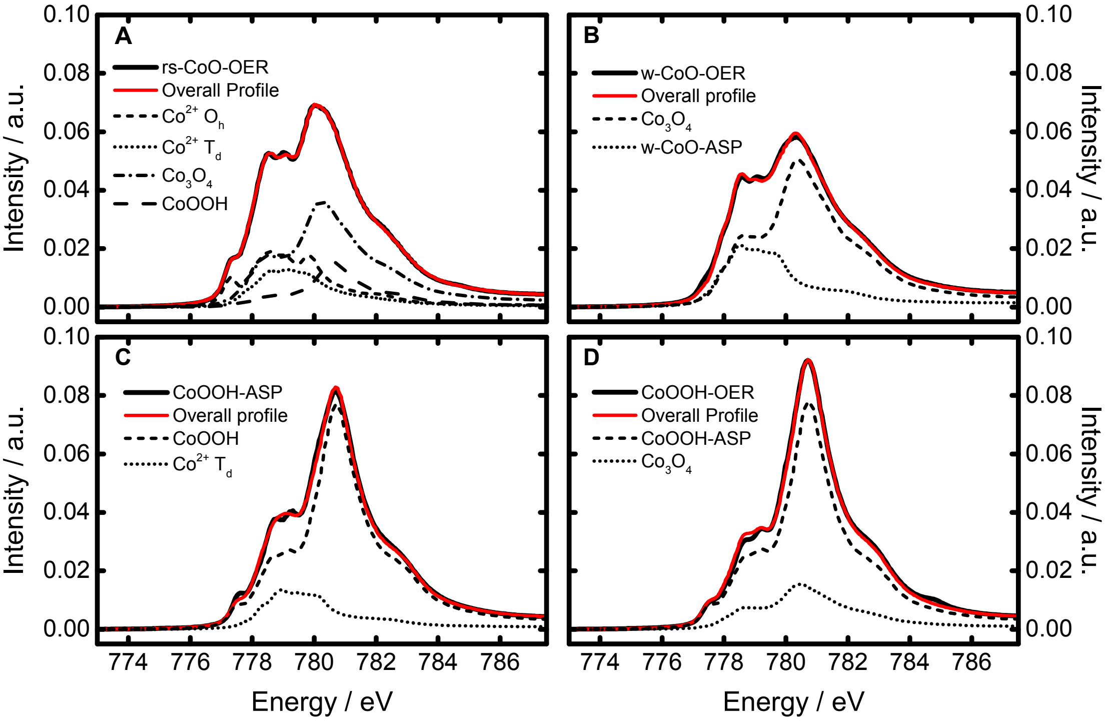

Figure A38: Fits of the Co L_3 XANES spectra of rs-CoO (A), w-CoO (B), CoOOH-ASP (C), and CoOOH-OER (D). The OER conditioned samples were treated for 15 min at 1.62 V in 0.1M KPi at pH 7.

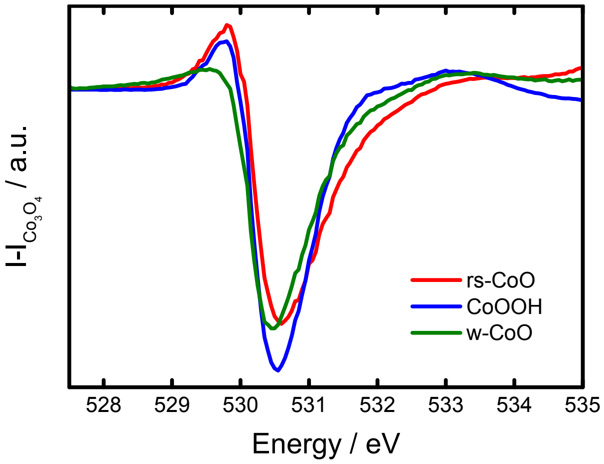

Figure A39: Difference of the pre-edge features of the O *K* XANES spectra of rs-CoO(red), CoOOH(blue) and w-CoO(green) with respect to Co_3O_4. The spectra were recorded in total-electron yield mode and after OER conditioning in 0.1M KPi at pH7.

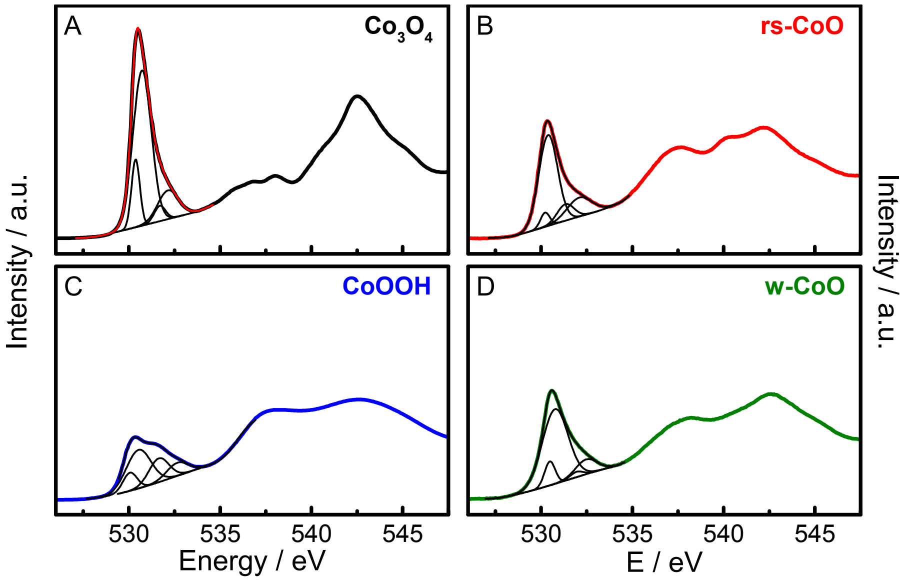

Figure A40: Fits of the pre-edge feature of the O *K* XANES spectra of Co_3O_4(A), rs-CoO(B), CoOOH(C) and w-CoO(D) after OER conditioning in 0.1M KPi at pH7.